DIODE-PUMPED IMM NEODYMIUM LASERS AND THEIR INTERNAL FREQUENCY DOUBLING

Carl Yelland

A Thesis Submitted for the Degree of PhD
at the
University of St Andrews

1997

Please use this identifier to cite or link to this item:
http://hdl.handle.net/10023/14788

Diode-Pumped 1 μm Neodymium Lasers And Their Internal Frequency Doubling

Thesis submitted for the degree of Doctor of Philosophy
to the University Of St. Andrews
by
Carl Yelland BSc ARCS

J. F. Allen Laboratories
School of Physics & Astronomy
University of St. Andrews
Fife
Scotland

July 1996

ProQuest LLC.
789 East Eisenhower Parkway
P.O. Box 1346
Ann Arbor, MI 48106 – 1346

ACKNOWLEDGEMENTS

I would like to thank Professor Wilson Sibbett for giving me the opportunity to study in his research group at St. Andrews, for his continued support of the work and for his efficient proof-reading of this thesis. I also wish to thank the Engineering and Physical Sciences Research Council for financial support.

I am greatly indebted to Dr Junhua Hong† for his sincere help, encouragement and advice during the early stages of the work, and for the many hours of his time spent in informative and stimulating discussion. Thanks are also due to the staff of the mechanical and electronic workshops for their frequent assistance.

Finally, I wish to thank my family for their moral support over the last few years.

---

† Current address: Institute for Information Technology,
National Research Council of Canada, Ottawa, Ontario.

DECLARATION AND COPYRIGHT

I, Carl Yelland, hereby certify that this thesis, which is approximately 50,700 words in length, has been written by me, that it is the record of work carried out by me and that it has not been submitted in any previous application for a higher degree. I was admitted as a research student on 1st July 1992 and as a candidate for the degree of PhD on 1st July 1993. The higher study for which this is a record was carried out in the University of St. Andrews between 1st July 1992 and 30th June 1996.

In submitting this thesis to the University of St. Andrews I understand that I am giving permission for it to be made available for use in accordance with the regulations of the University Library for the time being in force, subject to any copyright vested in the work not being affected thereby. I also understand that the title and abstract will be published, and that a copy of the work may be made and supplied to any *bona fide* library or research worker.

……………………………………………………*Carl Yelland BSc ARCS*
25th July, 1996……………*Date*

CERTIFICATE

I hereby certify that the candidate has fulfilled the conditions of the Resolution and Regulations appropriate for the degree of PhD in the University of St. Andrews and that the candidate is qualified to submit this thesis in application for that degree.

……………………………………………………*Professor Wilson Sibbett*
25 July 1996……………*Date*

ABSTRACT

In this thesis the design, construction and performance of several diode-laser pumped continuous-wave neodymium lasers are described. These lasers were operated both around 1 μm and, by internal frequency-doubling, at 0.5 μm. The main emphasis has been on the assessment of the various laser designs with regard to their potential for efficient, high-power visible operation.

A variety of pumping geometries, resonator configurations, gain media and internal frequency-doubling schemes were investigated, and their relative merits explored. Both side-pumping and end-pumping arrangements were employed, with Nd:YAG, Nd:YLF and Nd:YVO_4 being used as gain media. Travelling-wave and standing-wave resonator designs were used. The polarisation-rotation effect in non-planar ring resonators was investigated and used to obtain single-frequency output.

Single-frequency 0.5 μm powers up to 1.2 W were generated, and the highest 0.5 μm output power achieved was 4 W on two-longitudinal modes spaced by 450 MHz. The highest 1 μm output power achieved was 10 W, with a slope efficiency of 43%. Maximum pump powers for the lasers were in the region 15 - 35 W.

A review of diode-laser pumped devices is included, with particular emphasis on the role of the spatial distributions of the pump and signal fields, because this is an important limiting factor in the performance of diode-pumped bulk laser systems. The criteria governing the harmonic output power when internally frequency-doubling are discussed. Issues relating to noise in the harmonic output, and techniques for its avoidance, are also discussed.

CONTENTS

Chapter 1 **Review of Diode-Laser Pumped Solid-State Lasers**

Chapter 2 **Diode-Laser Devices for Pumping Solid-State Lasers**

Chapter 3 **Internal Second Harmonic Generation**

Chapter 4 **Side-Pumped Nd:YAG Slab Ring Laser**

Chapter 1

REVIEW OF DIODE-LASER PUMPED SOLID-STATE LASERS

1.1 Overview

1.1.1 General

Probably the first use of a semiconductor source to pump a solid-state material was by Newman in 1963 [1.1], who found that radiation in the region 865 - 890 nm emitted by GaAs LEDs could excite 1.06 μm fluorescence in Nd^{3+}:$CaWO_4$, a material in which laser action had been achieved in 1961 [1.2]. Newman recognised some of the advantages of semiconductor pump sources, such as high electrical-to-optical efficiency, compactness and the possibility of good spectral overlap with the strong absorption bands of rare-earth ions such as neodymium. In 1964 Ochs and Pankove demonstrated an LED-pumped laser of Dy^{2+}:CaF_2, in which a rod of the gain material was transversely pumped by 10 arrays of 10 GaAsP LEDs arranged in a cylindrical geometry. 100 mW of pump power at 720 nm could be applied to the rod during 200 ms pulses, giving laser action at 2.36 μm [1.2a]. The low energy of the lower laser level and the primitive LED technology meant that the entire laser had to be cooled in liquid helium. Two years after the development of the first GaAs diode-lasers [1.3-6] Keys and Quist took advantage of this brighter and more powerful pumping technology and operated the first diode-laser pumped solid-state laser (DPSSL) [1.7]. This consisted of a 3 mm diameter, 4 cm long rod U^{3+}:CaF_2 rod with confocal end faces side-pumped by five GaAs diode-lasers. The experimental arrangement is shown in Figure 1.1. The pumping system could deliver 4.5 W of average power at 840 nm in 3 ms pulses at 10 Hz. The lasing wavelength was 2.613 μm. This device also had to be cooled to liquid helium temperatures. Keyes and Quist recognised the advantages of diode-laser pumping over flashlamps, and predicted fewer thermal problems in high power systems due to the more efficient use of the pump light. However, due to the poor performance of early pump devices, where CW operation was difficult even at cryogenic temperatures, little attention was paid to these early DPSSLs.

After the development of Nd^{3+}:YAG and its flashlamp-pumped laser operation by Geusic *et al* in 1964 [1.8], interest was firmly shifted to ions of the rare-earth elements, especially neodymium. These elements possess many narrow fluorescent transitions in the near infra-red, relatively unaffected by crystal field effects due to the shielding of the *5p* and *6s* electrons. The pump-bands of these ions conveniently coincide spectrally with emission from what where then (and still are) the most

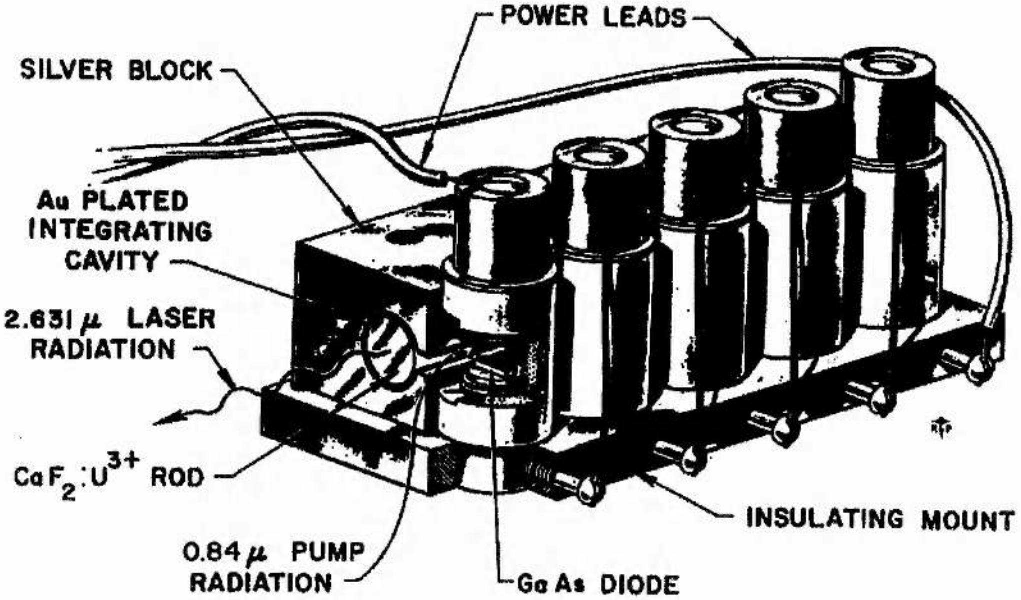

F

Figure 1.1. The first diode-laser pumped solid-state laser [1.7].

technologically advanced diode-lasers, namely double heterostructures of the GaAs - $Al_xGa_{1-x}As$ system. To date, diode-pumped laser action has been demonstrated in Pr^{3+}, Pm^{3+}, Nd^{3+}, Ho^{3+}, Er^{3+}, Tm^{3+} and Yb^{3+}. Ross demonstrated the first diode-laser pumped Nd^{3+}:YAG laser in 1968 [1.9]. This consisted of a rod side-pumped by a single GaAs diode-laser, and there followed a number of reports on side-pumped schemes. That of Ostermayer *et al* [1.10] owed something to flashlamp technology, 64 dicrete diode-lasers being coupled into a Nd^{3+}:YAG rod by a semi-elliptical reflector. Conant and Reno [1.11] noted that the higher brightness of diode-lasers produced greater inversion and higher gain compared to lasers pumped by LEDs. After a short delay, end-pumped lasers were developed in parallel with their side-pumped counterparts. The more efficient collinear pumping due to better mode-matching and a longer absorption path was first utilised by Rosenkrantz [1.12], who end-pumped a Nd^{3+}:YAG rod at 868 nm using a pulsed single-stripe device. Some hybridisation of the side- and end-pumped geometries occured in the use of "tightly-folded resonators" (TFRs) [1.13], in which the signal mode undergoes many total internal reflections across a side-pumped slab of gain material and is therefore "quasi-end-pumped". These devices are noted for very high efficiencies. During the last 15 years many novel pumping geometries have been demonstrated, all of them having beneficial impacts on thresholds, slope efficiencies, maximum output power and longitudinal and transverse mode quality.

In addition to the investigation of various active species, considerable effort has been devoted to the study of host materials. Ease of fabrication, low scatter losses, hardness and chemical inertness are desirable in all laser host materials, however the choice of a particular host material for a given type of laser device also requires attention to thermal conductivity, absorption coefficient, spectral width of absorption and emission features, birefringence effects and change of refractive index with temperature. It is impossible to generalise about which hosts are "better" than others without knowledge of the particular application for which a host is intended.

In the early 1980s, diode-lasers and diode-laser arrays of the GaAs - $Al_xGa_{1-x}As$ system became available which could be operated pulsed or CW at room temperature in the region 780 - 810 nm at the multi-watt output level, giving scope for vast improvements in rare-earth ion lasers in a variety of host materials. Commercially, the main driving force behind this development was diode-laser usage in mass markets such as CD players, laser printers and optical memories. Their use in DPSSLs was seen to arise from tasks requiring efficient, reliable, diffraction-limited laser output, such as remote sensing from satellites, space-based communications and wind-shear sensing from aircraft or at airports.

The modern DPSSL can be viewed as a device which combines the advantages of diode-laser bars (compactness, longevity, robustness, efficiency) with the features of conventional laser resonators, *i.e.* coherence, directionality and brightness. When operated above threshold we essentially have a beam quality, wavelength and coherence converter. For every n pump photons per second input to the laser above threshold, we obtain ηn photons per second out of the laser, where η is the slope efficiency of the device. However, the output photons have improved properties compared to the pump radiation: they are coherent, they have been wavelength converted, and they are now contained in a diffraction limited beam. In addition, we have in the case of a free-space system an external resonator which can be accessed for a variety of applications, for example frequency conversion or short-pulse generation.

1.1.2 Non-Bulk Forms of Diode-Pumped Solid-State Laser

In addition to side and end-pumped bulk amplifiers in external resonators, there have been several evolutionary extremes of the diode-pumping concept, each with its own particular advantages, limitations and uses.

1.1.2.1 Fibre Lasers

The concept of doping optical fibres with ions of the rare-earth elements to form fibre lasers and amplifiers was implemented soon after the operation of the first laser. Although these devices were initially flashlamp-pumped by winding the fibre directly onto the lamp [1.14, 15] the main method of excitation has been by end-pumping with diode-lasers. Active fibres have several advantages. The long pump-signal interaction length results in low thresholds and high efficiencies [1.16 - 18], immunity from thermal problems and allows the operation of weak laser transitions. In addition, low intrinsic fibre losses allow the use of weak absorption bands and the exploitation of weak nonlinearities. Most glass fibre devices have broad linewidths allowing tuning and short pulse operation. The technology can also accommodate in-fibre devices such as gratings, couplers and etalons. The most important application of the fibre architecture is the erbium-doped silica fibre amplifier, which operates near 1.54 μm [1.19], and can be pumped at 980 nm and 1.48 μm: this system is used for long-haul optical communications. The development of low-phonon energy glasses such as ZBLAN has given rise to visible up-conversion lasers operating in the range 455 - 635 nm, by pumping in the region 650 nm -1 μm. Fibre lasers have also been extended to high power operation by use of cladding-pumping technology, in which an inner active monomode core of ≈ 10 μm diameter confines the signal radiation, and a much larger surrounding core (*e.g.* 400 μm diameter) confines the pump. The use of a large-diameter pump-core allows more pump radiation to be coupled into the system due to the higher etendue. Recently, such a device has produced over 9 W of output power at 1070 nm for a pump power of 35 W at 810 nm [1.20].

1.1.2.2 Planar and Channel Waveguide Lasers

Active waveguides combine the advantages of low thresholds and high efficiencies with the opportunity for integration into monolithic devices, and therefore much of the work in this area has concentrated on materials with high electrooptic and nonlinear coefficients such as $LiNbO_3$ and $LiTaO_3$. Several fabrication methods exist, including ion-implantation, ion-exchange and epitaxial growth.

Ion-implantation has been used to create Nd^{3+}-doped active waveguides in YAG [1.21, 22], YAP [1.23], MgO:$LiNbO_3$ [1.24] and GGG [1.25], as well as other rare-earth systems such as Tm^{3+}:lead germanate glass [1.26], and Er^{3+}:glass [1.27, 28.]. The process involves the bombardment of a polished surface of the doped material with He^+ ions with energies of several MeV. Initially, the ions are slowed by electronic excitation, forming colour-centres which can subsequently be removed by annealing. After several microns, the ions undergo nuclear collisions, creating a well-defined low-index optical barrier. Light launched into the top few microns of the implanted crystal will be confined by the crystal-air interface and the low-index barrier. However, it has been found that in many materials such as YAG, $LiNbO_3$, $BeAl_2O_3$ (alexandrite) and $LiCaAlF_6$ there is also a small increase in refractive index in the electronic stopping region.

Channel guides can be formed by coating the surface with a suitable metal (e.g. chromium or gold) followed by a layer of photoresist and then using standard photolithographic techniques to define the channels, which are typically 4 - 20 μm wide. Ion bombardment is used as before and the remaining metal masking is removed. The additional pump and signal mode confinement provided by the channel architecture has led to order-of-magnitude reductions in threshold pump powers compared to planar devices. For example in [1.29], a channel guide Nd^{3+}:YAG laser was reported to have a threshold of 500 μW; planar structures typically require several milliwatts of pump power to achieve threshold.

Epitaxial growth of Nd:YAG planar waveguides can be achieved by dipping a pure YAG substrate into a Nd-doped melt to form a 10 - 50 μm active layer, followed by a pure YAG melt to form a 50 - 100 μm cladding layer. Pumping with single-stripe AlGaAs diode-lasers has produced thresholds of a few milliwatts and slope efficiencies as high as 40% [1.30]. Epitaxially grown Nd^{3+}:YAG waveguide lasers have also been side-pumped [1.31], and operated on the weak $^4F_{3/2}$ - $^4I_{9/2}$ 946 nm transition [1.32].

Planar guides have also been developed with nonlinear materials as the high-index layer; for example in $KNbO_3$ [1.33]. These systems provide very high conversion efficiencies (up to 30%) and can be monolithically integrated with waveguide lasers. Similarly, self-doubling materials such as Nd:YAB show enhanced conversion efficiency over bulk devices.

1.1.2.3 Monolithic Micro-lasers

A simple extension to the diode-pumped laser concept is to create very small laser oscillators by coating dielectric mirrors directly onto small pieces of gain material. Two examples of this approach are the microchip laser and the monolithic non-planar ring oscillator (NPRO).

A microchip laser consists of a small piece of gain material typically a few millimeters square and 300 - 1000 μm in length (depending on the gain material) with dielectric coatings deposited directly on the ends. They are normally end-pumped by diode-laser arrays. There has been considerable interest in these devices due to their highly desirable operating characteristics, such as single longitudinal and transverse mode operation, high efficiency, tunability and a narrow linewidth, which can be as low as a few kHz. Their compactness, reliability and cheapness have made them targets for commercial mass production. Thermal guiding has been shown to be the predominant mechanism that gives cavity stability, either through a change of refractive index with temperature or a thermally induced bulge on the mirror surfaces, although in quasi-three-levels devices, such as Yb:YAG, soft aperture guiding by off-axis reabsorption loss may also be involved [1.34]. Nd^{3+} doped devices operating around 1.06 μm have been demonstrated in a variety of hosts including YAG [1.35], YLF [1.36], YVO_4 [1.37], GSGG [1.38] and LMA ($LaMgAl_{11}O_{19}$) [1.39]. Since very short cavities are required for single frequency operation and wide tunability, materials with a strong absorption at the pump wavelength are required. Nd^{3+} microchip lasers have also been operated at 1.3 μm [1.40, 41]. Tuning has been achieved over tens of MHz by the use of electrooptic materials in composite cavities [1.42], separate piezoelectric-mounted cavity mirrors [1.43], heating of the gain medium [1.44], and modulation of the pump power [1.45].. Other rare-earth systems have also been operated, such as Ho, Tm:YLF [1.46], and

$Tm:YVO_4$ [1.47]. These form compact sources for the eye-safe 2 μm region. $Tm:YVO_4$ can be pumped around 800 nm by AlGaAs diodes, with emission at 1.9 μm. This emission coincides with strong absorption in Ho doped materials; the $Tm:YVO_4$ microchip laser is therefore an attractive alternative to relatively inefficient InGaAsP diodes for Ho pumping. Other candidates for microchip materials are those that can be highly doped with the active species without concentration quenching, such as Cr^{3+} in coloquirites [1.48] (e.g. LiSAF, LiCAF, LiSGaF) and stochiometric materials such as LNP [1.49]. Telecommunications applications have been accommodated by Er, Yb:glass devices operating at 1.53 μm. [1.50]; the Yb concentration being adjusted to give strong absorption at 980 nm for pumping with InGaAs diode-lasers.

The current lack of reliable room-temperature blue and green semiconductor lasers has given rise to much effort in the frequency doubling of 1 μm microchip lasers for data storage applications. Generally this is achieved using composite cavity $Nd:YVO_4$ systems [1.51, 52] although self-doubling in Nd:YAB has also been demonstrated [1.53, 54]. Output powers up to hundreds of milliwatts have been achieved.

Diode-laser pumped monolithic non-planar ring oscillators (NPROs) have been studied since the mid-1980s [1.55]. These devices, made from Nd:YAG, consist of a single piece of gain material, cut such that the path of the laser oscillator describes an out-of-plane path inside the Nd:YAG itself. This non-planarity produces a reciprocal rotation of polarisation around the ring. Nd:YAG has an appreciable Verdet constant and by applying a magnetic field to the monolithic device, a non-reciprocal Faraday effect can be produced. These two effects are combined to give a small differential loss between the two directions resulting in unidirectional single frequency operation by elimination of spatial hole burning. The dependence of the reciprocal rotation on non-planarity in a bulk ring laser forms an important part of the experimental work in this thesis, and is fully described in Chapter 4. NPROs have shown exceptional frequency stability of less than 500 Hz [1.56] due to the rigid resonator. Frequency tuning over 100 MHz has been achieved by using a piezo-electric material bonded to the device, allowing efficient second-harmonic generation by external doubling in a monolithic nonlinear device [1.57]. Diode-pumped monolithic NPROs have been scaled to output powers at the 1 - 2 W level [1.58], and have shown slope efficiencies up to 60% [1.59].

1.2 Active Ions and Host Materials for Diode-Laser Pumping

1.2.1 Neodymium, Nd^{3+}

1.2.1.1 Nd:YAG (Nd:$Y_3Al_5O_{12}$)

Nd^{3+} was the first rare-earth ion to be used as a laser species, and has by far received the most attention, both in terms of operating wavelengths and number of host materials. The main reason for this is the strong absorption near 808 nm, which has allowed efficient and reliable AlGaAs diode-laser pumping. For 30 years YAG has been the principal crystalline host for Nd^{3+} due its good thermal conductivity, chemical inertness and hardness. Within a few years of the first laser operation of Nd:YAG [1.8] samples of high optical quality were available. The cubic structure of YAG favours narrow linewidth transitions, allowing the generation of highly coherent output. Absorption and fluorescence spectra are shown in Figures 1.2 and 1.3. Nd:YAG has found particular application in high power systems, where heat removal and high rupture stress are the main considerations, although its isotropy can give rise to thermally induced birefringence, limiting its performance. In addition, any kind of pumping with poor spatial overlap of pump and signal modes generally leads to an upper limit on power output due to thermal lensing. Concentration quenching of the upper state lifetime limits the Nd^{3+} concentration to ≈ 1.5%.

Laser oscillation has been achieved between the ${}^4F_{3/2}$ manifold and all four manifolds of the ${}^4I$ configuration by diode-laser pumping; the principal transitions to each terminal manifold are summarised in Table 1.1. The ${}^4F_{3/2}$ - ${}^4I_{15/2}$ gives weak emission at 1.833 μm [1.60]. Although flashlamp operation was achieved on this line in

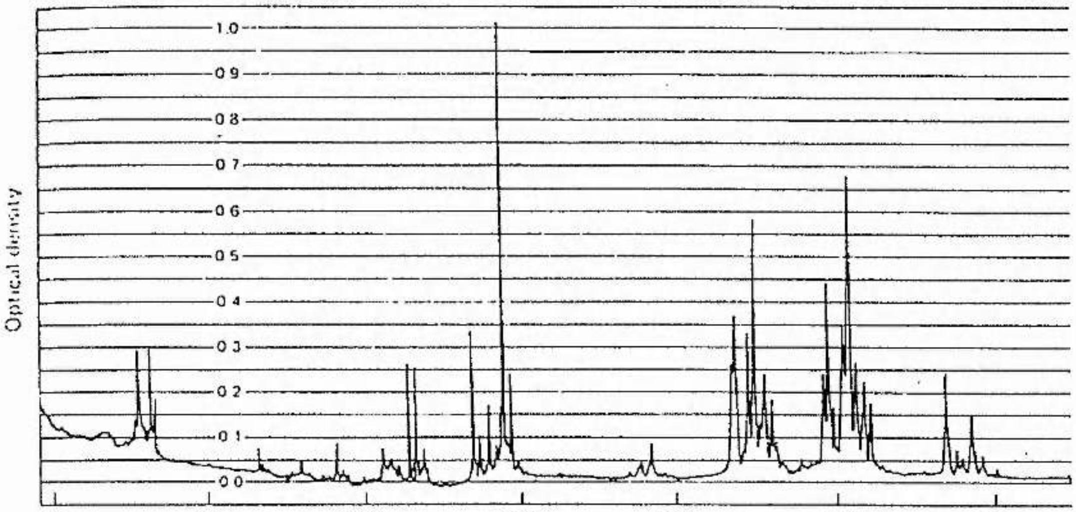

Figure 1.2. Absorption spectrum of Nd:YAG [1.81].

the 1960s, there are very few reports of its diode-pumped operation, probably due to the existence of more feasible eye-safe alternatives (Section 1.2.2 - 5). The advent of high power diode-laser devices has allowed exploitation of the quasi-three-level ${}^4F_{3/2}$ - ${}^4I_{15/2}$ 946 nm transition [1.61 - 64] with its associated opportunity for blue light generation by frequency doubling [1.65, 66]. Efficient operation on this line has required

Upper and lower laser manifolds	Upper and lower Stark-split laser levels (cm^{-1})	Emission wavelength (nm)	Stimulated emission cross-section (10^{-23} m^2)	Upper state lifetime (μs)	Fluorescence linewidth (GHz)
${}^4F_{3/2}$-${}^4I_{15/2}$	11502-958	1833			
${}^4F_{3/2}$-${}^4I_{13/2}$	11502-4028	1338	0.9 [1.73]		120 [1.85]
${}^4F_{3/2}$-${}^4I_{13/2}$	11502-3921	1319			120 [1.85]
${}^4F_{3/2}$-${}^4I_{11/2}$	11502-2111	1064	3.4 [1.73]	244 [1.73]	180 [1.84]
${}^4F_{3/2}$-${}^4I_{9/2}$	11414-848	946	0.58 [1.83]	230 [1.63]	

Table 1.1. Principal laser transitions in Nd:YAG from ${}^4F_{3/2}$ to the ${}^4I$ manifolds.

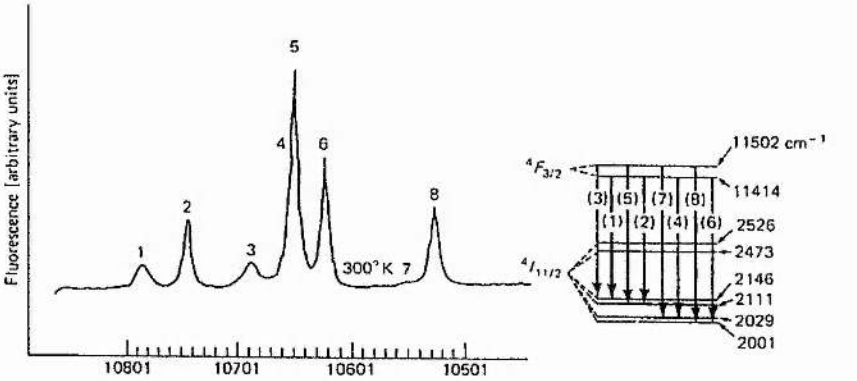

Figure 1.3a. Fluorescence spectrum of Nd:YAG near 1 μm [1.81].

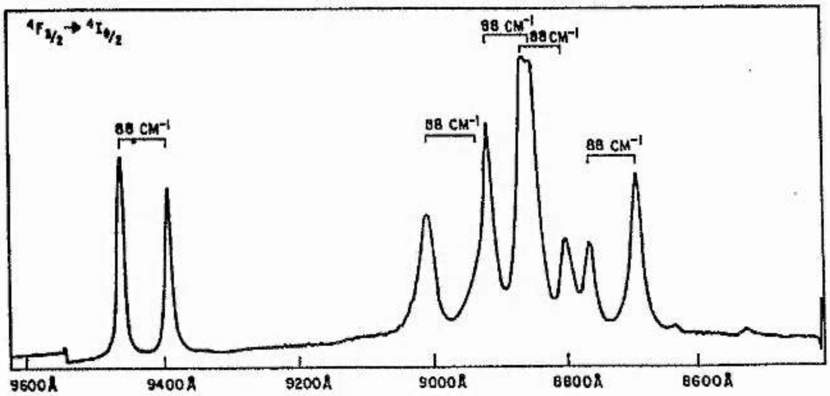

Figure 1.3b. Fluorescence spectrum of Nd:YAG, 0.8 - 0.9 μm [1.82].

diode-pumping due to the high inversion needed, reabsorption losses and the low stimulated emission cross-section, which is an order of magnitude lower than that for the ubiquitous 1064.15 nm line. The $^4F_{3/2}$ - $^4I_{13/2}$ transition results in emission on two lines with roughly equal gain, 1319 nm and 1338 nm. These lines have attracted interest for telecommunications and frequency doubling to ≈ 0.65 μm. Several diode-pumped devices have been demonstrated [1.67 - 70]. The 1064.15 nm line results from the $^4F_{3/2}$ - $^4I_{11/2}$ transition and is the most commonly used transition because of its high gain. The energy level diagram for this line is shown in Figure 1.4.

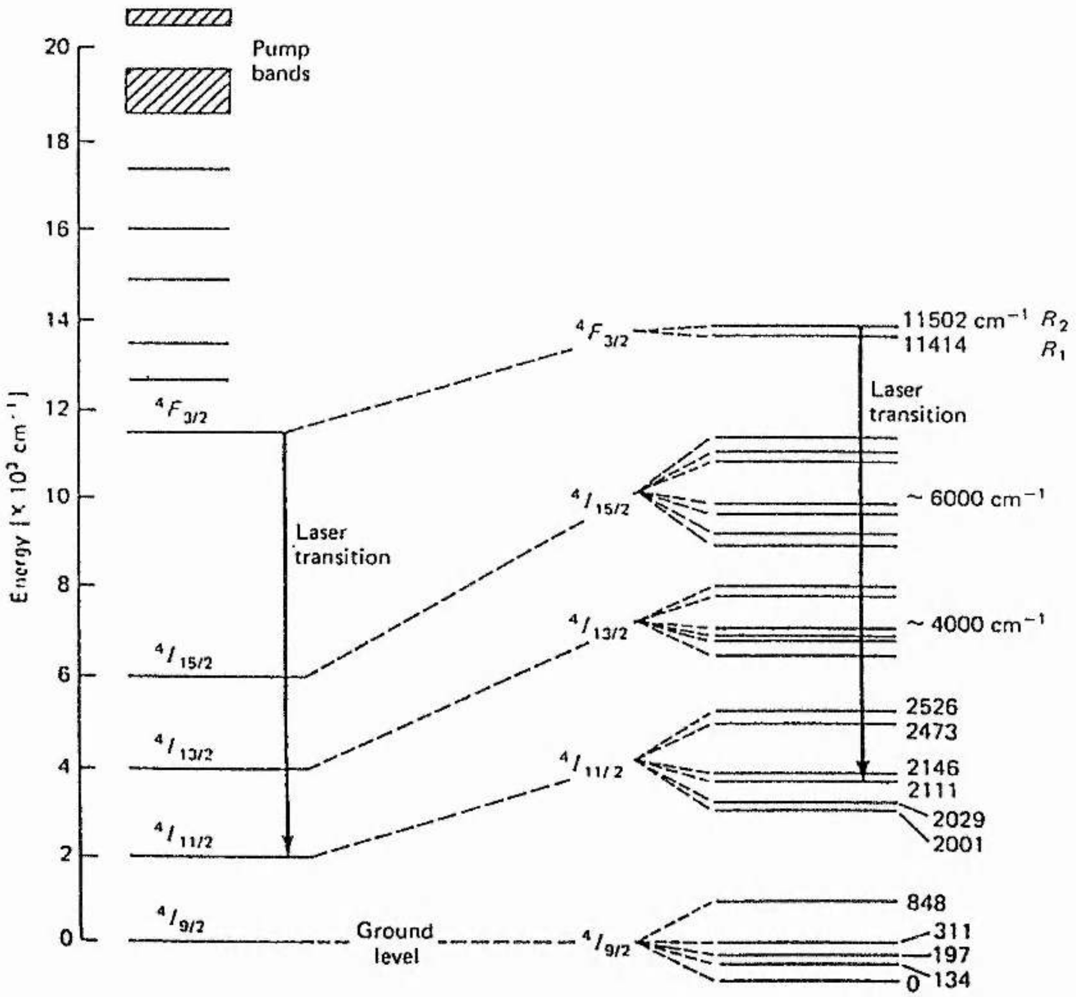

Figure 1.4. Energy level scheme for 1064 nm laser operation in Nd:YAG [1.81].

1.2.1.2 Nd:YLF (Nd:LiYF$_4$)

The positive uniaxial scheelite-structured host yttrium lithium fluoride was first investigated as a host crystal for Nd^{3+} by Harmer *et al* in 1968 [1.71], and more recently by Ryan and Beach [1.72]. Initially, the quality of the crystals was relatively poor, but substantial improvements have taken place over the last decade and this host now has a firm foothold for certain applications. Strong absorption occurs at 797 nm for σ polarisation (perpendicular to the c axis) and at 797 and 792 nm for π polarisation (parallel to the c axis). Absorption spectra are shown in Figure 1.5. $^4F_{3/2}$ - $^4I_{11/2}$ radiative emission occurs at 1047.1 nm (π, extraordinary) and 1053.0 nm (σ, ordinary). Although the stimulated emission cross-sections are roughly half that for Nd:YAG, the upper state lifetime of 480 μs allows high energy storage and makes the material attractive for diode-pumping and Q-switching. Its broader gain bandwidth makes it a more promising choice for 1 μm mode-locked systems than Nd:YAG, and the absorption peaks are also wider than YAG, particularly at 792 nm, giving improved spectral overlap with the emission of AlGaAs diode-laser arrays. Absorption spectra are shown in Figure 1.5. Typical reviews of Nd^{3+} hosts [1.73, 73a] indicate that the gain at 1047.1 nm is ≈ 40% higher than that of the 1053.0 nm line, although the 1053 nm transition is useful for matching the peak gain of Nd-doped phosphate and fluorophosphate glasses used in amplifier chains. Emission spectra are given in Figure 1.6.

In certain situations the uniaxial nature of YLF can be beneficial; its natural birefringence eliminating any thermal depolarisation that can occur in isotropic hosts such as YAG. CW laser operation of YLF was first demonstrated by Pollak *et al* in 1982 [1.74]. This work showed that YLF has negative *dn/dt* and is therefore less susceptible to thermal lensing than YAG. However the thermal conductivity of YLF (6

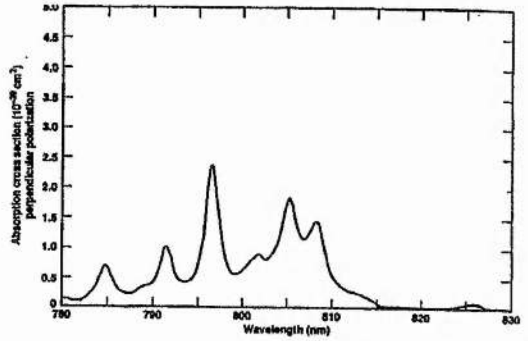

Figure 1.5. Absorption spectra of Nd:YLF for σ (left) and π (right) polarisations [1.72].

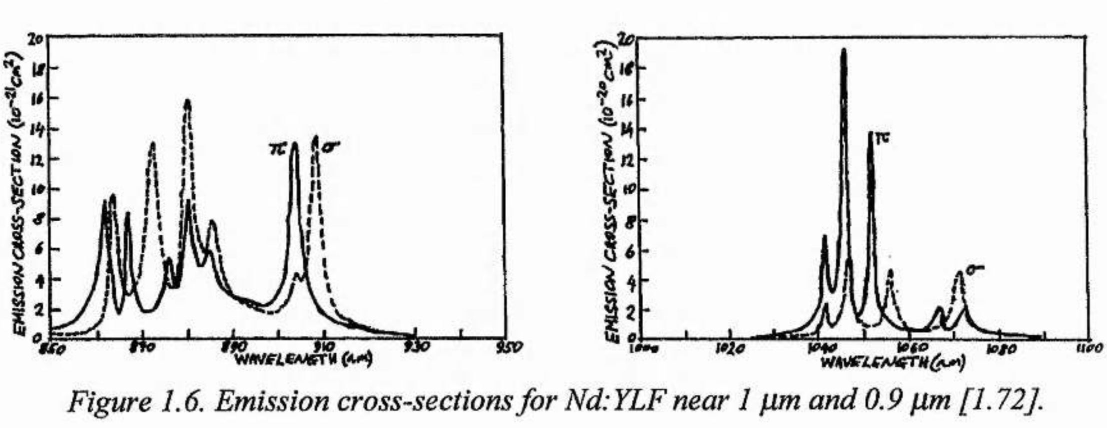

Figure 1.6. Emission cross-sections for Nd:YLF near 1 μm and 0.9 μm [1.72].

W cm^{-1} K^{-1}) is only around half that of YAG, making it prone to fracture under hard end-pumping. YLF is therefore not a good choice for high power end-pumped lasers.

The $^4F_{3/2}$ - $^4I_{13/2}$ 1.3 μm system has also been demonstrated [1.68], emission occurring on the two lines 1321 nm (π) and 1313 nm (σ). The gains are around one quarter of that for 1047.1 nm.

1.2.1.3 Nd:YVO$_4$

Yttrium orthovanadate was first investigated as a host material for Nd^{3+} in 1966 [1.75, 76] with spectroscopic investigations being carried out up to the mid-1970s [1.77-80]. Initially, the simultaneous crystallisation of the meta- (YVO$_3$) and ortho-crystal phases made production of good quality samples difficult. In the early 1970s, better growth methods revived interest, but its low thermal conductivity proved a serious disadvantage in flashlamp-pumped lasers. Additional improvements in optical quality over the last 2 - 3 years has now restored the fortunes of this host, and YVO$_4$ is now a serious choice for diode-pumped solid-state lasers.

The crystal is strongly birefringent (positive uniaxial) and is characterised by very strong peak absorption at 808.5 nm of $\approx$ 40 cm^{-1} (π, polarisation parallel to the c axis) which is around five times that of Nd:YAG. The very short absorption depths possible have made the material especially attractive for microchip lasers where the pump light has to be efficiently absorbed within a few hundred microns. Bulk lasers have also benefited from enhanced efficiency. In addition, the stimulated emission cross-section for the $^4F_{3/2}$ - $^4I_{11/2}$ 1064.1 nm σ line is an order of magnitude higher than that of Nd:YAG, although this can lead to significant amplified spontaneous emission. π polarised operation is possible without any polarisation selection element. One disadvantage is its relatively short upper state lifetime ($\approx$ 90 μs), making it less attractive for Q-switching than other hosts.

The cross-section for the $^4F_{3/2}$ - $^4I_{13/2}$ 1342 nm line is larger than that of the 1064.15 nm transition in Nd:YAG, making YVO$_4$ attractive for 1.3 μm operation [1.86].

1.2.1.4 Nd:Glass

Glass is a mixture of oxides. Its main constituents are non-metal oxides, such as SiO$_2$, B$_2$O$_3$ and P$_2$O$_5$. Different metal oxides alter the structure in various ways, making it possible to obtain a wide variety of properties. A large range of Nd-doped glasses can be produced, although among those commercially available, only silicates and phosphates have sufficient optical and mechanical properties to form the basis of laser systems. All are isotropic. The 1.05 μm stimulated emission cross-sections of phosphate glasses are in the region 3.0 - 4.3 x 10^{-24} m^2, which is typically around 50% higher than for the 1.06 μm lines in silicates. Both have fluorescence lifetimes in the region of 300 μs for doping levels of a few percent of Nd$_2$O$_3$. Some of the important physical and optical properties of commercially available phosphate and silicate glasses are summarised in Table 1.2

Properties	**LG-760 Phosphate (Schott)**	**Q-88 Phosphate (Kigre)**	**LG-670 Silicate (Schott)**	**Q-246 Silicate (Kigre)**
Peak Wavelength (nm)	1054	1054	1061	1062
Cross-Section (10^{-24} m^2)	4.3	4.0	2.7	2.9
FWHM Linewidth (nm)	19.5	21.9	27.8	27.7
Fluorescent Lifetime (μs)	330	330	330	340
Refractive Index	1.503	1.545	1.561	1.568
Thermal Conductivity (Wm^{-1}K^{-1})	0.67	0.84	1.35	1.30
dn/dt (20 - 40 °C) (10^{-6} K^{-1})	-6.8	-0.5	2.9	2.9

Table 1.2. Properties of Nd-doped glasses [1.81].

A major disadvantage of glass as a host is its low thermal conductivity, typically around 1 W m^{-1}K^{-1} compared to 13 W m^{-1}K^{-1} for YAG. This makes Nd:glass particularly susceptible to thermal effects, such as thermal lensing, thermal birefringence and thermal damage. However, Nd:glasses have useful spectroscopic properties. Unlike many crystals, the concentration of Nd^{3+} ions can be relatively high without significant concentration quenching of the upper state lifetime. For example, phosphates can be doped to approximately 7% of Nd_2O_3. The absorption peaks in Nd: glass are much wider than in Nd:YAG and have less fine structure. The absorption spectrum of Nd:glass is given in Figure 1.7. The peak around 802 nm has a FWHM of 14 nm, making it highly compatible with diode-laser pumping, even with little attention to the regulation of the diode-laser temperature. For 3% Nd_2O_3 doping, the absorption coefficient is comparable to that of 1% doped Nd:YAG. The fluorescence linewidths of the 1 μm transitions in Nd:glass are around 20 nm wide (FWHM) allowing the generation of sub-picosecond pulses at this wavelength from mode-locked devices. This large bandwidth, which is around 50 times larger than for the 1.06 μm transition in Nd:YAG, is due to the amorphous structure of glass, which causes the Nd^{3+} ions to "see" slightly different surroundings. This makes their energy splittings vary slightly, and consequently different ions radiate at slightly different frequencies, causing a broadening of the spontaneous emission spectrum. The broader linewidth also allows the storage of larger amounts of energy in the amplifying medium for the same linear amplification coefficient. Thus, glass and crystalline lasers compliment each other. Glasses are more suitable for high-energy pulsed operation, whilst crystalline lasers provide higher gain and greater thermal conductivity, making them more suited to CW or high repetition-rate operation.

Although flashlamp-pumped Nd:glass lasers were investigated in the 1960s [1.87], diode-laser pumped oscillation was not demonstrated until 1986 [1.88]. The gain

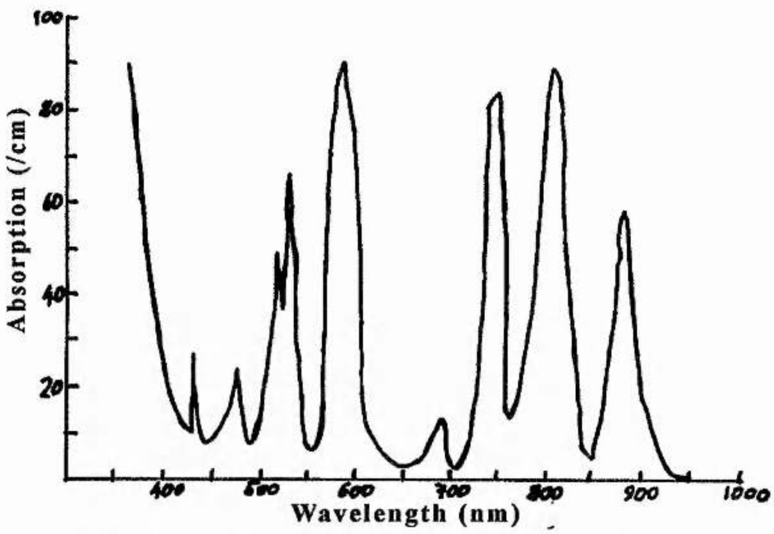

Figure 1.7. Absorpton spectrum of Nd doped ED-2 glass [1.81].

medium was LHG-5 phosphate glass doped with 3.8% wt of Nd_2O_3. A CW output power of 3 mW was achieved for 10 mW of input power from a single-stripe AlGaAs device; the slope efficiency was 42%. Hughes *et al* [1.89] showed substantial scaling by double end-pumping a LG-760 phosphate glass disc (8% wt Nd_2O_3) using four 500 mW diode-laser arrays. The maximum CW output power was 420 mW with 32% slope efficiency. Melting of the glass was cited as a problem for input powers of ≈ 600 mW at a single point. Fan achieved > 0.5 W CW output power by using a rotating glass disc [1.90]. Zig-zag path slabs, rotating discs and moving slabs have been proposed for further scaling [1.91, 92].

1.2.1.5 Nd:YAP (Nd:YAlO$_3$)

In 1969, yttrium orthoaluminate (or yttrium aluminium perovskite, YAP), a crystal host derived from the same physical-chemical Y_2O_3-Al_2O_3 system as YAG became commercially available [1.93]. The crystal has a distorted perovskite structure with an orthorhombic unit cell, making it optically negative biaxial. Growth and crystal features were first reported by Weber *et al* [1.94]. There were early reports on the possible use of YAP as a replacement for YAG, *e.g.* [1.95]. This early enthusiasm was based on the high thermal conductivity of YAP (approximately the same as YAG), and its birefringence which eliminates thermal depolarisation problems and allows polarised operation with no intracavity polarisation selector. Difficulties with purity in crystal growth eventually led to loss of interest in the material. However in the mid-1980s, crystals of high optical quality became available at the same time as the new generation of high power laser-diode devices, and this revived interest in the host particularly for DPSSLs [1.96]. Detailed spectroscopic and crystallographic investigations of the material were carried out in the late 1970s and early 1980s [1.97, 98]; Figure 1.8 shows the polarised absorption and emission features.

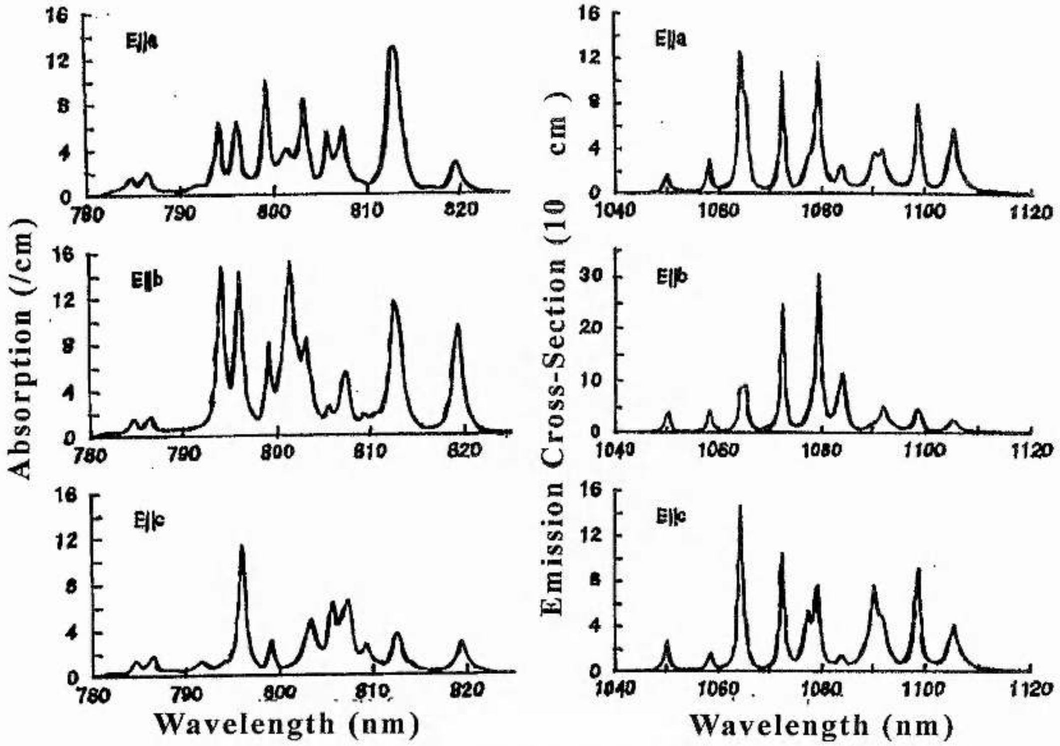

Figure 1.8. Polarised absorption and emission features of Nd:YAP [1.101].

The laser transition is at 1079.6 nm with the signal light polarised along the *b* axis in the Pnma system, with maximum absorption of 14 cm^{-1} also occurring for this polarisation at 803 nm. This value of local absorption wavelength together with its FWHM of around 3 nm makes the material attractive for diode-pumping. Oscillation with E||b is also possible at 1072.5 nm and 1084.5 nm. With E||a and E||c laser operation is also possible at 1064.5, 1090.9 and 1098.9 nm, although with substantially lower gain. Diode-pumped Nd:YAP was first demonstrated in 1988 at 1.34 μm by Scarl *et al* [1.99]. The laser comprised a rod end-pumped with a 500 mW diode system, and around 10 mW of CW output were obtained. The slope efficiency was only 5% due to poor mode-matching. Hanson obtained emission at 1.08 and 1.34 μm by side pumping a *b* axis rod with six quasi-CW arrays at 803 nm [1.100]. Slope efficiencies of 27% and 20% were obtained for operation at 1079.6 and 1341.4 nm respectively. Hanson and Poirier [1.101] have very recently side-pumped an *a* axis rod obtaining E||c operation at 1064.3, 1072.5, and 1099 nm using a birefingent filter.

1.2.1.6 Other Garnets

Several variations of YAG have been grown and investigated as possible hosts for Nd and other rare-earth ions, principally Ho and Er. Substitution of Gd for Y and Sc and Ga for Al has led to YGG ($Y_3Ga_5O_{12}$), YSGG ($Y_3Sc_2Ga_3O_{12}$), GSGG

($Gd_3Sc_2Ga_3O_{12}$), GGG ($Gd_3Ga_5O_{12}$), GSAG ($Gd_3Sc_2Al_3O_{12}$) and YSAG ($Y_3Sc_2Al_3O_{12}$). Most of the literature is concerned with Cr^{3+} sensitisation for flashlamp pumping. This is not helpful in the case of diode-laser pumping, due to the low absorption of the Cr^{3+} $^4T_2$ level near 800 nm. Nd:GSGG has attractive features for high average power Q-switched, diode-pumped operation. It can be grown in large core-free boules, allowing the fabrication of large aperture rods and slabs. It can be doped more heavily than YAG without concentration quenching due to its larger lattice parameter and lower phonon energies. The peak absorption at 808 nm is roughly twice that of YAG for 1% doping, and its lower emission cross-section allows higher energy storage before the onset of amplified spontaneous emission (ASE). Caffey *et al* [1.102] reported a slope efficiency of 41.5% for a pulsed side-pumped rod device. Diode-pumped Nd:GGG has formed the basis of highly frequency-stable non-planar ring oscillators [1.103, 104]. Diode-pumped operation of Nd:YSAG was investigated in 1990 [1.104a].

1.2.1.7 Nd:BEL (Nd:$La_2Be_2O_5$)

Lanthanum beryllate (BEL) was reported as a new host crystal in 1975 [1.105]. BEL is positive biaxial and has monoclinic symmetry so that two of the three independent polarisation directions are along axes of the index ellipsoid which are not crystallographic directions. The strongest 1 μm transition is at 1069.8 nm for light polarised with E||x which has an emission cross-section of 2.1 x 10^{-24} m^2 [1.106]. For operation with E||y and E||z, the 1079 nm line has the highest gain. The absorption feature near 810 nm has a FWHM of ≈ 3.5 nm giving good spectral overlap with the emission of diode-lasers. The fluorescence linewidths at 1069.8 and 1079 nm are both 30 cm^{-1} (compared to 6 cm^{-1} for Nd:YLF) allowing picosecond pulse generation in the mode-locked regime. The upper state lifetime is typically quoted as ≈ 150 μs for a doping level of 1%. Efficient diode-pumped CW [1.107] and mode-locked [1.108, 109] systems have been demonstrated.

1.2.1.8 Nd:LMA (Nd:$LaMgAl_{11}O_{19}$)

Lanthanum magnesium aluminate (LMA) is a negative uniaxial crystal first reported in 1981 [1.110]. Optical properties have been reported in [1.111-113]. The main features are high thermal conductivity (14 and 10 $Wm^{-1}K^{-1}$ perpendicular and parallel to the optic axis respectively) and low concentration quenching; samples are typically doped to 15 - 20 at. % without reduction in the upper state lifetime of 260 - 270 μs. Laser oscillation can be achieved on two lines, 1054.7 and 1082.0 nm, with highest gain occurring for light σ polarised perpendicular to the optic (c) axis. Several local absorption maxima occur near 800 nm, the stongest being at 794 nm for the σ polarisation. The 1054.7 nm line has a fluorescence width of 26 cm^{-1} [1.114] and is therefore useful in mode-locking applications, especially for seeding glass amplifier chains. The 1082 nm line is of use in the optical pumping of helium atoms. The broad linewidth at 1054.7 nm results from the fact that there are three different Nd^{3+} fluorescing sites in the crystal, each experiencing a slightly different crystal field [1.115]. Diode-laser pumped CW lasers have been reported by Hamel *et al* [1.116] and Fan and Kokta [1.117]. Fan suggested that pump and signal excited-state absorption (ESA) could be responsible for the unremarkable slope efficiencies seen from end-pumped systems. FM [1.118] and APM [1.119] mode-locked lasers have been demonstrated, the latter giving 600 fs pulses at 1054 nm.

1.2.1.9 Other Crystalline Hosts

Recently, Nd:YAB (Nd-doped yttrium aluminium borate, $YAl_3(BO_3)_4$) has emerged as an efficient self-frequency-doubling material for its 1063 and 1320 nm lines. The self-doubling concept was first demonstrated in Nd:MgO:$LiNbO_3$ [1.122]. Diode-pumped devices offer compact sources of visible light although at present output powers are less than 100 mW [1.123, 124]. Another new diode-pumpable material is Nd:BZAG (Nd:$Ba_2ZnGe_2O_7$) [1.125]. Apatite crystals have also been investigated recently; principally S-FAP ($Ca_5(PO_4)_3F$) and S-VAP ($Sr_5(VO_4)_3F$) [1.126].

1.2.1.10 Stoichiometric Materials

Stoichiometric materials are compounds which contain the laser species, rather than a host into which the active species is doped. The motivation for research into these materials is to increase the concentration of the active ion, increasing the gain of lasers and allowing the possibility of miniaturisation. Most diode-pumped devices have been concerned with microchips of lithium neodymium tetraphosphate, $LiNdP_4O_{12}$ or LNP, which has about thirty times the Nd concentration of 1% Nd:YAG with a similar cross-section. Diode-pumped operation of LNP has been shown at 1.05 [1.127] and 1.32 μm [1.128]. The very short absorption length in LNP has allowed diode-end-pumping by close-coupling with no collimating or focusing optics [1.129].

1.2.2 Holmium

Diode-pumped eyesafe 2.1 μm Ho^{3+} lasers have potential use in diverse applications such as altimetry, ranging, low altitude wind shear detection and atmospheric remote sensing tasks, for example Doppler lidar wind sensing and water vapour profiling. Ho^{3+} has mainly been operated in YAG or YLF co-doped with Tm^{3+} in order to provide absorption near 800 nm suitable for AlGaAs diode-laser pumping. Absorption peaks at 781.5 and 785.5 nm (both 3 - 4 nm FWHM) can be used to pump the Tm^{3+} $^3F_4$ level. For high enough Tm^{3+} doping (normally $\approx$ 6 at. %), this is mainly followed by a cross-relaxation process whereby one excited Tm ion in the $^3F_4$ level de-excites to produce two Tm ions in the $^3H_4$ level. Fast spatial energy migration of these ions leads to population of the $^5I_7$ level in Ho^{3+} and subsequent $^5I_7$ - $^5I_8$ three-level laser action at 2.1 μm. The 10 ms upper-state lifetime makes the system viable. Ho doping levels have normally been in the range 0.5 - 2 at. %. 2097 nm diode-pumped

Host material	λ_{sig} (nm)	λ_{pp} (nm)	$\Delta\lambda_{pp}$ (nm) (FWHM)	Gain bandwidth (GHz)	Upper state lifetime (μs)	Thermal conductivity ($Wm^{-1}K^{-1}$)
Nd:YAG	1064.1	807.5	1.2 [1.120]	180 [1.84]	230 [1.81]	13 [1.81]
Nd:YLF σ, $E\parallel a$	1053.0	806.0	2.8 [1.120]	360 [1.71]	480 [1.73]	6 [1.74]
π, $E\parallel c$	1047.1	792.5	1.7 [1.120]			6 [1.74]
Nd:YVO_4 π, $E\parallel c$	1064.1	808.5	20 [1.120]	210 [1.79]	98 [1.73]	5.2 [1.86a]
Nd:glass (LG760)	1054	802.0	20 [1.81]	5400 [1.81]	330 [1.81]	0.67 [1.81]
Nd:YAP $E\parallel b$	1079.6	802.0	2.5 [1.101]	360 [1.98]	150 [1.100]	11 [1.121]
$E\parallel c$	1064.5	797.0	2.5 [1.101]			
Nd:BEL $E\parallel x$	1069.8	811.0	1.2 [1.120]	900 [1.108]	140 [1.105]	{a, 4.6 [1.105]}
$E\parallel y$	1079	811.0	0.7 [1.120]			=b, 4.7 [1.105]
$E\parallel z$	1079	810.5	0.4 [1.120]			{c, 4.7 [1.105]}
Nd:LMA π, $E\parallel c$	1054.7	798.0	15 [1.118]	1190 [1.118]	270 [1.117]	10 [1.112]
σ, $E\parallel a$						14 [1.112]

Table 1.3. Comparison of 1 at. % Nd^{3+}-doped host materials for 1 μm operation.

operation in Ho:YAG was first reported by Allen *et al* [1.130]; Henderson and Hale also obtained output at 2090 nm [1.131]. CW output powers have been limited to < 100 mW. In the case of Ho:YLF, pumping is at 792 nm with lasing at 2067 nm; both π oriented [1.132]. An important recent breakthrough is the pumping of singly doped Ho:YAG with InGaAsP and GaInAsSb diode lasers operating at 1.9 μm. Nabors *et al* have recently obtained 700 mW CW output at 2.079 μm [1.133]. The improved quantum efficiency resulted in a slope efficiency of 35%.

Host material	*dn/dT* $(10^{-6}\ K^{-1})$	Stimulated emission cross-section $(10^{-23}\ m^2)$	Refractive Index	Max. dope conc (%)	Peak absorption coefficient (cm^{-1})
Nd:YAG	7 [1.74]	3.4 [1.73]	1.816 [1.81]	1.6	8 [1.86a]
Nd:YLF σ, E||a	-4.3 [1.74]	2.6 [1.73]	1.4481 [1.81]	2	8.6 [1.86a]
π, E||c	-2.0 [1.74]	3.7 [1.73]	1.4704 [1.81]		32.1 [1.86a]
$Nd:YVO_4$ π, E||c	8.5 [1.86a]	6.2 [1.73]	2.168 [1.121]	3	40.7 [1.86a]
σ, E||a	2.9 [1.86a]		1.958 [1.121]		101.5 [1.86a]
Nd:glass (LG-760)	-6.8 [1.81]	0.43 [1.81]	1.503 [1.81]	8	10 [1.81]
Nd:YAP E||b	9.75 [1.101a]	4.6 [1.100]	1.929 [1.98]	1	14 [1.101]
E||c	14.52 [1.101a]	1.5 [1.101]	1.952 [1.98]		12 [1.101]
E||a			1.943 [1.98]		
Nd:BEL E||x	{a, 7.0 [1.105]}	2.1 [1.106]	1.9641 [1.105]	1.4	2.82 [1.106]
E||y	=b, 7.9 [1.105]		1.9974 [1.105]		
E||z	{c, 9.5 [1.105]}		2.0348 [1.105]		
Nd:LMA π, E||c		4 [1.111]	1.7692 [1.112]	20	
σ, E||a			1.7766 [1.112]		

Table 1.3 cont'd. Comparison of 1 at. % Nd^{3+}-doped host materials for 1 μm operation.

1.2.3 Erbium

Interest in Er^{3+} has mainly been confined to Er doped silica fibres and mode-locked systems for low-loss, high-bit-rate fibre communication. However, bulk devices are also of interest for eye-safe applications such as coherent laser radar and medical research. Three diode-pumping schemes are possible: AlGaAs pumping of the $^4I_{9/2}$ level near 800 nm, 975 nm pumping of the $^4I_{11/2}$ level using strained-layer InGaAs, and 1.48 μm pumping of $^4I_{15/2}$ using more established InGaAsP diodes. CW lasing at 2.8 μm has been achieved on the $^4I_{11/2}$ - $^4I_{13/2}$ transition in Er:YLF by AlGaAs pumping at 797 nm [1.134]. Although the lifetimes of these levels (4 and 13 ms respectively) would normally make the system self-terminating, a cooperative up-conversion (energy-transfer) process causes $^4I_{13/2} \rightarrow {}^4I_{9/2}$ repopulation of the upper level allowing lasing. Pumping near 800 nm has, however, the disadvantage of ESA of the pump radiation. The development of strained layer InGaAs diode-lasers has allowed enhancement of $^4I_{13/2}$ - $^4I_{15/2}$ 1.5 and 1.6 μm laser action. These devices have higher output powers than the longer wavelength InGaAsP lasers. In addition, pumping near 975 nm can be made more efficient by using Yb^{3+} as a sensitiser; highly efficient energy transfer from

Yb($^2F_{5/2}$) to Er ($^4I_{11/2}$) occurs for suitable doping levels. This scheme allowed the first room-temperature CW operation of 1.5 μm Er:glass in 1991 [1.135], and 1.6 μm Er:YAG in 1995 [1.136]. Mode-locked bulk Er:glass lasers are capable of generating picosecond pulses at 1.5 μm [1.137].

1.2.4 Ytterbium

Strained-layer InGaAs devices have also opened up the possibility of efficient lasing in ytterbium itself. Previously its usefulness was limited because the trivalent ion has only one *4f* manifold, located at approximately 10 000 cm^{-1}; the next higher level is in the *5d* configuration at ≈ 100 000 cm^{-1}. The Yb laser is a three-level system and the lack of higher-lying states has hitherto limited it to inefficient AlGaAs pumping at liquid nitrogen temperatures [1.138]. The newer InGaAs diode-lasers have given a pumping solution, and allowed some of the advantages of Yb to be exploited. The lack of higher-lying levels means that there is no problem with excited-state absorption or up-conversion. The system cannot suffer from concentration quenching, so that high doping levels (*e.g.* 15 at. %) can be employed, mitigating the three-level nature of the laser. Broad absorption in Yb:YAG occurs at 941 nm with a FWHM of 18 nm; temperature regulation of diode temperature is therefore not an issue. The local absorption maximum at 968 nm has a FWHM of 4 nm. The strongest fluorescence occurs at 1030 nm. The first CW room-temperature diode-pumped Yb:YAG laser was reported in 1991, producing 345 mW with a slope efficiency of 31% [1.139]. The 1.2 ms upper-state lifetime has allowed efficient Q-switched operation [1.140]. Widely tunable high-power CW operation has recently been demonstrated in Yb:YAG [1.141]; this laser, comprising a Yb:YAG disc pumped by fibre-coupled diodes, produced more than 9 W at 1030 nm, and 2.5 W at the tuning extremities of 1020 and 1050 nm.

1.2.5 Thulium

Laser emission from the $^3H_4$ - $^3H_6$ transition in Tm^{3+} at 2.02 μm is another useful source of eye-safe coherent radiation. In Tm:YAG, AlGaAs emission at 785 nm is efficiently absorbed, populating the $^3F_4$ manifold. At Tm^{3+} concentrations above ≈ 3 at. %, cross-relaxation efficiently populates the $^3H_4$ level, from where laser action to a high-lying level in the $^3H_6$ manifold takes place. This cross-relaxation mechanism makes Tm:YAG efficient in CW operation, one absorbed photon leading to two ions in the upper laser level. Q-switched performance in Tm:YAG is aided by the 11 ms (4 at. %) fluorescence lifetime [1.142]. 35 ps pulses have been generated by AO mode-locking, under Ti:Al_2O_3 laser pumping at 785 nm [1.143]; a AlGaAs diode-pumped approach should also be possible.

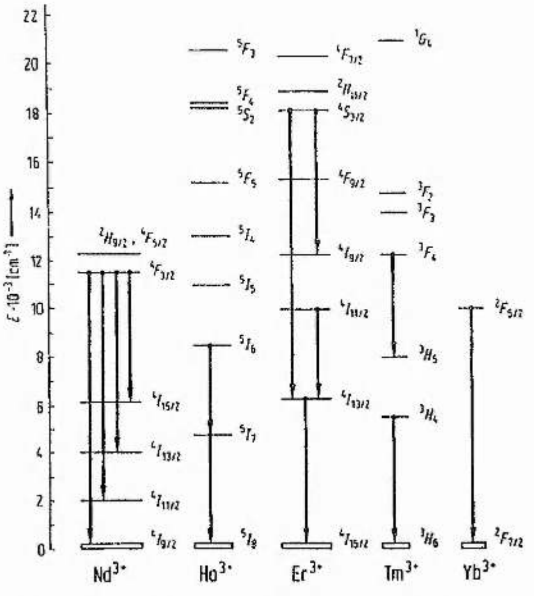

Figure 1.9. Energy levels and laser transitions of RE³⁺ ions in YAG [1.121].

1.3 Review of Four- and Quasi-Three-Level Bulk Laser Action

1.3.1 Longitudinally-Pumped Devices

1.3.1.1 Threshold and Output Behaviour

Although the basic principles of laser behaviour are well understood, treatments accounting for the spatial overlap of pump and signal modes are a comparatively recent development and so considerable emphasis is given here to this aspect. Quasi-three level systems are included since diode-laser pumping has allowed efficient operation of lasers such as 0.9 μm Nd^{3+}, 2.1μm Ho^{3+} and 2.0 μm Tm^{3+}. The starting point for quasi-three-level operation is the generalised energy level diagram shown in Figure 1.9. The lower and upper laser levels are denoted a and b, with respective population densities N_a and N_b. The lower and upper manifold population densities are N_1 and N_2. It is assumed that the populations of the Stark levels within each manifold are in quasi-thermal equilibrium at all times; the probabilities of occupation of the lower and upper laser levels within their respective manifolds are therefore given by Boltzmann factors f_a and f_b. Four-level behaviour can be obtained by taking the limit $f_a \rightarrow 0$. The populations of the upper and lower laser levels are

$$N_b = f_b N_2$$

$$N_a = f_a N_1 \approx f_a N_0.$$

$N_1 \approx N_0$ (the total dopant concentration), as the ground state depletion is assumed to be small. Under steady-state conditions at or below threshold, the population of the upper

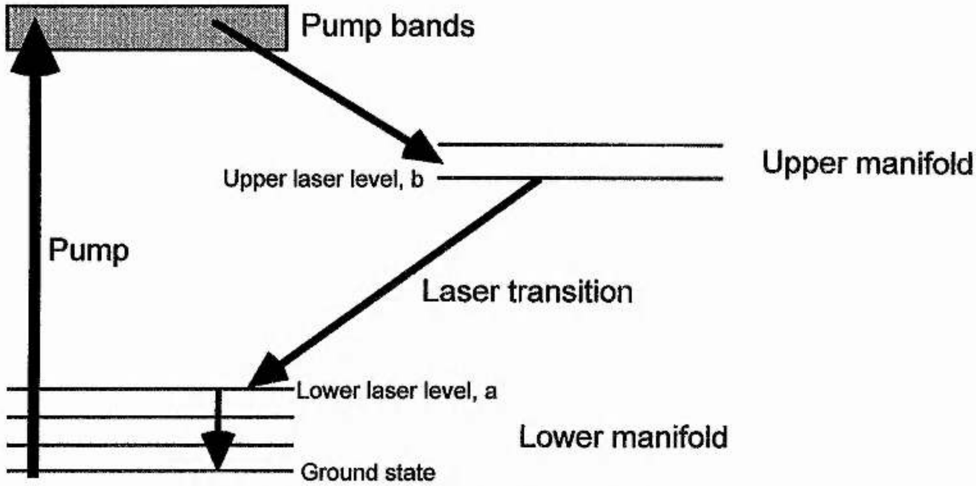

Figure 1.10. Energy level scheme for laser action.

manifold is given by

$$\frac{dN_2(\mathbf{r})}{dt} = 0 = -\frac{N_2(\mathbf{r})}{\tau} + Rp(\mathbf{r}), \tag{1.1}$$

where τ is the fluorescence lifetime, R the pumping rate into the upper manifold, and $p(\mathbf{r})$ is the normalised pump mode intensity distribution, *i.e.*

$$\iiint_{crystal} d^3\mathbf{r}.p(\mathbf{r}) = 1,$$

where the integration is over the volume of the laser crystal. The pumping rate is related to absorbed pump power by

$$R = \frac{\eta_1 P_{abs}}{h\nu_p} \tag{1.2}$$

where η_1 is the pump quantum efficiency. (1.1) gives the population of the upper laser level:

$$N_b(\mathbf{r}) = f_b \tau R p(\mathbf{r}). \tag{1.3}$$

The threshold condition is

$$\iiint_{crystal} d^3\mathbf{r}.2\gamma(\mathbf{r})l = \iiint_{crystal} d^3\mathbf{r}.2\sigma l \Delta \mathrm{N}_{th}(\mathbf{r}) s(\mathbf{r}) = \delta \qquad .(1.4)$$

where γ is the small signal gain, σ the stimulated emission cross-section (assumed equal to the absorption cross-section), l the laser crystal length, δ the distributed total loss (excluding reabsorption loss) and $\Delta N_{th}(\mathbf{r})$ is the threshold population inversion given by

$$\Delta N_{th}(\mathbf{r}) = f_b R_{th} p(\mathbf{r}) \tau - f_a N_0. \tag{1.5}$$

$s(\mathbf{r})$ is the normalised signal mode intensity distribution:

$$\iiint_{crystal} d^3\mathbf{r}.s(\mathbf{r}) = 1.$$

The signal is assumed to comprise only the fundamental TEM_{00} Gaussian transverse mode. From (1.4) and (1.5), the threshold pumping rate is given by

$$R_{th} = \frac{1}{J_1}\left[\frac{1}{f_b\tau}\left(\frac{\delta}{2\sigma l} + f_a N_0\right)\right] \tag{1.6}$$

where

$$J_1 \equiv \iiint_{crystal} d^3\mathbf{r}.p(\mathbf{r})s(\mathbf{r}) \tag{1.7}$$

is the pump-signal overlap integral. For perfect spatial overlap of pump and signal, J_1 will have a certain maximum value. In practical situations (especially under diode-laser pumping) J_1 is less than this, raising the threshold. The lower laser level population, $f_a N_0$, causes additional (re-absorption) loss in a quasi-three-level laser; in a four-level system this term is zero. For a four-level laser (1.6) gives the single pass gain at threshold as

$$\gamma_{th} l = \frac{\eta_1 f_b \sigma\tau P_{abs,th} l J_1}{h\nu_p}. \tag{1.8}$$

The quantity $1/lJ_1$ is the effective pump area. The pump-signal overlap integral J_1 determines threshold, slope and overall efficiencies and, where pump power is limited or restricted, the maximum output power.

Steady-state operation above threshold is described using equations for population inversion density and cavity photon number, S. In the steady-state, the rate of change of inversion is given by

$$\frac{d\Delta N(\mathbf{r})}{dt} = 0 = (f_a + f_b)Rp(\mathbf{r}) - \frac{\Delta N(\mathbf{r}) - \Delta N^0}{\tau} - \frac{(f_a + f_b)c\sigma}{n}\Delta N(\mathbf{r})Ss(\mathbf{r}) \text{ (qu-3-lev),} \tag{1.9}$$

$$\frac{d\Delta N(\mathbf{r})}{dt} = 0 = f_b Rp(\mathbf{r}) - \frac{\Delta \mathrm{N}(\mathbf{r})}{\tau} - \frac{(f_a + f_b)c\sigma}{n}\Delta N(\mathbf{r})Ss(\mathbf{r}) \qquad \text{(4-level),} \tag{1.10}$$

where in (1.9),

$$\Delta N^0 \equiv N_b^0 - N_a^0,$$

N_a^0 and N_b^0 being the thermal-equilibrium populations of levels a and b respectively when the laser is not pumped. n is the refractive index of the active medium. The steady-state cavity photon number is given by the balance in the rate at which photons are output from the laser and the rate at which they are generated by stimulated emission:

$$\frac{dS}{dt} = 0 = \frac{c\sigma}{n}\iiint_{crystal} d^3\mathbf{r}.\Delta N(\mathbf{r})Ss(\mathbf{r}) - \frac{S\delta c}{2ln}. \tag{1.11}$$

From (1.9) and (1.10), the inversion above threshold is given by

$$\Delta N(\mathbf{r}) = \frac{\tau(f_a + f_b)Rp(\mathbf{r}) + \Delta \mathrm{N}^0}{1 + \frac{(f_a + f_b)c\sigma\tau}{n}Ss(\mathbf{r})} \qquad \text{(quasi-three-level),} \tag{1.12}$$

$$\Delta \mathrm{N}(\mathbf{r}) = \frac{\tau f_b Rp(\mathbf{r})}{1 + \frac{(f_a + f_b)c\sigma\tau}{n}Ss(\mathbf{r})} \qquad \text{(four-level).} \tag{1.13}$$

Using (1.12) and (1.13) with (1.11), relations between pumping rate (or absorbed pump power) and cavity photon number can be obtained for quasi-three-level and four-level lasers:

$$\frac{\delta}{2\sigma l}=\iiint\limits_{crystal} d^3\mathbf{r}.\frac{\tau(f_a+f_b)Rp(\mathbf{r})s(\mathbf{r})}{1+\frac{(f_a+f_b)c\sigma\tau}{n}Ss(\mathbf{r})}+\Delta N^0\iiint\limits_{crystal} d^3\mathbf{r}.\frac{s(\mathbf{r})}{1+\frac{(f_a+f_b)c\sigma\tau}{n}Ss(\mathbf{r})}\quad\text{(qu-3-l)}\tag{1.14}$$

$$\frac{\delta}{2\sigma l}=\iiint\limits_{crystal} d^3\mathbf{r}.\frac{\tau f_b Rp(\mathbf{r})s(\mathbf{r})}{1+\frac{(f_a+f_b)c\sigma\tau}{n}Ss(\mathbf{r})}\qquad\text{(four-level).}\tag{1.15}$$

In (1.14), $\Delta N^0 < 0$ so that the last term is an additional (re-absorption) loss due to the significant lower level population. This loss is saturable, so that when the laser is operated well above threshold, *i.e.* S is large, the term in ΔN^0 is negligible. Well above theshold therefore, quasi-three-level and four-level lasers behave in the same way.

To precisely model laser output therefore requires two things. Firstly the functional forms of $p(r)$ and $s(r)$ must be known; this will depend on the pumping device, the pump-signal interaction geometry (*e.g.* side-pumping, end-pumping) and the extent of diffraction of the pump and signal modes inside the laser crystal. Secondly, the volume integrals in (1.14) and (1.15) must be evaluated, and this is not, in general, possible analytically. Numerical methods can be employed for this, *e.g.* [1.144], however, a simple approximation [1.145] leads to a heuristic description for output and slope efficiency. An approximation is made for the integral J_2, where

$$J_2\equiv\iiint\limits_{crystal} d^3\mathbf{r}.\frac{p(\mathbf{r})s(\mathbf{r})}{1+\frac{(f_a+f_b)c\sigma\tau}{n}Ss(\mathbf{r})}.$$

Soon after threshold is reached, the second term in the denominator of the integrand dominates. The approximation is

$$\frac{1}{J_2}\approx\frac{1}{J_1}+\frac{(f_a+f_b)c\sigma\tau S}{n\eta_2}\tag{1.16}$$

where

$$\eta_2\equiv\iiint\limits_{V} d^3\mathbf{r}.p(\mathbf{r})$$

and V is the common volume of the pump and signal fields. The output power in terms of the cavity photon number is given by

$$P_{out}=Sh\nu_s\frac{c}{2\ln}T\tag{1.17}$$

where T is the output coupling. Using (1.6), (1.15), (1.16) and (1.17) the slope efficiency, ε, can be obtained:

$$\varepsilon\equiv\frac{P_{out}}{P_{abs}-P_{abs,th}}=\eta_1\eta_2\frac{\lambda_p}{\lambda_s}\frac{T}{\delta}.\tag{1.18}$$

(1.18) can be rewritten as

$$P_{out} = \frac{1}{2}\eta_2 I_{sat} A_{eff} T\left\{\frac{g_0}{L+T} - 1\right\} \tag{1.19}$$

where $A_{eff} = 1/lJ_1$ is the effective pump area, I_{sat} the saturation intensity,

$$I_{sat} \equiv \frac{h\nu_s}{(f_a + f_b)\sigma\tau},$$

L the internal loss ($\delta = L + T$) and $g_0 = 2\gamma_0 l$ the round-trip gain. The single pass unsaturated gain is given by

$$\gamma_0 l = \frac{f_b \sigma\tau\eta_1 P_{abs} l J_1}{h\nu_p}. \tag{1.20}$$

In the case of a unidirectional ring laser, the output power is given by

$$P_{out} = \eta_2 I_{sat} A_{eff} T\left\{\frac{g_0}{L+T} - 1\right\}$$

In this case, $g_0 = \gamma_0 l$ so that the single-pass unsaturated gain at threshold is doubled, but the slope efficiency is the same as for a standing-wave laser. η_2 and J_1, both measures of the extent of spatial overlap of pump and signal, are therefore key factors in laser performance. Two useful results obtainable from (1.19) are the optimum output coupling for a given pumping level,

$$T_{opt} = \sqrt{g_0 L} - L, \tag{1.21}$$

and the maximum output power possible at a given pumping level (*i.e.* the power output when the output coupling is T_{opt}):

$$P_{out,\max} = \frac{1}{2}\eta_2 I_{sat} A_{eff}(\sqrt{g_0} - \sqrt{L})^2. \tag{1.22}$$

For a unidirectional ring laser, we have

$$P_{out,\max} = \eta_2 I_{sat} A_{eff}\left(\sqrt{g_0} - \sqrt{L}\right)^2.$$

Figure 1.11 shows the idealised output power of a Nd:YAG laser as a function of output coupling for a fixed unsaturated gain of $g_0 = 0.4$ for various internal losses, and for $g_0 = 0.2$ a fixed internal loss of 3%. The results were generated assuming 1.1% Nd^{3+} doping and pump and signal $1/e^2$ waists of 500 and 750 μm respectively. η_2 was taken as 1, and the Nd:YAG rod length as 8 mm. (g_0 values of 0.4 and 0.2 correspond to absorbed pump powers of 12.6 and 6.3 W respectively, using (1.20).) It is also quite straight forward to use (1.14) and (1.15) to numerically calculate the output of four- and quasi-three-level lasers under various operating conditions. Figure 1.12 shows the output power of a four-level 8 mm 1% Nd:YAG rod laser for various values of output coupling and internal loss. Pump and signal modes are assumed Gaussian and non-diffracting with $1/e^2$ radii of 200 and 350 μm respectively. Figure 1.13 shows the output power from the same laser for 10% output coupling and 2% internal loss with and without reabsorption loss. Well above threshold the slope efficiencies become equal. (In the case with reabsorption loss, f_a has been taken as 0.5 to exaggerate the effect of reabsorption loss; in actual quasi-three-level lasers, for example the 946 nm Nd:YAG laser, the value is

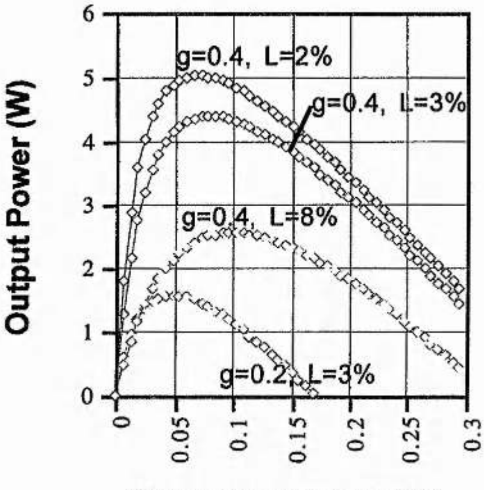

Figure 1.11. Output power versus output coupling for various pumping levels and internal losses.

much smaller, around 0.007.)

1.3.1.2 Estimation and Effect of Pump-Signal Spatial Overlap

The extent of pump-signal spatial overlap influences both threshold and slope efficiency, through J_1 and η_2 respectively. The maximisation of these quantities is especially important for diode-laser pumped lasers, since the low brightness of semiconductor pump devices limits the pump-signal interaction length. The magnitude and effect of pump-mode overlap is most easily evaluated for the case of non-diffracting Gaussian pump and signal modes. Although in the case of diode-laser pumping the pump profile is neither diffraction-limited nor Gaussian, it is useful to consider the effect of overlap in this case as it gives insights into the behaviour of all types of laser regardless of the pumping scheme. The normalised signal and pump intensity functions are

$$s(r)=\frac{2}{\pi w_s l}e^{-\frac{2r^2}{w_s{}^2}},\qquad p(r,z)=\frac{2\alpha e^{-\alpha z}e^{-\frac{2r^2}{w_p{}^2}}}{\pi w_p{}^2(1-e^{-\alpha l})}\tag{1.23}$$

where l is the length of the crystal, α the absorption coefficient (8 cm^{-1} for 1% Nd:YAG) and r,z the cylindrical coordinates with respect to the axis of the Nd:YAG rod. The overlap integral is

$$J_1=2\pi\int_0^l\int_0^\infty s(r)p(r,z)rdrdz.\tag{1.24}$$

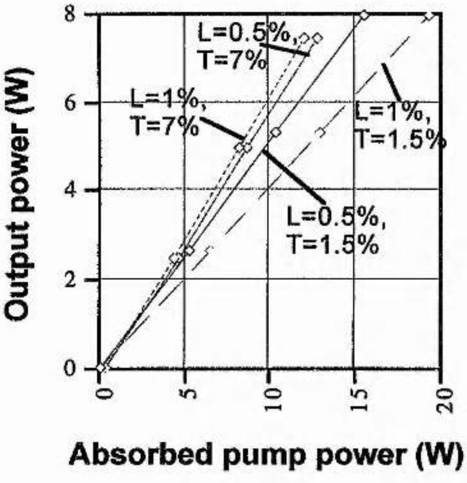

Figure 1.12. Power output for various values of output coupling and internal loss.

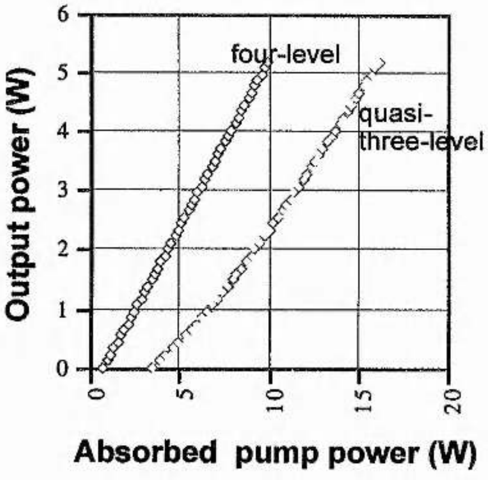

Figure 1.13. Output power with and without reabsorption loss.

Figure 1.14 shows the effect on η_2, J_1 and slope efficiency when the pump waist is varied between zero and 350 µm in the case of an end-pumped 8 mm long 1% Nd:YAG rod laser with 10% output coupling, 2% internal loss and a signal mode radius of 350 µm. Clearly a small pump mode is desirable to give the highest slope efficiency, although for very small pump mode sizes < ≈ 20 µm, overlap and slope fall rapidly. The fall off of η_2 as ω_p approaches ω_s is not as rapid as the drop in the value of the overlap integral might suggest. In terms of practical laser physics, therefore, the adjustment of ω_p to maximise slope efficiency is not a critical or difficult one.

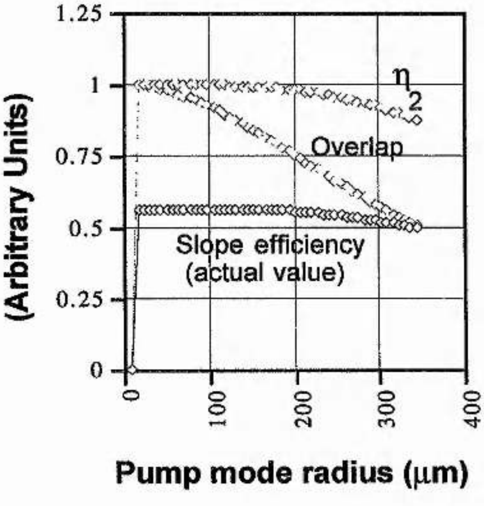

Figure 1.14. Effect of pump mode radius on slope efficiency and overlap.

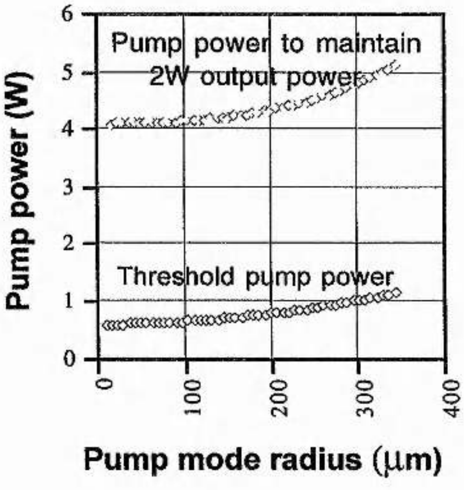

Figure 1.15. Effect of pump mode radius on threshold and input power.

For non-diffracting Gaussian beams, the threshold absorbed power can be obtained analytically from (1.6) and (1.23):

$$P_{abs,th} = \frac{h\nu_p \delta \pi (w_s^2 + w_p^2)}{4\eta_1 f_b \sigma \tau}. \tag{1.25}$$

Figure 1.15 shows the variation of threshold absorbed power with w_p for the laser described above, and also the absorbed pump power required to maintain an output power of 2 W.

Diffraction of the pump beam can be accounted for by assuming a pump intensity function

$$p(r,z) = \frac{2\alpha e^{-\alpha z} e^{-\frac{2r^2}{w_p^2(z)}}}{\pi . w_p^2(z).(1 - e^{-\alpha l})} \tag{1.26}$$

with

$$w_p^2(z) = w_{0p}^2\left(1 + \frac{z^2}{z_0^2}\right); \quad z_0 = \frac{\pi w_{0p}^2 n}{\lambda_p}. \tag{1.27}$$

w_{0p} is the pump beam waist and λ_p the pump wavelength. The absorption factor $e^{-\alpha z}$ remains valid since the beam is diffraction-limited; even if the waist is focussed to 5 μm, the far field diffraction angle is only 1.6°. The value of the overlap integral (1.24) obtained using (1.26) departs from that obtained by using (1.23) only for very small values of the pump mode waist w_{0p}. This is intuitively obvious because significant spreading of the pump beam occurs only in the regime of relatively tight focussing. The departure of J_1 from the non-diffracting case is also predictable; the fall off as $w_{0p} \rightarrow 0$ is less rapid, the diffraction effect increasing the extent of the overlap. Figure 1.16 shows the variation of the overlap for w_{0p} between 5 and 30 μm, with a signal mode waist of 350 μm. For $w_{0p} > 30$ μm, the two calculations differ by only ≈ 0.5%, and, since this is the domain where J_1 is maximum, the assumption of no diffraction of the pump beam is accurate for practical purposes.

An estimate of the optimum confocal parameter for the case of a diffracting Gaussian pump beam can be made by defining an average pump mode waist within the crystal:

$$\langle w_p \rangle^2 = \frac{1}{l}\int_0^l w_p^2(z)dz. \tag{1.28}$$

Using (1.27), and minimising $\langle w_p \rangle$ in order to maximise overlap, the optimum pump mode waist is

$$w_{0p,opt} = \left(\frac{l\lambda}{2\sqrt{3}\pi n}\right)^{1/2}. \tag{1.29}$$

The optimum confocal parameter is therefore on the order of l, a result similar to that for optimum focusing in nonlinear optical parametric processes such as second harmonic generation. Several other accounts of optimum overlap are given in the literature [1.146 - 150].

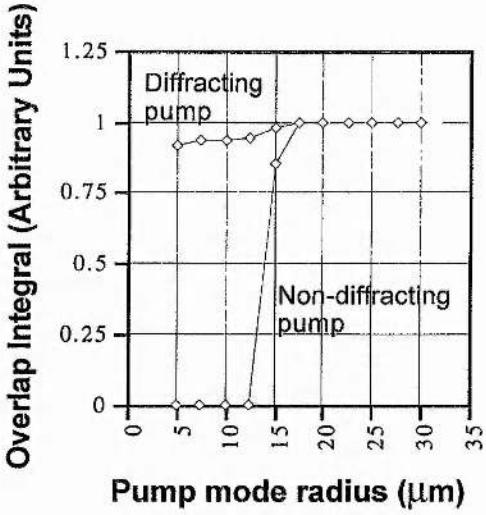

Figure 1.16. Overlap integral for small pump mode radii calculated for diffracting and non-diffracting pump beams.

1.3.2 Photometric Aspects of End-Pumping with Diode-Laser Devices

1.3.2.1 Pump Beam Quality; Brightness, Etendue

Although the use of diode-laser-based devices as pump sources offers the potential advantages of compactness, reliability and efficiency, the output beams of these sources are generally poor in quality, being many times diffraction-limited and often highly astigmatic. This limits the extent of the spatial overlap of the pump mode with the fundamental TEM_{00} signal mode, and some measure of pump beam quality is useful to assess the potential of a given source for end-pumping. Brightness and etendue are the principal parameters used for this.

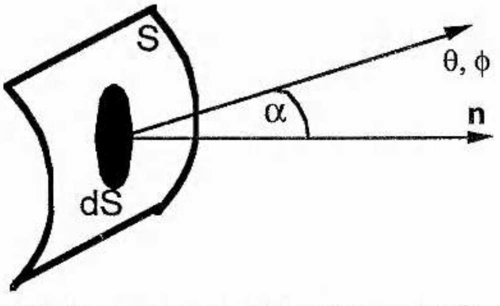

Figure 1.17. Energy transmission from a surface element.

Figure 1.17 shows an emitting surface *S*, not necessarily plane, and a surface element *dS* under consideration. The amount of power radiated into elemental solid-angle $d\Omega$ in the direction θ, ϕ is

$$d^2P = B(\zeta,\eta,\theta,\phi).\cos\alpha.dSd\Omega. \tag{1.30}$$

ζ, η are any convenient set of curvilinear coordinates on S. a is the angle between the normal to dS and the direction θ, ϕ. In the case of most pump devices we can assume that the brightness B is independent of position on S and is isotropic (independent of θ, ϕ). B is then simply a constant. The etendue of the source is defined by [1.151]

$$\mathfrak{E} \equiv n^2 \iint \cos\alpha.dS.d\Omega, \tag{1.31}$$

and the brightness of a source of total power P is therefore

$$B = n^2 \frac{P}{\mathfrak{E}}. \tag{1.32}$$

Etendue is the volume of "radiance space" occupied by the output beam of the diode-laser device and governs the depth of focus possible in the gain medium: sources with low etendue can be focused to a small spot size over a greater distance. From (1.31) the characteristics of a good pump device are therefore a small emitting aperture and a low solid-angle. The emitting surface is plane in most cases, and we can assume for design purposes that a is small so that

$$\mathfrak{E} \approx n^2 S\Omega. \tag{1.33}$$

A TEM_{00} Gaussian beam from a bulk laser is diffraction limited (or close to the limit) and therefore has the highest brightness for a given power of any practical source:

$$\mathfrak{E}_{Gaussian} = \lambda^2. \tag{1.34}$$

The etendue of a typical diode-laser device is tens of thousands of times greater than this diffraction-limited case.

(1.30) can be useful for calculating the intensity profiles of pumping devices. Figures 1.18 and 1.19 show the intensity profiles of a fibre-coupled diode-laser system at 5 mm and 10 µm from the fibre-tip respectively. B is assumed to be a constant.

1.3.2.2 Brightness Theorems

Pump light from diode-laser based devices is normally coupled into the end of a laser rod via some optical system, for example low *f*-number lenses. Two important theorems govern the radiation through an optical system and into the laser rod itself. The first is the brightness theorem [1.152] which states that if the object and image spaces have equal refractive index, the brightness of the light distribution produced by an optical system B_1 cannot be greater than the original source brightness B_0, and the two can only be equal if the losses in the system are negligible:

$$B_1 \leq \left(\frac{n_1}{n_0}\right)^2 B_0. \tag{1.35}$$

(1.32) and (1.35) have the important consequence that if the losses in the optical system are zero so that no power is lost, the etendue is a constant. In practice this means that focused pump spot size and divergence angle are not independent variables but are

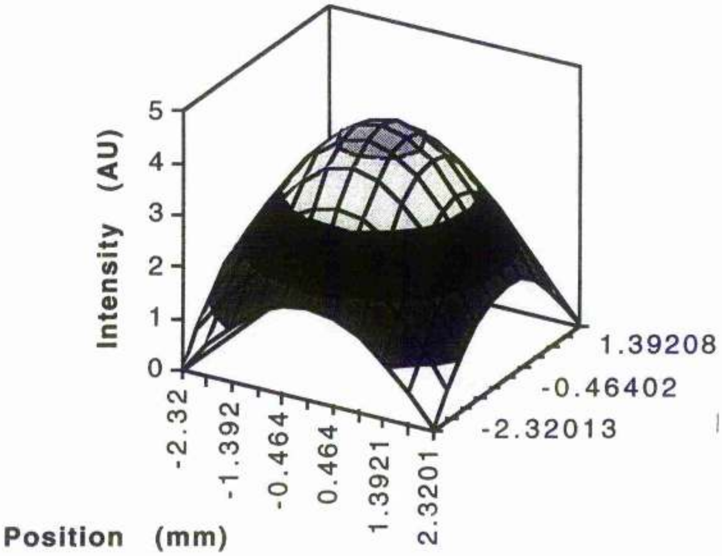

Figure 1.18. Far-field intensity pattern from a fibre-coupled diode-laser.

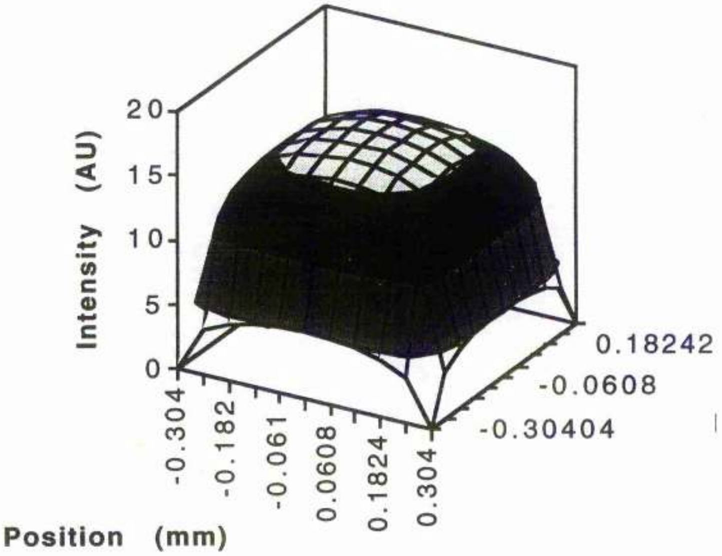

Figure 1.19. Near-field intensity pattern from a fibre-coupled diode-laser.

constrained by (1.33). The second, related theorem [1.153] states that the brightness of a collection of mutually incoherent (but otherwise identical) sources cannot be increased by a passive optical system to a level greater than the single brightest source. There are, however, certain cases where the total brightness of a laser array *can* exceed the brightness of the individual elements. First, if mutual coherence is established across the array, the entire source behaves as a single spatial mode and the phase and amplitude can in principle be made uniform. This is limited to individual low-power diode-laser arrays; high power diode-bars consist of arrays of arrays, and this method cannot be applied to them.

A second way to increase radiance is to use lasers with different average properties, such as wavelength or polarisation. Passive optical elements such as diffraction gratings and polarising beam splitters can then be used to multiplex the individual beams.

1.3.2.3 Photometric Requirements of Diode-Laser Pumps

Given the poorer beam quality of diode-laser pumps, optimum focusing is more difficult to describe quantitatively. Most attempts have been extensions of Gaussian beam models [1.154]. A simple model which gives the brightness requirements of the pump source assumes that the pump mode is entirely contained within the signal mode over a fixed crystal length L [1.155], as shown in Figure 1.20. The pump mode is assumed to have the form

$$w_p(z) = w_{0p} + |z|\,\theta_p \qquad (1.36)$$

where w_{0p} is the waist radius at the centre of the crystal and θ_p is the corresponding divergence angle. The non-diffracting signal mode has a $1/e^2$ radius w_s. Optimum focusing is achieved by minimising the pump radius at the ends of the crystal, $w_p(L/2)$. An azimuthally symmetric pump with an emitting aperture of radius r and divergence α, has an etendue

$$\mathfrak{E} = 2\pi^2 n^2 r^2 (1-\cos\alpha) \approx (\pi n r \alpha)^2. \qquad (1.37)$$

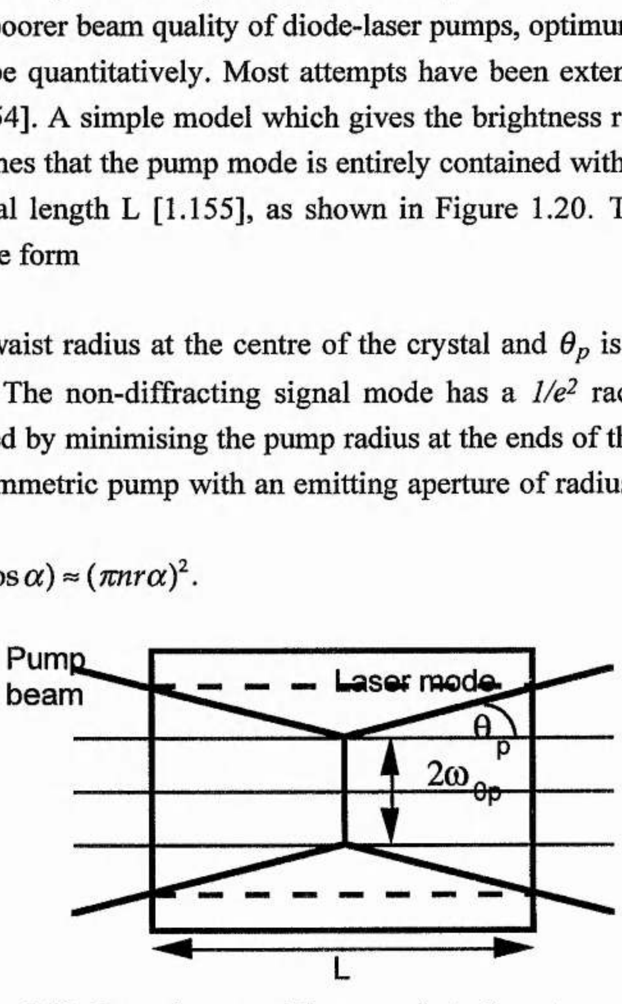

Figure 1.20. Pump beam and laser mode in the gain medium.

Minimizing $w_p(L/2)$ using (1.36) subject to the constraint (1.37), the optimum pump spot size and divergence are

$$w_{0p,opt} = \mathfrak{E}^{1/4}\sqrt{\frac{L}{2\pi n}}; \qquad \theta_{p,opt} = \mathfrak{E}^{1/4}\sqrt{\frac{2}{\pi n L}}. \qquad (1.38)$$

One result implied by (1.38) is that if the emitting dimension of the pump source were to be increased (to obtain higher power, for example) at constant far-field angle and fixed L, then the pump beam could be focused to a spot that increases with only the square root of the emitting dimension. This seems counter-intuitive, but occurs because L is not increased as well. The etendue clearly limits the minimum spot size. Using (1.38),

$$[w_p(L/2)]_{\min} = \mathfrak{E}^{1/4}\sqrt{\frac{2L}{\pi n}}. \tag{1.39}$$

This is therefore the maximum w_s for given L and $\mathfrak{E}$. Increasing L from the fixed value used to obtain (1.39) may improve interaction length but there will be a trade off eventually with actual overlap and hence threshold and slope efficiency. If w_s is fixed there is a limit on the etendue of the pump source in order to preserve the overlap defined above:

$$\mathfrak{E} \le \frac{A_s^{\,2} n^2}{4L^2}. \tag{1.40}$$

A_s is the cross-sectional area of the signal mode. The corresponding minimum brightness in air of the pump is

$$B_{air} \ge \frac{4L^2 P}{A_s^{\,2} n^2}. \tag{1.41}$$

Azimuthal symmetry of the pump is also an important factor in beam quality. For example, fibre-coupling of a diode-laser bar may be a better alternative to pumping with just a diode-bar alone, although other issues such as overall laser efficiency also need to be considered. The etendue of an asymmetric pump source with perpendicular emitting dimensions r_x, r_y and emission angles θ_x, θ_y can be approximated by

$$\mathfrak{E} \approx n^2 \pi r_x r_y . \pi \theta_x \theta_y = (n\pi r_x \alpha_x)(n\pi r_y \alpha_y) = \sqrt{\mathfrak{E}_x}\sqrt{\mathfrak{E}_y}. \tag{1.42}$$

The effect of astigmatism can be modelled if $\mathfrak{E}_x$ and $\mathfrak{E}_y$ are made unequal. For example, in the case of a high-power diode-laser linear bar, the output beam is diffraction limited in the plane perpendicular to the junction, and typically more than 800 times diffraction-limited in the plane parallel to the junction. If

$$\mathfrak{E}_y = Q^2 \mathfrak{E}_x; \qquad \mathfrak{E}_x = \mathfrak{E}$$

where Q is an asymmetry factor greater than 1, and the minimum brightness is calculated as before, the result is

$$B_{air} \ge \frac{4LPQ}{A_s^{\,2} n^2}. \tag{1.43}$$

In other words the required pump brightness is Q times larger than than for a symmetric pump beam.

1.3.2.4 Pump Focusing Criteria for Diode-Pumped Solid-State Lasers

Generally, the signal mode radius w_s in the gain medium is determined by resonator design. For example, in the case of intracavity-doubled lasers, the resonator geometry is often fixed by arranging for a given waist size and confocal parameter in the nonlinear medium. Even if this is not the case, w_s is usually only slightly variable for a given resonator configuration. Given that for a particular pump source the etendue $\mathfrak{E}$ is also a constant, only the focusing, crystal length and pump wavelength are generally available as variables in laser head design. Although in section 1.3.2.3 the crystal length L was fixed to give pump brightness requirements, here it is assumed to be a variable since commercial crystals can be obtained with any desired length. For maximum efficiency and output, the usual design aim is to maximise the physical pump-signal interaction length by varying the focusing, subject to the constraint of constant etendue (1.37) and the requirement that all the pump mode be contained inside the laser mode, as in Figure 1.20. If the pump spot size and divergence are arranged as w_{0p}, θ_p , and the pump and signal waists are made equal at the front end of the laser rod, then the length over which the pump is contained inside the signal is

$$l = \frac{2(w_s - w_{0p})}{\tan\theta_p}. \tag{1.44}$$

Since etendue is constant for all focusing, the condition

$$\mathfrak{E} = (n\pi w_{0p}\theta_p)^2 \tag{1.45}$$

can be used with (1.44) to find the (optimum) value of w_{0p} which maximises l. (1.45) can be used to find the corresponding optimum θ_p.

Figure 1.21 shows the focusing behaviour for a circular symmetric source of radius 300 μm and numerical aperture 0.37 when used to pump a signal mode of radius 750 μm. (These are the characteristics of the *B030* fibre-coupled diode-laser system available from *OptoPower Corporation.*) The graph also shows the percentage fill factor as the pump spot size increases, *i.e.* the percentage of the signal mode volume overlapped with the pump beam. Variation of the overlap length with pump spot size is shown in Figure 1.22. This graph has a simple intuitive explanation. Initially, as the pump spot size increases from a very small value, the pump divergence falls rapidly, as shown in Figure 1.21. The pump spot therefore moves further into the crystal, increasing the overlap length. As the pump spot size increases further, however, the pump divergence decreases much more slowly and the pump spot has to move back toward the front end of the laser rod if pump and signal are to maintain equal waists at the front surface. The benefit of a lower etendue is shown in Figure 1.23, which shows the maximum overlap length as the signal mode size is varied, using the *OptoPower B030* system and the *SDL 3450 P6* fibre-coupled diode system. The latter has a much lower etendue as the fibre has a 250 μm radius core and a numerical aperture of 0.2. Geometrically, the *SDL* system has the advantage, giving a longer interaction length. (However, this may not be the only consideration as lower etendue means that the system is capable of delivering less power. Nonetheless, if the two are run at full power, the 12 W *SDL* device is more than twice as bright as the 28 W *OptoPower* system.)

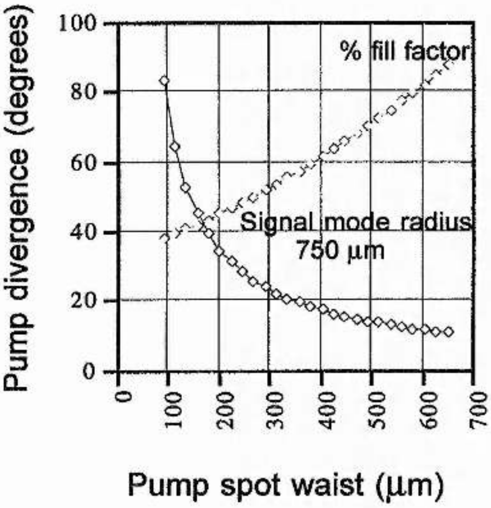

Figure 1.21. Pump focusing behaviour and % fill factor v. pump spot radius.

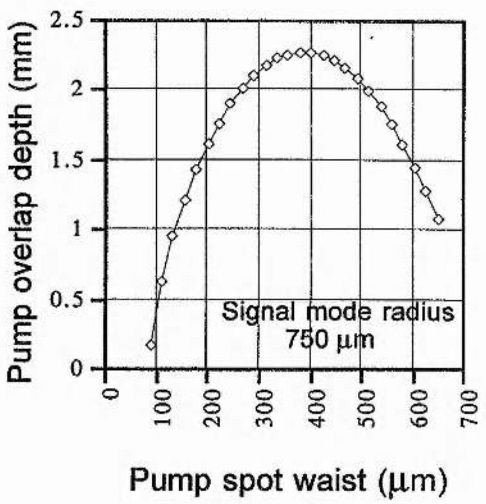

Figure 1.22. Pump overlap length v. pump spot radius.

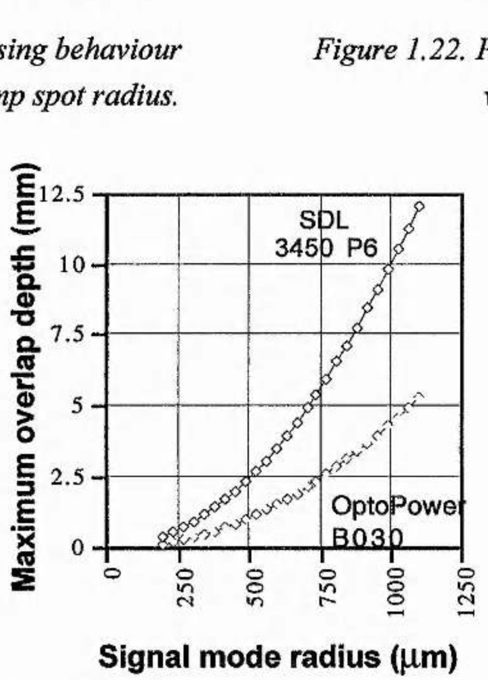

Figure 1.23. Maximum overlap length v. signal mode radius.

1.3.2.5 Elimination of Asymmetry in Diode-Laser Pumps; Reshaping and Stacking of Diode-Laser Devices.

The idea of reshaping the output beams from low-power broad-area diode-lasers using anamorphic prism pairs is well known to improve their quality [1.156]. Recently there has been considerable interest in reshaping the output from high-power linear diode-laser bars to reduce asymmetry [1.157, 158], and their subsequent use in end-pumping. The results obtained to date show this to be a highly effective method of end-pumping [1.159, 160]. The success of this method is due to the fact that, notwithstanding their asymmetery, diode-laser bars have high brightness due to the fact that perpendicular to the emitting junction, the output beam is diffraction-limited. For example, a 20 W *SDL 3460-S* diode-bar has a brightness of 3.2 x 10^{10} $Wm^{-2}sr^{-1}$, which is three orders of magnitude brighter than the 28 W *OptoPower B030* fibre-coupled system, which is based on two 20 W diode-bars. Reshaping is a route to very high brightness *and* azimuthally symmetric pump sources.

In reshaping, the output beam is first collimated by a fibre lens and then split into several sections in a direction perpendicular to the emitting junction. These sections are then stacked vertically in an attempt to make the output beam an equal number of times diffraction-limited in the planes parallel and perpendicular to the emitting junction. In the notation of (1.42) and (1.43), $\sqrt{\mathfrak{C}_x}$ and $\sqrt{\mathfrak{C}_y}$ are made more equal to reduce the asymmetry factor *Q*.

For example, in the scheme of Edwin [1.158] as adapted for the 1 cm 20 W *SDL 3460-S* diode-laser array, the output is first collimated to a 100 μm beam with 0.4° divergence perpendicular to the junction, using a cylindrical lens. Parallel to the junction, the divergence remains at 5°. The device then slices this 1 cm beam into 12 833 μm sections which are stacked on top of each other. The improvement in the beam quality is evident from Table 1.4. Although the brightness is unaffected, the beam is now much more symmetric.

A similar concept was introduced by Fan *et al* [1.161], in which several 500 mW broad-area diode-lasers are stacked vertically to reduce asymmetry. For an asymmetry factor of *Q*, it can be shown that *Q* diode-lasers can be vertically stacked to eliminate the asymmetry in the aperture-divergence product for the two planes parallel and perpendicular to the emitting junction.

	Normal diode-bar output		**Reshaped output**	
	Parallel	Perpendicular	Parallel	Perpendicular
Aperture	1 cm	1 μm	833 μm	1.2 mm
Divergence	5°	40°	5°	0.4°
Q	1250		8.6	
Ratio of M^2	800		8.7	

Table 1.4. Effect of re-shaping SDL 3460-S *diode-bar [1.158].*

1.3.3 Transverse and Hybrid Pumping Geometries

1.3.3.1 Basic Side-Pumping

Relatively little work on the theory of pump-signal overlap in side-pumped lasers has been published, although a large number of side-pumped systems have been reported. The imbalance is due to the fact that, compared to longitudinal pumping, the scope for novelty of design is very much wider in the case of transverse pumping. Each design has its own overlap properties which need to be discussed on a system-by-system basis, and so generalisation is difficult. In the 1970s, some theoretical work was carried out for side-pumping laser rods with LEDs [1.162 - 4], but today these are of limited use in the design of multi-watt diode-pumped lasers.

The aim in side-pumping is the same as for end-pumping: to efficiently absorb as much pump power as possible inside the TEM_{00} mode volume of the resonator. Simple devices, such as a side-pumped rod with the laser mode along its axis, have the disadvantage of low interaction length, which is often only the diameter of the signal mode. In addition, there is significant absorption in the region between the edge of the rod and the signal mode. Even if the pump light is collimated and wavelength-tuned exactly to an absorption peak, the thresholds and slope efficiencies of CW systems do not compare favourably with end-pumped lasers. Poor spatial overlap also means that the transverse signal mode control is more difficult.

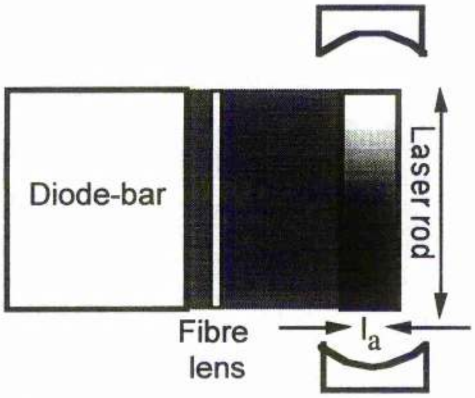

Figure 1.24. Side-pumped laser rod.

Side-pumped systems do have certain advantages, and simplicity is certainly one. Such systems are also amenable to scaling which can be useful if pump devices are not limited in number, although expectations in terms of "output watts per dollar" cannot be high. The distributed nature of the pump also means that thermal lensing, thermal birefringence and thermal damage are much reduced, appearing only at high pump powers.

A simple model of basic side-pumping, which ignores refinements such as multi-passing of the pump light, assumes that the gain material is one absorption length thick, as in Figure 1.24;

$$l_a = \frac{1}{N\sigma_\alpha}. \tag{1.46}$$

N is the number density of active ions and σ_a the absorption cross-section. If the gain medium is of length L and height t, and is illuminated from the side by a collimated diode-bar of CW power P, then the steady-state population inversion n in the absence of stimulated emission is

$$n = \frac{P_{abs}\eta_1\tau}{h\nu_p l_a tL}. \tag{1.47}$$

τ is the upper state lifetime, P_{abs} the absorbed power, and η_l the pump quantum efficiency. The behaviour of the unsaturated gain is therefore

$$G = e^{n\sigma_e L} \propto e^{P_{abs}\sigma\tau/l_a}. \tag{1.48}$$

The main point to notice is the very strong dependence on l_a. For 1% Nd:YAG pumped at 807 nm, $l_a \approx 2$ mm, leading to the requirement of high pump powers, and in most materials l_a cannot easily be reduced by higher doping with the active species because of concentration quenching. Typical signal-mode diameters are only in the region of a few hundred microns.

Given the restriction on absorption length, incident pump power is the main experimental variable. Pulsed diode-laser devices are able to produce very high peak powers which are easily coupled into large volumes. The most successful side-pumped lasers have therefore been operated in the pulsed regime. Of course, if cost and complexity are no object, one can simply use multiple amplifiers to obtain the desired CW output power.

1.3.3.2 Gain Profile Shaping in Side-Pumped Lasers

Most side-pumped designs have included features to increase the useful absorption of the pump. In slab systems, the laser mode can be made to follow a "zig-zag" path inside the gain medium, increasing the pumped path length and bringing the laser mode closer to the edge of the gain medium [1.165]. HR coating the side of the rod or slab to reflect pump power unabsorbed after the first pass has allowed pulsed slope efficiencies up to 47% to be achieved [1.166]. The most effective designs, however, have been those where some attempt has been made to preferentially deposit the pump energy in the TEM_{00} mode volume at the centre of a rod, thereby avoiding the pump wastage characteristic of transverse pumping which leads to low performance and multi-transverse mode operation. Brioschi *et al* [1.167] used 12 diode-bars focused with $f\#$ 0.6 cylindrical lenses to circumferentially pump a 25 mm long, 6 mm diameter Nd:YAG rod. By adjusting the focusing, a bell-shaped gain profile of ≈ 5 mm diameter could be produced at the centre of the rod. Smaller inversion peaks near the edge of the rod could be reduced by using more diode-bars. In the scheme by Welford *et al* [1.168] near-Gaussian pump energy deposition was achieved in a rod of semi-circular cross-section, side-pumped by a *SDL 3230* quasi-CW 5 bar diode-stack. The rod was pumped through the curved side and was HR coated on the other to double-pass the pump. The system gave 22% slope efficiency in the pulsed mode. More recently, Jackson and Piper [1.169] gave an analysis of a novel design in which a Nd:YAG rod was embedded inside a right-angled glass prism using index matching epoxy. The rod was close to the 90° corner and the system was pumped through the prism face opposite the right-angle. This design resulted in highly efficient pump light absorption. This type of ingenuity is essential if side-pumped systems are to compete on an efficiency basis with end-pumped lasers.

1.3.3.3 Hybrid Pumping Schemes

Some hybridisation of diode-side-pumping and end-pumping has occurred in the case of slab lasers where the laser mode undergoes a very high number of passes through the gain medium in order to extract as much inversion as possible. These *tightly folded resonators* (TFRs) show good efficiency while having simple designs. The first example was reported by Baer *et al* [1.170]. Figure 1.25 shows the arrangement. The reflection points are located opposite the individual arrays of the diode-bars, resulting in multiple end-pumping of the laser mode, while the overall system has the simplicity associated with side-pumped lasers. Multi-watt CW TEM_{00} output was achieved at 45% slope efficiency. There were ten pump regions, each providing an effective small signal gain of about 35%. The total gain was therefore 350%, or about 15 dB. It is interesting to note that this hybrid design has the highest gain of any bulk solid-state laser reported to date.

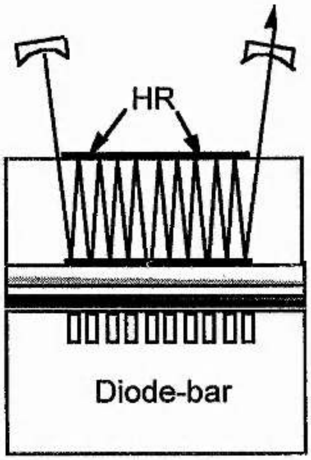

Figure 1.25. Tightly folded resonator (TFR).

1.4 Concluding Remarks

In this chapter, the general concept of diode-pumped systems has been introduced. In the case of bulk lasers, the various possible host materials for Nd^{3+} have been reviewed. The concept of pump-signal overlap has been discussed in detail. As will be seen in the experimental work described later, resonator design in general and the spatial distributions of pump and signal fields in particular, is the key factor governing performance whether the laser is operated at 1 μm or intracavity-doubled to 0.5 μm.

References

[1.1] R. Newman: "Excitation of the Nd^{3+} fluorescence in $CaWO_4$ by recombination radiation in GaAs": *J. App. Phys.* **34** 437 (1963)

[1.2] L.J. Johnson, N. Nassau: "Infra-red fluorescence and stimulated emision of Nd^{3+} in $CaWO_4$": *Proc. IEEE* **49** 1704 (1961)

[1.2a] S. A. Ochs, J. I. Pankove: "Injection-luminescence pumping of a CaF_2:Dy^{2+} laser": *Proc. IEEE* **52** 713 (1964)

[1.3] R.N. Hall, G.E. Fenner, J.D. Kingsley, T.J. Soltys, R.O. Carlson: "Coherent light emission from GaAs junctions": *Phys. Rev. Lett.* **9** 366 (1962)

[1.4] M.I. Nathan, W.P. Dumke, G. Burns, F.H. Dill Jr., G. Lasher: "Stimulated emission of radiation from GaAs *pn* junctions": *App. Phys. Lett.* **1** 62 (1962)

[1.5] T.M. Quist, R.H. Rediker, R.J. Keyes, W.E. Krag, B. Lax, A.L. McWhorter, H.J. Zeigler: "Semiconductor maser of GaAs": *App. Phys. Lett.* **1** 91 (1962)

[1.6] N. Holonyak Jr., S.F. Bevacqua: "Coherent visible light emission from $GaAs_{1-x}P_x$": *App. Phys. Lett.* **1** 82 (1962)

[1.7] R.J. Keyes, T.M. Quist: "Injection luminescent pumping of CaF_2:U^{3+} with GaAs diode-lasers": *App. Phys. Lett.* **4** 82 (1964)

[1.8] J.E. Geusic, H.M. Marcos, L.G. Van Uitert: "Laser oscillations in Nd-doped yttrium gallium and gadolinium garnets": *App. Phys. Lett.* **4** 182 (1964)

[1.9] M. Ross: "YAG laser operation by semiconductor laser pumping": *Proc. IEEE* **56** 196 (1968)

[1.10] F.W. Ostermayer, R.B. Allen, E.G. Dierschke: "Room temperature cw operation of $GaAs_{1-x}P_x$ diode pumped YAG:Nd laser": *App. Phys. Lett.* **19** 289 (1971)

[1.11] L.C. Conant, C.W. Reno: "GaAs laser diode pumped Nd:YAG laser": *App. Opt.* **13** 2457 (1974)

[1.12] L.J. Rosenkrantz: "GaAs diode pumped Nd:YAG laser": *J. App. Phys.* **43** 4603 (1972)

[1.13] M.K. Reed, W.J. Kozlovsky, R.L. Byer: "Diode-laser array pumped neodymium slab oscillators": *Opt. Lett.* **13** 204 (1988)

[1.14] C.J. Koester: "Laser action by enhanced total internal reflection": *IEEE J. Quant. Electron.* **2** 580 (1966)

[1.15] C.J. Koester, E. Snitzer: "Amplification in a fibre-laser": *Appl. Opt.* **3** 1182 (1964)

[1.16] J. Stone, C.A. Burrus: "Neodymium doped fibre lasers - room temperature cw operation with an injection laser pump": *Appl. Opt.* **13** 1256 (1974)

[1.17] J. Stone, C.A. Burrus, A.G. Dentai, B.I. Millar: ""Nd:YAG single crystal fibre lasers - room-temperature operation using a single LED as a pump": *App. Phys. Lett.* **29** 37 (1976)

[1.18] C.A. Burrus, J. Stone, A.G. Dentai: "Room temperature 1.3 μm operation of a glass-clad Nd:YAG single crystal fibre-laser end-pumped with a single LED": *Electron. Lett.* **12** 600 (1976)

[1.19] R. J. Mears, L. Reekie, I. M. Jauncey, S. B. Poole, D. N. Payne: "Diode-pumped operation of an erbium doped fibre laser": *Electron. Lett.* **23** 1076 (1987)

[1.20] H. Zellmer, U. Willamowski, A. Tuennermann, H. Welling, S. Unger, V. Reichel, H.-R. Mueller, J. Kirchof, P. Albers: "High power cw neodymium-doped fibre-laser operating at 9.2W with high beam quality": *Opt. Lett.* **20** 578 (1995)

[1.21] P.J. Chandler, S.J. Field, D.C. Hanna, D.P. Shepherd, P.D. Townsend, A.C. Tropper, L. Zhang: "Ion-implanted Nd:YAG planar waveguide laser": *Electron. Lett.* **25** 985 (1989)

[1.22] S.J. Field, D.C. Hanna, D.P. Shepherd, A.C. Tropper, P.J. Chandler, L. Zhang: "Ion implanted Nd:YAG waveguide lasers": *IEEE J. Quant. Electron.* **27** 428 (1991)

[1.23] S.J. Field, D.C. Hanna, D.P. Shepherd, A.C. Tropper, P.J. Chandler, L. Zhang: "Ion-implanted Nd:YAP planar waveguide laser": *Electron. Lett.* **26** 1826 (1990)

[1.24] S.J. Field, D.C. Hanna, D.P. Shepherd, A.C. Tropper, P.J. Chandler, L. Zhang: "Ion-implanted Nd:MgO:LiNbO$_3$ planar waveguide laser": *Opt. Lett.* **16** 481 (1991)

[1.25] S.J. Field, D.C. Hanna, A.C. Large, D.P. Shepherd, A.C. Tropper, P.J. Chandler, L. Zhang: "An efficient, diode-pumped, ion-implanted Nd:GGG planar waveguide laser": *Opt. Comm.* **86** 161 (1991)

[1.26] D.P. Shepherd, D.J.B. Brinck, J. Wang, A.C. Tropper, D.C. Hanna, G. Kakarantzas, P.D. Townsend: "1.9 μm operation of a Tm:lead germinate glass waveguide laser": *Opt. Lett.* **19** 954 (1994)

[1.27] T. Feuchter, E.K. Mwarania, J. Wang, L. Reekie, J.S. Wilkinson: "Erbium-doped ion-exchanged waveguide lasers in BK-7 glass": *IEEE Photon. Tech. Lett.* **4** 542 (1992)

[1.28] G. Nyolak, M. Haner, P.C. Becker, J. Shmulovich, Y.H. Wong: "Systems evaluation of an Er^{3+} -doped planar waveguide amplifier": *IEEE Photon. Tech. Lett.* **5** 1185 (1993)

[1.29] S.J. Field, D.C. Hanna, A.C. Large, D.P. Shepherd, A.C. Tropper, P.J. Chandler, L. Zhang: "A low threshold ion-implanted Nd:YAG channel waveguide laser": *Electron. Lett.* **27** 2375 (1991)

[1.30] I. Chartier, B. Ferrand, D. Pelenc, S.J. Field, D.C. Hanna, A.C. Large, D.P. Shepherd, A.C. Tropper: "Growth and low-threshold laser operation of an epitaxially grown Nd:YAG waveguide": *Opt. Lett.* **17** 810 (1992)

[1.31] D.C. Hanna, A.C. Large, D.P. Shepherd, A.C. Tropper, I. Chartier, B. Ferrand, D. Pelenc: "A side-pumped Nd:YAG expitaxial waveguide laser": *Opt. Comm.* **91** 229 (1992)

[1.32] D.C. Hanna, A.C. Large, D.P. Shepherd, A.C. Tropper, I. Chartier, B. Ferrand, D. Pelenc: "Low threshold quasi-three-level 946 nm laser operation of an epitaxially grown Nd:$Y_3Al_5O_{12}$ waveguide": *App. Phys. Lett.* **63** 7 (1993)

[1.33] D. Fluck, B. Binder, M. Kuepfer, H. Looser, Ch. Buchal, P. Guenter: "Phase-matched second harmonic blue light generation in ion-implanted $KNbO_3$ planar waveguides with 29% conversion efficiency": *Opt. Comm.* **90** 304 (1992)

[1.34] T. Y. Fan: "Aperture guiding in quasi-three-level lasers": *Opt. Lett.* **19** 554 (1994)

[1.35] B. Zhou, T.J. Kane, G. J. Dixon, R.L. Byer:: "Efficient, frequency stable laser-diode-pumped Nd:YAG laser": *Opt. Lett.* **10** 63 (1985)

[1.36] J. M. Auerbach, R.L. Schmitt: "Diode-laser-pumped monolithic Nd:YLF laser operating at 1.053 μm": *Opt. Lett.* **16** 1171 (1991)

[1.37] Q. Mingxin, D. J. Booth, G. W. Baxter, G. C. Bowkett: "Performance of a Nd:YVO_4 microchip laser with cw pumping at wavelengths between 741 and 825 nm" *App. Opt.* **32** 2085 (1993)

[1.38] J. J. Zayhowski, A. Mooradian: "Single-frequency microchip Nd lasers": *Opt. Lett.* **14** 24 (1989)

[1.39] N. Mermilliod, B. Francois, Ch. Wyon: "LMA:Nd microchip laser": *App. Phys. Lett.* **59** 3519 (1991)

[1.40] G. C. Bowkett, G.W. Baxter, D. J. Booth, T. Taira, H. Teranishi, T. Kobayashi: "Single mode 1.34 μm Nd:YVO_4 microchip laser with cw Ti:sapphire and diode-laser pumping": *Opt. Lett.* **19** 957 (1994)

[1.41] P. Gavrilovic, M. S. O'Neill, J. H. Zarrabi, S. Singh, J.E. Williams, W. H. Grodkiewicz, A. Bruce: "High-power, single -frequency diode-pumped Nd:YAG microcavity lasers at 1.3 μm": *App. Phys. Lett.* **65** 1620 (1994)

[1.42] J. J. Zayhowski, P. A. Schultz, C. Dill III, S. R. Henion: "Diode-pumped electrooptically tuned microchip laser": *IEEE Photon. Tech. Lett.* **5** 1153 (1993)

[1.43] F. Zhou, A.I. Ferguson: "Tunable single-frequency operation of a diode-laser pumped Nd:YAG microchip at 1.3 μm": *Electron. Lett.* **26** 490 (1990)

[1.44] P. Laporta, S. Taccheo, S. Longhi, O. Svelto, G. Sacchi: "Diode-pumped microchip Er-Yb:glass laser": *Opt. Lett.* **18** 1232 (1993)

[1.45] J. J. Zayhowski, J. A. Keszenheimer: "Frequency tuning of microchip lasers using pump power modulation": *IEEE J. Quant. Electron.* **28** 1118 (1992)

[1.46] G. J. Koch, J. P. Deyst, M. E. Storm: "Single-frequency lasing of monolithic Ho, Tm:YLF": *Opt. Lett.* **18** 1235 (1993)

[1.47] J. J. Zayhowski, J. Harrison, C. Dill III, J. Ochoa: "Tm:YVO_4 microchip laser": *App. Opt.* **34** 435 (1995)

[1.48] J. M. Sutherland, S. Ruan, R. Mellish, P. M. W. French, J. R. Taylor: "Diode-pumped, single frequency Cr:LiSAF coupled cavity microchip laser": *Opt. Comm.* **113** 458 (1995)

[1.49] K. Kubodera, K. Otsuka: "Single-transverse mode LNP slab waveguide laser": *J. App. Phys.* **50** 653 (1979)

[1.50] P. Laporta, S. Taccheo, S. Longhi, O. Svelto, G. Sacchi: "Experimental analysis and theoretical modeling of a diode-pumped Er, Yb:glass microchip laser": *Opt. Lett.* **20** 889 (1995)

[1.51] N. MacKinnon, B. D. Sinclair: "A laser-diode pumped Nd:YVO_4 / KTP composite material microchip laser": *Opt. Comm.* **105** 183 (1994)

[1.52] T. Sasaki, T. Kojima, A. Yokotani, O. Oguri, S. Nakai: "Single-longitudinal-mode operation and second harmonic generation of Nd:YVO_4 microchip lasers": *Opt. Lett.* **16** 1665 (1991)

[1.53] J. H. Zarrabi, P. Gavrilovic, S. Singh: "Monolithic, self-frequency-doubled Nd:YAB green laser with low intensity noise": *Electron. Lett.* **29** 1769 (1993)

[1.54] T. Omatsu, Y. Kato, M. Shimosegawa, A. Hasegawa, I. Ogura: "Thermal effects in laser diode-pumped self-frequency-doubled Nd:YAB microchip laser": *Opt. Comm.* **118** 302 (1995)

[1.55] T.J. Kane, R.L. Byer: "Monolithic, unidirectional single-mode Nd:YAG ring laser": *Opt. Lett.* **10** 65 (1985)

[1.56] T. J. Kane, A. C. Nilsson, R. L. Byer: "Frequency stability and offset locking of a laser-diode-pumped Nd:YAG monolithic nonplanar ring oscillator": *Opt. Lett.* **12** 175 (1987)

[1.57] D. C. Gerstenberger, G. E. Tye, R. W. Wallace: "Efficient second-harmonic conversion of cw single-frequency Nd:YAG laser light by frequency locking to a monolithic ring frequency doubler": *Opt. Lett.* **16** 992 (1991)

[1.58] I. Freitag, A. Tuennermann, H. Welling: "Power scaling of diode-pumped monolithic Nd:YAG lasers to output powers of several watts": *Opt. Comm.* **115** 511 (1995)

[1.59] E. A. P. Cheng, T. J. Kane: "High-power single-mode diode-pumped Nd:YAG laser using a monolithic non-planar ring resonator": *Opt. Lett.* **16** 478 (1991)

[1.60] T. S. Kubo, T. J. Kane: "Diode-pumped lasers at five eye-safe wavelengths": *IEEE J. Quant. Electron.* **28** 1033 (1992)

[1.61] T. Y. Fan, R. L. Byer: "CW operation of a room-temperature, diode-laser pumped Nd:YAG laser": *Opt. Lett.* **12** 809 (1987)

[1.62] W. J. Kozlovsky, W. P. Risk: "Efficient diode-laser pumped Nd:YAG laser with resonantly enhanced pump absorption": *Conf. on Lasers & Electoopt. Tech. Dig.* paper CME1 (1991)

[1.62] J. P. Cuthbertson, G. J. Dixon: "Pump-resonant excitation of the 946 nm Nd:YAG laser": *Opt. Lett.* **16** 396 (1991)

[1.63] T. Y. Fan. R. L. Byer: "Modelling and cw operation of a quasi-three-level 946 nm Nd:YAG laser": *IEEE J. Quant. Electron.* **23** 605 (1987)

[1.64] W. A. Clarkson, R. L. Koch, K. I. Martin, D. C. Hanna: "High-power 946 nm Nd:YAG laser longitudinally pumped by a diode bar": *Conf. on Lasers & Electoopt. Tech. Dig.* paper CMD4 (1995)

[1.65] W. P. Risk, W. Lenth: "Room-temperature CW 946 nm Nd:YAG laser pumped by laser-diode arrays and intracavity frequency doubling to 473 nm": *Opt. Lett.* **12** 993 (1987)

[1.66] J. Hong, B. D. Sinclair, W. Sibbett, M. H. Dunn: "Frequency doubled and Q-switched 946 nm Nd:YAG laser pumped by a diode-laser array": *App. Opt.* **31** 1319 (1992)

[1.67] A. B. Neilson, W. A. Clarkson, D. C. Hanna: "Single-frequency CW and Q-switched operation of a diode-pumped Nd:YAG 1.3 μm ring laser": *Opt. Lett.* **18** 1426 (1993)

[1.68] W. M. Grossman, M. Gifford, R. W. Wallace: "Short-pulse Q-switched 1.3 and 1 μm diode-pumped lasers": *Opt. Lett.* **15** 622 (1990)

[1.69] W. R. Trutna, Jr., D. K. Donald, M. Nazarathy: "Monolithic non-planar ring oscillator at 1319 and 1338 nm": *Opt. Lett.* **12** 248 (1987)

[1.70] G. J. Hall, A. I. Ferguson: "Generation of single-frequency radiation at 1064, 1319, and 659.5 nm with an all-solid-state, out-of-plane Nd:YAG ring laser": *Opt. Lett.* **19** 557 (1994)

[1.71] A. L. Harmer, A. Linz, D. R. Gabbe: "Fluorescence of Nd^{3+} in lithium yttrium fluoride": *J. Phys. Chem. Solids* **30** 1483 (1968)

[1.72] J. R. Ryan, R. Beach: "Optical absorption and stimulated emission of neodymium in yttrium lithium fluoride": *J. Opt. Soc. Am. B* **9** 1883 (1992)

[1.73] N. P. Barnes, M. E. Storm, P. L. Cross, M. W. Skolaut, Jr.: "Efficiency of Nd laser materials with laser diode pumping": *IEEE J. Quant. Electron.* **26** 558 (1990)

[1.73a] N. P. Barnes, D. J. Gettemy, L. Esterowitz, R. E. Allen: "Comparison of 1.06 and 1.33 μm operation in various hosts": *IEEE J. Quant. Electron.* **23** 1434 (1987)

[1.74] T. M. Pollak, W. F. Wing, R. J. Grasso, E. P. Chicklis, H. P. Jenssen: "CW laser operation of Nd:YLF": *IEEE J. Quant. Electron.* **18** 159 (1982)

[1.75] J. R. O' Connor: "Unusual crystal-field energy levels and efficient laser properties of YVO_4:Nd": *App. Phys. Lett.* **9** 407 (1966)

[1.76] J. J. Rubin, L. G. Van Uitert: "Growth of large yttrium vanadate single crystals for optical maser studies": *App. Opt.* **6** 2920 (1966)

[1.77] KH. S. Bagdasarov, A. A. Kaminskii, V. S. Krylov, V. I. Popov: "Room-temperature induced emission of tetragonal YVO_4 crystals containing Nd^{3+}": *Phys. Stat. Sol.* **27** K1 (1968)

[1.77] A. A. Kaminskii: "High-temperature spectroscopic investigation of stimulated emission from lasers based on crystals activated with Nd^{3+} ions": *Phys. Stat. Sol. A.* **1** 573 (1968)

[1.78] P. P. Yaney, L. G. DeShazer: "Spectroscopic studies and analysis of the laser states of Nd^{3+} in YVO_4": *J. Opt. Soc. Am.* **66** 1405 (1976)

[1.79] A. W. Tucker, M. Birnbaum, C. L. Fincher: "Continuous-wave operation of $Nd:YVO_4$ at 1.06 and 1.34 μm": *J. App. Phys.* **78** 232 (1976)

[1.80] A. W. Tucker, M. Birnbaum, C. L. Fincher, J. W. Erler: "Stimulated-emission cross-section at 1064 and 1342 nm in $Nd:YVO_4$": *J. App. Phys.* **48** 4907 (1977)

[1.81] W. Koechner: "Sold-State Laser Engineering": *3rd edition, Springer Series in Optical Sciences, Volume 1,* (Springer-Verlag, 1992)

[1.82] J. A. Koningstein, J. E. Geusic: "Energy levels and crystal-field calculations of Nd:YAG": *Phys. Rev. A.* **136** 711 (1964)

[1.83] R. W. Wallace, S. E. Harris: "Oscillation and doubling of the 0.946 μm line in Nd^{3+}:YAG": *App. Phys. Lett.* **15** 111 (1969)

[1.84] A. Yariv: "Quantum Electronics": *3rd edition* (Wiley, 1992)

[1.85] J. C. Scott, R. A. M. Maddever, A. T. Paton: "Spectroscopy of methane using a Nd:YAG laser at 1.34 μm": *App. Opt.* **31** 815 (1992)

[1.86] R. K. Jain, D. L. Sipes, T. J. Pier, G. R. Hulse: "Diode-pumped 1.3 μm $Nd:YVO_4$ laser": *Conf. on Lasers & Electoopt. Tech. Dig.* paper THB5 (1988)

[1.86a] *Virgo Optics commercial crystal data sheet December 1993*

[1.87] E. Snitzer: "Glass Lasers": *Proc. IEEE* **54** 1249 (1966)

[1.88] W. J. Kozlovsky, T. Y. Fan, R. L. Byer: "Diode-pumped continuous-wave Nd:glass laser": *Opt. Lett.* **11** 788 (1986)

[1.89] D. W. Hughes, J. R. M. Barr, D. C. Hanna: "A high-power, high-efficiency, laser-diode-pumped, continuous wave miniature Nd:glass laser": *Opt. Comm.* **84** 401 (1991)

[1.90] T. Y. Fan: "Solid-state lasers pumped by advanced diode-laser sources": *OSA Annual Meeting Tech. Dig.* paper TVV4 (1990)

[1.91] S. Basu, R. L. Byer: "Average power limits of diode-laser-pumped solid-state lasers": *App. Opt.* **29** 1765 (1990)

[1.92] S. Basu, R. L. Byer: "40 W average power, 30 Hz moving slab Nd:glass laser": *Opt. Lett.* **11** 617 (1986)

[1.93] K. S. Bagdasarov, A. A. Kaminskii: "$YAlO_3$ with TR^{3+} ion impurity as an active laser medium": *JETP Lett.* **9** 303 (1969)

[1.94] M. J. Weber, M. Bass, K. Andringa: "Czochralski growth and properties of $YAlO_3$ laser crystals": *App. Phys. Lett.* **15** 342 (1969)

[1.95] G. A. Massey, J. M. Yarborough: "High average power operation and nonlinear optical generation with the Nd:$YAlO_3$ laser":*App. Phys. Lett.* **18** 576 (1971)

[1.96] L. Schearer, M. Leduc: "Tuning characteristics and new laser lines in a Nd:YAP CW laser": *IEEE J. Quant. Electron.* **22** 756 (1988)

[1.97] A. A. Kaminskii, S. E. Sarkisov, I. V. Mochalov, L. K. Aminov, A. O. Ivanov: "Anisotropy of spectroscopic characteristics in biaxial $YAlO_3:Nd^{3+}$ laser crystals": *Phys. Stat. Sol. A* **51** 509 (1979)

[1.98] B. Dischler, H. Ennen: "Polarised anisotropic photoluminescence of laser-related transitions in $YAlO_3$:Nd and $YAlO_3$:Er and line broadening by resonant lattice phonons": *J. App. Phys.* **60** 376 (1986)

[1.99] D. Scarl, R. Burnham, S. R. Bowman, B. J. Feldman: "Diode-pumped 1.34 μm $Nd^{3+}:YAlO_3$ laser": *App. Opt.* **27** 5005 (1988)

[1.100] F. Hanson:"Laser-diode side-pumped Nd:$YAlO_3$ laser at 1.08 and 1.34 μm": *Opt. Lett.* **14** 674 (1989)

[1.101] F. Hanson, P. Poirier: "Multiple wavelength operation of a diode-pumped Nd:$YAlO_3$ laser": *J. Opt. Soc. B* **12** 1311 (1995)

[1.101a] D. D. Young, K. C. Jungling, T. L. Williamson, E. R. Nichols: "Holographic interferometry measurement of the refractive index coefficient and the thermal expansion coefficient of Nd:YAG and Nd:YALO": *IEEE J. Quant. Electron.* **8** 720 (1972)

[1.102] D. P. Caffey, R. A. Utano, T. H. Allik: "Diode-array side-pumped GSGG rod and slab lasers": *App. Phys. Lett.* **56** 808 (1990)

[1.103] T. Day, A. C. Nilsson, M. M. Feyer, A. D. Farinas, E. K. Gustafson, C. D. Nabors, R. L. Byer: "30 Hz linewidth diode-laser-pumped nonplanar ring oscillators by active frequency stabilisation": *Electron. Lett.* **25** 810 (1989)

[1.04] T. Day, E. K. Gustafson, R. L. Byer: "Active frequency stabilisation of a 1.062 μm Nd:GGG diode-laser-pumped nonplanar ring oscillator to less than 3 Hz of relative linewidth": *Opt. Lett.* **15** 221 (1990)

[1.104a] T. H. Allik, M. J. Ferry, R. J. Reeves, J. B. Gruber, M. Kokta: "Crystallography, spectroscopic analysis and lasing properties of $Nd^{3+}:Y_3Sc_2Al_3O_{12}$": *Phys. Rev. B* **41** 21 (1990)

[1.105] R. C. Morris, C. F. Cline, R. F. Begley, M. Dutoit, P. J. Harget, H. P. Jenssen, T. S. La France, R. Webb: "Lanthanum beryllate: a new rare-earth ion host": *App. Phys. Lett.* **27** 444 (1975)

[1.106] H. P. Jenssen, R. F. Begley, R. Webb, R. C. Morris: "Spectroscopic properties and laser performance of Nd^{3+} in lanthanum beryllate": *J. App. Phys.* **47** 1496 (1976)

[1.107] R. Scheps: "Efficient diode-pumped Nd lasers": *App. Opt.* **27** 89 (1989)

[1.108] A. A. Godil, K. D. Li, D. M. Bloom: "Pulsed FM mode-locking of a Nd:BEL laser": *Opt. Lett.* **16** 1243 (1991)

[1.109] A. A. Godil, A. S. Hou, B. A. Auld, D. M. Bloom: "Harmonic mode-locking of a Nd:BEL laser using a 20 GHz dielectric resonator / optical modulator": *Opt. Lett.* **16** 1243 (1991)

[1.110] A. Kahn, A. M. Lejus, M. Madsac, J. Thery, D. Vivien: "Preparation, structure, optical and magnetic properties of lanthanum single crystals ($LnMAl_{11}O_{19}$)": *J. App. Phys.* **52** 6864 (1981)

[1.111] V. V. Gamarsh, A. A. Kaminskii, M. I. Polyakov, S. E. Sarkisov, A. A. Filimonov: "Luminescence and stimulated emission of Nd^{3+} ions in $LaMgAl_{11}O_{19}$ crystals in the $^4F_{3/2}$ - $^4I_{11/2}$ and $^4F_{3/2}$ - $^4I_{9/2}$ transitions": *Phys. Stat. Sol. A* **75** K111 (1983)

[1.112] K. S. Bagdasarov, L. M. Dorozhkin, L. A. Ermakova, A. M. Kervorkov, Y. I. Krasilov, N. T. Kuznetsov, I. I. Kuratev, A. V. Potemkin, L. N. Raiskaya, P. A. Tseitlin, A. V. Shestakov: "Spectroscopic and lasing properties of lanthanum neodymium magnesium hexaluminate": *Sov. J. Quant. Electron.* **13** 1082 (1983)

[1.113] D. Saber, J. Dexpert-Ghys, P. Caro, A. M. Lejus, D. Vivien: "Analysis and simulation of optical and magnetic properties of lanthanide aluminates $LnMgAl_{11}O_{19}$ (Ln=La/Nd/La/Eu/Pr) with magnetoplumbite-like structure": *J. Chem. Phys.* **82** 5648 (1985)

[1.114] Y. Shi, J. P. Ragey, H. K. Haugen: "CW, Q-switched and mode-locked opeartion of a laser-pumped Nd:LMA laser": *IEEE J. Quant. Electron.* **29** 435 (1993)

[1.115] L. D. Schearer, M. Leduc, D. Vivien, A. M. Lejus, J. Thery: "LMA: a new cw Nd laser tunable around 1.05 and 1.08 μm": *IEEE J. Quant. Electron.* **22** 713 (1986)

[1.116] J. Hamel, A. Cassimi, H. Abu-Safia, M. Leduc, L. D. Schearer:": Diode-pumping of LNA lasers for helium optical pumping": *Opt. Comm.* **63** 114 (1987)

[1.117] T. Y. Fan, M. R. Kokta: "End-pumped Nd:LaF_3 and Nd:$LaMgAl_{11}O_{19}$ lasers": *IEEE J. Quant. Electron.* **25** 1845 (1989)

[1.118] D. W. Hughes, A. Majdabadi, J. R. M. Barr, D. C. Hanna: "FM mode-locked laser-diode-pumped $La_{1-x}Nd_xMgAl_{11}O_{19}$ laser": *App. Opt.* **32** 5959 (1993)

[1.119] M. W. Phillips, J. R. M. Barr, D. W. Hughes, D. C. Hanna, Z, Chang, C. N. Danson, C. B. Edwards: "Self-starting additive pulse mode-locking of a Nd:LMA laser": *Opt. Lett.* **17** 1453 (1992)

[1.120] D. W. Hughes, J. R. M. Barr: "Laser diode pumped solid-state lasers": *J. Phys. D* **25** 563 (1992)

[1.121] A. A. Kaminskii: "Laser Crystals: their physics and properties": *2nd edition, Springer Series in Optical Sciences, Volume 14* (Springer-Verlag, 1990)

[1.122] T. Y. Fan, A. Cordova-Plaza, M. J. F. Digonnet, R. L. Byer, M. J. Shaw: "Nd:MgO:$LiNbO_3$ spectroscopy and laser devices": *J. Opt. Soc. Am. B* **3** 140 (1986)

[1.123] I. Schuetz, I. Freitag, R. Wallenstein: "Miniature self-frequency doubling cw Nd:YAB laser pumped by a diode-laser": *Opt. Comm.* **77** 221 (1990)

[1.124] S. G. Grubb, R. S. Cannon, G. J. Dixon: "Self-frequency doubling monolithic cube laser in neodymium yttrium aluminium borate": *Conf. on Lasers & Electoopt. Tech. Dig.* paper CFJ6 (1991)

[1.125] T. H. Allik, M. J. Ferry, R. J. Reeves, R. C. Powell, W. W. Hovis, D. P. Caffey, R. A. Utano, L. Merkle, C. F. Campana: "Crystallography, spectroscopic analysis and lasing properties of Nd^{3+}:$Ba_2ZnGe_2O_7$": *J. Opt. Soc. Am. B* 71190 (1990)

[1.126] P. Hong, X. X. Zhang, M. Bass, B. H. T. Chai: "Nd^{3+}-doped apatite crystals for diode-pumped 1.06 and 1.33 μm lasers": *Conf. on Lasers & Electoopt. Tech. Dig.* paper CTuP6 (1994)

[1.127] K. Kubodera, K. Otsuka: "Efficient $LiNdP_4O_{12}$ laser pumped with a laser-diode": *App. Opt.* **18** 3882 (1979)

[1.128] K. Kubodera, J. Noda: "Pure single-mode $LiNdP_4O_{12}$ laser pumped with a laser-diode": *App. Opt.* **18** 884 (1979)

[1.129] G. J. Dixon, L. S. Lingvay, R. H. Jarman: "Lithium neodymium tetraphosphate lasers pumped via close-coupling to high-power laser-diode arrays": *IEEE Photon. Tech. Lett.* **1** 97 (1989)

[1.130] R. Allen, L. Esterowitz, L. Goldberg, J. F. Weller, M. Storm: "Diode-pumped 2 μm holmium laser": *Electron. Lett.* **22** 947 (1986)

[1.131] S. W. Henderson, C. P. Hale: "Tunable, SLM, diode-laser-pumped Tm:Ho:YAG laser": *App. Opt.* **29** 1716 (1990)

[1.132] H. Hemmati: "2.07 μm cw diode-laser-pumped Tm, Ho:$YLiF_4$ room-temperature laser": *Opt. Lett.* **14** 435 (1989)

[1.133] C. D. Nabors, J. Ochoa, T. Y. Fan, A. Sanchez, H. K. Choi, G. W. Turner: "Ho:YAG laser pumped by 1.9 μm diode lasers": *IEEE J. Quant. Electron.* **31** 1603 (1995)

[1.134] G. J. Kintz, R. Allen, L. Esterowitz: "CW and pulsed 2.8 μm laser emission from diode-pumped Er^{3+}:$LiYF_4$ at room temperature": *App. Phys. Lett.* **50** 1553 (1987)

[1.135] P. Laporta, S. De Silvestri, V. Magni, O. Svelto: "Diode-pumped cw bulk Er:Yb:glass laser": *Opt. Lett.* **16** 1952 (1991)

[1.136] T. Schweizer, T. Jensen, E. Heuman, G. Huber: "Spectroscopic properties and diode-pumped 1.6 μm laser performance in Yb-codoped Er:$Y_3Al_5O_{12}$ and Er:Y_2SiO_5": *Opt. Comm.* **118** 557 (1995)

[1.137] P. Laporta, S. Longhi, M. Marchesi, S. Taccheo, O. Svelto: "2.5 and 5 GHz harmonic mode-locking of a diode-pumped erbium-ytterbium glass laser at 1.5 μm": *IEEE Photon. Tech. Lett.* **7** 155 (1995)

[1.138] D. C. Hanna, R. M. Percival, I. R. Perry, R. G. Smart, P. J. Suni, J. E. Townsend, A. C. Tropper: "Continuous-wave oscillations of a monomode Yb-doped fibre-laser": *Electron. Lett.* **24** 1111 (1988)

[1.139] P. Lacovara, H. K. Choi, C. A. Wang, R. L. Aggarawal, T. Y. Fan: "Room-temperature diode-pumped Yb:YAG laser": *Opt. Lett.* **16** 1089 (1991)

[1.140] T. Y. Fan, S. Klunk, G. Henein: "Diode-pumped Q-switched Yb:YAG laser": *Opt. Lett.* **18** 1952 (1993)

[1.141] U. Brauch, A. Giesen, M. Karszewski, C. Stewen, A. Voss: "Multi-watt diode-pumped Yb:YAG thin disc laser continuously tunable between 1018 and 1053 nm": *Opt. Lett.* **20** 713 (1995)

[1.142] P. J. M. Suni, S. W. Henderson: "1 mJ / pulse Tm:YAG laser pumped by a 3 W diode-laser": *Opt. Lett.* **16** 817 (1991)

[1.143] J. F. Pinto, L. Esterowitz, G. H. Rosenblatt: "Continuous-wave mode-locked 2 μm Tm:YAG laser": *Opt. Lett.* **17** 731 (1992)

[1.144] W. P. Risk: "Modeling of longitudinally pumped solid-state lasers exhibiting reabsorption losses": *J. Opt. Soc. Am. B* **5** 1412 (1988)

[1.145] M. J. F. Digonnet, C. J. Gaeta: "Theoretical analysis of optical fibre laser amplifiers and oscillators": *App. Opt.* **24** 333 (1985)

[1.146] T. Y. Fan, R. L. Byer: "Diode-laser pumped solid-state lasers": *IEEE J. Quant. Electron.* **24** 895 (1988)

[1.147] T. Y. Fan, R. L. Byer: "Modelling and CW operation of a quasi-three-level 946 nm Nd:YAG laser": *IEEE J. Quant. Electron.* **23** 605 (1987)

[1.148] K. Kubodera, K. Otsuka: "Single transverse mode LNP waveguide laser": *J. App. Phys.* **50** 653 (1979)

[1.149] D. G. Hall, R. J. Smith, R. R. Rice: "Pump-size effects in Nd:YAG lasers": *App. Opt.* **19** 3041 (1980)

[1.150] D. G. Hall: "Optimum mode-size criteria for low gain lasers": *App. Opt.* **20** 1579 (1981)

[1.151] R. W. Boyd: "Radiometry and the Detection of Optical Radiation": Wiley, 1983

[1.152] M. Born, E. Wolf: "Principles of Optics": *6th edition* Pergamon Press, 1993

[1.153] J. R. Leger, W. C. Goltsos: "Geometrical transformation of linear diode-laser arrays for longitudinal pumping of solid-state lasers": *IEEE J. Quant. Electron.* **28** 1088 (1992)

[1.154] P. Laporta, M. Brussard: "Design criteria for mode size optimisation in diode-pumped solid-state lasers": *IEEE J. Quant. Electron.* **28** 1088 (1991)

[1.155] T. Y. Fan, A. Sanchez: "Pump source requirements for end-pumped lasers": *IEEE J. Quant. Electron.* **26** 311 (1990)

[1.156] J. Hong: "Frequency-doubled and Q-switched 946 nm diode-pumped Nd:YAG laser": *PhD thesis, University of St. Andrews, 1992.*

[1.157] W. A. Clarkson, A. B. Neilson, D. C. Hanna: "Novel beam shaping technique for high-power diode-bars": *Conf. on Lasers & Electoopt. Tech. Dig.* paper CThL2 (1994)

[1.158] R. P. Edwin: "Stripe stacker for use with laser diode bars": *Opt. Lett.* **20** 222 (1995)

[1.159] W. A. Clarkson, R. L. Koch, K. I. Martin, D, C. Hanna: "High-power 946 nm Nd:YAG laser pumped by a diode-bar": *Conf. on Lasers & Electoopt. Tech. Dig.* paper CMD4 (1995)

[1.160] W. A. Clarkson, K. I. Martin, D, C. Hanna: "High-power single-frequency operation and efficient intracavity-doubling of a Nd:YAG ring laser end-pumped by a 20W diode bar": *Conf. on Lasers & Electoopt. Tech. Dig.* paper CMD8 (1995)

[1.161] T. Y. Fan, A. Sanchez, W. E. DeFoe: "Scalable, end-pumped, diode-laser-pumped laser": *Opt. Lett.* **14** 1057 (1989)

[1.162] N. P. Barnes: "Diode-pumped solid-state lasers": *J. App. Phys.* **44** 230 (1973)

[1.163] K. Kubodera, K. Otsuka: "Diode-pumped miniature solid-state laser": *App. Opt.* **16** 2747 (1977)

[1.164] J.-P. Budin, M. Neubauer, M. Rondot: "On the design of neodymium miniature lasers": *IEEE J. Quant. Electron.* **14** 831 (1978)

[1.165] S. Basu, R. L. Byer: "Average power limits of diode-laser-pumped solid-state lasers": *App. Opt.* **29** 1765 (1990)

[1.166] T. H. Allik, W. W. Hovis, D. P. Caffey, V. King: "Efficient diode-array-pumped Nd:YAG and Nd:Lu:YAG lasers": *Opt. Lett.* **14** 116 (1989)

[1.167] F. Brioschi, E. Nava, G. C. Reali: "Gain shaping and beam quality in diode-laser multiarray side-pumped solid-state lasers": *IEEE J. Quant. Electron.* **28** 1070 (1992)

[1.168] D. Welford, D. M. Rines, B. J. Dinerman, R. Martinsen: "Observation of enhanced thermal lensing due to near-Gaussian pump energy deposition in a laser-diode side-pumped Nd:YAG laser": *IEEE J. Quant. Electron.* **28** 1075 (1992)

[1.169] S. D. Jackson, J. A. Piper: "Theoretical modelling of a diode-pumped Nd:YAG laser with a solid non-focusing pump light collector": *App. Opt.* **33** 2273 (1994)

[1.170] T. M. Baer, T. F. Head, P. Gooding, G. J. Kintz, S. Hutchison: "Performance of diode-pumped Nd:YAG and Nd:YLF lasers in a tightly folded resonator configuration": *IEEE J. Quant. Electron.* **28** 1131 (1992)

Chapter 2

DIODE-LASER DEVICES FOR PUMPING SOLID-STATE LASERS

2.1 Introduction

The benefits of semiconductor pump sources outlined in Chapter 1 have resulted in diode-laser devices being the preferred excitation mechanism for solid-state lasers. The main restrictions on their use arise from the absorption wavelengths of the laser medium, which cannot always be matched by available devices, and the maximum brightness and/or power obtainable at the desired pumping wavelength, which has to be considered together with the $\sigma\tau$ product of the laser. As research continues on semiconductor lasers, the prospects for pumping a wider variety of active ions in host materials improve.

Single-stripe and broad-area devices have been employed in a variety of lasers, but it is the development of the diode-laser array that has greatly improved the performance of Nd lasers. Arrays have been investigated since the late 1970s. Initially, the aim was the production of high-power, coherent, diffraction-limited beams for applications such as free-space optical communication, optical signal processing and laser printing. However, around 1983 interest arose in spatially incoherent arrays as efficient pumps for solid-state lasers, and this remains the most widespread use of such arrays. Without the requirement of coherence to impede the progress of these pump devices, output powers were quickly scaled up to the multi-watt level. The most important development came in the mid 1980s with the commercial production of diode-bars consisting of multiple arrays spaced on a single wafer, and two-dimensional stacks of diode-bars. Commercial CW diode-bars such as the *SDL 3400* series can deliver up to 20 W of power, while quasi-CW 2D stacks such as the *SDL 3200* series are capable of up to 5 kW peak power in a 400 μs, 2 J pulse. Unfortunately, the cost of bars and stacks remains relatively high due to the labour-intensive production process, although increased demand and automation should lead to cheaper devices in the future.

High-power *coherent* arrays are also an important area, as they may soon replace bulk or microchip lasers for certain applications. Progress here has been much slower. Up until 1988, diffraction-limited coherent powers were restricted to around 100 mW, which is almost the same as that available from a single-stripe device. The original approach of evanescent-wave coupling of adjacent stripes in arrays (modelled by the coupled-mode theory) failed because it did not lead to strong overall coupling as intended. This "series coupling" resulted in weak overall coherence and poor intermodal discrimination. Parallel coupling could only be achieved by weakening the optical mode confinement, thereby making the devices vulnerable to thermal- and/or injected-carrier- induced variations in dielectric constant. This resulted in higher-order mode oscillation and instabilities at high drive levels. The breakthrough came with the development of antiguided (or negative index guided) arrays which support so-called "leaky-wave" modes, which are favoured to lase when gain is preferentially placed in the low-index regions of the array. The modes of these "resonant optical waveguides" (ROWs) comprise the fundamental element modes coupled in or out of phase. Strong overall coupling can be achieved simultaneously with strong optical mode confinement. Coherent powers up to 2 W have been achieved in a single-lobed, diffraction-limited output [2.1].

2.2 Review of Single-Stripe Heterostructure Devices

2.2.1 Basic Properties of AlGaAs Heterostructures

The double heterostructure laser was introduced in 1969 by Hagashi *et al* [2.2], a development which turned the semiconductor laser from a laboratory curiosity into a practical room-temperature device. Devices based on GaAs, having been widely researched, are the most advanced. Typical heterostructures based on this material consist of an active layer of AlGaAs 100 - 200 nm thick sandwiched between two AlGaAs cladding layers of opposite doping. To define a potential well for injected charge carriers in the active layer, the fraction x of substituent aluminium in the cladding layers is significantly higher than that of the active layer. x is normally in the range 0.3 - 0.7. The cladding layers are contacted by GaAs layers of the same doping-type. Epitaxial growth of these devices is possible because of the near perfect lattice match of $Al_xGa_{1-x}As$ to GaAs over the entire range $x = 0$ to 1. The band-gap of $Al_xGa_{1-x}As$ is given by

$$E_g(eV) = 1.42 + 1.27x, \tag{2.1}$$

with the result that a 1% change in the aluminium content of the active layer results in a ≈ 1 nm change in wavelength. The change in band-gap energy, $\Delta E_g = 1.27x$ is split between the conduction and valence band edges according to

$$\Delta E_c \approx \frac{2}{3}\Delta E_g ; \Delta E_v \approx \frac{1}{3}\Delta E_g . \tag{2.2}$$

The charge-carrier potential well and index-step produced by the active layer allow efficient operation due to the spatial coincidence of the population inversion and optical mode. The high gain (typically 150 cm^{-1}) and high refractive index (*e.g.* 3.6 for GaAs) mean that simple cleaving of the device perpendicular to the plane of the active layer provides sufficient optical feedback for lasing.

As far as is known, a direct-band-gap active layer is an essential requirement for laser operation [2.3]. Optical transitions between bands are restricted by the selection rule $\Delta k = 0$, so that in an indirect gap material a phonon must be absorbed to provide the necessary momentum change. This requirement of the simultaneous interaction of a phonon and a photon sharply reduces the probability of radiative recombination, compared to direct-gap materials.

For conventional heterostructures, the density of states in the conduction band in terms of the transition frequency ω is given by

$$\rho(\omega)=\frac{1}{2\pi^2}\left(\frac{2m_r}{\hbar}\right)^{3/2}\left(\omega-\frac{E_g}{\hbar}\right)^{1/2}, \tag{2.3}$$

where m_r is the reduced mass of the electrons and holes in the active layer. This can be used to obtain the small signal gain coefficient $\gamma(\omega)$

$$\gamma(\omega)=\frac{\mu^2}{\lambda_0\varepsilon_0 n\hbar}\left(\frac{2m_r}{\hbar}\right)^{3/2}\left(\omega-\frac{E_g}{\hbar}\right)^{1/2}\left[g_c(\omega)-g_v(\omega)\right]=\alpha_0(\omega)\left[g_c(\omega)-g_v(\omega)\right]. \tag{2.4}$$

μ is the matrix element for transition, and the factors $g_c(\omega)$, $g_v(\omega)$ are the probability distributions at the frequency ω for electrons in the conduction band and holes in the valence band respectively. $g_c(\omega)$ is given by the Fermi-Dirac function

$$g_c(\omega)=\frac{1}{e^{[E_c(\omega)-E_{Fc}]}+1}, \tag{2.5}$$

where E_{Fc} is the quasi-Fermi level for electrons in the conduction band, *i.e.* the energy (or transition frequency) for which the occupation probability is 1/2 under steady-state conditions. A similar expression applies to the distribution of holes in the valence band, $g_v(\omega)$. From (2.4), a frequency ω will experience gain provided

$$g_c(\omega)-g_v(\omega)>1,$$

or equivalently

$$E_{Fc}-E_{Fv}>\hbar\omega. \tag{2.6}$$

The maximum frequency amplified therefore depends on the energy separation of the quasi-Fermi levels which is fixed by the pumping current level; in fact the lowest amplified frequency is also dependent on the pumping level because the band-gap is a function of the injected-carrier density.

Some fine tuning of the operating wavelength may be carried out by adjusting the temperature of the diode-laser. In AlGaAs lasers, the peak emission shifts by typically +0.3 nm/°C. The full spectral width of the emission is typically 3nm. The threshold current is also a function of temperature, following the empirical relation

$$I_{th}=I_0 e^{T/T_0}, \tag{2.7}$$

where I_0 is a constant and $T_0 \approx 120$ K for AlGaAs, so that a 10 K rise in temperature causes a $\approx$ 9% increase in the threshold current. Significant reduction in threshold

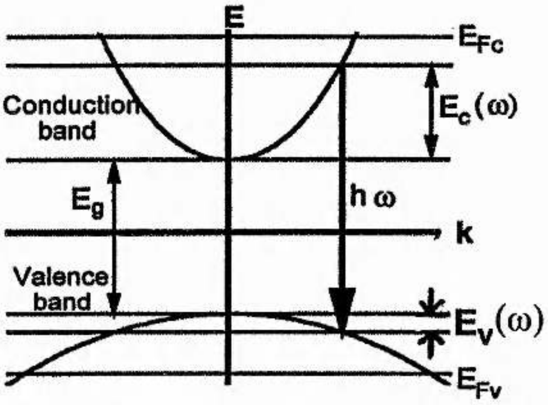

Figure 2.1. E - k diagram for laser operation.

current can be achieved by doping the active layer. This reduces the rate at which charge carriers have to be injected before inversion occurs. *n*-type doping is more effective in this regard than *p*-type, due to the higher *E* - *k* curvature of the conduction band. However, there is a balance to be struck: heavy doping leads to the formation of so-called "band-tail" states. These additional continua of states at the band edges contribute to spontaneous emission and therefore increase the threshold. In some cases transitions between band-tail states have sufficient gain for lasing to occur on them.

The threshold current is also affected by the thickness of the active layer. Although reducing the active-layer thickness generally lowers the threshold, concomitant reduction in the optical mode confinement means that this is only effective for thicknesses down to ≈ 100 nm.

Theoretical and experimental investigations have shown that the gain γ is approximately linearly dependent on the injected carrier density n [2.4],

$$\gamma(n) = a(n - n_0), \tag{2.8}$$

where a is a constant and n_0 is the carrier density required for transparency. an_0 is the absorption coefficient of the unpumped material. To determine threshold in a real system, the actual gain is taken to be

$$G = \Gamma\gamma, \tag{2.9}$$

where Γ is the confinement factor, representing the fraction of the optical mode energy contained in the active layer. Threshold is achieved when G is equal to the sum of mirror and internal losses:

$$\Gamma\gamma = \alpha_m + \alpha_{\text{int}}. \tag{2.10}$$

From (2.8) and (2.10), the threshold carrier density is

$$n_{th} = \frac{\alpha_m + \alpha_{\text{int}}}{\Gamma a} + n_0, \tag{2.11}$$

and the threshold current density

$$J_{th} = \frac{qdn_{th}}{\tau_{r,th}}, \tag{2.12}$$

where d is the active layer thickness, q the electronic charge and $\tau_{r,th}$ the recombination time at threshold.

The output power can be obtained by considering the steady-state rate of photon generation inside the cavity:

$$\frac{J-J_{th}}{qd}=\frac{N}{\tau_{ph}}. \tag{2.13}$$

N is the photon number density inside the cavity, and τ_{ph} is the photon lifetime, given by

$$\tau_{ph}{}^{-1}=(\alpha_m+\alpha_{\text{int}})v_g,$$

(2.14)

where v_g is the group velocity. The output power per facet is

$$P=\frac{1}{2}\hbar\omega v_g\alpha_m NV, \tag{2.15}$$

where V is the volume of the active layer. Using (2.13) and (2.14), (2.15) may be written as

$$P=\frac{\hbar\omega}{2q}\frac{\alpha_m}{\alpha_m+\alpha_{\text{int}}}(I-I_{th}-\Delta I_l), \tag{2.16}$$

where ΔI_l represents any increase in leakage current, *i.e.* current that does not flow through the active layer.

Since efficiency is cited as a major advantage of DPSSLs, the efficiency of diode-lasers merits some consideration. Before the onset of saturation, the slope dP/dI is approximately constant. The external or differential quantum efficiency is defined by

$$\eta_{ext}=\eta_{\text{int}}\frac{\xi_e}{\xi_g}=\eta_{\text{int}}\frac{\alpha_m}{\alpha_m+\alpha_{\text{int}}}, \tag{2.17}$$

where η_{int} is the internal quantum efficiency, and ξ_g , ξ_e are the photon generation and escape rates respectively. Above threshold, stimulated recombination dominates so that $\eta_{int}\approx 1$. Under steady-state conditions, photons are generated at a rate $1/\tau_{ph}$ and escape from the laser at a rate $v_g\alpha_m$, giving

$$\eta_{ext}=\eta_{\text{int}}\frac{\alpha_m}{\alpha_m+\alpha_{\text{int}}}=\frac{2q}{\hbar\omega}\eta_{\text{int}}\frac{dP}{dI}. \tag{2.18}$$

Internal losses are therefore the principal limiting factor for η_{ext}.

2.2.2 Lateral Waveguiding Schemes in Single-Stripe Lasers

Although a simple heterostructure can be operated as a "broad area" laser, most devices have some built-in lateral features to restrict the injection current and optical mode in the plane of the junction. This allows fundamental-mode operation in the plane of the junction, in addition to lowering the threshold current and heat-sink requirements. A lower threshold means a generally lower level of drive current, which increases the lifetime of the device.

2.2.2.1 Gain Guiding

Gain guiding can be achieved by restricting the area to which the injection current is applied. Two standard designs for this are the oxide-stripe laser, where a SiO_2 stripe confines the current flow to a small region through an opening in a top dielectric layer, and the proton (or deuteron) stripe laser where implanted protons (or deuterons) create a region of high resistivity around an unimplanted region.

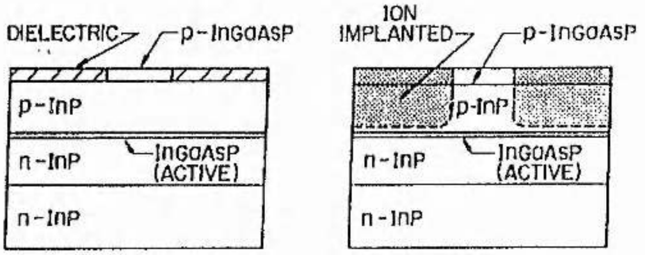

Figure 2.2. Oxide- (left) and proton-stripe InGaAsP gain-guided lasers [2.4].

2.2.2.2 Weak Index Guiding

In weak index-guiding, the laser structure is modified so as to introduce an effective lateral index-step of ~ 10^{-2}, which is larger than the carrier-induced reduction. This requires the thickness of at least one layer to be laterally non-uniform. Two common generic designs are the *ridge-* and *rib-waveguide* structures. In a ridge-type system, the injection current and optical mode are both confined by a ridged contact layer, while the rib-type devices give optical guiding by either a ribbed active layer or an additional ribbed layer next to the active layer.

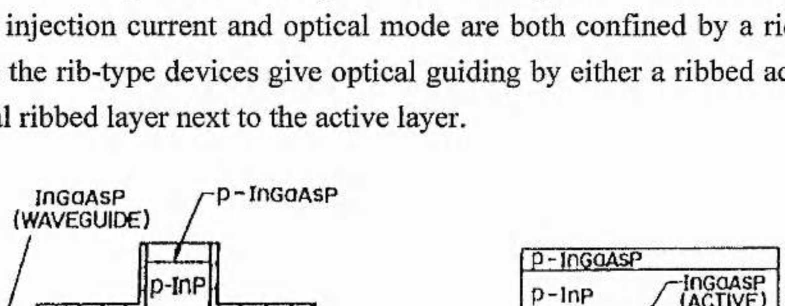

Figure 2.3. Ridge- (left) and rib-waveguide structures [2.4].

2.2.2.3 Strong Index-Guiding

In strongly-index guided lasers, the active region is buried in higher-band-gap layers on all sides; hence they are often referred to as *buried-heterostructure lasers.* The lateral index-step along the plane of the active layer is ~ 0.2, which is two orders of magnitude greater than carrier-induced effects. Lasing characteristics are primarily determined by the rectangular waveguide that confines the active layer. Figure 2.4 shows one example of a strongly-index guided design.

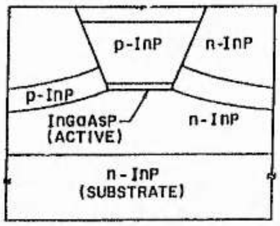

Figure 2.4. Etched-Mesa Buried Heterostructure [2.4].

2.2.3 Quantum Well Systems

2.2.3.1 Single Quantum-Well (SQW) Devices

If the thickness of the active layer is reduced to the region of 5 - 20 nm, *i.e.* an order of magnitude thinner than in a typical conventional heterostructure, the trapped charge carriers display quantum-mechanical effects because the well width is of the order of the de Broglie wavelength. The principal physical feature of a quantum well is the quantised density of states function which arises from the "particle in a box" nature of the system in the direction perpendicular to the junction, which is given by:

$$\rho_{QW}(E) = \frac{m_c}{\pi\hbar^2}\sum_{n=1}^{\infty} H(E - E_{nc}), \qquad (2.19)$$

where m_c is the mass of an electron in the conduction band, H is the Heaviside function, and E_{nc} is the energy of the nth quantum state in the conduction band:

$$E_{nc} = \frac{n^2\hbar^2\pi^2}{2m_c L_z^{\ 2}}, \qquad (2.20)$$

L_z being the well thickness.

Most of the advantages that QW lasers have over conventional systems are due

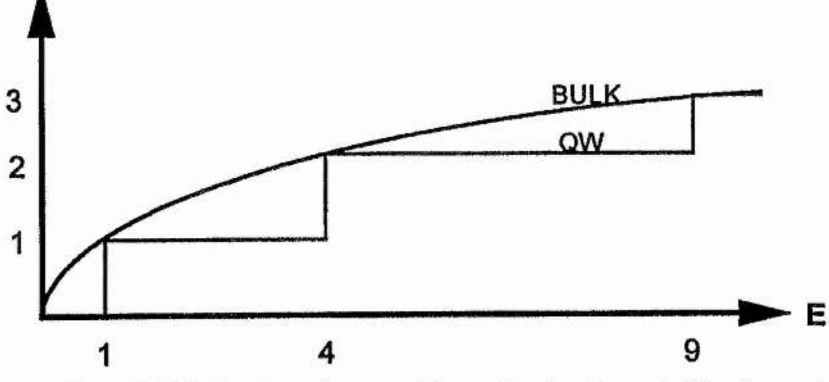

Figure 2.5. Bulk and QW density of states. The unit of ρ is $m_c/\pi h^2$; the unit of energy is $\pi^2 h^2/2m_c^{\,2}L_z^{\,2}$.

to this modification of the density of states [2.5]. The main benefits are:

lower threshold current, typically an order of magnitude
much greater gain difference between TE and TM modes (favouring TE mode)
narrower linewidth
reduced chirping (due to reduced refractive index change with current level)
lower optical absorption at the laser wavelengh, which is useful for monolithic integration with passive QW waveguides.

In addition to the normal band-gap engineering, emission wavelength can also be influenced by the thickness of the active layer L_z.

The much reduced active layer thickness means that additional optical confinement perpendicular to the active layer is required. This "separate confinement" can involve abrupt or graded-index (GRIN) steps as shown in Figure 2.6.

The first demonstration of a SQW laser-diode was by Van der Ziel *et al* in 1975 [2.6]. The performance (at 15K) was limited by the immaturity of the epitaxial technology of the time. Room-temperature AlGaAs SQW devices were first operated by Depuis *et al* [2.7] and Holonyak *et al* [2.8] in 1978.

2.2.3.2 Multiple Quantum-Well (MQW) Devices

To produce higher gain, several quantum wells can be epitaxially grown on top of each other, separated by high-band-gap barrier layers thick enough to prevent quantum-tunelling. At low drive currents, the smallness of the inversion factor $[g_c\text{-}g_v]$ means that the total gain can be less than that for a SQW laser [2.9], but for high current levels, the gain can be several times higher, in part due to the larger optical confinement factor Γ of multiple well lasers. Figure 2.7 shows the performance of a typical MQW system.

2.2.3.3 Strained-Layer Quantum-Well Lasers

The range of wavelengths available from bulk and QW AlGaAs lasers is

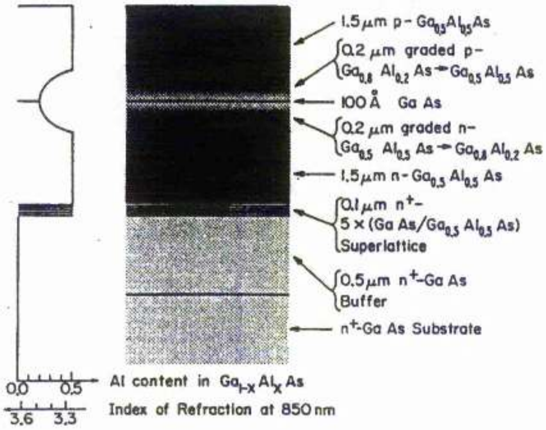

Figure 2.6. GRIN-SCH-MQW laser [2.10].

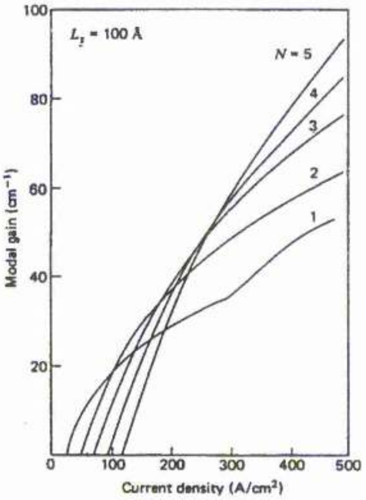

Figure 2.7. Gain in MQW lasers [2.9].

approximately 0.75 - 0.88 μm. The long wavelength limit is set by the band gap of GaAs, and either AlGaAs or the quantum size effect, or both, may be used to shift the emission to shorter wavelengths. This wavelength range covers several important applications, including the pumping of Nd^{3+}:YAG at 0.81 μm. Extension to longer wavelengths can be achieved by the use of $In_xGa_{1-x}As$ as the active layer, but there is no suitable binary substrate that can lattice match this system for the wavelength range of interest. The $In_xGa_{1-x}As$ lattice parameter can be up to 3.6% larger than that of GaAs; conventional heterostructures require differences of the order of 0.1%. The solution has been the use of quantum-well devices in which the active layer is below a certain "critical thickness", allowing the strain to be accommodated elastically without misfit dislocations. Although the band-gap reduction introduced by the In is somewhat offset by the increase due to strain, the emission range 0.88 - 1.1 μm can be covered by these lasers.

2.3 III-V Material Systems and Wavelengths

2.3.1 Band-Gap Engineering

Most semiconductor devices, including lasers, use elements in the second, third and fourth periods of the periodic table: group III elements Al, Ga, In and group V elements P, As, Sb. The range of properties (of which band-gap is the most relevant here) of the nine binary compounds can be extended by the use of ternary compounds, such as AlGaAs and InAsSb and quaternary compounds such as InGaAsP and AlGaInP. In ternary and quatenary systems, the ratio of group III to group V atoms is kept at 1:1, but either or both of the two classes of atom (III and V) consist of a mixture. Figure 2.8 shows the relation between band-gap and lattice constant for III-V systems. By choosing the right proportions for the mixture, a range of band-gaps can be selected. Lattice-matching for epitaxial layers is the other important consideration. For example, $In_{0.75}Ga_{0.25}As_{0.44}P_{0.56}$, which is grown on an InP substrate, produces photons of energy 1 eV. The lattice match to InP defines the lattice parameter and the band-gap defines the photon energy. To obtain a higher energy photon, the ratio of P:As would be increased and the ratio of Ga:In decreased to bring the lattice constant back to match InP.

III - V devices are capable of covering the spectral pump requirements of a large range of solid-state lasers, in addition to the useful 1.3 and 1.55 μm fibre-communication wavelengths. Wang and Groves have reviewed new materials for pumping applications [2.12]. The main active-layer systems are summarised in Table 2.1.

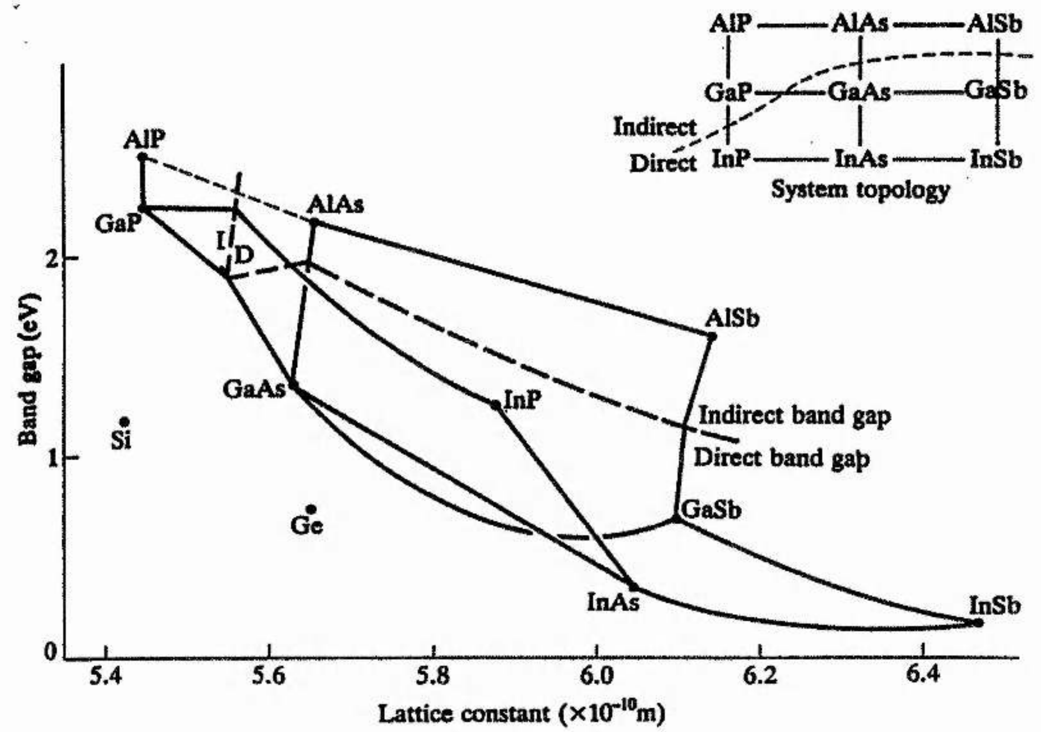

Figure 2.8. Variation of band-gap with composition for III-V semiconductors [2.11].

Active Layer	λ Range (μm)	Applications
AlGaAs	0.78 - 0.87	≈ 0.8 μm pump for Nd, Tm/Ho, Er, Tm
InGaAs	0.78 - 1.1	≈ 0.97 μm pump for Er, Er/Yb; 0.94 μm pump for Yb
InGaAsP	1.2 - 2.0	1.3, 1.5 μm telecom.; 1.9 μm pump for Ho
AlGaInP	0.63 - 0.69	≈ 0.67 μm pump for Cr in LiSAF, LiCAF, $BeAl_2O_4$

Table 2.1. Applications of III-V lasers.

2.3.2 Review of Growth Methods for III-V Materials

2.3.2.1 Liquid Phase Epitaxy (LPE)

LPE was the first epitaxial technique to be widely used. A substrate slice is held in a graphite container and is slid into contact with liquid from which the epitaxial layer can crystallise out. To deposit AlGaAs on GaAs, the liquid would be GaAs and Al dissolved in molten Ga at about 750°C. The temperature is adjusted so that the substrate grows rather than dissolves. Typical growth rates are on the order of 1 μm min^{-1}. Multiple layers can be produced by sliding the sample between different reservoirs.

2.3.2.2 Vapour-Phase Epitaxy (VPE), Chemical Vapour Deposition (CVD), Metal-Organic Chemical Vapour Deposition (MOCVD)

In these techniques, the atoms to form the growth layer are carried as volatile chemicals in a low pressure (0.1 - 1 atm.) gas stream (usually H_2) over the substrate. The molecules decompose on meeting the heated substrate, leaving the group III or V atoms to build up the epitaxial layer. Compounds used include AsH_3, PH_3, $AsCl_3$, PCl_3, $Al(CH_3)_3$ and $Ga(CH_3)_3$. The composition of the growing layer can be adjusted by changing the gas mixture flowing over the substrate. Growth rates are of the order of $0.1\ \mu m\ min^{-1}$.

2.3.2.3 Molecular Beam Epitaxy (MBE)

The atoms to form the new growth layers are produced by evaporation in high vacuum in separate containers. A molecular beam of each required element falls on the substrate. The atoms only meet on the substrate, and the separate control means that MBE is more flexible than either LPE or CVD. Growth rates are low (*e.g.* $0.01\ \mu m\ min^{-1}$) and the equipment is complex and expensive. Multiple layers of binary, ternary and quaternary compounds can be deposited.

2.4 Diode-Laser Arrays; Diode-Bars and Stacks

2.4.1 Phase-Locked Arrays

Conventional narrow stripe (3 - 4 μm wide) single-mode lasers provide at most 100 mW reliably. The early thinking on power scaling was that "large aperture" devices ($>\approx$ 100 μm wide) were necessary to obtain coherent powers in the watt-range. Although such lasers do emit substantial powers, the injection current tends to break up into filaments rather than spread evenly through the active region. The concomitant filamentary lasing causes localised damage at the facet, thereby reducing the operating lifetime. By the late 1970s diode-laser arrays, consisting of several closely spaced narrow stripe lasers, were being investigated as a possible route to reliable high-power semiconductor lasers. The challenge has been to maintain a stable, diffraction-limited spatial mode to the multi-watt level.

Arrays of gain-guided stripes were the first to be investigated due to their ease of fabrication. Unfortunately, these systems gave unstable beam patterns at high drive levels, and around 1983 the emphasis turned to arrays with "built-in" refractive index profiles. The aim here was to cause coupling of the stripes by evanescent-wave overlap. Some examples of these "positive-guides" are shown in Figure 2.9. Evanescent array-modes (*i.e.* with field maxima in the high-index regions) were successfully achieved by ensuring sufficient loss in the low-index interelement regions. These arrays invariably operated with adjacent stripes 180° out of phase, resulting in a dual-lobed far-field

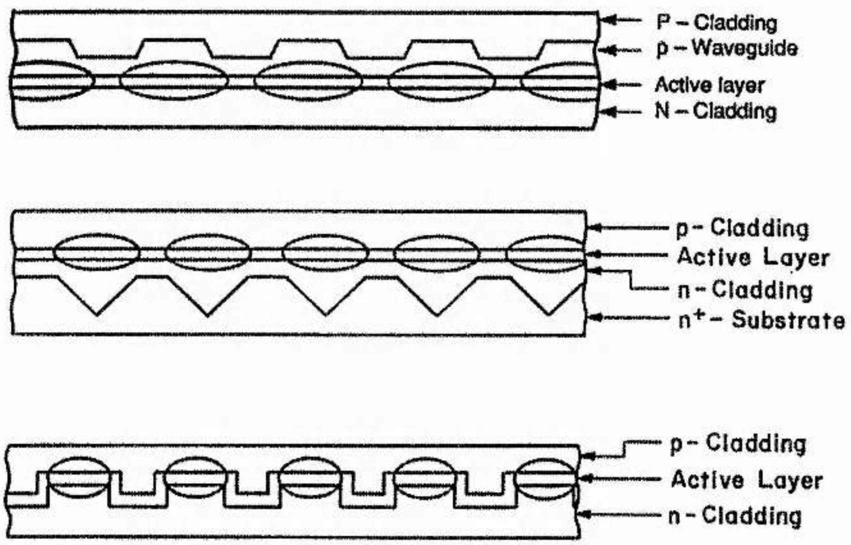

Figure 2.9. Ridge (top) and channelled evanescent-wave-coupled diode-laser arrays [2.1].

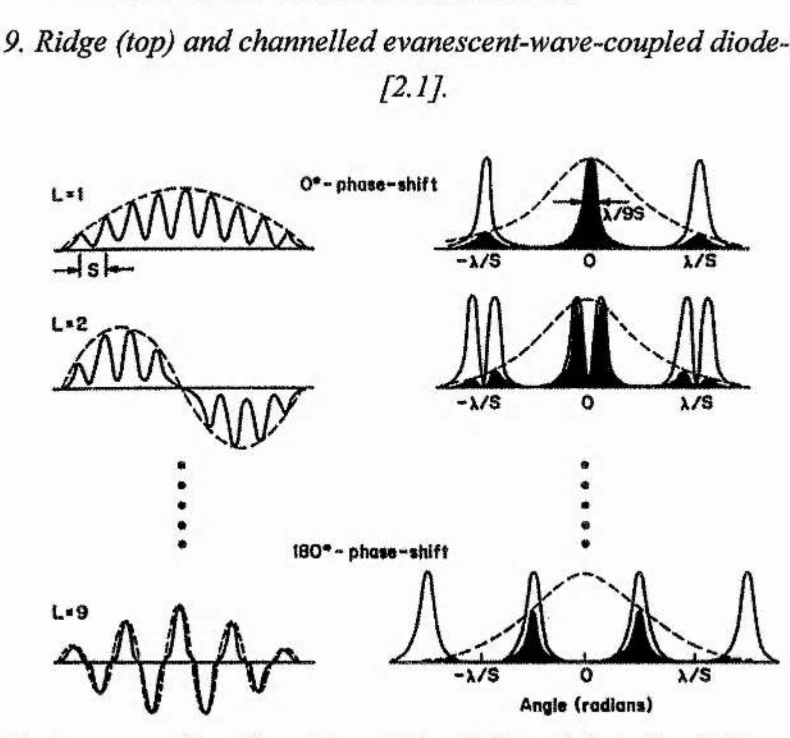

Figure 2.10. Arrays-modes of positive-guides (left) and their far-field patterns [2.15].

output which was clearly undesirable for applications, in particular the end-pumping of solid-state lasers. The array-modes were successfully modelled and linked to observed far-field beam patterns by, amongst others, Hardy and Streifer [2.13], and Kapon *et al* [2.14]. The various types of evanescent-wave array-mode and the corresponding far-field patterns are shown in Figure 2.10. The out-of-phase evanescent mode is favoured to lase in these systems simply because it has a greater degree of overlap with the gain regions than the in-phase mode.

Beam quality was also a problem, the outputs spreading rapidly from around 1.5 times threshold so that diffraction-limited powers never exceeded 100 mW: roughly the same power as that available from a single stripe device. Research was therefore directed at achieving in-phase, stable, diffraction-limited operation to high current levels. Several approaches were tried including varying the lateral index profile, creating longitudinally non-uniform devices, and using π phase shifting coatings or plates on alternate stripes.

An important advance came with the introduction of arrays of antiguides, in which gain is preferentially placed in the low-index regions. The index depressions are in the region of $1 - 2 \times 10^{-3}$ for gain-guided arrays and $2 - 5 \times 10^{-2}$ for strongly-index guided arrays. Array-modes for positive- and negative-index guides are shown in Figure 2.11. In negative-index guiding, the field maxima are in the low-index regions of the array. Again, gain-guided arrays were the first to be tried due to their relatively simple structure [2.16]. These are naturally antiguided because the injected carriers cause a localised reduction in refractive index. Although radiation losses can be quite high for a single antiguide, they are significantly reduced for arrays, the lateral field leakage mainly serving the purpose of coupling the array elements. The first real-index antiguided array was realised by Ackley and Engelmann [2.17]. Although phase-locking was observed, the threshold was quite high (5 - 7 kAcm^{-2}) because of the wide (≈ 14 μm) spacing of the active stripes. Practical devices have high-index regions with a width in the region of 1 - 3 μm. Modern devices are made by metal-organic chemical vapour deposition (MOCVD) and can be classified as either complementary-self-aligned stripe (CSA) or self-aligned stripe (SAS) arrays. Examples of each are shown in

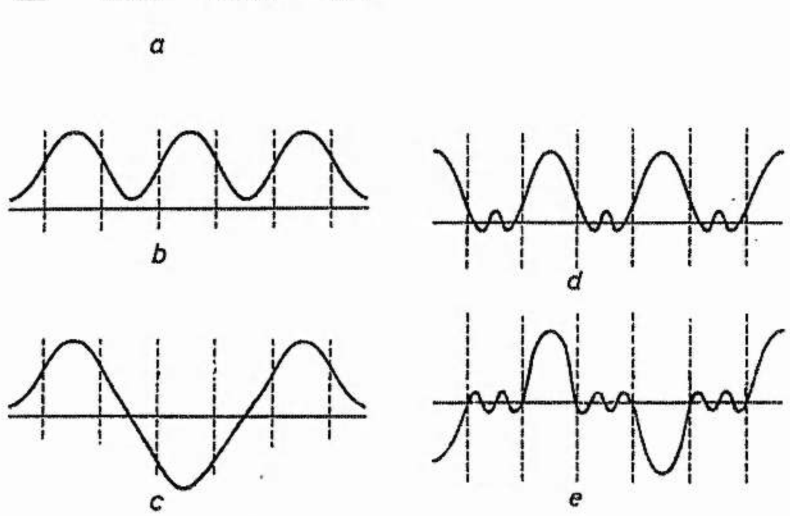

Figure2.11. Array-modes: (a) Refractive index profile, (b) In-phase evanescent mode, (c) Out-of-phase evanescent mode, (d) In-phase leaky mode, (e) Out-of-phase leaky mode.

Figure 2.12. In CSA devices, chemical etching and MOCVD regrowth are used in the interelement regions. In SAS schemes, the inter-element regions are built in during the initial growth, and the active stripes are defined by etching and MOCVD.

Single antiguided AlGaAs arrays are now able to deliver around 2 W of diffraction-limited optical power in stable beam, and are used for the end-pumping of Nd^{3+} lasers giving outputs in the region of 500 mW.

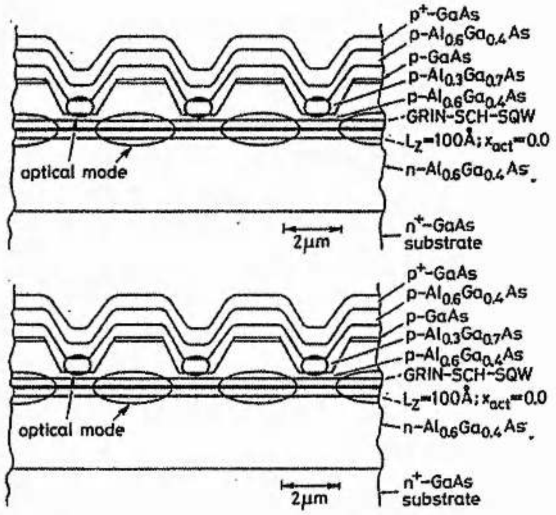

Figure 2.12. CSA (above) and SAS antiguided arrays [2.18, 19].

2.4.2 Linear Diode-Bars

For the optical pumping of solid-state lasers, coherence of the ouput is not an important requirement, although diffraction-limited output is highly desirable. More important is brightness in the case of end-pumping and total power in the case of side-pumping. Individual diode-laser arrays which form the emitters in monolithic diode-bars are typically gain-guided with around ten stripes. In the 1 cm bars produced by *SDL Inc.*, proton implantation is used to defines the stripes, as shown in Figure 2.13. The extended structure is shown in Figure 2.14. As an example, the *SDL 3460 S* 20W CW bar consists of 48 arrays, each 100 μm wide and spaced on 200 μm centres [2.20]. The bar is bonded to a metal sub-mount, *p*-side down to minimise thermal resistance. The arrays (emitters) are driven in electrical parallel. Reliability of these bars is enhanced by the relatively low energy emitted per array and the heat spreading between arrays. SQW structures are used to enhance output and efficiency.

In addition to 20 W AlGaAs systems, other *SDL* arrays currently available include 1 W CW InGaAs (970 - 980 nm), 500 mW InGaAsP (2 μm) and 500 mW AlGaInP (670-690 nm). Fibre-coupled devices, such as that shown in Figure 2.15, are also commercially available. In the case of AlGaAs these can deliver multi-watt output

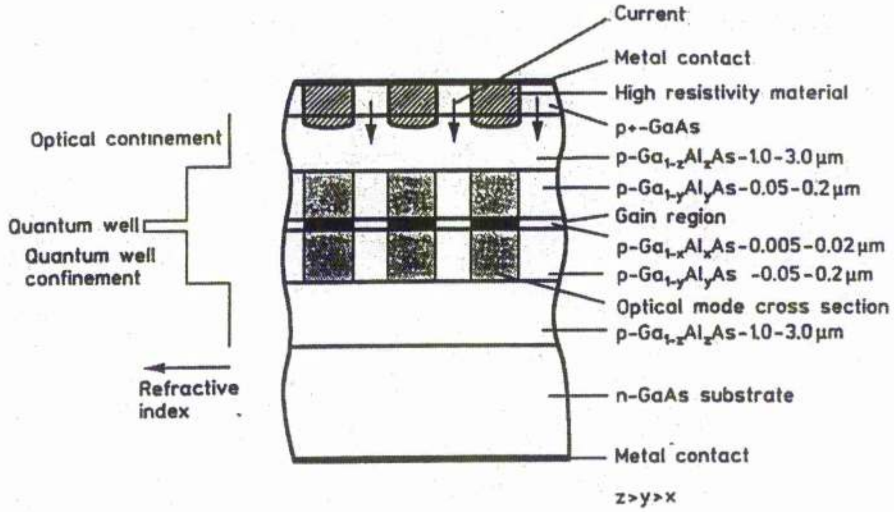

Figure 2.13. Structure of a commercial gain-guided array [2.21].

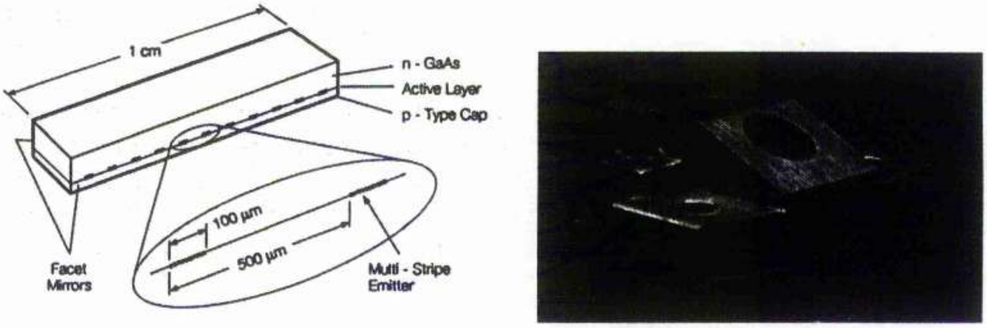

Figure 2.14. Commercial 1 cm diode-bar [2.22].

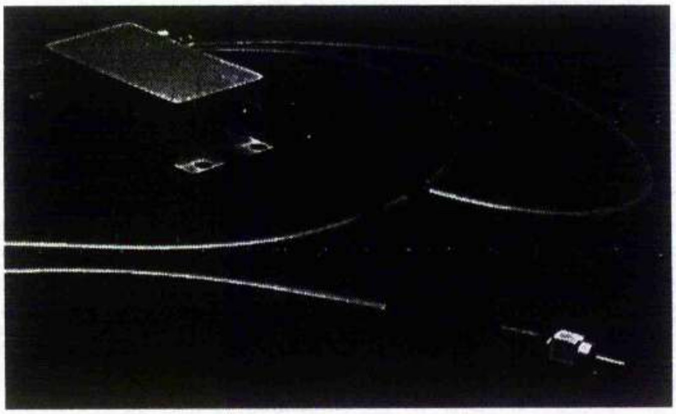

Figure 2.15. Commercial fibre-coupled diode-laser bar [2.22].

from a multimode fibre. Such systems have the advantage of circularly symmetric output. Since there is no compunction to achieve high emitter packing density in the case of fibre-coupled devices, the thermal mangement of these devices is less of a problem. However, there is the drawback of emitter-to-fibre coupling losses.

2.4.3 Two-Dimensional Stacks

A further stage in the integration of arrays is the extension of the bar concept to form two-dimensional arrays, or stacks. These are generally used to pump high-power industrial lasers. Removal of heat from the constituent bars is a key issue, and such systems are normally operated quasi-CW, *i.e.* in pulses of several hundred microseconds. The duty cycle (or average power output) is entirely dependent on the thermal design. The three most common stacking schemes, shown in Figure 2.16, are rack-and-stack micro-channel cooling, back-plane cooling and "bars-in-a-groove". In the rack-and-stack scheme, each bar has its own internal liquid heat exchanger; in the other two approaches, many diode-bars are mounted on one liquid-cooled structure. Average powers of up to 100 W are commercially available from AlGaAs-based stacks; InGaAs stacks are available with up to 60 W average power. Some commercial multi-bar stacks are shown in Figure 2.17.

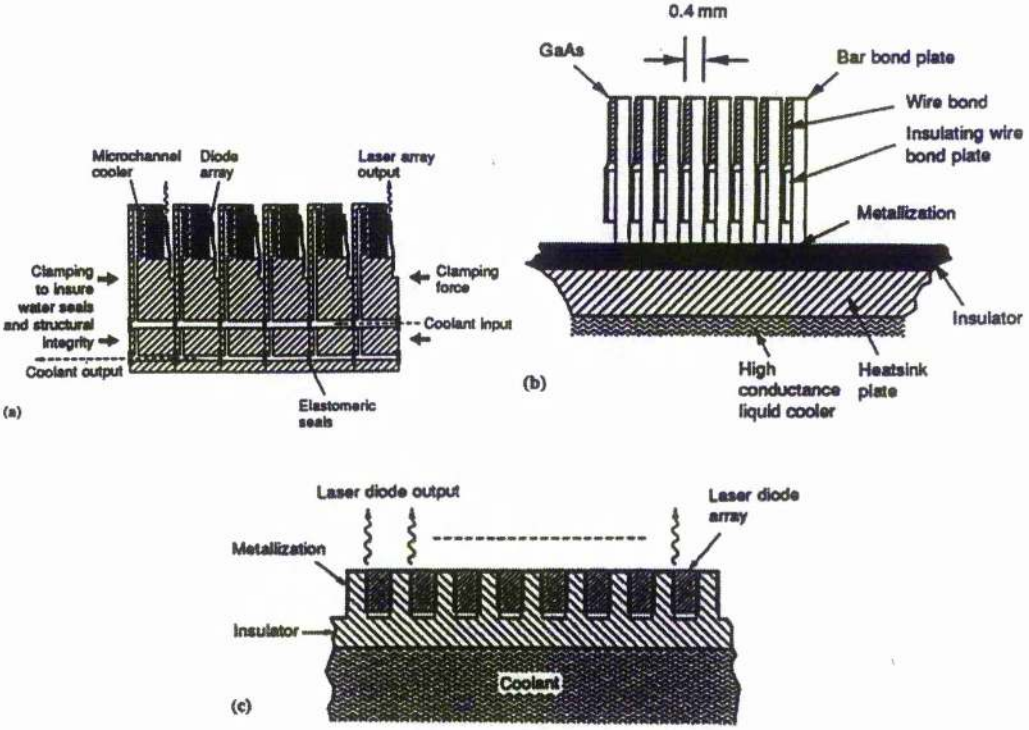

Figure 2.16. Cooling schemes for multi-bar arrays: (a) microchannel cooling, (b) pre-assembled bars on heat sink, (c) bars directly mounted on common heat sink [2.21].

2.4.4 Degradation and Reliability of Diode-Laser Bars

Failure modes of diode-laser bars generally fall into three categories: rapid degradation, gradual degradation and catastrophic failure. "Burn-in" of each bar can readily eliminate the rapid failure mode from the commercial population. Gradual

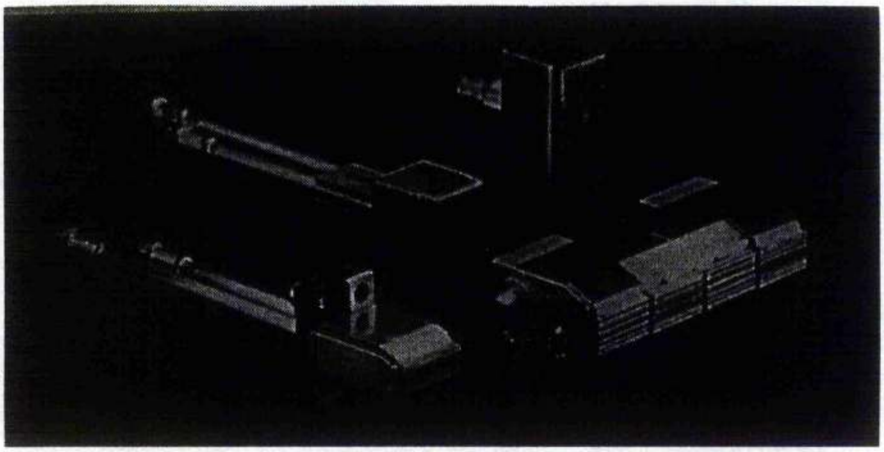

Figure 2.17. Commercial multi-bar stacks [2.22].

degradation is characterised by a gradual rise in the operating current, together with higher threshold and lower slope efficiency. During catastrophic failure, the bars exhibits a sudden large increase in the operating current and ceases to lase over a short period of time, usually several hours or less.

The main causes of degeneration are:

bulk degradation: this is associated with properties of the AlGaAs crystal which includes the epitaxial layers and the substrate.

facet degradation: this is brought about by the high power densities at the cleaved facets.

solder-related degradation: this is related to the soldered junction and the metal interfaces involved in the heat-sinking of the bar. Tens of watts of heat have to be dissipated during operation; inefficient heat-sinking raises the active-layer temperature, thus reducing lifetime.

Several tests of bar lifetime have been conducted. Sakamoto *et al,* of *SDL Inc.,* tested eleven 20 W CW diode-bars for 4000 hours [2.23]. The bars' packing density was 30%. The bars were run at full power, and the junction temperature was estimated to be 55°C. After 44 000 output-hours, the mean time between failures was 48 000 hours, or about 5.5 years. In a test with the junctions at 65°C, the projected lifetime was 10 000 hours.

2.5 Concluding Remarks

This chapter has given an overview of the technology of semiconductor pump sources. Although coherent, diffraction-limited arrays are highly desirable for end-pumping solid-state lasers, at present output powers are limited to a few watts. For DPSSLs with 1 μm output powers in the 10 - 20 W range, the pump sources are invariably diode-bars comprising multiple incoherent arrays. These are the only devices capable of providing sufficient pump powers.

At present CW powers up to 20 W are available commercially from 1 cm bars. Unless the array packing density can be increased, this is unlikely to increase substantially. However, increased efficiency and lower threshold currents are likely in the near future, and this will lead to better overall performance of diode-pumped Nd lasers.

References

[2.1] D. Botez, D. R. Scifres *(Eds.)*: "Diode-Laser Arrays": *Cambridge University Press* 1994

[2.2] J. Hagashi, M. B. Panish, P.W. Foy: "A low-threshold room-temperature injection laser": *IEEE J. Quant. Elec.* **5** 211 (1969)

[2.3] H. Kressel, J. K. Butler: "Semiconductor Lasers and Heterostructure LEDs": *Academic Press,* 1977

[2.4] G. P. Agarawal, N. K. Dutta: "Long-Wavelength Semiconductor Lasers": *Van Nostrand Reinhold Company, New York* 1986

[2.5] H. Okamoto: "Semiconductor quantum-well structures for optoelectronics - recent advances and future prospects": *Jap. J. App. Phys.* **26** 315 (1987)

[2.6] J. P. Van der Ziel, R. Dingle, R. C. Miller, W. Wiegmann, W. A. Nordland, Jr.: "Laser oscillation from quantum states in very thin GaAs-$Al_{0.2}Ga_{0.8}As$ multilayer structures": *App. Phys. Lett.* **26** 463 (1975)

[2.7] R. D. Depuis, P. D. Dapkus, N. Holonyak Jr., E. A. Rezak, R. Chin: "Room-temperature laser operation of quantum-well $Al_xGa_{1-x}As$ - GaAs laser diodes grown by metalorganic chemical vapor deposition": *App. Phys. Lett.* **32** 295 (1978)

[2.8] N. Holonyak Jr., R. M. Kolbas, E. A. Rezak, R. Chin, R. D. Depuis, P. D. Dapkus: "Bandfilling in chemical-vapor-deposited $Al_xGa_{1-x}As$ - GaAs - $Al_xGa_{1-x}As$ quantum-well heterostructure lasers": *J. App. Phys.* **49** 5392 (1978)

[2.9] Y. Arakawa, A. Yariv: "Theory of gain, modulation response and spectral linewidth in quantum-well lasers": *IEEE J. Quant. Elec.* **21** 1666 (1985)

[2.10] A. Yariv: "Quantum Electronics": *3rd Edition, Wiley,* 1989

[2.11] D. A. Fraser: "The Physics of Semiconductor Devices": Fourth Edition *Oxford Physics Series, Oxford University Press,* 1990.

[2.12] C. A. Wang, S. H. Groves: "New materials for diode laser pumping of solid-state lasers": *IEEE J. Quant. Elec.* **28** 942 (1992)

[2.13] A. Hardy, W. Streifer: “Analysis of phased-array diode lasers”: *Opt. Lett.* **10** 335 (1985)

[2.14] E. Kapon, J. Katz, A. Yariv: “Supermode analysis of phase-locked arrays of semiconductor lasers”: *Opt. Lett.* **10** 125 (1985)

[2.15] D. Botez, D. E. Ackley: “Phase-locked arrays of semiconductor diode lasers”: *IEEE Circuits & Devices Mag.* **2** 8 (1986)

[2.16] D. R. Scifres, R. D. Burnham, W. Streifer: "Phase-locked semiconductor laser array": *App. Phys. Lett.* **33** 1015 (1978)

[2.17] D. E. Ackley, W. H. Engelmann: "High-power leaky-mode multistripe lasers": *App. Phys. Lett.* **39** 27 (1981)

[2.18] D. Botez, L. J. Mawst, G. Peterson, T. J. Roth: "Resonant optical transmission and coupling in phase-locked diode-laser arrays of antiguides: the resonant optical waveguide array": *App. Phys. Lett.* **54** 2183 (1989)

[2.19] L. J. Mawst, D. Botez, C. A. Zmudzinski, M. Jansen, C. Tu, T. J. Roth, J. Yun: "Resonant self-aligned-stripe antiguided diode-laser array": *App. Phys. Lett.* **60** 668 (1992)

[2.20] *SDL Laser diode operator's manual and technical notes, 1993 (SDL Inc., San Jose, California)*

[2.21] W.Koechner: "Solid-State Laser Engineering": *4th Edition, Springer-Verlag,* 1995

[2.22] *1995 SDL Product Catalogu*e *(SDL Inc., San Jose, California)*

[2.23] M. Sakamoto, R. Craig, J. Endriz: "Highly reliable high-power CW AlGaAs (808 nm) 1 cm bar laser-diodes for Nd:YAG pump application": *SPIE* **2379** 130 (1994)

Chapter 3

INTERNAL SECOND HARMONIC GENERATION

3.1 Introduction

3.1.1 General

Compact solid-state lasers operating in the visible region have a variety of uses in the display, medical and data-storage fields, as well as more quantum-electronic applications such as high quality pump sources for vibronic lasers and optical parametric oscillators (OPOs). Given the early success and continual dominance of 1 μm Nd lasers since the mid-1960s, it is not surprising that the frequency doubling of these lasers has long been seen as a route to the generation of high power visible radiation. It was also a natural step to place the non-linear crystal inside the laser resonator to access the high intracavity field and thereby dramatically increase the conversion efficiency. Geusic and co-workers [3.1] were the first to report internal frequency doubling of a CW Nd:YAG laser in 1968. By today's standards the results were not impressive: 500 mW at 532 nm for 1.5 kW pump lamp input, representing an optical-to-optical conversion efficiency into the green of 0.03%. Overall efficiency was, of course, even less than this. Nevertheless, the concept of internal frequency doubling gained acceptance, and has been worked on ever since. Continuous developments in pump technology, laser crystals and nonlinear materials have led to highly efficient multi-watt visible sources based on diode-laser pumping. 10% optical conversion from pump light to visible output is now commonplace. Such lasers can form the pumping basis for efficient, compact and high performance short-pulse and widely tunable laser devices.

3.1.2 Second Harmonic Generation

The intense electric fields produced by lasers opened up the field of nonlinear optics in the 1960s. Second harmonic generation (SHG) is one of the simplest and most familiar effects. The basic theory is straightforward and widely known. Starting from the nonlinear wave equation

$$\nabla^2\mathbf{E} = \mu\sigma\frac{\partial \mathbf{E}}{\partial t} + \mu\varepsilon\frac{\partial^2 \mathbf{E}}{\partial t^2} + \mu\frac{\partial^2 \mathbf{P}^{NL}}{\partial t^2}, \tag{3.1}$$

where the nonlinear polarisation $\boldsymbol{P}^{NL}$ in the case of a material with a $\chi^{(2)}$ nonlinearity is given by

$$P_i^{NL} \equiv \varepsilon_0 \chi_{ijk}^{(2)} E_j E_k, \tag{3.2}$$

the interaction between two fields with frequencies ω_1, ω_2 and their sum-frequency field $\omega_3 = \omega_1 + \omega_2$ can be represented by three coupled equations giving the rate of change of field amplitude with distance in the non-linear medium for each wave. For the special case of second harmonic generation, $\omega_1 = \omega_2 = \omega$ and $\omega_3 = 2\omega$. For a plane wave incident on a nonlinear material of length L and effective nonlinear coefficent $d_{eff} = \chi_{eff}/2$, the single-pass conversion efficiency can be found as

$$\eta = \frac{P_{2\omega}}{P_\omega} = \frac{I_{2\omega}}{I_\omega} = 2\left(\frac{\mu_0}{\varepsilon_0}\right)^{3/2} \frac{\omega^2 d_{eff}^{\ 2} L^2}{n_\omega^{\ 2} n_{2w}} \left(\frac{P_\omega}{\mathrm{A}}\right) \frac{\sin^2(\Delta kL/2)}{(\Delta kL/2)^2}, \tag{3.3}$$

where $\Delta k = |\mathbf{k}_{2\omega} - 2\mathbf{k}_\omega|$ is the wave-vector mis-match and A the cross-sectional area of the incident fundamental beam. P and I represent total power and intensity respectively and the depletion of the fundamental beam is assumed to be negligible. As is well known, η depends on crystal features such as double refraction and absorption as well as optimisable parameters such as focusing strength and focal position in addition to wave-vector mis-match, so that (3.3) is somewhat removed from reality. The detailed analysis of the situation is a complex matter, and an exact general solution has not been given. However, in a comprehensive paper [3.2], Boyd and Kleinman showed that it can be simplified in several ways, so that numerical results can be obtained for any case of interest by using graphical data from computer solutions. For a uniaxial crystal, they demonstrated that maximum SHG conversion efficiency is achieved when double-refraction and absorption are both zero and when the focus is at the centre of the non-linear crystal. In addition, the strength of focusing has to be such that $L/2z_0$ is equal to 2.84 (where z_0 is the confocal parameter of the fundamental beam in the medium) and the wave-vector mis-match $\Delta k = 3.2/L$. Under these conditions the (maximum) conversion efficiency is

$$\eta_{\max} = 1.068 \frac{1024\pi^5 d_{eff}^{\ 2} L P_\omega}{n_\omega n_{2w} \lambda^3 c}. \tag{3.4}$$

The wave-vector mis-match is introduced to compensate for the phase shift due to the passage of the incident beam through its focus [3.3]. It should be noted that (3.4) is in the c.g.s. system of units. For practical use (3.4) is best stated in SI units:

$$\eta_{\max} = 6.36 \times 10^4 \frac{d_{eff}^{\ 2} L P_\omega}{n_\omega n_{2\omega} \lambda^3}. \tag{3.5}$$

Here $[d]$ = m/V, $[L]$ = m, $[\lambda] = m$, $[P]$ = W. The conversion efficiency is thus power dependent and a non-linear coupling coefficient can be defined:

$$\kappa_{\max} \equiv 6.36 \times 10^4 \frac{d_{eff}^{\ 2} L}{n_\omega n_{2w}} \ \mathrm{W}^{-1}. \tag{3.6}$$

For a given length of crystal L and effective d coefficient (3.6) gives the maximum κ, *i.e.* the value of κ which will produce maximum conversion efficiency η for a given fundamental power P_ω. As an example, the effective non-linear coefficient for type I non-critically phase-matched SHG in lithium triborate (LBO) is 1.2×10^{-12} m/V. For a 25 mm length of the crystal used to double a Nd:YAG laser, this gives $\kappa = 7.3 x 10^{-4}$ W^{-1}. The conversion efficiency for a 50 W fundamental field is therefore ≈ 3.5%, resulting in 532 nm output of 1.5 W. A 100 W field would give 7% efficiency.

(3.6) gives the maximum κ for a given length of crystal. Generally it will be assumed in what follows that the conditions of Boyd and Kleinman are satisfied so that the potential of a crystal is fully realised. Nonlinearity is then simply a linear function of L. The main reason for this is that in most practical lasers we want to obtain as much nonlinearity as possible; normally in bulk devices the maximum value is desirable. Notwithstanding the fact that in some cases a large nonlinearity *can* have a detrimental effect on performance (section 3.2.1), there are other good reasons why Boyd and Kleinman's conditions are desirable and that nonlinearity should be controlled by the length of the crystal L rather than by altering the focusing conditions. The main reason is that if L is no larger than necessary, scatter, absorption and other losses in the crystal are minimised. Clearly this is important for the second harmonic, but the main reason is to reduce such losses for the fundamental power. As will be shown below, the loss at the fundamental frequency is the single most important limitation on the output power at the second harmonic. Another reason to minimise L where possible is that the effect on the laser mode when the crystal is removed from the cavity is reduced. This serves to simplify the issue of resonator design. Additionally, the cost of the nonlinear sample can be kept to a minimum.

3.2 Internal SHG in CW Lasers

3.2.1 Theory of CW Internal Frequency-Doubling

The maximisation of the power output at the second harmonic frequency is obviously a major objective in the design of these systems. The following is a simple general discussion for the case of continuous-wave (CW) lasers, similar to that given in [3.4 - 8] where longitudinal mode structure is not explicitly considered. The transverse laser mode is assumed to comprise only the TEM_{00} mode.

Figure 3.1 shows schematics of two generic types of laser resonator. The first is a folded linear cavity that allows the frequency-doubled output to be extracted in one direction, given the right mirrors. The second is a ring laser, assumed to be unidirectional, thereby giving single-frequency output from a single point. Considering the linear cavity first, in the steady state we can equate round-trip gain and loss at a given pumping level:

$$\frac{2\gamma_0 l}{1+\frac{P_\omega}{P_{sat}}} = \delta + 2\kappa P_w. \tag{3.7}$$

P_{sat} is the saturation power of the laser, γ_0 the small signal gain and l the length of the laser crystal. δ is the round-trip linear loss. The factor of two on the RHS is due to the double passing of the fundamental light through the crystal. (3.7) assumes that the unsaturated gain is small, *i.e.*

$$e^{2\gamma_0 l} \approx 1 + 2\gamma_0 l.$$

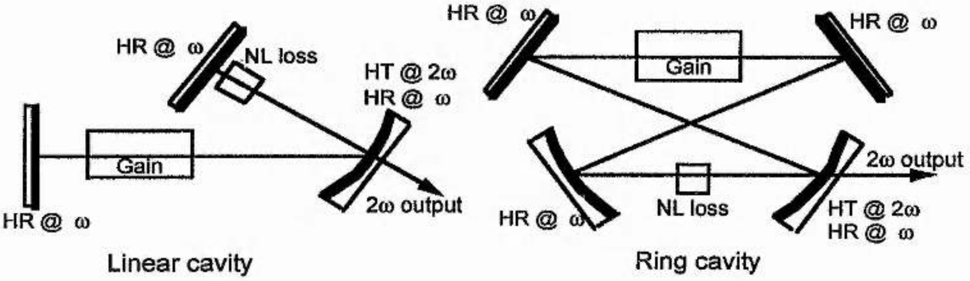

Figure 3.1. Standing-wave and travelling-wave cavity designs.

(3.7) is quadratic in P_ω with solution

$$\frac{P_\omega}{P_{sat}} = \frac{\sqrt{(\alpha-\beta)^2+4\beta}-(\alpha+\beta)}{2\beta}, \tag{3.8}$$

where α and β are measures of linear loss over gain and non-linearity respectively:

$$\alpha \equiv \frac{\delta}{2\gamma_0 l} \ ; \ \beta \equiv \frac{\kappa P_{sat}}{\gamma_0 l}. \tag{3.9}$$

The second harmonic output is

$$\frac{P_{2\omega}}{\gamma_0 l P_{sat}} = \frac{[\sqrt{(\alpha-\beta)^2+4\beta}-(\alpha+\beta)]^2}{4\beta}. \tag{3.10}$$

Figures 3.2 and 3.3 illustrate the behaviour of (3.8) and (3.10) over several decades of β. Maximising (3.8) with respect to β gives the optimum nonlinearity for a given loss α:

$$\beta_{opt} = \alpha. \tag{3.11}$$

This gives

$$\kappa_{opt} = \frac{\delta}{2P_{sat}}. \tag{3.12}$$

The resulting maximum extractable second harmonic output power is thus

$$\frac{P_{2\omega,\max}}{\gamma_0 l P_{sat}} = (1-\sqrt{\alpha})^2. \tag{3.13}$$

Figure 3.4 illustrates why it is so important to keep linear loss in the laser to a minimum. From (3.11), (3.12) and (3.13) two important pieces of information emerge. First, the optimum value of κ is directly proportional to the linear loss and independent

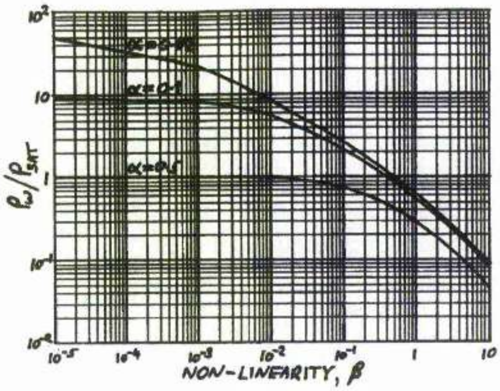

Figure 3.2. Circulating fundamental power against non-linearity.

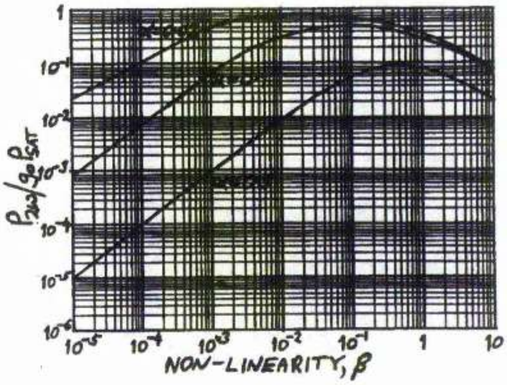

Figure 3.3. Second harmonic output power against non-linearity.

of the gain. Secondly, if the linear loss is increased, not only does the maximum theoretical harmonic power output drop sharply, but the amount of nonlinearity required to extract this reduced maximum is increased.

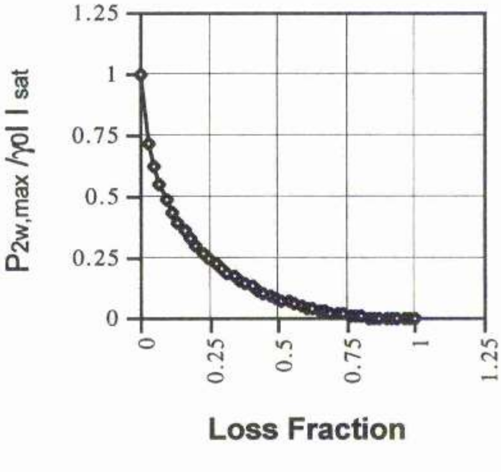

Figure 3.4. Maximum extractable second-harmonic power versus loss fraction.

In the case of the unidirectional ring laser, (3.7) becomes

$$\frac{\gamma_0 l}{1+\frac{P_\omega}{P_{sat}}} = \delta + \kappa P_\omega . \tag{3.14}$$

If γ_o and l are the same as before, the gain per round trip is halved, and in addition there is now only one pass through the nonlinear crystal per round-trip, effectively halving the nonlinear output coupling. This latter point may or may not be detrimental, depending on the laser. (3.8) and (3.10) are the same as for the linear cavity except that α is replaced by

$$\alpha' = \frac{\delta}{\gamma_0 l}. \tag{3.15}$$

β remains as in (3.9) since both round-trip gain and nonlinear output coupling are reduced by a factor of two. The optimum nonlinear coupling coefficient is now

$$\kappa_{opt}{}' = \frac{\delta}{P_{sat}}. \tag{3.16}$$

If gain and linear loss are the same as for the linear cavity, twice as much nonlinearity κ is needed for optimum operation. The effect on the maximum harmonic output power is obtainable from (3.13) with $\alpha \rightarrow \alpha'$. In practice, the loss fraction α may be *more* than doubled in going from a linear to a ring cavity due to the extra mirror and the unidirectional device. Harder pumping may recover the lost harmonic power, but clearly efficiency will be compromised.

The question naturally arises as to whether the laser is optimally output coupled when $\kappa = \kappa_{opt}$ and P_ω is maximised. To see that this is the case, the effective nonlinear output coupling under optimum nonlinear coupling needs to be considered. For the linear cavity,

$$T_{opt}{}^{NL} = 2\kappa_{opt}[P_\omega]_{\alpha=\beta} = 2\frac{\delta}{2P_{sat}}P_{sat}\left(\sqrt{\frac{2\gamma_0 l}{\delta}}-1\right) = \sqrt{2\gamma_0 l\delta}-\delta, \tag{3.17}$$

and for the ring cavity,

$$T_{opt}{}^{NL} = \kappa_{opt}{}'[P_\omega]_{\alpha'=\beta} = \frac{\delta}{P_{sat}}P_{sat}\left(\sqrt{\frac{\gamma_0 l}{\delta}}-1\right) = \sqrt{\gamma_0 l\delta}-\delta, \tag{3.18}$$

in agreement with equation (1.21).

As an example, Nd:YAG has a saturation intensity of 3.4 kWcm^{-2}, as calculated from the expression given in Chapter 1. If the effective laser mode radius inside the laser crystal is 300 μm, the saturation power is 9.6 W. If the linear loss is 2%, we then require $\kappa = 2.08 \times 10^{-3}$ W^{-1} for a linear cavity or alternatively 4.1×10^{-3} W^{-1} for a unidirectional ring cavity. Previously we calculated the most favourable κ in a 25 mm piece of LBO to be 7.3×10^{-4} under "Boyd and Kleinman" focusing. κ is therefore an order of magnitude below its optimum value. (It should be noted, however that notwithstanding its modest non-linearity, LBO has some distinct advantages.)

3.2.2 Single- and Multi-Longitudinal Mode Lasers

The optimisation of harmonic output power is a primary consideration in the design of intracavity frequency-doubled lasers. Another important concern is longitudinal mode structure. This will influence the behaviour of the system in terms of output power and amplitude stability, and set limits on the use of particular devices. If the laser is required to have a narrow spectral bandwidth, clearly the best option is to internally frequency-double a single-frequency laser. Although this often means that the maximum harmonic output power is limited due to the losses of components which enforce the single-longitudinal mode lasing, we benefit in terms of spectral purity. Single-frequency output is a necessity for any application which involves resonant enhancement of the harmonic output , such as in an OPO cavity or a cavity in which further frequency-doubling is intended. Another valuable feature of the single-frequency approach is that the harmonic output is amplitude-stable. Generally, low amplitude noise, or at least low power in the low-frequency end of the amplitude noise is an important feature if the laser is to be used to pump other laser media having short upper-state lifetimes. There are many other uses for narrow-linewidth, amplitude-stable, bright, coherent visible light.

Single-frequency operation can be obtained either by the use of a unidirectional ring resonator, or by suitable control of a linear cavity. The control could be provided by an intracavity etalon or etalons, by the use of some scheme to reduce spatial hole burning in a linear cavity (such as the "twisted mode" polarisation scheme) or it could be a feature of the laser itself, as in a microchip laser. Under these conditions, it is possible to have a single frequency ω which is doubled to another single frequency 2ω. If the single fundamental frequency has axial "quantum number" p, *i.e.* the length of the cavity is $p\lambda/2$, the amplitude of the standing wave inside the cavity at a distance z from one end of the cavity is given by

$$E_p(z,t) = \mathfrak{E}_p e^{i(2\pi z/\lambda_p + \pi/2)} e^{i(\omega_p t + \phi_p)}$$

where $\mathfrak{E}_p$ is the maximum amplitude of an antinode and ϕ_p is the phase of the mode. At a fixed position $z = z'$ in the cavity, the amplitude can be written as

$$E_p(t) = A_p e^{i\omega_p t},$$

where

$$A_p = \mathfrak{E}_p e^{i\phi_p'};$$

$$\phi_p' = \phi_p + \frac{z'\omega_p}{c} + \frac{\pi}{2}.$$

The average intracavity fundamental and second harmonic intensities are

$$\langle I_\omega \rangle = B A_p A_p^* = B\mathfrak{E}_p^{\ 2}, \tag{3.19}$$

$$\langle I_{2\omega} \rangle = \kappa B^2 (A_p A_p^*)^2 = \kappa B^2 \mathfrak{E}_p^{\ 4}, \tag{3.20}$$

where $B = c\varepsilon_0/2$.

Another approach is to intracavity frequency-double a CW laser having more than one longitudinal mode, where the modes are randomly phased. The number of longitudinal modes could be anything greater than one, *e.g.* 2, 50, even 100 or more. The added complexity of sum-frequency-mixing between different longitudinal modes as well as doubling of each mode can lead to instabilities, as detailed in section 3.2.3. Of course, the gain bandwidth of the laser crystal and frequency bandwidth of the nonlinear crystal will place a limits on the number of fundamental modes and the efficiency with which any two modes are mixed or summed. The intracavity field amplitude at a distance *z* from one end of a multimode laser is

$$E_{total}(z,t)=\sum_{p=1}^{N}\mathfrak{C}_p e^{i(z\omega_p/c+\pi/2)}e^{i(\omega_p t+\phi_p)}.$$

Again taking a fixed position $z=z'$ from one end of the cavity, the total field amplitude can be written as

$$E_{total}(t')=\sum_{p=1}^{N}A_p e^{i\omega_p t'},$$

where

$$A_p=\mathfrak{C}_p e^{i\phi_p'},$$

$$\phi_p'=\phi_p+\frac{\pi}{2},$$

$$t'=t+\frac{z'}{c}.$$

If all modes have the same maximum antinode field amplitude $\mathfrak{C}_p$, the average total fundamental intracavity intensity is

$$\langle I_\omega\rangle=NB\mathfrak{C}_p^{\ 2}.$$

The second harmonic intensity involves summing over pairs of modes, so that

$$I_{2\omega}=\kappa B^2\sum_p\sum_q\sum_r\sum_s A_pA_qA_r{}^*A_s{}^*e^{i(\omega_p+\omega_q-\omega_r-\omega_s)t'} \qquad (3.21)$$

(3.21) assumes perfect phase-matching for all pairs of modes, which is not necessarily the case in practice. The detailed description of the interaction between the modes due to sum-frequency mixing is complicated, and is reviewed in section 3.2.3. However, to quantify the *average* harmonic power it is necessary only to seek out and sum the phase-independent terms in the sum in (3.21), *i.e.* the cases where $\phi_p'+\phi_q'-\phi_r'-\phi_s'=0$. This situation occurs for the three cases $p=q=r=s$; $p=r$, $q=s$; and $p=s$, $q=r$. Hence

$$\langle I_{2\omega}\rangle=\kappa B^2\sum_{p=1}^{N}(A_pA_p{}^*)^2+2\kappa B^2\sum_{p=1}^{N}\sum_{q(\neq p)=1}^{N}(A_pA_p{}^*)^2(A_qA_q{}^*)^{2}{}',$$

which reduces to

$$\langle I_{2\omega}\rangle=\kappa B^2\mathfrak{C}_p^{\ 4}[N+2N(N-1)], \qquad (3.22)$$

where again all the fundamental modes are assumed to have the same intensity. To make a direct comparison between the multi-mode and single-mode cases, we should consider one mode of *N* times the average fundamental intensity given in (3.19), and a single-frequency average second-harmonic intensity N^2 times that in (3.20). We are then starting with two cases with the same average fundamental intensity, differing only in mode structure. (3.20) and (3.22) then give

$$\frac{\langle I_{2\omega}\rangle_{multi-mode}}{\langle I_{2\omega}\rangle_{single-mode}}=2-\frac{1}{N}. \qquad (3.23)$$

Although (3.23) implies that for a large number of modes there is an enhancement factor of 2 in the average harmonic power generated, the phase-dependent terms will give rise to noiselike fluctuations on top of this mean power. The precise relation between the amount of noise and the number of modes is still the subject of debate. Magni *et al* [3.9] found in practice that amplitude noise decreased as the number of modes was increased. The amount of amplitude noise will clearly place limits on the use of a multi-mode internally doubled system.

3.2.3 Instabilities in Intracavity Frequency-Doubled Multi-Mode CW Lasers

3.2.3.1 General

Although the internal frequency-doubling of a multi-mode CW laser may lead to a higher average power output at the second harmonic than in the single-mode case, it is well known that non-linear coupling between different longitudinal modes by sum-frequency mixing leads to various types of instability, collectively known as the "green problem". Oscillations, bistability and chaos have all been observed and predicted theoretically.

An intracavity doubled multi-mode laser actually has *two* sources of nonlinear coupling between any two modes. First there is the coupling between any two modes arising from sum-frequency mixing by the nonlinear crystal. In the case of a mode interacting with itself, this is simply frequency doubling. Secondly, there is the effect of cross-saturation between any two modes, *i.e.* one mode can help saturate the gain of another mode due to the finite linewidth of the laser transition. The detailed study of the behaviour of this type of system is a complicated topic in its own right and beyond the scope of this thesis. In fact there are many physical, chemical and biological systems that can be accurately modelled as a collection of globally coupled nonlinear oscillators. Essential dynamical aspects of Josephson-junction arrays [3.10], chemical turbulance [3.11] and heartbeat rhythms [3.12] for example have been explained using such models. Trajectories in gain or intensity phase space, stable and unstable periodic orbits, stability criteria, attraction, repulsion and chaos have all been the subject of research over the last ten years [3.13 - 23]. The subject is by no means closed. At the time of writing, the most recent work on the subject was published in *Optics Communications* in January 1996 [3.24]. The cause of instability is usually given as the fact that chaotic attractors to certain regions of intensity or gain phase space have a large number of unstable periodic orbits associated with them.

3.2.3.2 Intracavity Frequency-Doubling of a Two-Mode Laser

The simplest case, involving the intracavity doubling of two fundamental modes has been extensively investigated by Baer [3.25]. In this work, a low power diode-pumped Nd:YAG laser internally doubled using KTP was investigated. Due to the birefringence of the KTP, the two fundamental modes were linearly polarised along the two KTP axes. Given this polarisation scheme and the type II phase matching, it is not clear how Baer achieved the doubling of each mode in addition to sum-frequency mixing. Despite this he states that the green output comprised three peaks when viewed on a scanning interferometer. Probably this was not the simplest example to start with; a cavity with all the modes linearly polarised in a single plane and employing type I phase-matching would certainly give mixing *and* doubling. Nevertheless, the theoretical treatment has a satisfactory basis, and Baer's rate equations have been restated in subsequent work [3.13 - 23].

A single intracavity-doubled mode can be modelled by the coupled equations

$$\dot{I}(t) = \frac{[G(t) - \alpha - \kappa I(t)]I(t)}{\tau_c} \tag{3.24a}$$

$$\dot{G}(t) = -\frac{G(t)}{\tau_f} - \frac{\beta I(t)G(t)}{\tau_f} + \frac{G^{(0)}}{\tau_f}, \tag{3.24b}$$

where I and G are the instantaneous intensity and gain of the mode respectively, a is the linear loss, $\beta = 1/I_{sat}$, τ_c is the cavity round-trip time and τ_f is the upper state lifetime. $G^{(0)}$ is the unsaturated gain. To model two modes we need to account for sum-frequency mixing and cross-saturation, resulting in the system

$$\tau_c\dot{I}_1 = (G_1 - \alpha_1 - \kappa I_1 - 2\kappa I_2)I_1 \tag{3.25a}$$

$$\tau_f\dot{G}_1 = -(1 + \beta I_1 + \beta_x I_2) + G_1^{(0)} \tag{3.25b}$$

$$\tau_c\dot{I}_2 = (G_2 - \alpha_2 - \kappa I_2 - 2\kappa I_1)I_2 \tag{3.25c}$$

$$\tau_f\dot{G}_2 = -(1 + \beta I_2 + \beta_x I_1) + G_2^{(0)}. \tag{3.25d}$$

β_x is the cross-stauration parameter. The last term in (3.25a) and (3.25c) accounts for the sum generation process. By numerical integration of (3.25), Baer predicted that the two modes would pulse on and off alternately. In addition he was able to accurately predict the pulse shape and duration. The results are shown in Figures 3.5, 3.6 and 3.7. Figure 3.6 shows the calculated loss and gain of one of the modes with the amplitude as a timing reference. Baer described the cycle in terms of four distinct regions (a) to (d).

(a) Mode 2 pulses on increasing the sum-generation loss for mode 1 and causing mode 1 to fall below threshold and switch off.

(b) The intensity of mode 2 reaches a steady state, stabilising the losses for mode 1. The gain of mode 1 rises approximately linearly with time passing threshold and thus oscillating.

(c) Mode 1 pulses on causing mode 2 to cease lasing due to sum-generation loss.

(d) The intensity of mode 1 stabilises and the gain of mode 2 rises approximately linearly with time until threshold is reached and the cycle repeats.

Baer also reported two other interesting effects. Firstly, the period of oscillation was only a weak function of the pumping level and secondly, the frequency of oscillation increased as the amount of nonlinear coupling decreased. As can been seen from Figure 3.7, the extent of modulation also increases with nonlinearity. Weak

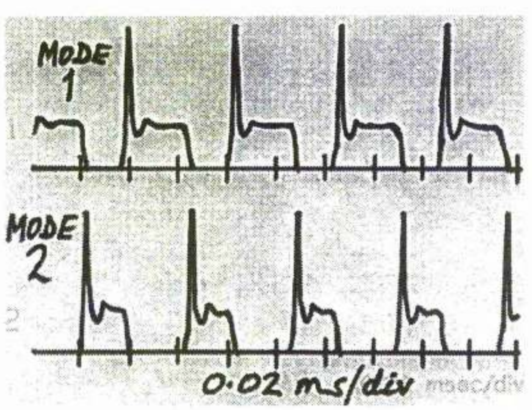

Figure 3.5. Alternate pulsing in a two-mode intracavity-doubled CW laser [3.26].

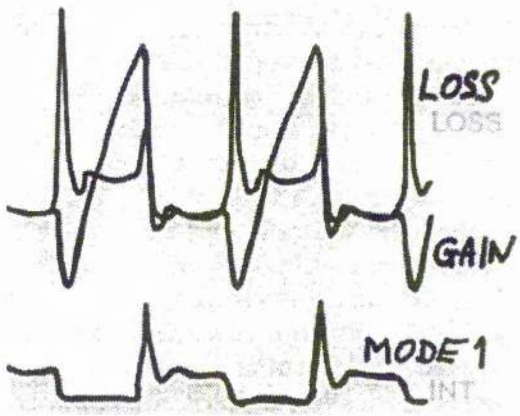

Figure 3.6. Loss and gain of a single mode [3.26].

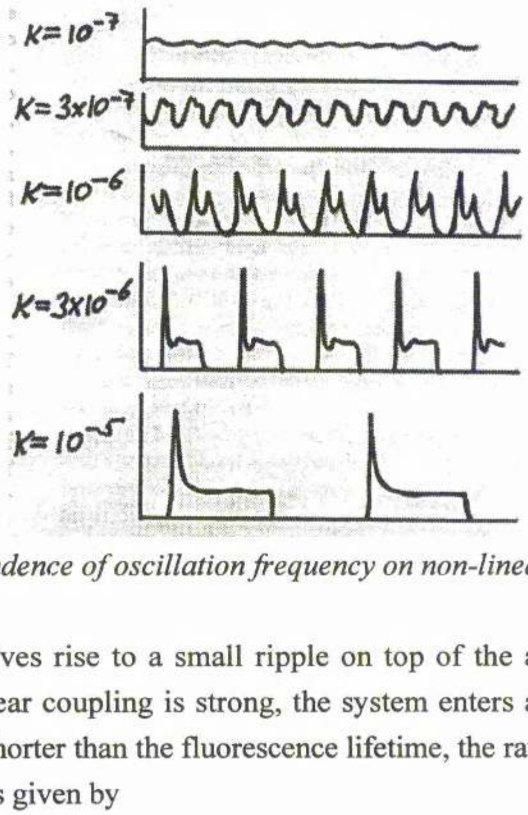

Figure 3.7. Dependence of oscillation frequency on non-linear coupling [3.26].

nonlinear coupling gives rise to a small ripple on top of the average power output, whereas if the nonlinear coupling is strong, the system enters a pulsed regime. For a time interval t much shorter than the fluorescence lifetime, the rate of change of gain of, for example mode 1, is given by

$$\frac{\Delta G}{t} = \frac{G_1^{(0)}}{\tau_f}.$$

Baer therefore stated the period of the oscillations to be

$$T_{osc} = \frac{I_{ss}\kappa\tau_f}{G_1^{(0)}}, \qquad (3.26)$$

where I_{ss} is the steady state value of the intensity of mode 2. (3.26) is simply the amount of nonlinear loss to be overcome divided by the rate at which the gain is changing. T_{osc} is almost independent of the pump intensity because both I_{ss} and $G_1^{(0)}$ are both approximately linearly dependent on the pumping level.

3.2.3.3 Intracavity Frequency-Doubling of Multi-Mode CW Lasers

In considering the behaviour of multi-mode systems we need to account for the interaction of each mode with every other mode, assuming perfect phase matching. Although the Nd:YAG/KTP multimode system has been investigated by several researchers, *e.g.* Anthon *et al* [3.26], this system has the added complication of orthogonally polarised fundamental mode eigenpolarisations and type II phase-matching. Nonlinear coupling can therefore only occur between pairs of modes that comprise one mode from each polarisation set. Frequency doubling can only occur if by accident the two modes happen to be frequency degenerate. (This is very unlikely in practice. For a 30 cm cavity containing a 5 mm piece of KTP, the frequency spacing between degenerate modes in the two sets is ≈ 350 GHz or ≈ twice the gain bandwidth of Nd:YAG.) Anthon *et al* took account of this, but as in Baer's work it is not the simplest case. A more general system in which every mode can couple to every other mode was discussed by Magni *et al* [3.9], and employed type I phase-matching with all the fundamental modes linearly polarised in the same plane. The equations of motion for the *i*th mode in such a generalised *N*-mode system are

$$\tau_c \dot{I}_i = (G_i - \alpha_i - \sum_{j=1}^{N} D_{ij} I_j) I_i \tag{3.27a}$$

$$\tau_f \dot{G}_i = -(1 + \sum_{j=1}^{N} \beta_{ij} I_j) G_i + G_i^{(0)}, \tag{3.27b}$$

where

$$\begin{aligned} D_{ij} &\equiv \kappa, \quad i = j, \\ &\equiv 2\kappa, \quad i \neq j. \end{aligned}$$

In the steady state, equations (3.27) reduce to a single equation:

$$G_i = \frac{G_i^{(0)}}{1 + \sum_{j=1}^{N} \beta_{ij} I_j} = \alpha_i + \sum_{j=1}^{N} D_{ij} I_j,$$

i.e. gain equals loss. Since G_i increases with intracavity intensity, the gain does not remain clamped at threshold as in a laser with conventional output coupling. At any time, there are many modes that would be above threshold except for nonlinear losses. Generalised stability criteria have been examined by Wu and Mandel [3.13] and James *et al* [3.14].

Bistability and chaos are closely related to the existence of mode pairs that double less efficiently than they sum. If the laser is operating in one of these modes, it will induce a large nonlinear loss that will prevent the other mode from reaching threshold. This interaction is symmetrical so that stable operation on either mode is possible. In the absence of spatial hole burning, this makes a mode pair bistable and gives rise to mode hops that cause large spontaneous shifts in the laser output. Adding the slow feedback mechanism of gain saturation to the system causes the laser to switch back and forth between the two stable states , leading to oscillation and chaos.

Bistability can be observed when the pump level is cycled up and down. As the pump level is increased form zero, the first mode to operate will be the one with the highest gain. Once this is established, it introduces a nonlinear loss into all the other modes. If all the linear losses α_i are equal, a second mode will appear if

$G_1 - D_{11}I_1 < G_2 - D_{21}I_1$,

while a mode hop will occur if

$G_2 - D_{22}I_2 > G_1 - D_{12}I_2$.

For two modes to operate together is not impossible, but it requires a relatively close coincidence in the non-linear couplings. Regions of two-mode hops are often found in the vicinity of mode hops.

An additional problem, due to the effect of finite phase-matching bandwidth, can affect single-mode as well as multi-mode devices. The ${}^4F_{3/2}$ - ${}^4I_{11/2}$ system in Nd:YAG has a total of 12 transitions, all of which will not be fully phase-matched. Lines at 1064.15 and 1064.4 nm are doubled while the next strongest transitions at 1061 and 1074 nm are not. As the circulating fundamental field builds up, modes near 1061 nm become viable because of the high nonlinear loss at 1064 nm. Mirror losses at 1061 nm can then become comparable to the nonlinear loss at 1064 nm. The 1064 nm gain will reach a fixed level and no further increase in green output will occur. This limits nonlinear conversion in lasers which have access to other transitions; the laser will simply shift wavelength to avoid the nonlinear output coupling.

A similar effect can occur with higher-order transverse modes. Nonlinear losses for the TEM_{00} mode are higher than for higher-order modes so that during high power operation, multi-transverse mode operation often results unless an intracavity aperture is used.

3.3 Internal SHG in Q-Switched and Mode-Locked Lasers

3.3.1 Q-Switching with Internal Frequency Doubling

Given the power-dependent efficiency of the frequency-doubling process, the Q-switching of an intracavity-doubled laser is a useful technique for raising the overall conversion efficiency from pump to visible output. The main situations in which this technique is useful are where nonlinearity and/or laser gain is limited, and where further nonlinear processes are intended for which a pulsed output would be beneficial. Early work on this method centred around the frequency-doubling of the main transitions of Nd:YAG. One of the first devices was that of Wallace and Harris [3.27] who obtained a peak power of 2 kW at 473 nm by internally doubling a flashlamp-pumped Nd:YAG laser using KDP. Doubling of the 1064 nm line was achieved using $Ba_2NaNb_5O_{15}$ [3.28] and $LiIO_3$ [3.29]. Massey and Yarborough obtained 6 W average power at 0.5 μm by internal doubling of an Nd:YAP laser using $LiNbO_3$ [3.30]. Modern diode-pumps and high quality nonlinear crystals have greatly improved the performance of these *Q*-switched systems. For instance, Hanson and Poirer [3.31] obtained 50 kW peak power at 532 nm from an Nd:YAG - LBO device. The overall optical - optical conversion efficiency was 10%. There is also current interest in using KTP both as the Q-switch and as the frequency-doubling crystal [3.32, 33]. This technique is of major importance in microchip lasers where gain is limited and compactness of the device is an important design aim.

The numerical analysis of Q-switching with intracavity doubling is quite straightforward, allowing the optimisation of a given system. The speed of the numerical approach also mitigates against the attempting of a full analytical solution, at least for the laser designer. The numerical approach was first reported by Murray and Harris [3.34]. For a particular laser the key variables are

the maximum (unsaturated) gain producible by the pump, G^0
the linear loss, δ
the non-linear coupling, κ
the cavity round trip time, τ_c
the fluorescence lifetime, τ_f

and the laser saturation power, P_{sat}, which depends on the gain medium and the laser mode cross-section.

When the cavity quality-factor Q is high, the gain and intracavity fundamental power evolve according to the coupled rate equations

$$\dot{G}(t)=\frac{1}{\tau_f}\left[G^0-\left(1+\frac{P(t)}{P_{sat}}\right)G(t)\right] \tag{3.28a}$$

$$\dot{P}(t)=\frac{1}{\tau_c}\left[G(t)-\delta-\kappa P(t)\right]P(t). \tag{3.28b}$$

Gain build up when the cavity Q is zero can be obtained by putting $P=0$. The result is

$$G(t)=G^0-(G^0-G_1)e^{-t/\tau_f}, \tag{3.29}$$

where G_1 is the initial gain. The time required to establish a gain G_2 starting from an initial value G_1 is

$$T(G_1\rightarrow G_2)=\tau_f\ln\left(\frac{G^0-G_1}{G^0-G_2}\right). \tag{3.30}$$

To obtain the best results when internally doubling, the initial gain should be as high as possible, *i.e.* a short gain build-up time is traded for nonlinear conversion efficiency. For example, we might wait until $G_2 = 0.99\ G_0$ before switching the cavity Q. Starting with zero population inversion, *i.e.* $G_1 = 0$, this would give a gain build-up time for Nd:YAG of roughly 1 ms.

To model the gain and intracavity fundamental power when the cavity Q is high, equations (3.28) can be put into iterative form and evaluated by any mathematical application, for example *MathCad®©™*:

$$\begin{pmatrix} G_{t+1} \\ P_{t+1} \end{pmatrix} = \begin{pmatrix} G_t + \frac{1}{\tau_f}\left[G^0 - (1 + \left(\frac{P_t}{P_{sat}} \right) G_t \right] \Delta t \\ P_t + \frac{1}{\tau_c}(G_t - \delta - \kappa P_t)\Delta t \end{pmatrix}. \tag{3.31}$$

As the fundamental intracavity intensity increases, the loss resulting from second harmonic generation increases as the square of the fundamental power. Peak power is reached when this loss has increased to equal the gain. Once this point is reached, the laser power can no longer increase, and the remaining inversion serves to lengthen the pulse. If the nonlinear coupling κ is substantially greater than that necessary to maximise the peak harmonic power, the majority of the inversion is used to lengthen the pulse. For such nonlinear couplings, there is a direct trade-off between pulse amplitude and duration, and the energy of the second harmonic pulse remains constant as a function of the nonlinear coupling.

Figures 3.8 - 3.17 show the results of a calculation based on (3.31) for the case of a Nd:YAG laser. The *1/e²* laser mode radius is taken as 300 μm, and the resonator length is 15 cm, giving a round-trip-time of 1 ns. Given the saturation intensity in 1 at. % Nd:YAG of 3.4 kW cm^{-2}, this implies a saturation power of 9.6 W. The linear loss δ has been taken as 1%. Figures 3.8 to 3.13 show the intracavity fundamental and the second harmonic peak powers, energies and full-width half-maxima for various values of initial gain and non-linear coupling. Figure 3.14 shows the timing of the peak output for $\kappa = 10^{-6}$ assuming an initial intracavity power of 1 mW at $t = 0$. In reality, switch-on is provided by the small amount of spontaneous emission reflected along the axis of the resonator. Figure 3.15 shows the variation in optimum nonlinear coupling with initial gain. Figures 3.16 and 3.17 show the time evolution of the gain, fundamental power and harmonic power once the cavity Q is switched high.

These results can be summarised as follows. Firstly, whatever the value of κ, more initial gain always results in a higher peak harmonic power and total energy, and a faster rise time. Secondly, for a given initial gain, there is an optimum nonlinear coupling κ. The optimum value of κ decreases with initial gain, although once G^0 is more than a few times above CW threshold it falls more slowly, so that for most practical systems it is only a weak function of the pumping level. Thirdly, optimum κ is characterised by the shortest pulses, both fundamental and harmonic. Once the system is over coupled, the harmonic pulses get longer but the peak power falls so that the energy per pulse remains constant (See Figure 3.11 for $\kappa >= 10^{-6}$). Increasing κ beyond the optimum value gives a direct trade-off between peak power and pulse duration. If the nonlinear coupling κ is too high, the gain does not fall below the CW

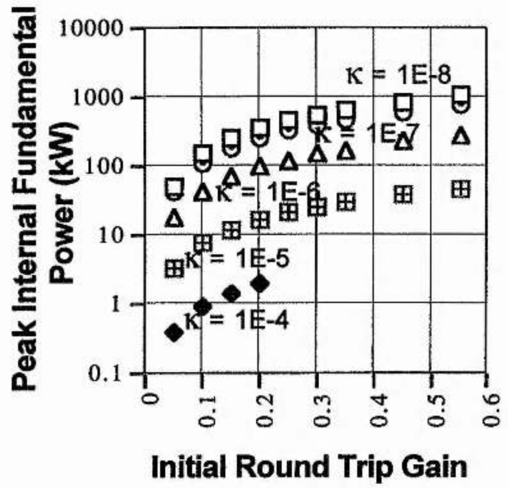

Figure 3.8. Peak fundamental power.

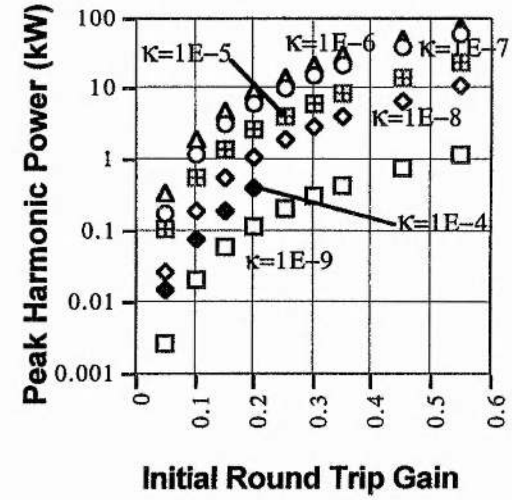

Figure 3.9. Peak harmonic power.

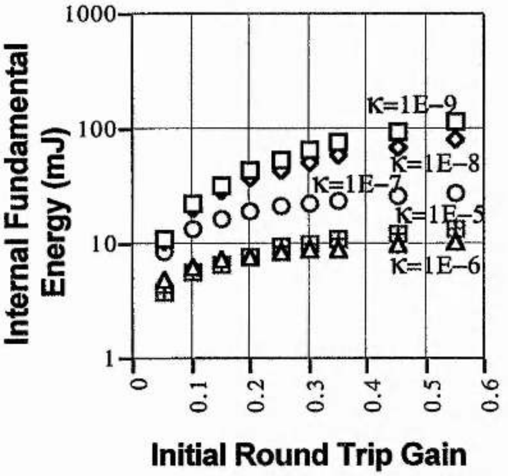

Figure 3.10. Fundamental pulse energy.

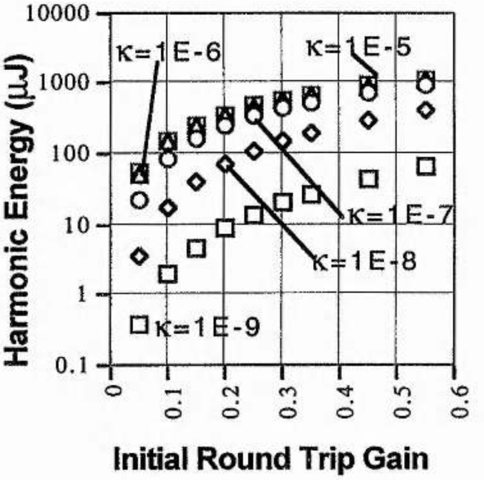

Figure 3.11. Harmonic pulse energy.

threshold so that the laser does not switch off at the end of the pulse.

In Figures 3.8 and 3.9, the peak fundamental and second harmonic powers for the case where $\kappa = 10^{-6}, G^0 = 30\%$ are 149 kW and 22.1 kW respectively, corresponding to a peak conversion efficiency of 15%. This is to be compared with CW internal conversion efficiencies on the order of 1%.

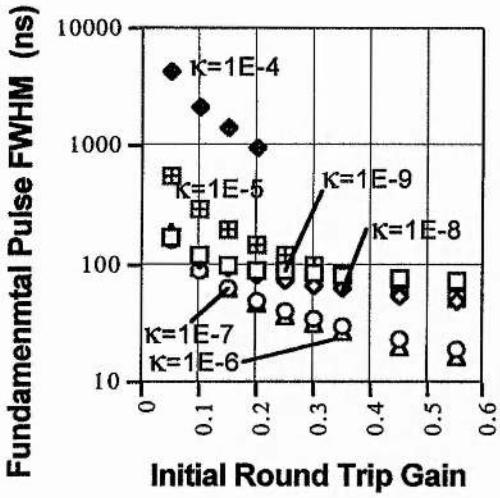

Figure 3.12. Fundamental pulse width.

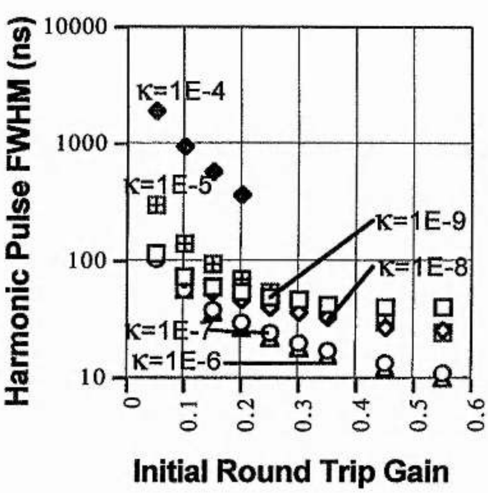

Figure 3.13. Harmonic pulse width.

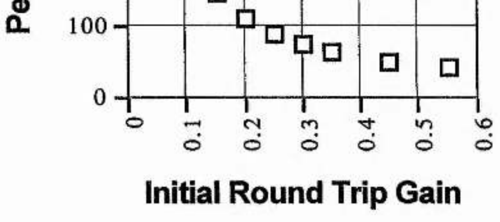

Figure 3.14. Timing of peak powers.

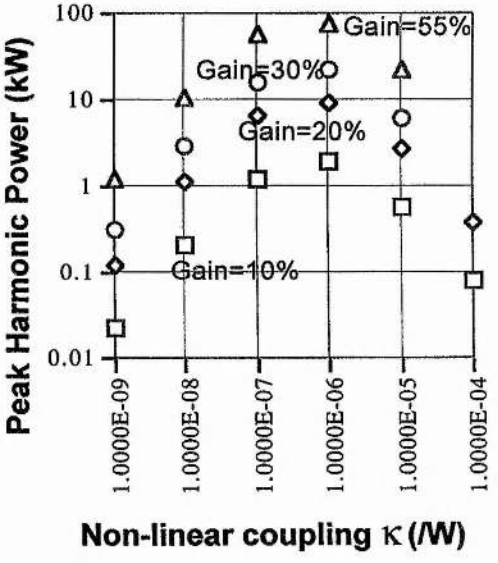

Figure 3.15. Variation of peak harmonic power with non-linear coupling.

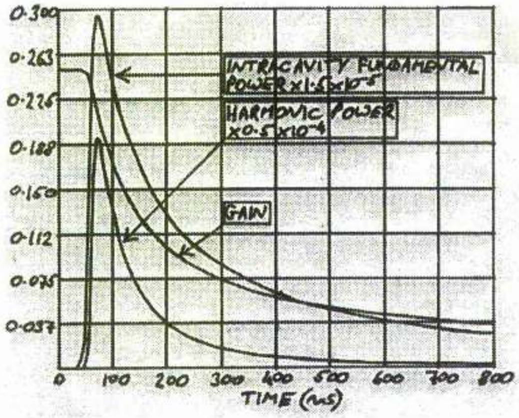

Figure 3.16. Gain and pulse evolution for $\delta = 2\%$, $G^0 = 25\%$, $\kappa = 10^{-5}$.

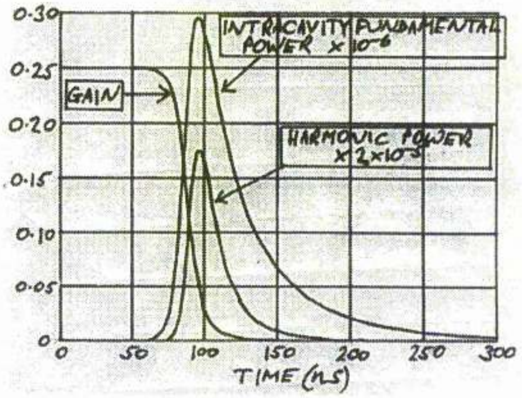

Figure 3.17. Gain and pulse evolution for $\delta = 2\%$, $G^0 = 25\%$, $\kappa = 10^{-7}$.

3.3.2 Internal SHG in Mode-Locked Lasers

The internal frequency-doubling of modelocked lasers is another method that can be used to improve conversion efficiencies under certain conditions. Modelocking is generally used where high linear loss or low nonlinearity means that a CW laser is under-coupled for the extraction of the harmonic power. Modelocked harmonic output can be used *inter alia* for resonant redoubling [3.35] and the synchronous pumping of ultrashort-pulse lasers and OPOs [3.36].

Theoretical analyses of internally doubled actively modelocked lasers were carried out by Bernecker [3.37] and Falk [3.38] in the early 1970s. The principal feature is the lengthening of the pulses over those produced without internal doubling. This is due to the opposing actions of the nonlinear crystal, which attenuates the peak of a pulse more strongly than the wings, and the modulator which imposes minimum loss on the peak of the pulse. Hitz and Osterink [3.39] suggested that to a first approximation, the fundamental pulse duration would be that which minimised the sum of these two losses. Early neodymium lasers produced harmonic pulse durations on the order of hundreds of picoseconds, and often employed FM modelocking by applying an RF signal to the nonlinear crystal (generally $LiNbO_3$ or $Ba_2NaNb_5O_{15}$) rather than by using an additional loss modulator [3.39 - 41]. Both Bernecker and Falk correctly predicted significant pulse lengthening even at small values of nonlinearity and modulation depth. An important deduction by Falk was that if an internally-doubled CW laser is optimally coupled, its AM mode-locked counterpart can at best produce an average harmonic power which is a factor of $\sqrt{2}$ lower than the ideal CW case. In terms of average harmonic power, therefore, AM modelocking is of assistance only in cases of CW undercoupling. As mentioned above, this is generally brought about by an excessively high linear loss, or low nonlinearity in the doubling crystal.

By 1980, the use of synchronously pumped mode-locked dye lasers allowed the generation of UV pulses as short as a few picoseconds to be demonstrated [3.42, 43] and later these pulse durations were reduced to 120 fs [3.44]. In 1994, Backus *et al* used a Ti:Al_2O_3 / LBO system to produce 14 fs pulses at 416 nm [3.45], which is the shortest reported pulse duration to date for this region of the spectrum. A theoretical analysis of the intracavity-doubled synchronously modelocked laser was given by Yamashita *et al* [3.46], in which rapid pulse lengthening was predicted for conversion efficiencies >≈ 0.1%.

The behaviour of *passively* modelocked and internally doubled lasers was treated by Zhang *et al* [3.47]. The main findings were that for conversion efficiencies consistent with laser operation (<≈ 5%), a stable modelocking regime always exists (although it narrows with increasing conversion) and that if the nonlinearity is increased both the original fundamental pulse duration and energy can always be restored by a suitable adjustment of the saturable gain and loss. This contrasts sharply with the synchronously-pumped and actively-modelocked cases as reported by Yamashita and Falk.

Diode-pumped internally-doubled Nd lasers are generally AM modelocked because they are usually employed as primary pump sources for other systems. Two typical diode-pumped Nd:YAG / KTP 0.5 μm AM devices which together illustrate Falk's theory are those of Dimmick [3.48] and Marshall *et al* [3.49], which are summarised in Table 3.1. The average visible output power of both these lasers was increased by modelocking, although Dimmick saw the greatest improvement because

	Dimmick [3.49]	**Marshall *et al* [3.50]**
Pumping scheme	Longitudinal; two multiplexed broad area diodes	Transverse cylindrical; two banks of 3-fold symmetric diode arrays
Maximum pump power	1.4 W	55 W
Repetition rate	250 MHz	160 MHz
Linear loss	5.5%	0.02%
Optimum output coupling	10%	4%
Conversion efficiency	1.53% (ML) 0.64% (CW)	1.2% (ML) 0.94% (CW)
0.5 μm max. average output power	76 mW (ML) 47 mW (CW)	3.0 W (ML) 2.8 W (CW)
Pulse duration	520 ps	260 ps

Table 3.1. Comparison of AM modelocked internally doubled 0.5 μm Nd:YAG lasers.

of the presence of a large linear loss. Marshall *et al* had only 0.02% linear loss with the result that their CW laser was very close to optimum coupling. Falk's √2 factor therefore meant that relatively little additional harmonic power was extractable by modelocking the laser.

Recently, Lincoln and Ferguson reported an AM intracavity-doubled 1.3 μm diode-end-pumped Nd:YLF laser producing 300 mW of average power at 659 nm [3.50], which more or less represents state-of-the-art performance for this type of laser. Modelocking enhanced the conversion efficiency from 0.25% in the CW case to 1%. The average red output power showed a less-than-quadratic dependence on the intracavity fundamental power, which was attributed to the broadening of the fundamental pulses as the pump power is increased. At full pump power the red pulse FWHM duration was 2 ps. This laser was subsequently used as a pump source for a Kerr-lens modelocked Cr:LiSAF laser [3.36].

3.4 Nonlinear Crystals for Internal Frequency-Doubling of 1μm Lasers

3.4.1 Introduction

For a crystalline material to exhibit a second-order optical nonlinearity, it must belong to a non-centrosymmetric crystal class. In addition to this, Miller [3.51] gave the useful empirical rule that a material should have a high refractive index if its non-linearity is to be high. The most familiar class having some of the largest nonlinear coefficients is the oxygen-octahedra ferroelectrics containing Nb-O, Ti-O and I-O bonds, such as $LiNbO_3$, $KNbO_3$, $Ba_2NaNb_5O_{12}$, $KTiOPO_4$ (KTP) and $LiIO_3$. Research on borate crystals has shown that the planar structure of $(B_3O_6)^{3-}$ in boron-oxygen compounds provides high non-linear effects [3.52]. Crystals such as beta-barium borate (β-BBO) and lithium triborate (LiB_3O_5) have been developed on this basis.

Frequency-doubling of 1 μm radiation from Nd lasers based on hosts crystals such as YAG, YLF, YVO_4 and YAP has been achieved using a range of nonlinear crystals. From the 1960s to the mid-1980s the principal inorganic crystals used were the negative uniaxial crystals KH_2PO_4 (KDP), KD_2PO_4 (KD*P), $LiIO_3$, $LiNbO_3$, β-BBO and the negative biaxial crystal $Ba_2NaNb_5O_{12}$ (Banana), all in a type I phase-matching geometry. In addition, frequency-doubling of 1 μm lasers has been achieved in certain organic crystals such as saccharose ($C_{12}H_{22}O_{11}$, negative biaxial, type I or II phase-matching), MAP ($C_{10}H_{11}N_3O_6$, positive biaxial, type II), and mNA ($NO_2C_6H_4NH_2$, negative biaxial, type I). Organic materials are generally not practical as they are soft and require special protective coatings. Often they are hygroscopic. Desirable properties in a nonlinear crystal include

high conversion efficiency
high damage threshold
hardness
chemical inertness (*e.g.* non-hygroscopic)
wide transparency range, low residual absorption and scatter losses
wide phase-matching bandwidth
ease of fabrication and low cost.

Since the late 1980s, two crystals have come to dominate the 1 μm → 0.5 μm application. These are potassium titanyl phosphate, $KTiOPO_4$ (KTP), a positive biaxial crystal used with type II phase-matching, and lithium triborate, LiB_3O_5 (LBO,) which is negative biaxial and is often used in a type I non-critically phase-matched geometry. These crystals will be reviewed in detail in sections 3.4.3 and 3.4.4.

3.4.2 Review of Biaxial Non-Linear Crystals

3.4.2.1 Optics of Biaxial Crystals; Phase Matching Conditions

Given the current importance of KTP and LBO for 1 μm frequency-doubling, the emphasis here is placed upon the main features of orthorhombic biaxial crystals having point symmetery *mm2*, *i.e.* structures with two orthogonal mirror planes and an axis of two-fold rotation symmetry. For this class the crystallophysical (*xyz*) and crystallographic (*abc*) axes coincide, although the exact correpondence depends on the particular crystal. Generally, it is accepted in the literature that for LBO $x,y,z \rightarrow a,c,b,$ and for KTP $x,y,z \rightarrow a,b,c.$ (A discussion of crystal nomenclature has been given by Roberts [3.52a]). For both crystals the principal refractive indices have the order $n_z > n_y > n_x$. The *xz* plane of the index-ellipsoid therefore contains the longest and shortest axes of the ellipsoid and also the two optic axes. The angle β that the optic axis in the first octant makes with the z axis is given by [3.53, 54]

$$\tan\beta = \frac{n_z}{n_x}\sqrt{\frac{n_y^{\,2} - n_x^{\,2}}{n_z^{\,2} - n_y^{\,2}}}. \tag{3.32}$$

A biaxial crystal is designated positive or negative depending on whether the optic axes make an angle less than or greater than 45° with the z axis, repectively. A general direction of wave propagation with unit wavevector s is specified by the polar and azimuthal angles θ and ϕ, as in Figure 3.18. As is well known, when light propagates in an anisotropic medium, it decomposes into two orthogonal linearly polarised waves. For a uniaxial crystal these are known as the ordinary and extraordinary rays. In biaxial crystals the same effect occurs although the polarisation directions cannot be labelled ordinary or extraordinary, but instead are referred to "fast" or "slow" depending on the two corresponding values of refractive index, $n^{(1)}$, $n^{(2)}$. It can be shown that the two planes of vibration of the electric displacement vectors $\boldsymbol{D}$ are the internal and external

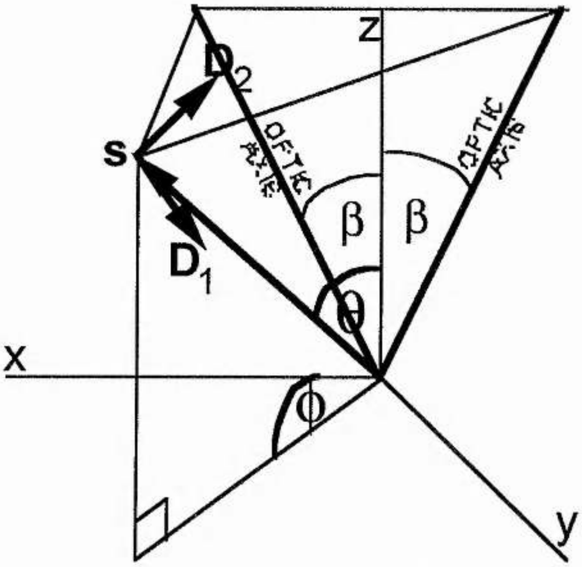

Figure 3.18. Light propagation in a biaxial crystal.

bisectors of the angles between two planes, each of which contains the direction of propagation **s** and one of the optic axes [3.53]. With the assumption that $n^{(2)} > n^{(1)}$, $\boldsymbol{D}^{(2)}$ lies in the internal bisector plane and $\boldsymbol{D}^{(1)}$ in the external bisector plane, for both positive and negative biaxial crystals, as indicated in Figure 3.18.

To determine the phase-matching conditions and other relevant optical features of a crystal, we need to know, for a given direction of propagation $\mathbf{s}(\theta,\phi)$, the two allowed directions of vibration for the electric field and displacement vectors **E** and **D**, and the associated two values of refractive index, $n^{(1)}$, $n^{(2)}$. Starting from Maxwell's equations, the components of the electric field vector are found to be

$$E_i = \frac{s_i n^2 (\mathbf{s} \bullet \mathbf{E})}{n^2 - n_i^2} \tag{3.33}$$

where $i = x, y, z$ and n can take on one or other of the two allowed values of refractive index. By multiplying both sides of (3.33) by s_i and summing over x,y,z the Fresnel equation can be obtained,

$$\frac{s_x^2}{n^{-2} - n_x^{-2}} + \frac{s_y^2}{n^{-2} - n_y^{-2}} + \frac{s_z^2}{n^{-2} - n_z^{-2}} = 0, \tag{3.34}$$

the solutions of which are the two allowed values of refractive index for given direction of propagation. (3.33) can also be used to obtain the components of the electric displacement vector:

$$D_i = \frac{s_i n_i^2 n^2 (\mathbf{s} \bullet \mathbf{E})}{n^2 - n_i^2}. \tag{3.35}$$

The components of the unit electric field and displacement vectors are therefore

$$\hat{e}_i = \frac{s_i}{n^2 - n_i^2}\left[\left(\frac{s_x}{n^2 - n_x^2}\right)^2 + \left(\frac{s_y}{n^2 - n_y^2}\right)^2 + \left(\frac{s_z}{n^2 - n_z^2}\right)^2\right]^{-1/2}, \tag{3.36}$$

$$\hat{d}_i = \frac{s_i n_i^2}{n^2 - n_i^2}\left[\left(\frac{s_x n_x^2}{n^2 - n_x^2}\right)^2 + \left(\frac{s_y n_y^2}{n^2 - n_y^2}\right)^2 + \left(\frac{s_z n_z^2}{n^2 - n_z^2}\right)^2\right]^{-1/2}. \tag{3.37}$$

Since ***e*** and ***d*** are unit vectors, (3.36) and (3.37) are also numerically equal to the direction cosines of ***e*** and ***d***. In all there are six unit vector components consisting of three pairs of the type $\hat{e}_i^{(l)}, \hat{d}_i^{(l)}$ where $i = x, y, z$ and $l = 1, 2$ (slow or fast) depending on which of the two eigenpolarisations are under consideration, or equivalently which of the two allowed values of refractive index are chosen.

At a given frequency, the index-surface $n(\theta, \phi)$ consists of an outer and an inner sheet: $n_\omega^{(2)}(\theta,\phi)$ and $n_\omega^{(1)}(\theta,\phi)$, with $n_\omega^{(2)}(\theta,\phi) \geq n_\omega^{(1)}(\theta,\phi)$. Normal dispersion requires that at the second-harmonic frequency 2ω, the refractive indices are higher than at the fundamental ω: $n_{2\omega}^{(l)} > n_\omega^{(l)}$, where $l = 1, 2$ indicates the two possible values of refractive index associated with a given direction θ, ϕ. From this it follows that the refractive index surface $n_{2\omega}^{(2)}(\theta,\phi)$ cannot coincide with $n_\omega^{(j)}(\theta,\phi)$, whereas $n_{2\omega}^{(1)}(\theta,\phi)$ *can* coincide with $n_\omega^{(2)}(\theta,\phi)$ and $(1/2)[n_\omega^{(1)}(\theta,\phi) + n_\omega^{(2)}(\theta,\phi)]$. There are therefore two types of phase matching to be distinguished: type I with $n_{2\omega}^{(1)}(\theta,\phi) = n_\omega^{(2)}(\theta,\phi)$, involving fundamental waves of parallel polarisation, and type II with $n_{2\omega}^{(1)}(\theta,\phi) = (1/2)[n_\omega^{(1)}(\theta,\phi) + n_\omega^{(2)}(\theta,\phi)]$, involving fundamental waves of orthogonal polarisation.

The two values of refractive indices $n_\omega^{(l)}$ and $n_{2\omega}^{(l)}$ $(l = 1, 2)$ of the fundamental and harmonic frequencies in the given direction $\mathbf{s}(\theta, \phi)$ must satisfy the two Fresnel equations

$$\frac{\sin^2\theta\cos^2\phi}{(n_\omega^{(l)})^{-2} - n_{\omega,x}^{-2}} + \frac{\sin^2\theta\sin^2\phi}{(n_\omega^{(l)})^{-2} - n_{\omega,y}^{-2}} + \frac{\cos^2\theta}{(n_\omega^{(l)})^{-2} - n_{\omega,z}^{-2}} = 0, \tag{3.38}$$

$$\frac{\sin^2\theta\cos^2\phi}{(n_{2\omega}^{(l)})^{-2} - n_{2\omega,x}^{-2}} + \frac{\sin^2\theta\sin^2\phi}{(n_{2\omega}^{(l)})^{-2} - n_{2\omega,y}^{-2}} + \frac{\cos^2\theta}{(n_{2\omega}^{(l)})^{-2} - n_{2\omega,z}^{-2}} = 0, \tag{3.39}$$

where $n_{\omega,x}, n_{\omega,y}, n_{\omega,z}$ and $n_{2\omega,x}, n_{2\omega,y}, n_{2\omega,z}$ are the principal refractive indices for the fundamental and second-harmonic waves respectively. The phase-matching directions for type I and type II SHG are obtainable by numerical calculation, θ and ϕ satifying (3.38) and (3.39) and the refractive index condition quoted above. A procedure for this was given by Yao and Fahlen [3.55]. Full analyses of phase-matching are given in [3.56 - 60]. Phase-matching limitations in high efficiency conversion have been treated by Eckardt [3.61].

3.4.2.2 Effective Nonlinear Coefficient

The effective nonlinear coefficient for second harmonic generation is given by the scalar product

$$d_{eff} = \hat{e}_{2\omega,i}{}^{(1)} d_{ijk} \hat{e}_{\omega,j}{}^{(1)} \hat{e}_{\omega,k}{}^{(l)}, \tag{3.40}$$

where, following convention, summation over repeated suffices is implicit. d_{ijk} is the nonlinear tensor, and the polarisation state of one of the two fundamental waves (l) depends on the type of phase-matching used. Under the symmetry conditions of Kleinman [3.62] there is no physical distinction between the cases ijk and ikj, and the number of independent elements in the nonlinear tensor is therefore reduced from 27 to 18. Counting a particular j,k pair only once (3.40) can be written as

$$d_{eff} = \hat{e}_{2\omega,i}{}^{(1)} d_{ijk} [\hat{e}_{\omega,j}{}^{(2)} \hat{e}_{\omega,k}{}^{(2)}](2-\delta_{jk}) \qquad \text{type I},$$

$$d_{eff} = \hat{e}_{2\omega,i}{}^{(1)} d_{ijk} [\hat{e}_{\omega,j}{}^{(1)} \hat{e}_{\omega,k}{}^{(2)} + \hat{e}_{\omega,k}{}^{(1)} \hat{e}_{\omega,j}{}^{(2)}]\left(1-\frac{\delta_{jk}}{2}\right) \qquad \text{type II}.$$

The notation is much simplified if the j,k pairs are re-labelled according to the rule

$j = k = x \Rightarrow q = 1$

$j = k = y \Rightarrow q = 2$

$j = k = z \Rightarrow q = 3$

$j = y, k = z; j = z, k = y \Rightarrow q = 4$

$j = x, k = z; j = z, k = x \Rightarrow q = 5$

$j = x, k = y; j = y, k = x \Rightarrow q = 6$

in which case the effective nonlinear coefficient is given by

$$d_{eff} = \hat{e}_{2\omega,i}{}^{(1)} d_{iq} f_q. \tag{3.41}$$

The nonlinear tensor is thus reduced to the matrix

$$\mathbf{d} = \begin{pmatrix} d_{11} & d_{12} & d_{13} & d_{14} & d_{15} & d_{16} \\ d_{21} & d_{22} & d_{23} & d_{24} & d_{25} & d_{26} \\ d_{31} & d_{32} & d_{33} & d_{34} & d_{35} & d_{36} \end{pmatrix}, \tag{3.42}$$

and the form of the vector ***f*** depends on the type of phase-matching. For a type I process

$$\mathbf{f} = \begin{pmatrix} f_1 \\ f_2 \\ f_3 \\ f_4 \\ f_5 \\ f_6 \end{pmatrix} = \begin{pmatrix} (\hat{e}_{\omega,x}{}^{(2)})^2 \\ (\hat{e}_{\omega,y}{}^{(2)})^2 \\ (\hat{e}_{\omega,z}{}^{(2)})^2 \\ 2\hat{e}_{\omega,y}{}^{(2)} \hat{e}_{\omega,z}{}^{(2)} \\ 2\hat{e}_{\omega,x}{}^{(2)} \hat{e}_{\omega,z}{}^{(2)} \\ 2\hat{e}_{\omega,x}{}^{(2)} \hat{e}_{\omega,y}{}^{(2)} \end{pmatrix}, \tag{3.43}$$

and for a type II process

$$\mathbf{f} = \begin{pmatrix} f_1 \\ f_2 \\ f_3 \\ f_4 \\ f_5 \\ f_6 \end{pmatrix} = \begin{pmatrix} \hat{e}_{\omega,x}{}^{(1)} \hat{e}_{\omega,x}{}^{(2)} \\ \hat{e}_{\omega,y}{}^{(1)} \hat{e}_{\omega,y}{}^{(2)} \\ \hat{e}_{\omega,z}{}^{(1)} \hat{e}_{\omega,z}{}^{(2)} \\ \hat{e}_{\omega,y}{}^{(1)} \hat{e}_{\omega,z}{}^{(2)} + \hat{e}_{\omega,z}{}^{(1)} \hat{e}_{\omega,y}{}^{(2)} \\ \hat{e}_{\omega,x}{}^{(1)} \hat{e}_{\omega,z}{}^{(2)} + \hat{e}_{\omega,z}{}^{(1)} \hat{e}_{\omega,x}{}^{(2)} \\ \hat{e}_{\omega,x}{}^{(1)} \hat{e}_{\omega,y}{}^{(2)} + \hat{e}_{\omega,y}{}^{(1)} \hat{e}_{\omega,x}{}^{(2)} \end{pmatrix}. \tag{3.44}$$

The electric field unit-vector components are given by (3.36). In most practical cases, (3.41) is considerably simplified. For the *mm2* crystal class, the nonlinear matrix takes the form

$$\mathbf{d}=\begin{pmatrix} 0 & 0 & 0 & 0 & d_{15} & 0 \\ 0 & 0 & 0 & d_{24} & 0 & 0 \\ d_{31} & d_{32} & d_{33} & 0 & 0 & 0 \end{pmatrix},$$

and under Kleinman symmetry $d_{15} = d_{31}$, $d_{24} = d_{32}$. Both LBO and KTP are normally phase-matched in the *xy* plane ($\theta = 90°$), so that the effective nonlinear coefficients for SHG are given by

$$d_{eff}{}^{LBO}(\text{type I}) = d_{32}\cos\phi, \tag{3.45}$$

$$d_{eff}{}^{KTP}(\text{type II}) = d_{15}\sin^2\phi + d_{24}\cos^2\phi. \tag{3.46}$$

General expressions for the effective nonlinear coefficient for arbitrary direction are derived in [3.63, 64]. Dmitriev and Nikogosyan have given expressions for d_{eff} in the case of *mm2* crystals for all possible assignments of the crystallographic axes *abc* to the dielectric axes *xyz*. [3.65].

3.4.2.3 Poynting Vector Walk-Off

In an anisotropic medium the directions of the vectors ***E*** and ***D*** for a given polarisation do not generally coincide because of the relation

$$\begin{pmatrix} D_x \\ D_y \\ D_z \end{pmatrix} = \varepsilon_0 \begin{pmatrix} n_x{}^2 & 0 & 0 \\ 0 & n_y{}^2 & 0 \\ 0 & 0 & n_z{}^2 \end{pmatrix} \begin{pmatrix} E_x \\ E_y \\ E_z \end{pmatrix}. \tag{3.47}$$

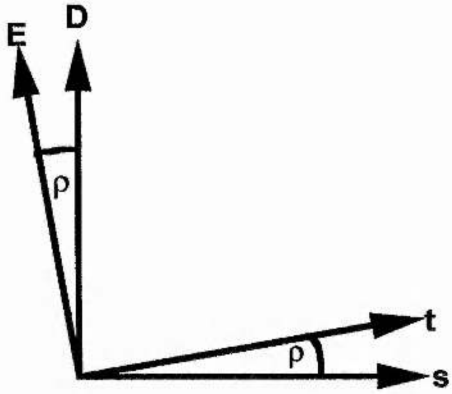

Figure 3.19. Double-refraction angle ρ.

Although ***E*** and ***D*** lie in the same plane, a small double-refraction angle ρ exists between them, as shown in Figure 3.19, which is given by

$$\cos\rho = \hat{\mathbf{e}} \bullet \hat{\mathbf{d}}. \tag{3.48}$$

This angle also exists between the unit wavevector

$$\hat{\mathbf{s}} = \frac{\mathbf{D}\times\mathbf{H}}{|\mathbf{D}\times\mathbf{H}|}$$

and the unit Poynting vector

$$\hat{t} = \frac{\mathbf{E}\times\mathbf{H}}{|\mathbf{E}\times\mathbf{H}|}.$$

Consequently, the direction of wave propagation and the direction of energy propagation do not coincide. ***E***, ***D***, ***s*** and ***t*** all lie in the same plane [3.53], with ***E***, ***H***, ***t*** and ***D***, ***H***, ***s*** forming mutually perpendicular sets of vectors. In frequency-doubling, the result is that the energy propagation directions of the fundamental and second harmonic waves diverge, limiting the spatial extent of the interaction and hence the conversion efficiency, even though they have a common wavevector direction. The magnitude of ρ depends on the particular crystal, the phase-matching direction and the type of interaction. The walk-off angle w is the angle between the two most divergent Poynting vectors in the interaction. For a type I interaction, as in Figure 3.20, the walk-off angle is given by

$$\cos w = \cos\rho_{\omega}{}^{(2)} \cos\rho_{2\omega}{}^{(1)}, \tag{3.49}$$

[3.66]. This also holds good for a type II interaction (Figure 3.21) since the double-refraction angle $\rho_{2\omega}{}^{(1)}$ is greater than or equal to $\rho_{\omega}{}^{(1)}$, as found by calculation using (3.49).

If the walk-off effect is significant, it will place an upper limit on the length of crystal that can be usefully employed. The more general effect of double refraction may also be a problem particular to internal frequency-doubling, because the deviation of the fundamental wave may cause some self-misalignment of the laser resonator. Both of these problems can be circumvented by the use of a non-critically phase-matched

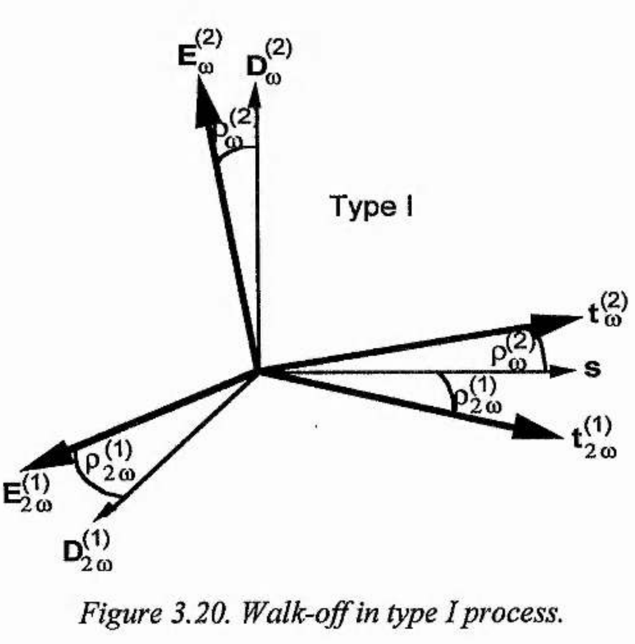

Figure 3.20. Walk-off in type I process.

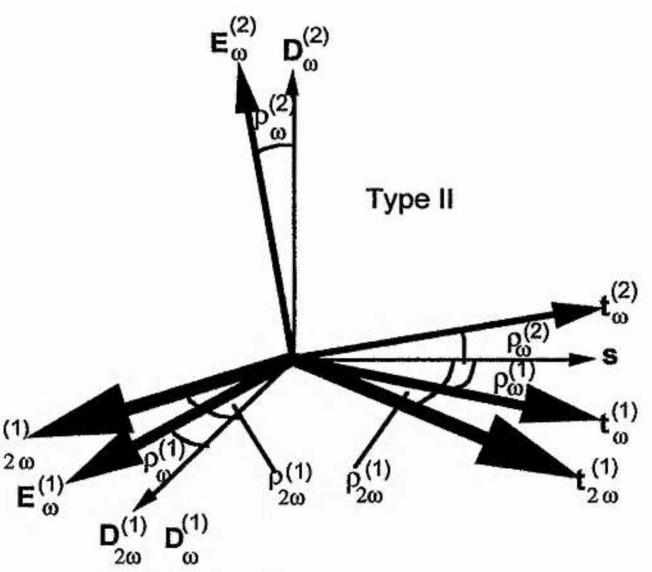

Figure 3.21. Walk-off in a type II process.

condition, in which ***s*** and ***d*** are along principal axes, thereby making ρ zero, by (3.47).

3.4.2.4 Acceptance Parameters for SHG

Angular, spectral and temperature bandwidths are useful indicators of the tolerance of the frequency-doubling efficiency to deviations from the optimum values of these parameters [3.67, 68]. Angular acceptance is a useful concept since this may limit the strength of focusing in a crystal. If the angular width is small, it may be the case that the Boyd and Kleinman focusing condition used to obtain (3.6) is not the optimum value.

Although spectral bandwidth is not normally an important parameter from a practical viewpoint in the doubling of Nd^{3+} lasers, it can be useful when using a crystal with a particular cut in different lasers. For example, it may be required to know how a KTP crystal cut for the doubling of a Nd:YAG laser will perform if used in a Nd:YLF or Nd:YAP laser.

If the doubling crystal has to be heated for phase-matching purposes, the temperature acceptance bandwidth is a useful measure of the temperature stability required of the heating oven.

The basic idea that underlies all of the acceptance parameters is the same. From (3.3) we know that the nonlinear coupling parameter (and hence the conversion efficiency and the second harmonic power output) varies as

$$\kappa \propto \mathrm{sinc}^2(\Delta kl / 2),$$

where Δk is the wavevector mismatch. A convenient measure of the maximum acceptable mismatch is when

$$\Delta k = \pm\frac{\pi}{l}, \tag{3.50}$$

in which case the conversion efficiency falls to 40.5% of its optimum ($\Delta k = 0$) value. If a particular parameter X is varied the mismatch varies as

$$\Delta k(X) = \frac{4\pi}{\lambda_\omega}\left(n_{2\omega}{}^{(1)}(X) - n_\omega{}^{(2)}(X)\right), \text{ for type I, or} \tag{3.51}$$

$$\Delta k(X) = \frac{4\pi}{\lambda_\omega}\left[n_{2\omega}{}^{(1)}(X) - \frac{1}{2}\left(n_\omega{}^{(1)}(X) + n_\omega{}^{(2)}(X)\right)\right], \text{ for type II.} \tag{3.52}$$

Expanding Δk in a Taylor series to second order about $\Delta k = 0$, the acceptance parameter ΔX is given by the smallest solution of the equation

$$\left.\frac{\partial^2 \Delta k}{\partial X^2}\right|_{X=X_0} \frac{(\Delta X)^2}{2} + \left.\frac{\partial \Delta k}{\partial X}\right|_{X=X_0} (\Delta X) = \pm\frac{\pi}{l}, \tag{3.53}$$

where X_0 is the value of the parameter at perfect phase-matching. (All other parameters are assumed constant and equal to their optimum values.) To evaluate the derivatives in (3.53), the allowed values of refractive index for the fundamental and second harmonic need to be differentiated with respect to the parameter X. This is a lengthy but straightforward procedure. The allowed values of refractive index are obtainable from the Fresnel equations (3.38), (3.39) as

$$n_\omega{}^{(l)} = \sqrt{\frac{2}{-B_1 \pm \sqrt{B_1{}^2 - 4C_1}}} \text{ and}$$

$$n_{2\omega}{}^{(l)} = \sqrt{\frac{2}{-B_2 \pm \sqrt{B_2{}^2 - 4C_2}}},$$

where l is the polarisation state (1 = fast, 2 = slow, corresponding to + and - solutions) and B_1, B_2, C_1, C_2 are functions of the direction θ, ϕ and the principal refractive indices $n_{\omega,x}, n_{\omega,y}, n_{\omega,z}, n_{2\omega,x}, n_{2\omega,y}, n_{2\omega,z}$, with forms explicitly given in, for example, [3.55].

For critical phase-matching two angular acceptance parameters, $\Delta\theta, \Delta\phi$ are normally given. To calculate spectral acceptance, the Sellmeier equations for the principal refractive indices are required, and changes in the fundamental and second harmonic wavelengths away from optimum phase-matching are constrained by the relation $\Delta\lambda_\omega = 2\Delta\lambda_{2\omega}$.

In the case of temperature acceptance bandwidth, only the first-order term in (3.53), is important, so that

$$\Delta T.l = \pm\left[\frac{4}{\lambda_\omega}\left(\frac{\partial n_{2\omega}{}^{(1)}}{\partial T} - \frac{\partial n_\omega{}^{(2)}}{\partial T}\right)\right]^{-1}, \text{ for type I, and} \tag{3.54}$$

$$\Delta T.l = \pm\left[\frac{4}{\lambda_\omega}\left\{\frac{\partial n_{2\omega}{}^{(1)}}{\partial T} - \frac{1}{2}\left(\frac{\partial n_\omega{}^{(1)}}{\partial T} + \frac{\partial n_\omega{}^{(2)}}{\partial T}\right)\right\}\right]^{-1}, \text{ for type II.} \tag{3.55}$$

3.4.3 Lithium Triborate, LiB_3O_5 (LBO)

LBO was reported as a new nonlinear crystal in 1989 [3.69]. The lattice parameters have been given as $a = 8.45$ Å, $b = 7.38$ Å, $c = 5.14$ Å [3.70]. The crystal is chemically stable, non-hygroscopic and has a hardness similar to that of fused silica [3.69]. The transparency range has been given as 0.16 - 2.6 μm [3.70] and 0.16 - 3.5 μm [3.71].

Wavelength (nm)	n_x	n_y	n_z
523.5	1.5791	1.6074	1.6223
532	1.5785	1.6065	1.6212
1047	1.5659	1.5907	1.6059
1064	1.5656	1.5905	1.6055

Table 3.2. Refractive indices of LBO [3.69].

Some refractive indices measured by Chen *et al* [3.69] are listed in Table 3.2. To four decimal places they are consistent with the Sellmeier equations

$$n_x^{\ 2} = 2.4517 + \frac{0.01177\lambda^2}{\lambda^2 - 0.00921} - 0.009600\lambda^2,$$

$$n_y^{\ 2} = 2.5279 + \frac{0.01652\lambda^2}{\lambda^2 - 0.005459} - 0.001137\lambda^2,$$

$$n_z^{\ 2} = 2.5818 + \frac{0.01414\lambda^2}{\lambda^2 - 0.001186} - 0.001457\lambda^2.$$

The highest effective nonlinear coefficient results from type I critical room-temperature phase-matching in the *xy* plane, and is given by equation (3.45). At 1064 nm the phase-matched direction is $\theta = 90^\circ$, $\phi = 10.76^\circ$, and for 1047 nm (the high gain line for Nd:YLF) $\theta = 90^\circ$, $\phi = 13.36^\circ$. These quite small values of ϕ result in walk-off angles of 0.38° for the doubling of 1064 nm radiation, and 0.45° for 1047 nm based on Table 3.2 and equation (3.48). Xie *et al* characterised the SHG of Nd:YAG in this scheme [3.71a]. The phase-matching direction ϕ is given by the solution of

$$n_{\omega,z} = n_{2\omega,y}\sqrt{\frac{1+\tan^2\phi}{1+\left(\dfrac{n_{2\omega,y}}{n_{2\omega,x}}\right)^2\tan^2\phi}}.$$

Given the closeness of the principal refractive indices $n_{2\omega,y}$ and $n_{\omega,z}$ for 1 and 0.5 μm (as illustrated by the quite low values of ϕ needed for critical phase-matching in the *xy* plane), LBO may also be used for SHG in a non-critically phase matched (NCPM) type I geometry by temperature tuning [3.71 - 75]. This feature is extremely attractive since the angular acceptance is greatly enhanced, allowing tight focusing, and walk-off effects are eliminated so that there is no intrinsic limit on the interaction length. The fact that the fundamental wave experiences no birefringence in the type I interaction makes the use of LBO in this geometry very attractive for intracavity doubling, since it produces no complications relating to the internal polarisation states of the laser. Efficient harmonic generation can be achieved simply by using a Brewster plate inside the cavity. Velsko *et al* [3.70] measured the rates of change of the principal refractive indices with temperature in the range 20 - 70 °C, which gives a first estimate of the phase-matching temperature of 156 °C for the frequency-doubling of the 1064 nm Nd:YAG transition. However, the thermo-optic coefficients are themselves functions of temperature, and most experimental reports give a lower temperature of 148 - 149 °C. Figure 3.22 shows the variation in NCPM temperature with wavelength near 1 μm. Ukachi *et al* [3.73] measured the FWHM 1064 nm angular acceptances as $\Delta \phi . l^{1/2} = 99.1$ mrad.cm$^{1/2}$ and $\Delta\theta\ l^{1/2} = 71.9$ mrad.cm$^{1/2}$. For 25 mm crystal these values give 3.6° and 2.6° respectively. For temperature acceptance the same authors quoted $\Delta T . l = 3.9$ °C cm at 148 °C for 1064 nm. Gontijo [3.75] quoted 4.2 °C cm. Figure 3.23 shows the variation in FWHM temperature acceptance as a function of fundamental wavelength for a 3.9 mm length of crystal.

LBO crystals are normally grown by the top-seeded solution method. A typical crystal-growth procedure is as follows: a melt of Li_2O:B_2O_3 is kept in a platinum crucible at 814 °C, which is 3 °C above the liquidus temperature, for at least 24 hours. A seed crystal is then introduced and kept in contact with the surface of the melt for half an hour, at which time slight dissolution occurs. The melt is then cooled to a temperature just below the liquidus temperature, 811 °C, and maintained at this temperature until no growth takes place on the seed crystal for at least 24 hours. The melt is then cooled to 800 °C at a rate of 0.5 °C per day. After growth, the crystal is

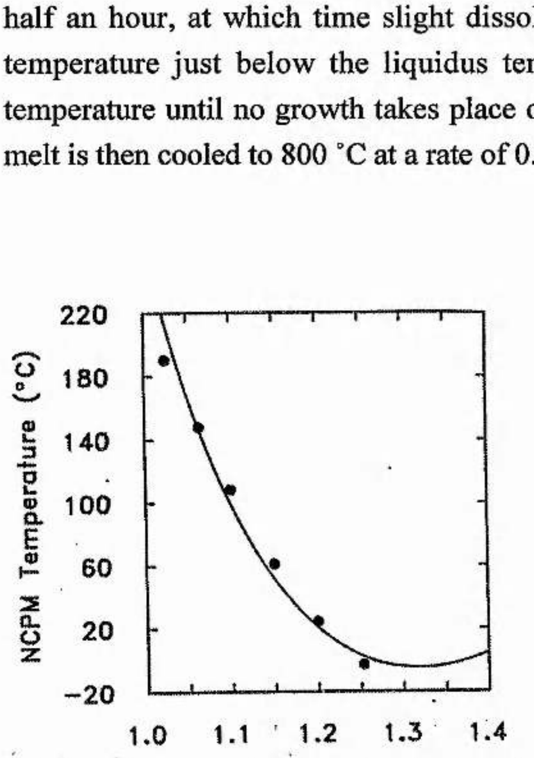

Figure 3.22. Variation of NCPM temperature with wavelength [3.74].

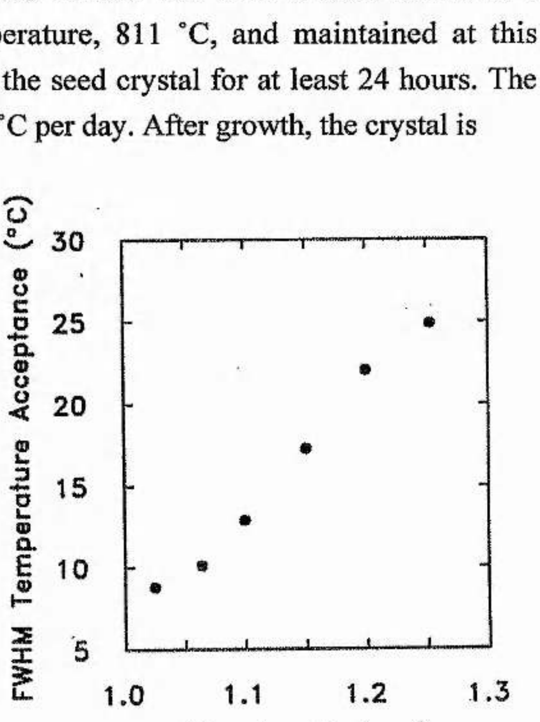

Figure 3.23. Variation of temperature acceptance with wavelength [3.74].

slowly pulled up from the melt and cooled to room temperature at a rate of 3 °C per hour. Typically, a boule 20 x 20 x 15 mm can be produced by this procedure.

Chen *et al* [3.69] cited the helices of (B_3O_7) units and the compact, wide-bandgap lattice as the major contributors to LBO's high damage threshold. They quoted the damage threshold as 25 GW/cm^2 at 1064 nm (0.1 ns pulse). Furukawa *et al* [3.76, 77] found the damage threshold to be dependent on wavelength and pulse duration. At 1064 nm they quoted 45 GW/cm^2 (1.1 ns pulse), and 11.2 GW/cm^2 (25 ns pulse). At 532 nm, they quoted 26 GW/cm^2 (1 ns pulse). LBO has the highest bulk damage thresholds of any inorganic nonlinear crystal developed to date.

	[3.69] calc.	[3.69] exp.	[3.78]	[3.70]	[3.71]
$\vert d_{31}\vert$	0.94	1.15 ± 0.09	1.4 ± 0.1	-	1.15
$\vert d_{32}\vert$	1.13	1.24 ± 0.09	1.5 ± 0.3	0.83 ± 0.06	1.24
$\vert d_{33}\vert$	0.26	0.06 ± 0.006	0.08 ± 0.008	0 ± 0.1	0.063
$\vert d_{24}\vert$	-	-	1.4 ± 0.3	-	1.15
$\vert d_{15}\vert$	-	-	1.3 ± 0.3	0.71 ± 0.05	1.24

Table 3.3. Nonlinear coefficients of LBO in pm/V.

3.4.4 Potassium Titanyl Phosphate, $KTiOPO_4$ (KTP)

KTP belongs to the family of *mm2* compounds with formula $MTiOXO_4$ where M can be *K, Rb, Tl,* NH_4*, or Cs* and X is *P,* or *As*. The system $K_xRb_{1-x}TiOPO_4$ was originally investigated by Zumsteg *et al* [3.79] in 1976. The lattice constants have been given as a = 12.81 Å, b = 6.40 Å, c = 10.62 Å [3.80]. Each unit cell contains eight formula units. The structure is characterised by chains of TiO_6 octahedra which are linked at two corners, and the chains are separated by PO_4 tetrahedra [3.80]. Alternating long and short Ti-O bonds occur along these chains, which result in a net z directed polarisation and are the major contributor to the large nonlinear and electrooptic coefficients of KTP. The transparency range has been given as 0.35 - 4.5 µm [3.80a].

There are two main growth methods, which result in two types of crystal with slightly different sets of principal refractive indices. In the hydrothermal growth process, the seed crystal and nutrient are sealed in a gold tube which is inserted into a high temperature - high pressure autoclave. The contents are kept at a constant pressure of ≈ 1.7 x 10^8 Pa (25 000 psi) and a fixed temperature gradient, typically 600 °C at the nutrient and 550 °C at the seed. To produce a crystal boule measuring around 20 x 20 x 60 mm takes around six weeks.

In the second method, the KTP crystallises on cooling a molten flux. This occurs at temperatures anywhere between 700 and 1000 °C depending on the

Wavelength (nm)	n_x	n_y	n_z
523.5	1.7808(1.7803)	1.7920(1.7912)	1.8896(1.8922)
532	1.7790(1.7785)	1.7900(1.7892)	1.8868(1.8894)
1047	1.7404(1.7386)	1.7481(1.7463)	1.8303(1.8309)
1064	1.7399(1.7381)	1.7474(1.7458)	1.8296(1.8302)

Table 3.4. Refractive indices of KTP [3.81, 82].

composition of the flux. Growth sizes are of the order of 60 x 55 x 30 mm, with the process lasting between 10 days and two months, depending on the apparatus used.

Some of the refractive indices are summarised in Table 3.4. Flux-grown values are shown in parentheses. The Sellmeier equations have been given as [3.81, 82]

$$n_x^{\ 2} = 2.1146 + \frac{0.89188\lambda^2}{\lambda^2 - 0.04352} - 0.01320\lambda^2,$$

$$n_y^{\ 2} = 2.1518 + \frac{0.87862\lambda^2}{\lambda^2 - 0.04753} - 0.01327\lambda^2,$$

$$n_z^{\ 2} = 2.3136 + \frac{1.00012\lambda^2}{\lambda^2 - 0.05679} - 0.01679\lambda^2,$$

for hydrothermally grown KTP, and

$$n_x^{\ 2} = 2.16747 + \frac{0.83733\lambda^2}{\lambda^2 - 0.04611} - 0.01713\lambda^2,$$

$$n_y^{\ 2} = 2.19229 + \frac{0.83547\lambda^2}{\lambda^2 - 0.04970} - 0.01621\lambda^2,$$

$$n_z^{\ 2} = 2.25411 + \frac{1.06543\lambda^2}{\lambda^2 - 0.05486} - 0.02140\lambda^2,$$

for flux-grown crystals.

The most efficient phase-matching scheme for the frequency-doubling of 1μm radiation is type II with propagation in the xy plane, i.e. $\theta = 90°$. The effective nonlinear coefficient is given by (3.46). In the xy plane the birefringence is too small to compensate for dispersion over a large spectral range, so that SHG is limited to wavelengths near 1 μm, although in the xz and yz planes, KTP is phase-matchable for SHG in the range 1 - >3 μm [3.80]. In the xy plane, the phase-matching direction ϕ is the solution of

$$n_{2\omega,y}\sqrt{\frac{1+\tan^2\phi}{1+\left(\frac{n_{2\omega,y}}{n_{2\omega,x}}\right)^2\tan^2\phi}} = \frac{1}{2}\left\{ n_{\omega,y}\sqrt{\frac{1+\tan^2\phi}{1+\left(\frac{n_{\omega,y}}{n_{\omega,x}}\right)^2\tan^2\phi}} + n_{\omega,z} \right\}.$$

For frequency-doubling of 1064 nm Nd:YAG, $\phi = 24.6°$ for flux-grown KTP and 26.5° for hydrothermal crystals. For 1047 nm, the angles are 37.5° and 38.0° respectively.

Fan *et al* [3.82] calculated the full-width angular acceptances for SHG in flux-grown crystals as $\Delta\phi .\ l = 1.05°\text{cm}$ and $\Delta\theta\ \ l^{1/2} = 3.37°\text{cm}$. For a 5 mm length of KTP, this corresponds to 2.1° and 4.8°. For frequency-doubling of both 1064 and 1047 nm, the walk-off angle is 0.27°, for both hydrothermal and flux-grown crystals.

The nonlinear coefficients of KTP are summarised in Table 3.5. Although KTP has the advantage of high nonlinearity, the type II critical phase-matching scheme presents two particular problems when the crystal is used intracavity. The first problem arises from the fact that linearly polarised light must be incident on the crystal, with the direction of polarisation at 45° in the plane containing the z axis and the allowed direction of polarisation in the xy plane, which is fixed by ϕ, in order to achieve the type II phase-matching. The crystal therefore acts as a birefringent element, and unless the birefringence is tuned-out either electrooptically or by temperature, some thought has to be given to stabilising the polarisation eigenstates within the laser cavity. The birefringence also means that the fundamental radiation will not be completely linearly polarised throughout the crystal, compromising the phase-matching along its length. The second problem is that of walk-off of one of the fundamental waves in the crystal, again due to the type II phase-matching. This will cause some self-misalignment of the laser resulting in loss which would not occur in for example, type I critically phase-matched LBO. The high nonlinearity of KTP is not therefore, a licence to build a laser with high linear losses, because to avoid these problems with KTP, the length of crystal used for internal doubling should be kept as short as possible.

	[3.79]	[3.83]	[3.84]
$\lvert d_{31}\rvert$	6.5	1.9 ± 0.2	-
$\lvert d_{32}\rvert$	5.0	3.5 ± 0.3	-
$\lvert d_{33}\rvert$	13.7	-	-
$\lvert d_{24}\rvert$	7.6	-	3.3
$\lvert d_{15}\rvert$	6.1	-	2.6

Table 3.5. Nonlinear coefficients of KTP in pm/V.

The occurrence of laser damage, caused by an effect referred to as "grey tracking" in KTP crystals has limited the use of this material in high-average-power laser systems. The formation of grey tracks is initiated when the passage of a 1 μm beam produces photo-excited electron-hole pairs along the beam path by the generation of above-band-gap photons, for example by frequency-tripling of the fundamental or by two-photon absorption ($\omega + \omega$ or $\omega + 2\omega$). Many of the pairs recombine; however, some become trapped at stabilising entities such as vacancies or impurities and form stable grey tracks. Halliburton and Scripsick [3.85] linked the effect in flux-grown crystals to the presence of Ti^{3+} ions which occur where there is an adjacent oxygen vacancy. These sites trap electrons, while impurity Fe^{3+} ions trap holes to form Fe^{4+} centres. The half-life of these entities was quoted as ≈ 2 hours at room temperature. The tracks cause absorption of the fundamental which can lead to catastrophic bulk damage. The presence of 0.5 μm radiation alone is a necessary and sufficient condition to produce grey tracks [3.86]. The threshold for the appearance of grey tracks depends on the individual crystal and the growth method, and ranges from tens to hundreds of MW/cm^2. Jacco *et al* [3.86a] observed the onset of grey tracks at a fluence of 352 MW/cm^2 and catastrophic damage at 600 MW/cm^2 using a Q-switched Nd:YAG laser. The problem does not therefore usually arise in the internal doubling of CW lasers, unless the crystal is particularly impure. Modelocked and Q-switched devices can be limited by the effect.

A principal feature of grey tracks is their disappearance by annealing. At room temperature the tracks disappear over a period days to months. Heating to 65 °C was reported to remove the tracks in about an hour [3.87]. Grey tracking in KTP is similar to photorefractive damage in $LiNbO_3$ in that heating to 100 - 200 °C significantly reduces or elimates the problem [3.86].

3.5 Concluding Remarks

In this chapter, the theoretical aspects of intracavity frequency-doubling have been reviewed. In the practical systems described in chapters 4, 5 and 6, this knowledge was used both in the design of the lasers, and in the assessment of their harmonic output power performance. The avoidance of chaotic behaviour in the intensity of the second-harmonic output is an important subject because internally-doubled lasers are very often used as pump sources for other devices. Any practical internally-doubled laser design must therefore have regard to either the control or elimination of the nonlinear coupling between longitudinal modes. This chapter has also reviewed the properties of the two nonlinear crystals which are most commonly used for the internal frequency-doubling of 1 μm Nd lasers, LBO and KTP.

References

[3.1] J. E. Geusic, H. J. Levinstein, S. Singh, R. G. Smith, L. G. Van Uitert: "Continuous 0.532 μm source using $Ba_2NaNb_5O_{15}$": *App. Phys. Lett.* **12** 306 (1968)

[3.2] G. D. Boyd, D. A. Kleinman: "Parametric interaction of Gaussian light beams": *J. App. Phys.* **39** 3597 (1968)

[3.3] R. W. Boyd: "Non-Linear Optics": *Academic Press*, 1992

[3.4] J. E. Geusic, H. J. Levinstein, S. Singh, R. G. Smith, L. G. Van Uitert: "Continuous 0.532 μm solid-state source using $Ba_2NaNb_5O_{15}$": *App. Phys. Lett.* **12** 306 (1968)

[3.5] R. G. Smith: "Theory of intra-cavity optical second harmonic generation": *IEEE J. Quant. Elec.* **6** 215 (1970)

[3.6] V. G. Dmitriev, E. A. Shalaev, E. M. Shvom: "Efficient second harmonic generation in a resonator": *Soviet J. Quant. Elec.* **3** 450 (1974)

[3.7] V. D. Volosov, S. G. Karpenko, N. E. Kornienko, V. N. Krylov, A. A. Man'ko, V. L. Strizhevskii: "Second-harmonic generation in a resonator": *Soviet J. Quant. Elec.* **3** 450 (1974)

[3.8] J. D. Barry: "Optical design of a frequency-doubled Nd:YAG laser": *IEEE J. Quant. Elec.* **12** 254 (1976)

[3.9] V. Magni, G. Cerullo, S. De Silvestri, O. Svelto, L. J. Qian, M. Danailov: "Intracavity frequency doubling of a CW high power TEM_{00} Nd:YLF laser": *Opt. Lett.* **18** 2111 (1993)

[3.10] P. Hadley, M. Beasley: "Dynamical states and stability of linear arrays of Josephson junctions": *App. Phys. Lett.* **50** 621 (1987)

[3.11] Y. Kuramoto: "Chemical Oscillations, Waves and Turbulance": *Springer-Verlag*, 1984

[3.12] A. T. Winfree: "The Geometry of Biological Time": *Springer-Verlag*, 1980

[3.13] X.-G. Wu, P. Mandel: "Second-harmonic generation in a multi-mode laser cavity": *J. Opt. Soc. Am. B* **4** 1870 (1987)

[3.14] G. E. James, E. M. Harrell II, R. Roy: :Intermittancy and chaos in intracavity doubled lasers": *Phys. Rev. A* **41** 2778 (1990)

[3.15] K. Wiesenfeld, C. Bracikowski, G. James, R. Roy: "Observation of antiphase states in a multimode laser": *Phys. Rev. Lett.* **65** 1749 (1990)

[3.16] R. F. Fox, J. Keizer: "Amplification of intrinsic fluctuations by chaotic dynamics in physical systems": *Phys. Rev. A* **43** 1709 (1991)

[3.17] C. Bracikowski, R. Roy: "Energy sharing in a chaotic multimode laser": *Phys. Rev. A* **43** 6455 (1991)

[3.18] C. Bracikowski, R. F. Fox, R. Roy: "Amplification of intrinsic noise in a chaotic multimode laser system": *Phys. Rev. A* **45** 403 (1992)

[3.19] R. Roy, T. W. Murphy Jr., T. D. Maier, Z. Gills, E. R. Hunt: "Dynamical control of a chaotic laser: experimental stabilisation of a globally coupled system": *Phys. Rev. Lett.* **68** 1259 (1992)

[3.20] K. Otsuka, J.-L. Chern: "Synchronisation, attractor fission and attractor fusion ina globally coupled laser system": *Phys. Rev. A* **45** 5052 (1992)

[3.21] O.E. Nanii, M. R. Paleev: "Intracavity second-harmonic generation in multimode solid-state lasers with anisotropic cavities": *Quant. Elec.* **24** 522 (1994)

[3.22] E. A. Viktorov, D. R. Klemer, M. A. Karim: "Shil'nikov case of antiphase dynamics in a multi mode laser": *Opt. Comm.* **113** 441 (1995)

[3.23] T. Erneux, P. Mandel: "Minimal equations for antiphase dynamics in multimode lasers": *Phys. Rev. A* **52** 4137 (1995)

[3.24] B. K. Goswami: "The interaction between period 1 and period 2 branches and the recurrance of the bifurcation structures in the periodically forced laser rate equations": *Opt. Comm.* **122** 189 (1996)

[3.25] T. Baer: "Large amplitude fluctuations due to longitudinal mode coupling in diode-pumped intracavity-doubled Nd:YAG lasers": *J. Opt. Soc. Am. B* **3** 1175 (1986)

[3.26] D. W. Anthon, D. L. Sipes, T. J. Pier, M. R. Ressl: "Intracavity doubling of CW diode-pumped Nd:YAG lasers with KTP": *IEEE J. Quant. Elec.* **28** 1148 (1992)

[3.27] R. W. Wallace , S. E. Harris: "Oscillation and doubling of the 0.946 μm line in Nd^{3+}:YAG": *App. Phys. Lett.* **15** 111 (1969)

[3.28] A. Stein, R. A. Kaplan: "One watt average second harmonic power with a repetitively Q-switched Nd:YAG laser": *App. Phys. Lett.* **16** 338 (1970)

[3.29] R. B. Chesler, M. A. Karr, J. E. Geusic: "Repetitively Q-switched Nd:YAlG-$LiIO_3$ 0.53 μm harmonic source": *J. App. Phys.* **41** 4125 (1970)

[3.30] G. A. Massey, J. M. Yarborough: "High average power operation and non-linear optical generation with the Nd:$YAlO_3$ laser": *App. Phys. Lett.* **18** 576 (1971)

[3.31] F. Hanson, P.Poirer: "Efficient intracavity frequency doubling of a high-repetition-rate diode-pumped Nd:YAG laser": *Opt. Lett.* **19** 1526 (1994)

[3.32] T. Taira, T. Kobayashi: "Q-switching and frequency doubling of solid-state lasers by a single intracavity KTP crystal": *IEEE J. Quant. Elec.* **30** 800 (1994)

[3.33] T. Taira, T. Kobayashi: "Intracavity frequency doubling and Q-switching in diode-laser pumped Nd:YVO_4 lasers": *App. Opt.* **34** 4298 (1995)

[3.34] J. E. Murray, S. E. Harris: "Pulse lengthening via overcoupled internal second-harmonic generation": *J. App. Phys.* **41** 609 (1970)

[3.35] G. P. A. Malcolm, M. Ebrahimzadeh, A. I. Ferguson: "Efficient frequency conversion of mode-locked diode-pumped lasers and tunable all-solid-state lasers sources": *IEEE J. Quant. Elec.* **28** 1172 (1992)

[3.36] J. R. Lincoln, M. J. P. Dymott, A. I. Ferguson: "Femtosecond pulses from an all-solid-state Kerr-lens modelocked Cr:LiSAF laser": *Opt. Lett.* **19** 1210 (1994)

[3.37] O. Bernecker: "Limitations for mode-locking enhancement of internal SHG in a laser": *IEEE J. Quant. Elec.* **9** 897 (1973)

[3.38] J. Falk: "A theory of the mode-locked, internally frequency-doubled laser": *IEEE J. Quant. Elec.* **11** 21 (1975)

[3.39] C. B. Hitz, L. M. Osterink: "Simultaneous intracavity frequency-doubling and mode locking in a Nd:YAG laser": *App. Phys. Lett.* **18** 378 (1971)

[3.40] T. R. Gurski: "Simultanoeus mode-locking and second-harmonic generation by the same non-linear crystal": *App. Phys. Lett.* **15** 5 (1969)

[3.41] R. R. Rice, G. H. Burkhart: "Efficient mode-locked frequency-doubled operation of an Nd:$YAlO_3$ laser": *App. Phys. Lett.* **19** 225 (1971)

[3.42] M. Yamashita, W. Sibbett, D. Welford, D. J. Bradley: "Intracavity second-harmonic generation in a synchronously modelocked CW dye laser": *J. App. Phys.* **51** 3559 (1980)

[3.43] D. Welford, W. Sibbett, J. R. Taylor: "Intracavity second-harmonic generation using a synchronously modelocked CW dye laser": *Opt. Comm.* **35** 283 (1980)

[3.44] F. Laermer, J. Dobler, T. Elsaesser: "Generation of femtosecond UV pulses by intracavity frequency doubling in a modelocked dye laser": *Opt. Comm.* **67** 58 (1988)

[3.45] S. Backus, M. T. Asaki, C. Shi, H. P. Kapteyn, M. M. Murnane: "Intracavity frequency-doubling in a Ti:sapphire laser: generation of 14 fs pulses at 416 nm": *Opt. Lett.* **19** 399 (1994)

[3.46] M. Yamashita, K. Yamada, T. Sato: "Analysis of a synchronously mode-locked and internally frequency-doubled CW dye laser": *IEEE J. Quant. Elec.* **18** 95 (1982)

[3.47] T. R. Zhang, G. Focht, P. E. Williams, M. C. Downer: "Theory of intracavity frequency-doubling in passively modelocked femtosecond lasers": *IEEE J. Quant. Elec.* **24** 1877 (1988)

[3.48] T. E. Dimmick: "Semiconductor-laser-pumped, mode-locked, and frequency-doubled Nd:YAG laser": *Opt. Lett.* **14** 677 (1989)

[3.49] L. R. Marshall, A. D. Hays, A. Kaz, R. L. Burnham: "Intracavity doubled mode-locked and CW diode-pumped lasers": *IEEE J. Quant. Elec.* **28** 1158 (1992)

[3.50] J. R. Lincoln, A. I. Ferguson: "All-solid-state intracavity-doubled Nd:YLF laser producing 300 mW of 659 nm light": *Opt. Lett.* **19** 1213 (1994)

[3.51] R. C. Miller: "Optical second-harmonic generation in piezoelectric crystals": *App. Phys. Lett.* **5** 17 (1964)

[3.52] R. S. Adhav, S. R. Adhav, J. M. Pelaprat: "BBO's nonlinear optical phase-matching properties": *Laser Focus World* (September, 1988)

[3.52a] D. A. Roberts: "Simplified characterisation of uniaxial and biaxial nonlinear optical crystals: a plea for standardisation of nomenclature and conventions": *IEEE J. Quant. Elec.* **28** 2057 (1992)

[3.53] M. Born, E. Wolf: "Principles of Optics": *Sixth Edition* (Pergamon Press, 1993)

[3.54] A. Yariv, P. Yeh: “Optical Waves in Crystals”: (Wiley, 1984)

[3.55] J. Q. Yao, T. S. Fahlen: "Calculations of optimum phase match parameters for the biaxial crystal $KTiOPO_4$": *J. App. Phys.* **55** 65 (1984)

[3.56} M. Kaschke, C. Koch:"Calculation of non-linear optical polarisation and phase-matching in biaxial crystals": *App. Phys. B* **49** 419 (1989)

[3.57] M. V. Hobden: "Phase-matched second-harmonic generation in biaxial crystals": *J. App. Phys.* **38** 4365 (1967)

[3.58] M. A. Dreger, J. H. Erkkila: "Improved method for calculating phase-matching criteria in biaxial non-linear crystals": *Opt. Lett.* **17** 787 (1992)

[3.59] J. E. Midwinter, J. Warner: "The effects of phase-matching method and of uniaxial crystal symmetry on the polar distribution of second-order non-linear optical polarisation": *Brit. J. App. Phys.* **16** 1135 (1965)

[3.60] R. A. Morgan: "Phase matching considerations for generalised three-wave mixing in nonlinear anisotropic crystals": *App. Opt.* **29** 1259 (1990)

[3.61] R. C. Eckardt: "Phase matching limitations of high efficiency second harmonic generation": *IEEE J. Quant. Elec.* **20** 1178 (1984)

[3.62] D. A. Kleinman: "Non-linear dielectric polarisation in optical media": *Phys. Rev.* **126** 1977 (1962)

[3.63] B. Wyncke, F. Brehat: "Calculation of the effective second-order non-linear coefficients along the phase matching directions in acentric orthorhombic biaxial crystals": *J. Phys. B* **22** 363 (1989)

[3.64] H. Ito, H. Naito, H. Inaba: "Generalised study on angular dependence of induced second-order nonlinear polarisations and phase matching in biaxial crystals": *J. App. Phys.* **46** 3992 (1975)

[3.65] V. G. Dmitriev, D. N. Nikogosyan: "Effective nonlinearity coefficients for three-wave interactions in biaxial crystals of *mm2* point group symmetery": *Opt. Comm.* **95** 173 (1993)

[3.66] F. Brehat, B. Wyncke: "Calculation of double-refraction walk-off angle along the phase-matching directions in non-linear biaxial crystals": *J. Phys. B* **22** 1891 (1989)

[3.67] J. Yao, W. Sheng, W. Shi: "Accurate calculation of the optimum phase-matching parameters in three-wave interactions with biaxial non-linear crystals": *J. Opt. Soc. Am. B* **9** 891 (1992)

[3.68] N. P. Barnes, V. J. Corcoran: "Parametric generation processes: spectral bandwidth and acceptance angles": *App. Opt.* **15** 696 (1976)

[3.69] C. Chen, Y. Wu, A. Jiang, B. Wu, G. You, R. Li, S. Lin: "New non-linear optical crystal: LiB_3O_5": *J. Opt. Soc. Am. B* **6** 616 (1989)

[3.70] S. P. Velsko, M. Webb, L. Davis, C. Huang: "Phase-matched harmonic generation in lithium triborate (LBO)": *IEEE J. Quant. Elec.* **27** 2182 (1991)

[3.71] J. Y. Huang, Y. R. Shen, C. Chen, B. Wu: "Non-critically phase-matched second-harmonic generation and optical parametric amplification in lithium triborate crystal": *App. Phys. Lett.* **58** 1579 (1991)

[3.71a] F. Xie, B. Wu, G. You, C. Chen: "Characterisation of LiB_3O_5 crystal for second-harmonic generation": *Opt. Lett.* **16** 1237 (1991)

[3.72] J. T. Lin, J. L. Montgomerey, K. Kato: "Temperature-tuned noncritically phase-matched frequency conversion in LiB_3O_5 crystal": *Opt. Comm.* **80** 159 (1990)

[3.73] T. Ukachi, R. J. Lane, W. R. Bosenberg, C. L. Tang: "Phase-matched second-harmonic generation and growth of a LiB_3O_5 crystal": *J. Opt. Soc. Am. B* **9** 1128 (1992)

[3.74] T. Ukachi, R. J. Lane, W. R. Bosenberg, C. L. Tang: "Measurements of noncritically phase-matched second-harmonic generation in a LiB_3O_5 crystal": *App. Phys. Lett.* **57** 980 (1990)

[3.75] I. Gontijo: "Determination of important parameters for second harmonic generation in LBO": *Opt. Comm.* **108** 324 (1994)

[3.76] Y. Furukawa, S. A. Markgraf, M. Sato, H. Yoshida, T. Sasaki, H. Fujita, T. Yamanaka, S. Hakai: "Investigation of the bulk laser damage of lithium triborate, LiB_3O_5 single crystals": *App. Phys. Lett.* **65** 1480 (1994)

[3.77] Y. Furukawa, M. Sato, S. A. Markgraf, H. Yoshida, T. Sasaki: "Crystal growth and laser damage of LiB_3O_5": *SPIE* **2379** 245 (19**)

[3.78] S. Lin, Z. Sun, B. Wu, C. Chen: "The nonlinear optical characteristics of a LiB_3O_5 crystal": *J. App. Phys.* **67** 634 (1990)

[3.79] F. C. Zumsteg, J. D. Bierlein, T. E. Gier: " $K_xRb_{1-x}TiOPO_4$: a new nonlinear optical material": *J. App. Phys.* **47** 4980 (1976)

[3.80] J. D. Bierlein, H. Vanherzeele: "Potassium titanyl phosphate: properties and new applications": *J. Opt. Soc. Am. B* **6** 622 (1989)

[3.80a] T. Nishikawa, N. Uesugi, H. Ito: "Angle tuning characteristics of second harmonic generation in $KTiOPO_4$": *App. Phys. Lett.* **55** 1943 (1989)

[3.81] H. Vanherzeele, J. D. Bierlein, F. C. Zumsteg: "Index of refraction measurements and parametric generation in hydrothermally grown $KTiOPO_4$": *App. Opt.* **27** 3314 (1988)

[3.82] T. Y. Fan, C. E. Huang, B. Q. Hu, R. C. Eckardt, Y. X. Fan, R. L. Byer, R. S. Feigelson: "Second harmonic generation and index of refraction measurements in flux-grown $KTiOPO_4$": *App. Opt.* **26** 2390 (1987)

[3.83] K. Kato: "Parametric oscillation at 3.2 μm in KTP pumped at 1.064 μm": *IEEE J. Quant. Elec.* **27** 1137 (1991)

[3.84] R. C. Eckardt, H. Masuda, Y. X. Fan, R. L. Byer: "Absolute and relative nonlinear optical coefficients of KDP, KD*P, BaB_2O_4, LIO_3, MgO:$LiNbO_3$, and KTP measured by phase-matched second-harmonic generation": *IEEE J. Quant. Elec.* **26** 922 (1990)

[3.85] L. E. Halliburton, M. P. Scripsick: "Mechanisms and point defects responsible for the formation of grey tracks in KTP": *SPIE* **2379** 235 (19**)

[3.86] G. M. Loiacono, D. N. Loiacono, T. McGee, M. Babb: "Laser damage formation in $KTiOPO_4$ and $KTiOAsO_4$ crystals: grey tracks": *J. App. Phys.* **72** 2705 (1992)

[3.86a] J. C. Jacco, D. R. Rockafellow, E. A. Teppo: "Bulk-darkening threshold of flux-grown KTP": *Opt. Lett.* **16** 1307 (1991)

[3.87] R. Blackman, P. F. Bordui, M. M. Fejer: "Laser-induced photochromic damage in KTP": *App. Phys. Lett.* **64** 1318 (1994)

Chapter 4

SIDE-PUMPED Nd:YAG SLAB RING LASER

4.1 Introduction

This chapter describes the design and performance of a ring laser which used a side-pumped slab of Nd:YAG as the amplifier. By using an optical diode in the resonator, highly reliable single-frequency output was achieved at 1 μm with powers up to 2.6 W in a TEM_{00} beam, and by intracavity frequency-doubling up to 1.1 W of single-frequency 0.5 μm output was obtained. This laser system was used as a pump source for a CW OPO [4.1] and a holosteric $Ti:Al_2O_3$ ultra-short pulse laser. The 1 μm laser was also operated with a non-planar ring resonator in order to investigate the phenomenon of polarisation rotation in non-planar rings. The purpose of this was to examine the possibility of using a non-planar resonator to allow a reduction in the number of intracavity elements in the laser, thereby reducing the internal losses and increasing the amount of extractable second-harmonic power when intracavity frequency doubling.

4.2 Pump Sources

4.2.1 Power Output and Beam Properties

Two 20 W CW AlGaAs 1 cm diode-laser bars (model *SDL 3460 S)* were used as pump sources. The bars were consecutive production units and had very similar operating characteristics. These are summarised in Table 4.1. The beam divergence half-angle for containing 100% of the output radiation was 40° in the plane perpendicular to the bar, and 5° in the plane parallel to the bar.

4.2.2 Dependence of Emission Wavelength on Temperature and Current

Temperature-tuning of the output wavelength was examined for both devices, by varying the bars' heat-sink temperature at fixed drive current and scanning the output with a monochromator. Changes in wavelength with current at fixed heat-sink temperatures were also investigated. These measurements were important to establish the heat-sink temperature which would result in the coincidence of the emission wavelength with the peak absorption wavelength for Nd:YAG of 807.5 nm at the

	GH 900	GH 901
Differential Quantum Efficiency	71%	73%
Threshold	10.2 A	10.3 A
Slope Efficiency	1.081 W/A	1.105 W/A
I @ 20 W	28.7 A	28.4 A
Specified λ @ 25°C	808 nm	808 nm
Specified spectral FWHM	1.6 nm	1.7 nm
Power Output	P = 1.081(I-10.2)	P = 1.105(I-10.3)

Table 4.1. Diode-bar properties.

maximum pump level. A typical scanning monochromator trace is shown in Figure 4.1. The FWHM of the emission was measured to be typically (2 ± 0.2) nm and was independent of the heat-sink temperature and drive current. The variations in the emission wavelengths of the two bars with temperature at a fixed current of 17 A are shown in Figure 4.2. The temperature dependent wavelength shift was +0.27 nm/°C for GH 900 and +0.22 nm/°C for GH 901. Because the amplifier was side-pumped, the absorption path was relatively short so the two bars were operated with their heat sinks at 29 °C to obtain emission as close as possible to the peak absorption wavelength for Nd:YAG of 807.5 nm. The actual temperature of the bars' active layers would have been significantly higher than this at full drive current.

The change in emission wavelength with drive current at fixed heat-sink temperature was also investigated. Figure 4.3 shows the behaviour for heat-sink temperatures of 18 °C and 28 °C. Bar GH 900 gave gradients of +0.15 and +0.19 nm/A at 18 °C and 28 °C respectively. Bar GH 901 gave +0.20 and +0.16 nm/A. Due to the narrow absorption features of Nd:YAG together with the short absorption path in side-pumping, this drift in the bars' wavelength with drive current was sufficient to have a

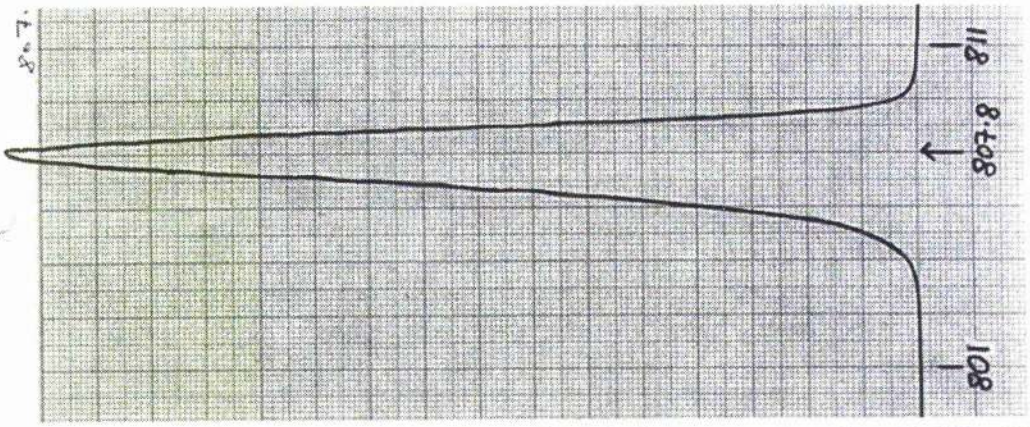

Figure 4.1. Scanning monochromator trace of diode-bar output wavelength. (Bar GH 900, 28°C, 25 A.)

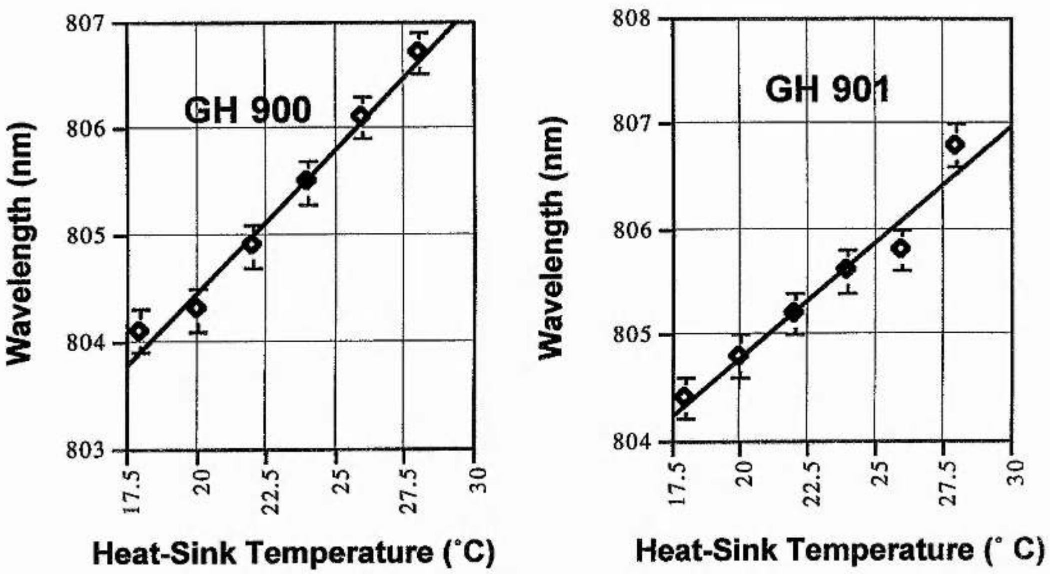

Figure 4.2. Temperature tuning of emission wavelength for the diode-bars. Current = 17 A.

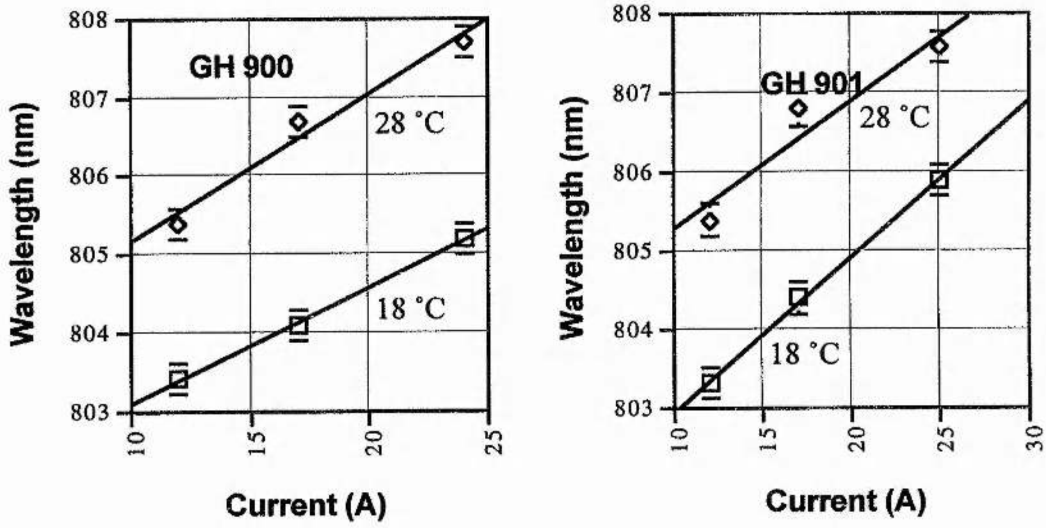

Figure 4.3. Variation of emission wavelength with drive current at fixed heat-sink temperatures.

detrimental effect on the maximum output power of the laser if the heat-sink temeperatures were not carefully chosen. This is a particularly important consideration for side-pumped systems.

4.2.3 Temperature Regulation of Diode-Bars

The narrow absorption feature of Nd:YAG at 807.5 nm meant that the diode-bars had to be temperature regulated. The arrangement used for this is shown in Figure 4.4. The bar package is bolted to a brass or copper block in which a thermistor is embedded. High-purity 125 μm thick indium foil was used between the package and the block to establish good thermal contact. A thermo-electric cooler (Peltier cooler) is permanently bonded between this block and a water-cooled heat sink using thermally conductive setting epoxy. A commercial temperature controller supplies whatever current is necessary to the Peltier device in order to keep the upper block at the required set point. A typical Peltier cooler (*e.g.* Marlow DT 1089) is able to sink 20 - 30 W for a current of 2 - 3 A. The temperature controller's differential and integral time constants were set to give a fast response to changes in the heat load brought about by varying the bar's drive current. The drive current was provided by a low-voltage current supply. The cathode contact is the bar's upper casing; the anode contact is at the base of the package so that the copper block could be used for this. Copper multi-core switch-gear cable with a DC rating of 50 A was used to connect the current supply to the bar. Although the current supply was capable of driving the two bars in series, two separate supplies were used to allow greater flexibility in the pump power delivered to the slab.

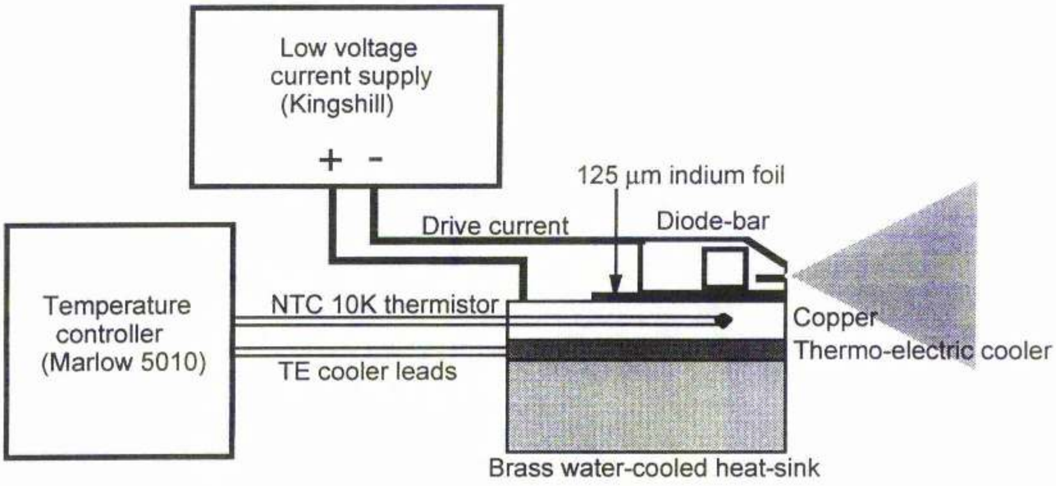

Figure 4.4. Diode-bar operating arrangement.

4.3 Amplifier

A plan view of the gain element used for the laser is shown in Figure 4.5. The Nd:YAG slab was of 1.1% doping and was cut into a slab measuring 6 mm high, 20 mm long and 2.6 mm thick. No special dielectric coatings were used on any part of the slab which was mounted in a water-cooled brass block such that heat was removed via the top and bottom surfaces. Indium foil was used between the block and the mount to provide good thermal contact. The design of the slab was such that the laser mode, on entering the slab at the Brewster angle (polarising the laser in the horizontal plane) was first expanded and then effectively spread over a 1 cm length at one edge of the slab, thereby coinciding spatially with the emission of the first diode-bar. The mode undergoes a total internal reflection at this site (grazing angle 10.5°) and is reflected to the other side of the slab where it is pumped by the second bar. After a second total internal reflection the mode exits the slab, again at the Brewster angle.

The aperture of the slab (D in Figure 4.5) was designed to be 1.3 mm, which was estimated as the largest likely mode diameter at the slab for the ring resonator to be used. Inside the slab, the saggital mode diameter is expanded by a factor of 1.8 to about 2.4 mm (D' in Figure 4.5). This has two highly beneficial effects. First, the mode is expanded so that the full 1 cm emission width of the diode-bars is utilised. Second, the saggital expansion of the mode together with the mode's reflection at the edges of the slab results in half the width of the slab being filled with the laser mode at the sites opposite the diode-bars. The useful aborption path of the pump light was therefore about 1.3 mm, which is more than one aborption length at 807.5 nm. This is a considerable improvement over a simple side-pumped rod not only because of the increased pump-mode interaction length, but also because very little of the pump light

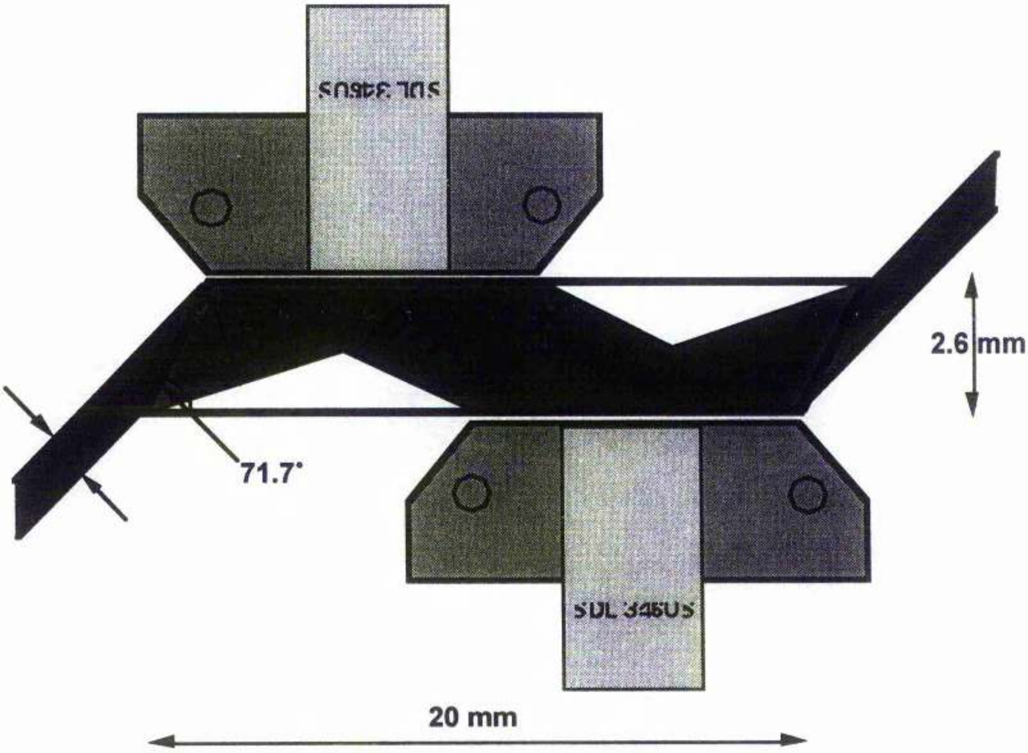

Figure 4.5. Side-pumped Nd:YAG slab amplifier.

is wasted outside the mode volume.

Another benefit of this amplifier design is evident from the equivalent pump scheme shown in Figure 4.6. The reflection of the laser mode at the edges of the slab means that the mode is effectively pumped across its entire width, improving efficiency and allowing TEM_{00} transverse mode operation to be easily achieved. At the central portion of the slab's length where the mode overlaps the last few millimeters of the diode-bar, the mode reflection ensures that the absorption path is kept up to ≈ 1.3 mm.

Although the saggital width of the laser mode is inflated within the slab, the astigmatism is removed when the mode exits the slab at the complementary Brewster angle. Thus the slab does not introduce any net astigmatism into the resonator mode which might have a detrimental effect on other aspects of the laser's performance.

The diode-bars together with their heat-sinking systems were mounted on *xyz*translation stages and positioned so that the facets were as close as possible to the sides of the slab. No special coupling optics were used. The aim was to absorb the pump in a short depth before the 40° divergence caused reduction in the pump-mode-overlap. Possibly this was the main weakness of the design; fibre lenses could have been used to collimate the bars' output, allowing the benefits of the slab design to be more fully exploited. However, this would have made the alignment of the laser much more critical in that the laser mode and the diode-bars' facets would needed to have been exactly in the same plane. Further mechanical positioning flexibility would have been required, adding to the complexity of the system.

Thermal lensing and thermal birefringence are well known to be limiting factors in the maximum output of this type of laser. In this slab design the pumping and concomitant thermal load were distributed over a length of 20 mm so that these effects were minimised.

This side-pumped design had the potential to be scaled up by simply adding further amplifier elements, should this have been required.

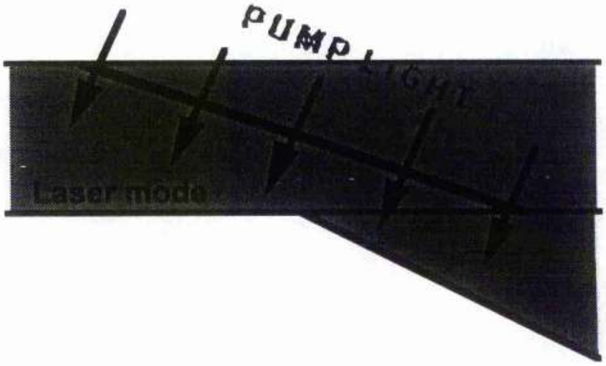

Figure 4.6. Equivalent pumping scheme.

4.4 Resonator

4.4.1 Estimation of Mode-Sizes; Stability Ranges

The full layout of the resonator for intracavity frequency-doubling is shown in Figure 4.7. A four-mirror bow-tie arrangement was used to keep the angles of incidence on the two curved mirrors to a minimum, thereby limiting the astigmatism in the output beam produced by these mirrors. In practice, the mimimum angle achievable was approximately 30° because of the size of the oven housing the LBO crystal, which had a diameter of 30 mm. A large oven was required to give thermal stability for the temperature-tuned LBO crystal.

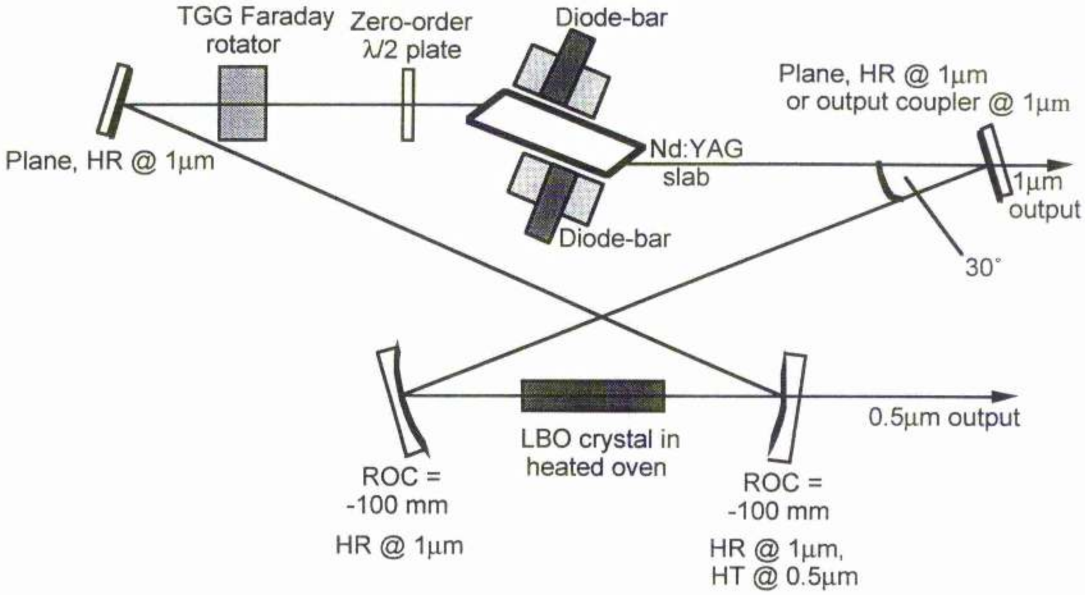

Figure 4.7. Single-mode intracavity-doubled Nd:YAG slab ring-laser.

Estimation of the mode size at a given point for various cavity configurations was made by finding the relevant *ABCD* matrix for one round-trip and requiring that the complex beam parameter q reproduce itself after one trip round the ring. In other words we seek the solution of the equation

$$q = \frac{Aq + B}{Cq + D}, \tag{4.1}$$

where the complex beam parameter q is given by

$$\frac{1}{q(z)} = \frac{1}{R(z)} - \frac{i\lambda}{\pi n w^2(z)}. \tag{4.2}$$

Stable cavities are characterised by real values of the wavefront radius of curvature $R(z)$ and the $1/e$ electric field radius $w(z)$. For a round-trip matrix *ABCD* these quantities are given by

$$R = \frac{2B}{D - A} \tag{4.3}$$

and

$$w = \sqrt{\frac{\lambda}{\pi}} \left[-\frac{C}{B} - \frac{(A - D)^2}{2B^2} \right]^{-1/4} . \tag{4.4}$$

The results of such an analysis for an empty four-mirror bow-tie ring with a plane mirror separation of 250 mm and an angle of 30° are shown in Figure 4.8. The cavity is stable for curved mirror separations between 100 and 115 mm. Even at the large separation end (towards 115 mm) where the saggital mode radius increases rapidly, the mode radius is less than 600 μm so that the 1.3 mm aperture of the slab amplifier is quite adequate. However, the astigmatism introduced by the large internal angle of 30° is quite clear. Figure 4.9 shows the behaviour when the Nd:YAG slab is introduced into the cavity midway between the plane mirrors. The distance from the plane mirrors to the slab faces was taken to be 120 mm. The stability range remains the same as before although there is a significant increase in the mode radii. Figures 4.10 and 4.11 model the mode radius in the slab and the waist radius at the focus of the ring when a 25 mm LBO crystal is placed midway between the two curved mirrors. The range of curved mirror separations for which the resonator is stable is now 98 - 109 mm. The tangential mode radius in the slab is now quite sensitive to the curved mirror separation. The waist at the focus of the ring is minimised by setting the curved mirror separation close to the stability limit of ≈ 109 mm. At this point the astigmatism is quite severe, the saggital waist radius being around 60 μm while the tangential waist radius is about 30 μm.

An important question to be answered was whether the Boyd and Kleinman focusing condition could be achieved in the LBO crystal while maintaining a stable cavity configuration. For a 25 mm length of LBO, optimum focusing is achieved for a confocal parameter of 4.4 mm. The corresponding waist radius needed is given by

$$w_0 = \sqrt{\frac{z_0 \lambda}{\pi n}}, \tag{4.5}$$

which in this case is 31 μm. The conclusion was therefore that by operating the laser with the curved mirrors as far apart as possible optimum focusing could be achieved in the tangential plane, although the ≈ 60 μm saggital waist meant that optimum nonlinear coupling could not be achieved. The fact that optimum nonlinear coupling coefficient could not be attained was unfortunate given that the modest non-linear coefficient of LBO and the modest gain over linear loss for a ring laser together meant that non-linear under-coupling was likely even if the Boyd and Kleinman conditions could be reached. However the use of a ring laser enabled single-frequency operation to be reliably achieved at all puming levels, and the type I non-critical phase-matching in LBO meant that the horizontally polarised laser mode was not disturbed by birefringence effects in the nonlinear crystal.

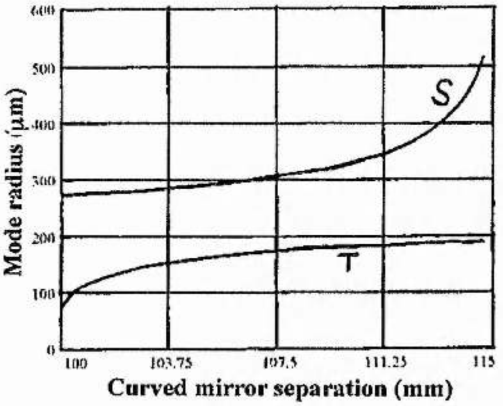

Figure 4.8. Mode sizes in the empty ring.

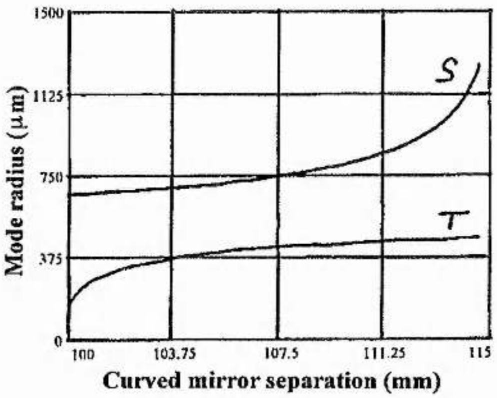

Figure 4.9. Modes sizes with slab in the ring.

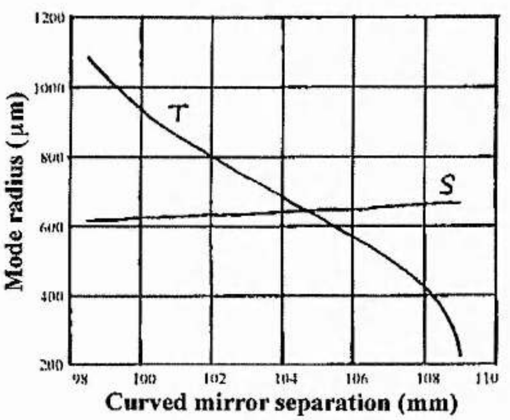

Figure 4.10. Mode sizes in the slab for doubled laser.

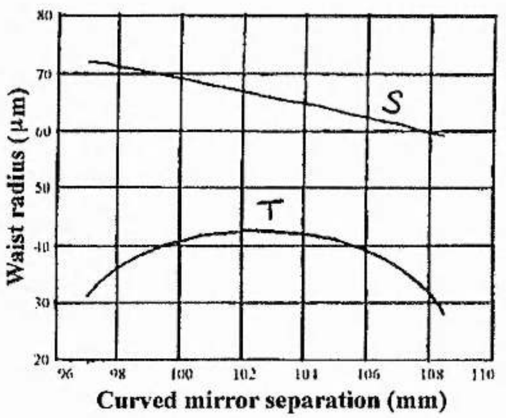

Figure 4.11. Waist sizes in LBO crystal.

4.4.2 Unidirectional Operation

Single-longitudinal mode operation was achieved by causing only one of the two possible directions around the ring to lase. The travelling wave in the ring has the effect of eliminating spatial hole burning so that only the mode with the highest gain operates. Unidirectional operation is achieved in a ring laser by introducing a differential loss between the two directions so that the lower-loss direction is preferentially amplified and establishes itself, excluding the other direction. Unidirectional lasing was achieved in this case by inserting a Faraday rotator and a half-wave plate into the cavity, so that for one direction there was no loss on entering the Nd:YAG slab at the Brewster angle, while for the other direction, rotation of the (linear) polarisation out of the plane of the ring caused significant loss to be introduced. The principle is illustrated in Figure 4.12. The method relies on the non-reciprocal rotation

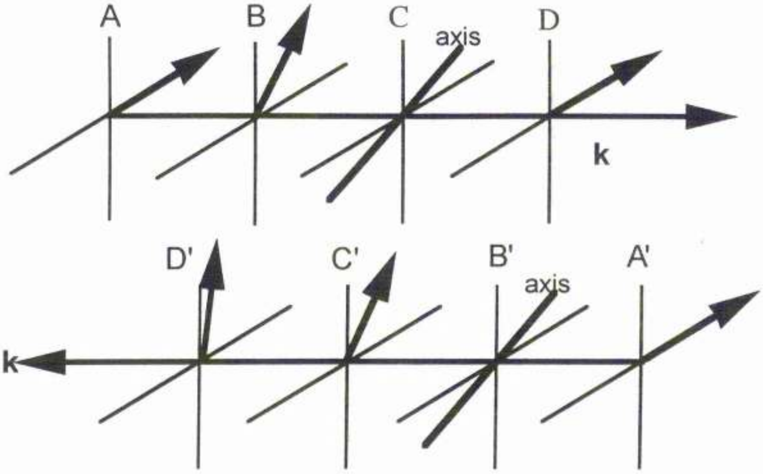

Figure 4.12. Action of an optical diode.

produced by the Faraday-rotator, *i.e.* the sense of rotation depends on the direction of travel for a fixed direction of the magnetic field through the TGG material. At point A in Figure 4.12, the laser is polarised in the plane of the ring. After passing through the Faraday rotator, the plane of polarisation is rotated, say in right-handed sense, by a certain angle which is typically a few degrees. The half-wave plate C is rotated so that one of its axes bisects the angle that the polarisation direction at B makes with the horizontal. Thus at D the polarisation is restored to the horizontal plane and no loss is experienced on entering the Nd:YAG slab at the Brewster angle. For the opposite direction (starting at A') the half-wave plate is encountered first, giving an effective rotation which is the same as that produced in going from A to B. The polariation at C' is therefore the same as that at B. However on passing through the Faraday rotator the rotation sense is now left-handed so that the plane of polarisation is rotated further away from the horizontal plane rather than being restored. Consequently this direction will experience Fresnel loss on entering the Nd:YAG slab.

4.5 Laser Performance

4.5.1 Operation at 1 μm

4.5.1.1 Output Power

The laser was operated at 1 μm by replacing one of the plane HR mirrors by a series of plane output couplers. Figure 4.13 shows the output obtained without the optical diode (*i.e.* bidirectional operation) and Figure 4.14 shows the unidirectional single-frequency performance obtained by inserting the optical diode into the cavity. For the bidirectional laser the highest output achieved was 3.04 W at 19.2% slope efficiency, obtained by using a 5% output coupler. When the laser was operated

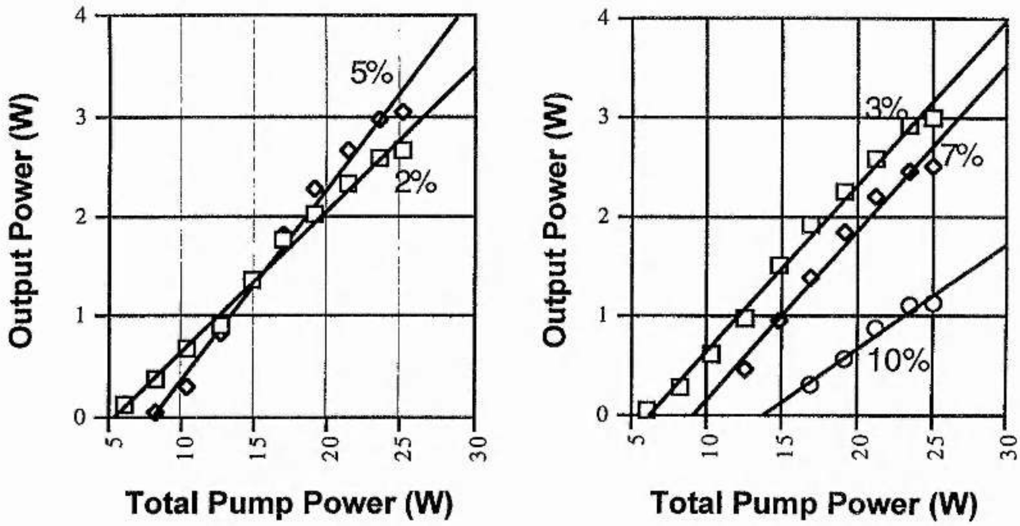

Figure 4.13. Output from bidirectional ring laser.

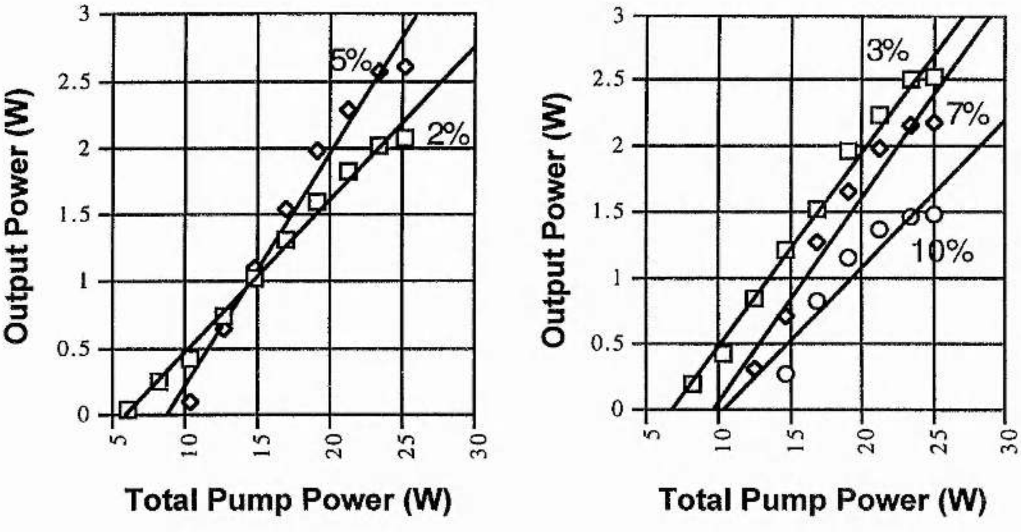

Figure 4.14. Output from unidirectional laser.

unidirectionally the highest output obtained was 2.6 W at 17.4% slope efficiency. The optimum coupling remained at 5%. As can be seen from Figures 4.13 and 4.14, the output begins to roll off at about the 25 W pumping level. This was probably due to a combination of thermal lensing in the Nd:YAG slab affecting cavity stability, and thermal birefringence causing the laser mode to become slightly elliptically polarised. This causes loss at the ends of the slab.

In order to assess the performance of the laser when intracavity frequency-doubling, estimates of internal linear losses were made. This was done by comparing pairs of slopes in Figures 4.13 and 4.14. The ratio of two slopes s and s' obtained using output couplers T and T' is

$$\frac{s}{s'} = \left(\frac{T}{T'}\right)\left(\frac{L+T'}{L+T}\right), \tag{4.6}$$

where L is the internal loss. This gave the internal loss as 1.6% for the bidirectional laser and 4.5% for the unidirectional laser. The somewhat high value of L for the unidirectional laser was attributed to the loss introduced by the TGG Faraday rotator which probably accounted for much of the additional 2.9% loss.

Estimates of the amplifier's unsaturated gain were made by replotting the output power as a function of output coupling at certain fixed pumping levels. The results of this are shown in Figure 4.15. At the points T_z where the curves fall to zero, the gain is equal to $L + T_z$. For the pump powers shown, the unsaturated gain was in the region of 9 to 15%. At the full pump power of 25 W, the gain was approximately 25%.

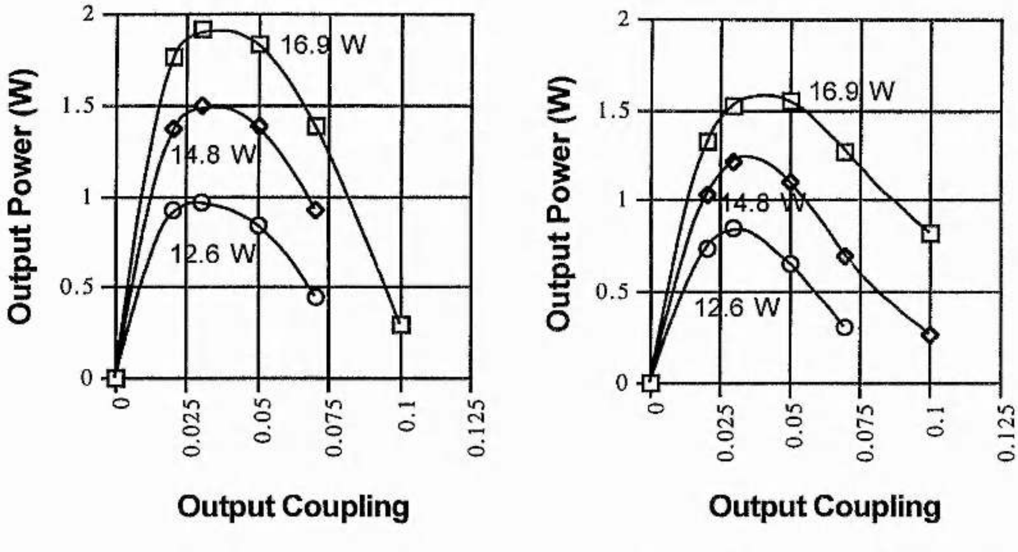

Figure 4.15. Output power against output coupling for the bidirectional (left) and unidirectional (right) ring laser. Incident pump powers are as indicated.

4.5.1.2 Beam Quality

The beam profile of the single-frequency 1 μm output at a pump power of 23.5 W was obtained by scanning its cross-section with a 5 μm diameter pinhole over an ordinary silicon photodiode. A typical pair of horizontal and vertical profiles is shown in Figure 4.16. At this high pump level, the departure of the beam from a true Gaussian shape is pronounced, and the astigmatism predicted from section 4.4.1 is also evident. At pump powers of <≈ 10 W, the profiles were Gaussian, although the output was still astigmatic. The M^2 factor of the beam in the horizontal and vertical planes was estimated at the 23.5 W pumping level by focussing the output beam with a lens and measuring the subsequent waist W_0 and far-field diffraction angle θ, again using a scanning 5 μm pinhole. The M^2 value is given by

$$M^2 = \frac{W_0 \pi \theta}{\lambda}.. \tag{4.7}$$

The results obtained for the two planes are summarised in Table 4.2. The beam quality clearly deteriorates at high pumping levels, although this laser compares favourably with other side-pumped systems of similar output power.

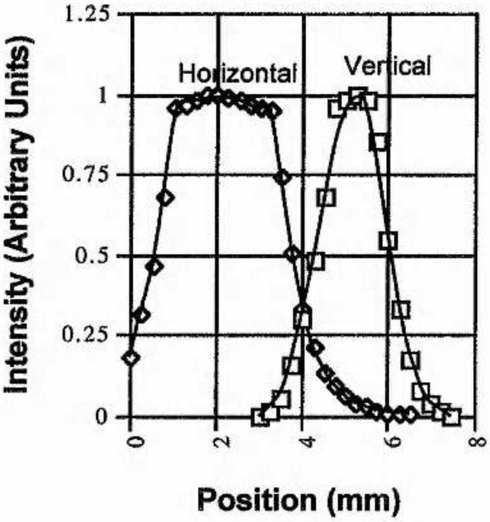

Figure 4.16. 1 μm beam profiles at 23.5 W pump power.

	Waist W_0 (μm)	Far-field angle θ (mrad)	M^2
Saggital (Horizontal plane)	601	0.77	1.37
Tangential (Vertical plane)	258	1.72	1.31

Table 4.2. Beam parameters after focussing with f = 200 mm lens. Pump level = 23.5W.

4.5.2 Operation at 0.5 μm

4.5.2.1 Output Power Behaviour

Single-frequency 0.5 μm output was obtained by replacing the output coupler with a plane high reflector and inserting an oven-heated LBO crystal (length 25 mm) at the resonator focus. The oven was mounted on a small prism table which was itself mounted on an *xyz* translation stage. The crystal therefore had six degrees of freedom (*xyz* plus yaw, pitch and roll) allowing the visible output power to be fully maximised. Non-critical phase-matching was achieved at a temperature of 143 °C. The variation of the second harmonic output with temperature is shown in Figure 4.17. The FWHM temperature bandwidth was measured as 1.3 °C. In order to prevent drifting of the

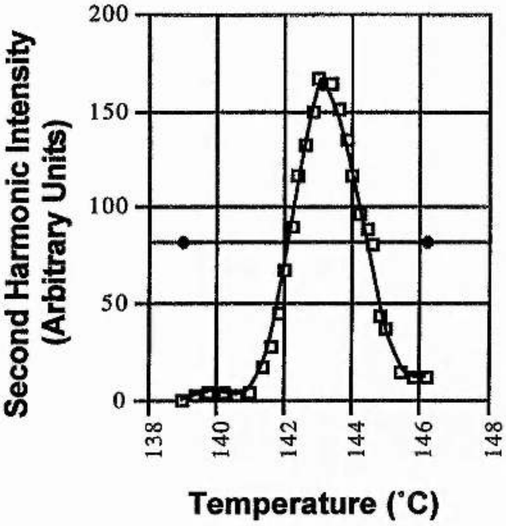

Figure 4.17. Temperature tuned phase-matching in the 25 mm LBO crystal.

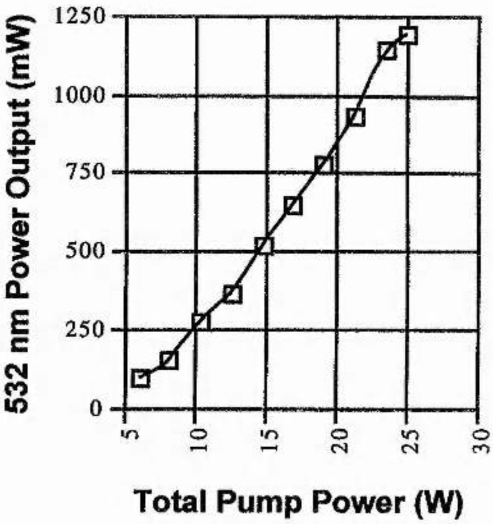

Figure 4.18. 0.5 μm output power.

harmonic output power, a commercial temperature controller (Smatex model LAB10) was used to stabilise the oven temperature to <± 0.01 ˚C. The maximum harmonic output power achieved for the maximum pump power of 25 W was 1.2 W, representing a conversion efficiency from 810 nm to 532 nm of 4.8%. However, the output power was limited to approximately 1 W on a regular basis. As for the 1 μm operation, the single-frequency output was confirmed using a scanning confocal Fabry-Perot interferometer. The small amount of 1 μm leakage from one of the high reflectors was used for this. The best output power characteristic that was observed is shown in Figure 4.18. This curve was obtained by "tweaking" the crystal position and orientation at each pumping level. Simply increasing the pump power was never sufficient on its own to achieve the full potential visible output for a given pumping level.

The theory outlined in chapters 1 and 3 can be used to assess the second-harmonic output-power performance of the laser. The maximum unidirectional, single-frequency 1 μm output power was 2.6 W. The unsaturated gain $\gamma_0 l$ at this output level was estimated to be ≈ 25%, and the internal linear loss δ of the laser was estimated to be 4.5%. Assuming that this output was achieved at close-to-optimum output coupling, the saturation power of the laser is given (approximately) by

$$P_{sat} \approx \frac{P_{\omega,out\,\max}}{\left(\sqrt{\gamma_0 l} - \sqrt{\delta}\right)^2}.$$

This gives $P_{sat} \approx 31$ W. For a standing-wave cavity the relevant expression is

$$P_{sat} \approx \frac{2P_{\omega,out\,\max}}{\left(\sqrt{2\gamma_0 l} - \sqrt{\delta}\right)^2}.$$

In both the travelling and standing-wave cases, $P_{sat} = I_{sat}A_{eff}$, so that the saturation power figure is a measure of the extent of the pump-signal overlap. The optimum nonlinear coupling is given by (3.16) as 1.45 × 10^{-3} W^{-1}, while the maximum obtainable from a 25 mm LBO crystal, using "Boyd and Kleinman" focusing is 7.3 × 10^{-4} W^{-1}. Thus even with the most favourable focusing possible, the laser would have been under-coupled by a factor of two. Using equation (3.10) it can be shown that with "Boyd and Kleinman" focusing this particular laser should have produced 2.44 W at 532 nm. The actual maximum harmonic output power of 1.2 W, indicates an actual nonlinear coupling factor κ of ≈ 15% of the "Boyd and Kleinman" value. Some of this under-coupling may be attributed to inadequate focusing and the quite severe astigmatism of the laser mode in the LBO crystal, although it should also be noted that this calculation can only serve as a guide to the laser's performance. This is because the values for unsaturated gain, linear loss and saturation power were only estimates.

4.5.2.2. Beam Quality at 0.5 μm

The beam profile of the harmonic output was scanned using a 5 μm diameter pinhole and photodiode as for the 1 μm output. Again, the pump power was 23.5 W and at the time the scanning was carried out this resulted in 922 mW of green power. After collimation with a 100 mm focal length lens, a beam waist was produced using a lens of 200 mm focal length. A typical pair of far-field profiles is shown in Figure 4.19. Although astigmatism is again evident, the harmonic beam profile is clearly much closer to a true Gaussian shape than the 1 μm beam at the same pumping level. This can be attributed to the dependence of the green intensity on the square of the 1 μm intensity at a given transverse point in the beam cross-section.

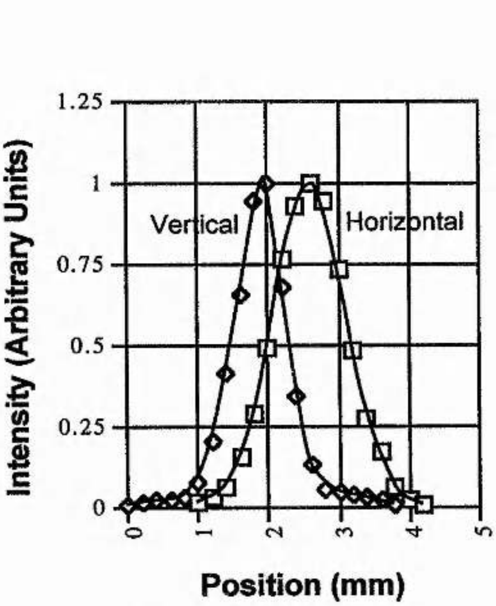

Figure 4.19. 0.5 μm beam profiles at 23.5 W pump power.

As for the 1 μm case, the M^2 value of the beam was obtained by locating and measuring the beam waist, and measuring the far-field diffraction angle. The results are shown in Table 4.3. The harmonic beam quality is clearly better than that in the 1 μm case, and this was again due to the nature of the doubling process.

	Waist W_0 (μm)	Far-field angle θ (mrad)	M^2
Saggital (Horizontal plane)	114	1.48	1.11
Tangential (Vertical plane)	93	1.83	1.10

Table 4.3. Harmonic beam parameters after collimation and focussing. Pump level = 23.5 W.

4.6 Use of Non-Planar Ring Resonators to Obtain Unidirectional, Single-Frequency Lasing

4.6.1 Introduction

In ring lasers it is well known that single-frequency operation can be obtained by enforcing unidirectional operation so as to eliminate spatial hole burning. To achieve such operation, it is necessary to introduce some small differential loss between the two lasing directions, so that the low-loss direction exclusively dominates the laser action. At present two methodologies exist for introducing the differential loss.

The first technique, based on the acoustooptic (AO) effect, can be implemented in two ways [4.2]. In the "intrinsic" method, a travelling-wave AO modulator is placed inside the laser resonator, and the resonator is aligned so that the circulating field is diffracted from the two sides of the modulator. Since the grating in the modulator is moving, the angles of incidence for which the Bragg condition is satisfied are slightly different for the two counter-propagating beams, and as a result they experience slightly different losses. The loss difference is usually more than enough to obtain unidirectional operation. In the "feedback" method, a single pathway through the modulator is defined and the diffracted beam is reintroduced to the main laser cavity via the modulator by a second ring. The diffracted beams for the two directions have different frequencies, and therefore experience different round-trip phase-shifts in the feedback path. As a consequence, the counter-propagating beams in the main laser cavity are generally attenuated by different amounts, allowing unidirectional operation. The AO technique has been successfully demonstrated in several lasers [4.3 - 5].

The second method, which is more established than the AO schemes, uses the Faraday effect, and has been discussed in section 4.4.2. A variation on this method has been to use non-planar rings in place of the wave-plate to provide the reciprocal rotation, but keeping the Faraday effect to provide non-reciprocal rotation, as in for example [4.6]. In particular, the rotation effect of non-planar rings has been successfully combined with the Faraday effect in Nd:YAG in "monolithic non-planar ring oscillators" [4.7 - 10].

The laser so far described in this chapter was operated in a non-planar ring arrangement in order to investigate the possibility of removing the half-wave plate whist still achieving unidirectional operation. For deformations of the ring of a specific kind (descibed below) the effect of the polarisition rotation was both measured and calculated. The calculation of the amount of rotation was performed in two ways. The first used a standard method based on coordinate systems set in the beams between the mirrors. Other researchers had used this method [4.11 - 14], although the non-planar geometries they had investigated were simple in comparison to the present laser, generally being skew-square rings (or slight variations thereof) in which the beam is confined to two planes only. This method was found to be quite complicated for the laser geometry used here and therefore a vector method was developed in parallel with the standard method which was much simpler. The two methods were consistent with each other and with experimental results [4.15].

4.6.2 Deformation of the Ring

The ring laser described above was rebuilt in the vertical plane for the purposes of the investigation. Elevation and plan views of the arrangement are shown in Figure 4.20. The two curved mirrors M2, M3 were mounted on a rotatable aluminium bridge with axis of rotation X-X, such that the "non-planar angle" Ω could be set to any desired value. The angle Ω was used as a measure of the extent of deformation and non-planarity of the ring. Various geometries were possible by varying the plane mirror separation L, the curved mirror separation D, and the perpendicular height h between beams 3 and 1. Two rings were investigated for the dependence of their amount of polarisation rotation on the angle Ω.. In the first case the dimensions were L = 220 mm, D = 100 mm , h = 55 mm. For the second ring the values were L = 215 mm, D = 100 mm, h = 85 mm.

4.6.3 Calculation of the Amount of Rotation

4.6.3.1 Beam-based Method

If we assume that beam 1 in Figure 4.20 is linearly polarised in the horizontal plane (*i.e.* in the plane of the paper in the "plan" view) the effect of the non-planarity of the ring is such that in moving from point P to point Q on the path M1-M2-M3-M4, the electric field vector is rotated so that at Q it makes some angle with the horizontal plane. This "characteristic rotation" of a given arrangement (*i.e.* for given values of L, D, h, Ω) was denoted θ_c . The calculation of θ_c is a geometrical problem.

In the first method of calculation, a beam-based approach was taken, *i.e.* using coordinate systems set in the beams as shown in Figure 4.21 for the first reflection. An example program for the method is given in Appendix 1. In Figure 4.21, $\mathbf{n_1}$ is the mirror normal and $\mathbf{N_1}$ is the normal to the plane of incidence. The frames $x_1y_1z_1$ and $x_1'y_1'z_1'$ are the beam-based coordinate systems before and after the first reflection repectively. To implement this method, the four angles of incidence have to be determined and also the angles between consecutive plans of incidence. In order to find these two sets of angles, the whole system is referred to the coordinate system **ijk** (see Figure 4.20) in which the **j** direction is collinear with the straight line joining the two plane mirrors and the **k** direction is in the vertical direction. The angle α can be calculated given L, D and h. In addition the unit vectors representing the incident and reflected ray directions for each of the four reflections can be found. The scalar product of these two vectors leads to the angle of incidence while the vector products allows the normal to the plane of incidence to be found. The scalar products of such normals give the angles between the various planes of incidence.

The normal to the plane of incidence and the incident and reflected ray vectors can also be used to calculate the mirror normals. Although these are not required for the beam-based method they *are* required for the vector method described in section 4.6.3.2 below.

With these geometrical preliminaries completed, the rotation calculation can be started. This begins on line 99 of the program given in Appendix 1. Starting with the part of beam 1 immediately before mirror M1, the field is taken here as horizontally polarised. A system of coordinates *XYZ* is set up with Z as the direction of propagation and X and Y parallel and perpendicular to the horizontal plane, as shown in Figure 4.22. In this system, the initial unit vector of the E field is (1,0,0). This is easily converted to the ***ijk*** system using the angle α. The scalar product of the E vector in the ***ijk*** system and the unit vector normal to the first plane of incidence ($\mathbf{N_1}$) gives the angle between the horizontal plane and the first plane of incidence, and this is used to construct a matrix which transforms the E field components in the *XYZ* frame to the frame $x_1y_1z_1$ in the first plane of incidence. Given the E field components in this system, those in the $x_1'y_1'z_1'$ frame (the coordinate system immediately after the first reflection) are the same except that the x component is reversed in sign. These components are then transformed into the frame $x_2y_2z_2$ which is the frame used for the polarisation of the incident ray of the second reflection. The direction x_2 is parallel to the second plane of incidence, while the direction y_2 is perpendicular to this plane. z_2 coincides with the beam direction between mirrors M1 and M2. To carry out this transformation the $x_1'y_1'z_1'$ system is rotated about the z_1' axis by the angles between the first two planes of

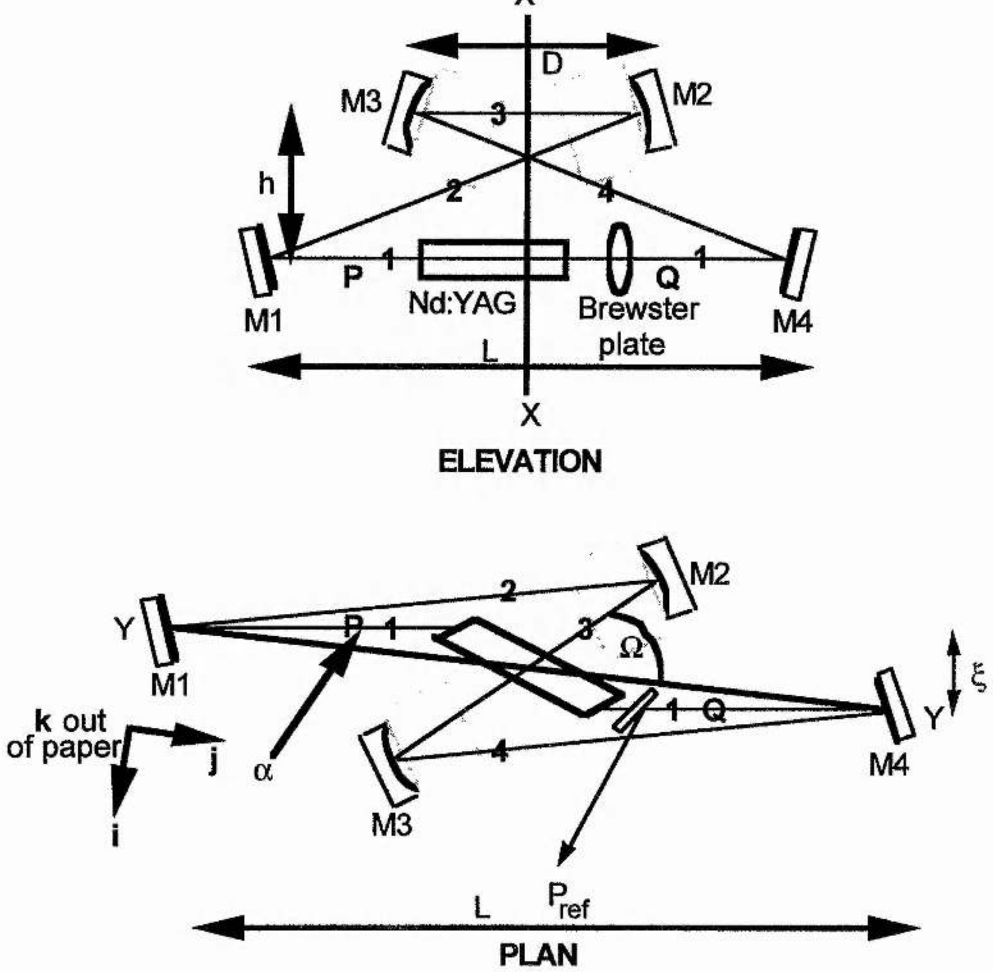

Figure 4.20. Elevation and plan views of the non-planar ring resonator.

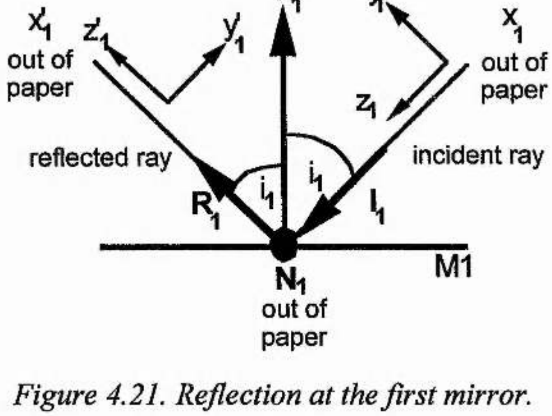

Figure 4.21. Reflection at the first mirror.

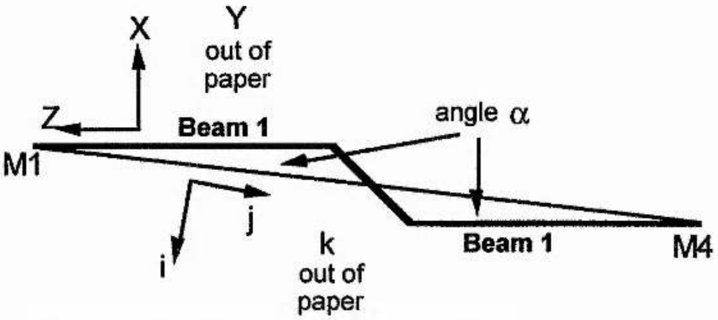

Figure 4.22. Relation between XYZ and ijk systems.

incidence. This process of reflection plus coordinate tranformation between consecutive planes of incidence is carried out for all four reflections. Finally the components have to be transformed from the frame $x_4'y_4'z_4'$ to $x_1y_1z_1$ so that the initial and final polarisation states can be compared. The scalar product of the initial and final unit E field vectors gives the amount of polarisation rotation produced by the ring θ_c.

Given the complexity of this method for this particular ring, a simple check on the various transformations was built into the program. If *C(a,b)* is the transformation between planes of incidence *a* and *b* (*i.e.* to transform between frames $x_a'y_a'z_a'$ and $x_by_bz_b$) and *R(a)* is the transformation for reflection at mirror *a* (*i.e.* to transform between frames $x_ay_az_a$ and $x_a'y_a'z_a'$) then the matrix *C(4,1)R(4)C(3,4)R(3)C(2,3)R(2)C(1,2)R(1)* should be equal to the identity matrix, and this was found to be the case (see lines 190 - 192 in the program in Appendix 1).

The form of a transformation matrix *C(a,b)* is

$$\begin{pmatrix} \cos\xi & \pm\sin\xi & 0 \\ \mp\sin\xi & \cos\xi & 0 \\ 0 & 0 & 1 \end{pmatrix},$$

i.e. a rotation about the z_a' axis where ξ is the angle between planes of incidence *a* and *b*, while that of a reflection *R(a) is*

$$\begin{pmatrix} 1 & 0 & 0 \\ 0 & \cos(\pi - 2i_a) & \pm\sin(\pi - 2i_a) \\ 0 & \mp\sin(\pi - 2i_a) & \cos(\pi - 2i_a) \end{pmatrix},$$

i.e. a rotation about the x_a axis where i_a is the angle of incidence for the *a*th reflection. The choice of ± depends on the particular sense of coordinate-frame rotation.

As the non-planar angle Ω is reduced, two critical points are reached where the form of some of the matrices in the program need to be changed. The first is when beams 1 and 2 (and beams 3 and 4) lie in a vertical plane; this occurs for $\Omega \approx 13^\circ$. The second, and more interesting, point is when the angle bewteen the first two (and last two) planes of incidence is 180°. This happens when $\Omega = \alpha$, *i.e.* when beams 1 and 3 are parallel. At this point the net rotation produced by the ring is zero; further reduction of the non-planar angle Ω causes polarisation rotation in the opposite sense. Thus although the ring is never exactly planar (due to the displacement of beam 1 by the Nd:YAG slab) there is nevertheless a point of zero net rotation. To cover the three regimes, two others programs were written, both very similar to that given in Appendix 1, but with the forms of some of the matrices slightly modified. The results of the calculation for the two rings under consideration are shown in Figure 4.23.

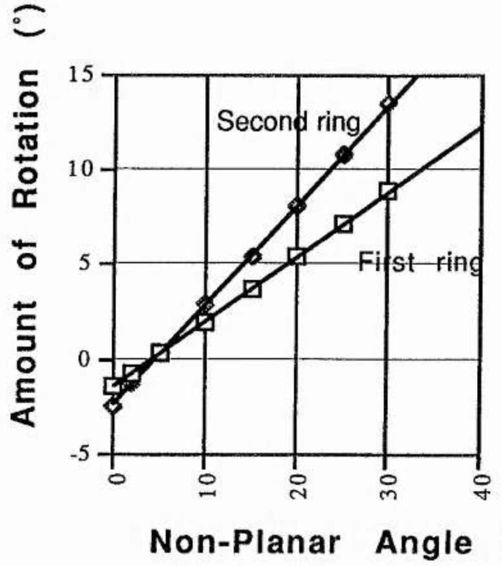

Figure 4.23. Polarisation rotation versus non-planar angle.

4.6.3.2.Vector Method

Although the beam-based method is easily applied to simple non-planar geometries, it is clearly unwieldy for the four-mirror system here. A much simpler vector method for the calculation of polarisation rotation was therefore developed. In this method, the polarisation vector incident on a given mirror is resolved into two orthogonal components in the plane containing the mirror normal **n** and the incident polarisation (electric field) vector **p**, as shown in Figure 4.24. One component is parallel to the mirror normal **n**, and the other is in the direction (**p**x**n**)x**n**. This latter component is reversed in sign upon reflection while the former remains unchanged. The input and output polarisation vectors (***p*** and ***p'*** respectively) for a reflection are thus

$$\mathbf{p} = (\hat{\mathbf{p}} \bullet \hat{\mathbf{n}})\hat{\mathbf{n}} + \left\{ \hat{\mathbf{p}} \bullet \frac{(\hat{\mathbf{p}} \times \hat{\mathbf{n}}) \times \hat{\mathbf{n}}}{|(\hat{\mathbf{p}} \times \hat{\mathbf{n}}) \times \hat{\mathbf{n}}|} \right\} \frac{(\hat{\mathbf{p}} \times \hat{\mathbf{n}}) \times \hat{\mathbf{n}}}{|(\hat{\mathbf{p}} \times \hat{\mathbf{n}}) \times \hat{\mathbf{n}}|},$$

$$\mathbf{p}' = (\hat{\mathbf{p}} \bullet \hat{\mathbf{n}})\hat{\mathbf{n}} - \left\{ \hat{\mathbf{p}} \bullet \frac{(\hat{\mathbf{p}} \times \hat{\mathbf{n}}) \times \hat{\mathbf{n}}}{|(\hat{\mathbf{p}} \times \hat{\mathbf{n}}) \times \hat{\mathbf{n}}|} \right\} \frac{(\hat{\mathbf{p}} \times \hat{\mathbf{n}}) \times \hat{\mathbf{n}}}{|(\hat{\mathbf{p}} \times \hat{\mathbf{n}}) \times \hat{\mathbf{n}}|}.$$

This procedure is applied to the four mirrors in turn, the output polarisation vector from one reflection forming the input polarisation vector for the next. The entire calculation is performed with respect to a single (laboratory) coordinate frame. As in the previous method the amount of polarisation rotation is obtained from the scalar product of the initial and final polarisation unit vectors. The program for this method is given in Appendix 2, and produced exactly the same results as the beam-based method, although it is clearly much shorter.

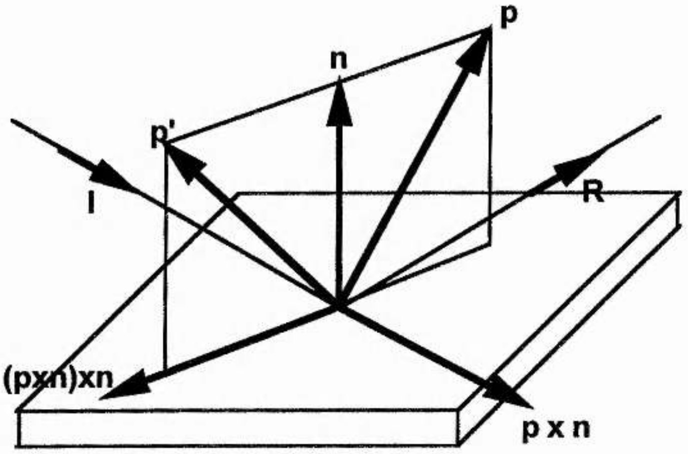

Figure 4.24. Vector method for calculating polarisation rotation.

4.6.4 Polarisation Eigenstates of a Non-Planar Ring

The analysis of the polarisation eigenstates of a non-planar ring can be carried out using the simple Jones matrix formalism. The electric field vector **E** at point P in Figure 4.20 can be referred to axes *xy* with *y* as the vertical direction and *x* horizontal, as shown in Figure 4.25. Suppose it makes some angle α with the *x* axis. After one trip round the ring to the point Q, the vector is rotated by the characteristic angle θ_c so that the angle with the *x* axis is now $\alpha+\theta_c$. If there is no attenuation of the field on the path M1-M2-M3-M4 the field vector at Q will have the same magnitude as that at P: $|\mathbf{E}'| = |\mathbf{E}| = E$.

In vector-matrix form

$$\mathbf{E}' = \mathbf{R}\mathbf{E}$$

where

$$\mathbf{E} = \begin{pmatrix} E\sin\alpha \\ E\cos\alpha \end{pmatrix}, \quad \mathbf{E}' = \begin{pmatrix} E\sin(\alpha+\theta_c) \\ E\cos(\alpha+\theta_c) \end{pmatrix},$$

and the rotation matrix

$$\mathbf{R} = \begin{pmatrix} \cos\theta_c & \sin\theta_c \\ -\sin\theta_c & \cos\theta_c \end{pmatrix}.$$

If one of the mirrors causes loss (*e.g.* an output coupler) the magnitude of the field is reduced ($|\mathbf{E}'| < |\mathbf{E}|$), although the amount of rotation is unaffected unless the components

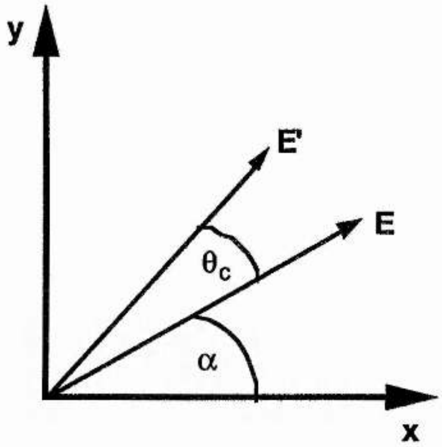

Figure 4.25. Polarisation rotation by angle θ_c.

parallel and perpendicular to the plane of incidence are attenuated by different amounts. This only occurs when the angle of incidence is quite large (>≈ 10°).

The partial polarisation of the Brewster surfaces can be introduced by the matrix

$$\mathbf{T} = \begin{pmatrix} t & 0 \\ 0 & 1 \end{pmatrix}$$

where t is the electric field amplitude transmission, which can be obtained using the Fresnel equations. For example, for the Nd:YAG slab only, t = 0.7128; if a glass Brewster plate is also introduced next to the slab (between P and Q), t = 0.6076. The experimental part of the investigation required measurement of the power reflected from the Brewster surface of the Nd:YAG slab. However, because this was obscured by the cooling block for the slab, a glass Brewster plate was added into the cavity. The round-trip Jones matrix for the ring starting and finishing at Q and following the path M1-M2-M3-M4 is therefore

$$\mathbf{M} = \mathbf{RT} = \begin{pmatrix} t\cos\theta_c & \sin\theta_c \\ -t\sin\theta_c & \cos\theta_c \end{pmatrix}. \tag{4.8}$$

where in the present case $t = 0.6076$. For general t the eigenvalues are

$$\lambda_{1,2} = \frac{(1+t)\cos\theta_c \pm \sqrt{(1+t)^2\cos^2\theta_c - 4t}}{2}. \tag{4.9}$$

The intensity transmissions for the two eigenstates are

$$T_{1,2} = \left|\lambda_{1,2}\right|^2. \tag{4.10}$$

There is clearly an upper limit on θ_c if linearly polarised eigenstates and comcomitant real eigenvalues are to be preserved. The critical characteristic angle above which the states are elliptically polarised is given by the discriminant in (4.9):

$$\theta_{c,critical} = \cos^{-1}\left\{\sqrt{\frac{4t}{(1+t)^2}}\right\}. \tag{4.11}$$

The form of this function is shown in Figure 4.26. For the regime where the two eigenstates are linearly polarised ($\theta < \theta_c$) the angles of inclination of the electric field vectors to the x axis are given by

$$\psi_{1,2} = \tan^{-1}\left(\frac{E_{1,2.y}}{E_{1,2.x}}\right) = \tan^{-1}\left(\frac{\sin\theta_c}{\lambda_{1,2} - t\cos\theta_c}\right). \tag{4.12}$$

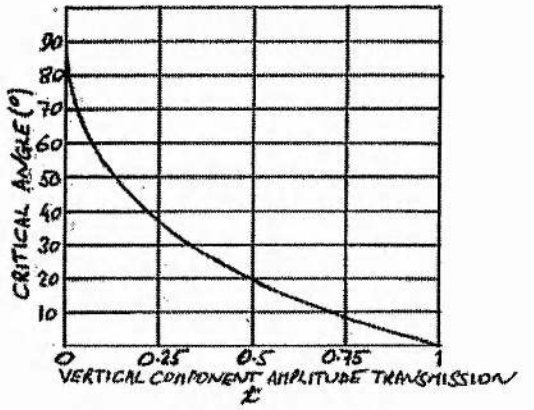

Figure 4.26. Variation of the critical (bifurcation) angle with t.

Graphs of the inclination angle of the low-loss state as a function of non-planar angle Ω for the two rings are shown in Figure 4.27. The intensity transmission and angle of inclination for pairs of eigenstates under different t values are shown in Figures 4.28 and 4.29 respectively. The points of bifurcation mark the onset of elliptically polarised states. The upper (low loss) branches of the intensity plots correspond to the lower (low

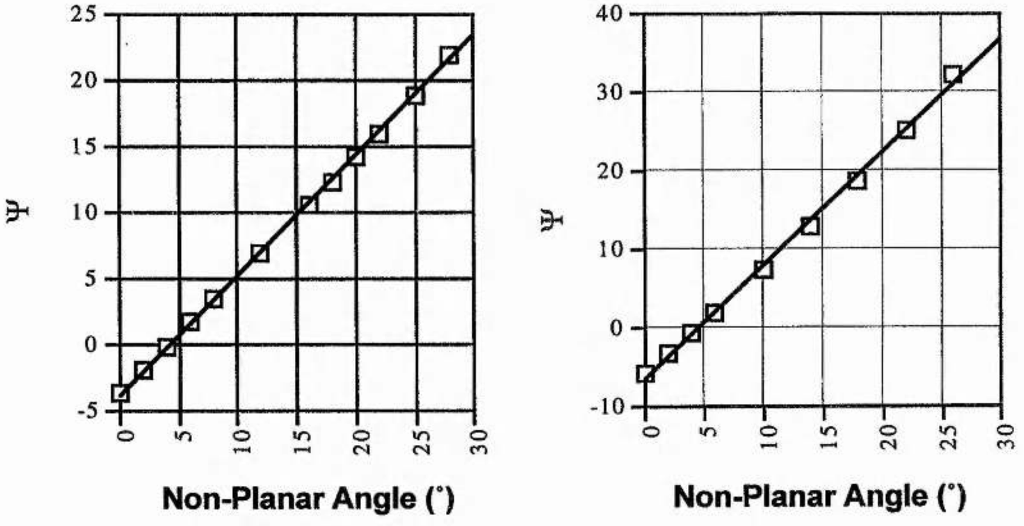

Figure 4.27. Inclination angle ψ (in degrees) of the low loss linearly polarised eigenstates for the first ring (left) and second ring (right) as a function of non-planar angle Ω

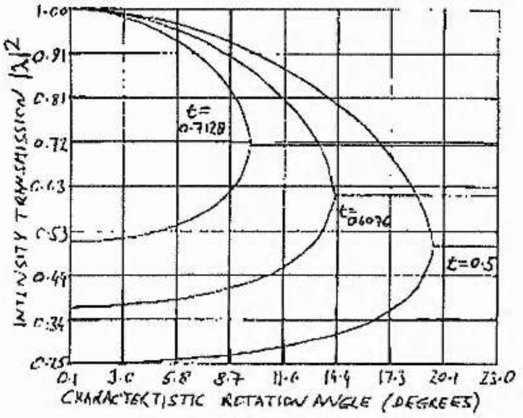

Figure 4.28. Round-trip intensity transmission of the eigenstates.

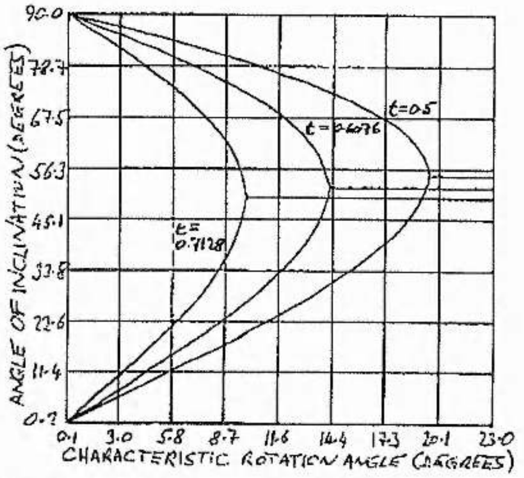

Figure 4.29. Inclination of the linear states.

angle) branches of the inclination plots. In practice, only the low-loss (low angle) state was observed to lase; the other was always below threshold.

Two special cases are of interest for completeness. In the case $t = 0$, the two eigenvalues are $\cos\theta$ and zero, and the critical rotation angle is 90°. Thus there is only one possible state with intensity transmission $\cos^2\theta$. The angle of inclination of this state to the horizontal axis is

$$\psi = \theta.$$

In the case $t = 1$, *i.e.* no attenuation at all, the two eigenvalues are $e^{\pm i\theta}$ so that both states have an intensity transmission of unity. Using (4.12), we find

$$\frac{E_y}{E_x} = e^{\pm i\pi/2},$$

indicating that the two polarisation eigenstates are right and left-handed circularly polarised.

Some examination of the general elliptical states is also of interest. If the characteristic rotation θ_c is above the critical value, (4.9) can be re-written

$$\lambda_{1,2} = \frac{(1+t)\cos\theta_c \pm i\sqrt{4t-(1+t)^2\cos^2\theta_c}}{2}, \tag{4.13}$$

which reduces to

$$\lambda_{1,2} = \sqrt{t}e^{\pm i\beta}, \quad \beta = \tan^{-1}\sqrt{\frac{4t}{(1+t)^2\cos^2\theta} - 1}. \tag{4.14}$$

Interestingly, the intensity transmission is t and not t^2, and is independent of the amount of rotation produced by the ring. The extent of ellipticity of the states can also be found. Analysis yields

$$\frac{E_y}{E_x} = \frac{1}{\sqrt{t}}e^{\mp i\chi}, \quad \chi = \tan^{-1}\sqrt{\frac{4t}{(1-t)^2\cos^2\theta} - \frac{(1+t)^2}{(1-t)^2}}. \tag{4.15}$$

(4.14) and (4.15) explain the constancy of Figures 4.26 and 4.27 in the elliptical region (after the bifurcations). (4.15) confirms that at the critical angle (4.11) the states are linearly polarised ($\chi = 0$) while for $\theta = 90^\circ$, $\chi = 90^\circ$.

4.6.5 Experimental

The theory described above was tested for the two rings over a range of non-planar angles Ω by measuring the total power output (both directions) from mirror M1 (P_{out}) and the power reflected from one side of the Brewster plate (P_{ref}). For this, M1 was a 2% output coupler. Assuming both directions have the same circulating power

$$\frac{P_{ref}}{P_{out}} = \frac{(0.3843)^2 \sin^2 \psi}{0.04}, \tag{4.16}$$

where ψ is the inclination of the polarisation state to the horizontal. Calculation of this function and measurements are shown for the two rings in Figure 4.30. An error of ± 2° in the non-planar angle for the experimental points has been introduced; this was the typical deviation of the non-planar angle during lasing from that intended when the laser mirrors were arranged. The agreement between the theory and the measurements is close up to a non-planar angle of ≈ 20°. "Large" values of Ω (>≈ 20°) result in angles of incidence on the four mirrors >≈ 10°. Under these conditions, the ratio P_{ref} / P_{out} is less than expected. A possible explanation for this is for large angles of incidence, the *p* and *s* reflection coefficients for the mirrors are not equal. For high reflectors comprising a quarter-wave dielectric stack, the *p* coefficient declines more rapidly with increasing angle of incidence than the *s* coefficient. This has the effect of reducing the amount of rotation, and hence also the inclination of the polarisation to the horizontal plane (see

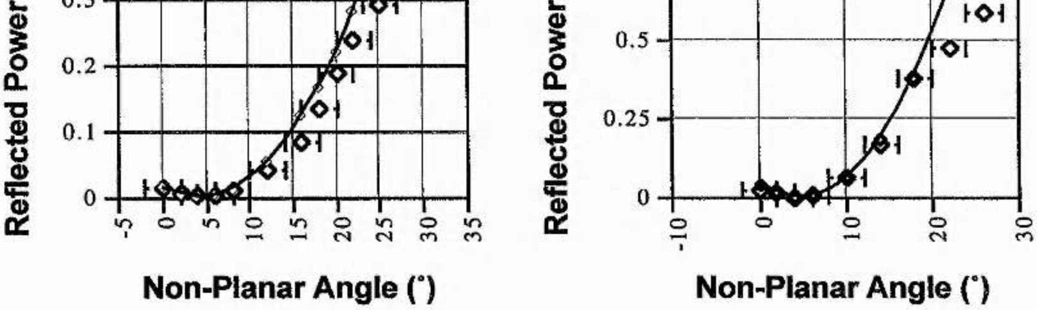

Figure 4.30. Reflected power over output power for the first ring (left) and second ring (right).

Figure 4.27). The power reflected from the Brewster plate would therefore be expected to diminish. Modification of the two programs was made to test this with the result that the calculated rotation was indeed reduced.

Having established the validity of the model and computer programs, the value of θ_c required to match the 5° rotation of the Faraday rotator was estimated as ≈ 18° for the first ring and ≈ 14° for the second ring. By setting up the first ring accordingly, and inserting the Faraday rotator, a bi-directional output power of 1 W was converted to a unidirectional output power of 940 mW, indicating a good match between the rotation effects of the non-planar ring and the Faraday rotator.

4.7. Concluding Remarks

This laser had a number of distinct advantages. The modified side-pumping scheme allowed higher efficiency than in conventional side-pumped-rod lasers. Both the laser head and the resonator were quite simple to align. The use of a ring resonator allowed highly reliable 1 μm and 0.5 μm operation to be achieved at all pumping levels. The polarisation scheme in the frequency-doubled laser was uncomplicated due to the type I non-critical phase-matching in the LBO crystal. Overall the system was a reliable 1 W single-frequency green source suitable for pumping doubly resonsant CW OPOs and low threshold $Ti:Al_2O_3$ and Cr:LiSAF lasers.

On the negative side, the modest efficiency and limited 0.5 μm power were mainly a result of certain compromises in the overall design. For example, a side-pumped amplifier design has the benefit of simplicity but cannot hope to approach the efficiency of end-pumped lasers. Lack of coupling optics may increase the maximum incident pump power but the high divergence of the diode-bars' output drastically reduces pump-signal overlap. A unidirectional ring resonator will give reliable single-frequency operation, but the gain per round trip is half that of a standing-wave cavity and additional loss is introduced by the optical diode. Low round-trip gain over linear loss is the Achilles heel of intracavity doubling, as seen in Chapter 3. Furthermore, although LBO is attractive as an intracavity doubler because of its type I NCPM scheme, its nonlinearity is quite modest, generally resulting in under-coupling. Finally, the large internal angle of the ring added to the under-coupling of the laser when intracavity doubling, by preventing the achievement of Boyd and Kleinman focusing. However, this is more of an engineering question; small ovens are now available, so that this problem can now be surmounted.

The concept of non-planar ring resoators was explored, theory and experiment being brought together. There are important conclusions for the use of this method in practical systems to obtain unidirectional single-frequency lasing. First, when such an arrangement is operating, the polarisation state makes some finite angle with the horizontal plane so that some loss is introduced to the lasing state. This can be kept to a minimum by using only slightly non-planar rings. Secondly, having introduced some extra loss, it is desirable to remove more loss than is introduced, especially if intracavity-doubling is desired. In the laser here the nonplanar ring allowed the removal of the half-wave plate, but the Faraday rotator was kept in to provide the non-reciprocal rotation. Unfortunately, it was the rotator and not the waveplate that was responsible for most of the loss of the optical diode. To obtain low-loss operation using this technique, the Faraday effect in Nd:YAG needs to be exploited so that no intracavity elements are required, as in, for example, [4.6] or any of the monolithic non-planar ring lasers [4.7 - 10].

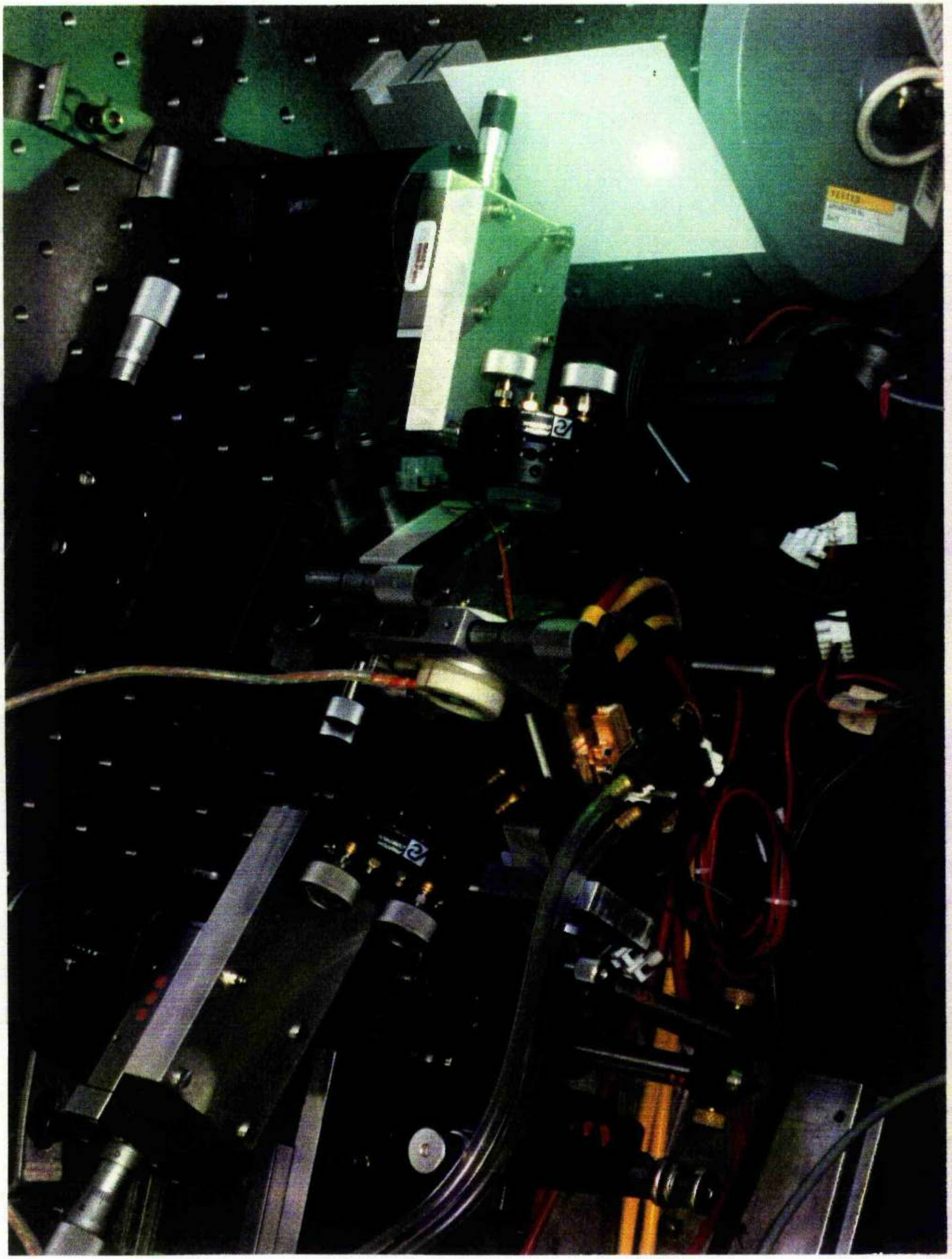

References

[4.1] A. J. Henderson, J. Hong, C. Yelland, J. Zhang, W. Sibbett, M. H. Dunn: "All-solid-state continuous wave optical parametric oscillators in KTP and LBO": *Conf. on Lasers & Electrooptics* paper CTuK18 p 93 **8** 1994 OSA Technical Digest Series

[4.2] W.A. Clarkson, A. B. Neilson, D. C. Hanna: "Unidirectional operation of a ring laser via the acoustooptic effect": *IEEE J. Quant. Elec.* **32** 311 (1996)

[4.3] R. Roy, P. A. Schultz, A. Walther: "Acoustooptic modulator as an electronically selectable unidirectional device in a ring laser": *Opt. Lett.* **12** 248 (1987)

[4.4] Y. D. Golayaev, A. A. Zadernovskii, A. L. Livintsev: "Solid-state ring laser with an acoutsooptic phase non-reciprocity of the opposite waves": *Soviet J. Quant. Elec.* **57** 583 (1987)

[4.5] W. A. Clarkson, D. C. Hanna: "Acoustooptically induced unidirectional single-mode operation of a Q-switched miniature Nd:YAG ring laser": *Opt. Comm.* **81** 375 (1991)

[4.6] G. T. Maker, G. P. A. Malcolm, A. I. Ferguson: "Single-frequency diode-pumped Nd:YAG ring laser with no intracavity elements": *Opt. Lett.* **18** 1813 (1993)

[4.7] T. J. Kane, R. L. Byer: "Monolithic, unidirectional single-mode Nd:YAG ring laser": *Opt. Lett.* **10** 65 (1985)

[4.8] T. J. Kane, A. C. Nilsson, R. L. Byer: "Frequency stability and offset locking of a laser-diode-pumped Nd:YAG monolithic non-planar ring oscillator": *Opt. Lett.* **12** 175 (1987)

[4.9] A. C. Nilsson, E. K. Gustafson, R. L. Byer: "Eigenpolarisation theory of monolithic nonplanar ring oscillators": *IEEE J. Quant. Elec.* **25** 767 (1989)

[4.10] E. A. P. Cheng, T. J. Kane: "High-power single-mode diode-pumped Nd:YAG laser using a monolithic nonplanar ring oscillator": *Opt. Lett.* **16** 478 (1991)

[4.11] I. I. Savel'ev, A. M. Khromykh: "Longitudinal modes of a cavity ring resonator": *Soviet J. Quant. Elec.* **6** 821 (1976)

[4.12] F. Biraben: "Efficacite des systemes unidirectionnels utilisables dans les lasers en anneau": *Opt. Comm.* **29** 353 (1979)

[4.13] Y. D. Golyaev, K. N. Evtyukhov, L. N. Kaptsov, S. P. Smyshlyaev: "Spatial and polarisation characteristics of radiation from a cw neodymium-doped garnet laser with a non-planar ring resonator": *Soviet J. Quant. Elec.* **11** 1421 (1981)

[4.14] H. R. Bilger, G. E. Stedman, P. V. Wells:"Geometrical dependence of polarisation in near-planar ring lasers": *Opt. Comm.* **80** 133 (1990)

[4.15] C. Yelland, J. Hong, M. J. Padgett, M. H. Dunn, W. Sibbett: "A vector approach to the geometrical dependence of polarisation rotation in a non-planar cw Nd:YAG ring laser": *Opt. Comm.* **109** 451 (1994)

Chapter 5

INTERNALLY-FOLDED END-PUMPED Nd:YLF RING LASER

5.1 Introduction

In this chapter the design, operation and performance of an end-pumped Nd:YLF ring laser is described, in which the laser head consisted of a truncated prism of the active material. The design aim was to utilise end-pumping to allow greater efficiency and higher maximum output power for both the fundamental and second harmonic, whilst maintaining the ring resonator concept which allows single-frequency operation to be easily achieved when an optical diode is used in the cavity. The design of the gain element was such that standing wave cavities were also possible if required. Intracavity frequency doubling was carried out using both LBO and KTP. The maximum single-frequency 1047 nm output power obtained in a TEM_{00} beam was 2.92 W; the maximum single-frequency 523.5 nm output was 1.14 W (using LBO), with 1 W being achievable on a regular basis. The pumping powers for these results were 12 W and 15.8 W respectively, representing optical-to-optical efficiencies of 24% and 7% respectively.

This laser system was used as a pump source for CW optical parametric oscillators based on LBO and KTP, but the main application was in the pumping of the first all-solid-state Ti:sapphire laser [5.1, 2].

5.2 Pumping Arrangement

5.2.1 Diode-Bars

Two *SDL 3460S* 20 W AlGaAs diode bars were used as the pump devices. A summary of the bars' characteristics is given in Table 5.1. As in the side-pumped laser, two separate current supplies were used to drive the bars, giving greater flexibility in the delivery of the pump power. Mounting and temperature regulation of these bars was the same as in the laser described in Chapter 4. At 25°C the bars (serial numbers GC 098 and GB 973) had specified wavelengths of 801 and 802 nm respectively so they had to be operated in the temperature range 15 - 24 °C to obtain spectral coincidence of the emission with the main absorption feature of Nd:YLF at 797 nm. Temperature

Serial Number	GC 098	GB 973
Differential Quantum Efficiency	59%	59%
Threshold Current	11.2 A	12.0 A
Slope Efficiency	0.9091 W/A	0.9091 W/A
Current at 20 W	33.2 A	34.0 A
Specified centre λ at 25°C	801 nm	802 nm
Specified Spectral FWHM	1.6 nm	1.6 nm
Power Output Characteristic	P=0.9091(I-11.2)	P=0.9091(I-12.0)

Table 5.1. Diode-bar characteristics.

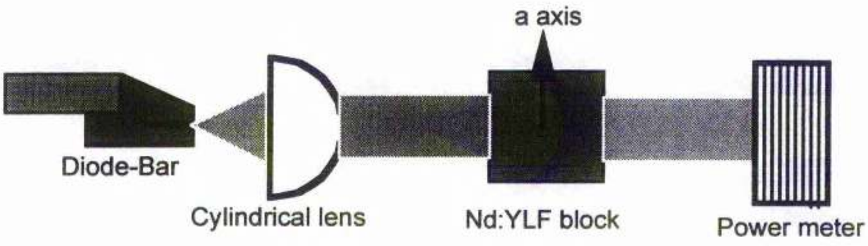

Figure 5.1. Arrangement for optimising pump-light absorption.

tuning of the bars' emission wavelengths to this absorption peak was carried out for a range of drive currents by minimising the power transmission through a suitably cut Nd:YLF sample, as shown in Figure 5.1. At a given current, the set-point temperature of the copper mounting block was adjusted via the temperature controller until the power received at the power meter was minimised. Figure 5.2 shows the resulting optimum current-temperature combinations for each bar. The slopes of these lines were

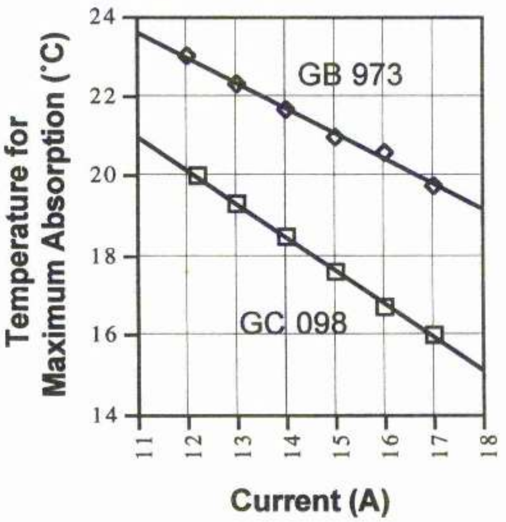

Figure 5.2. Optimum set-point temperature versus drive current for the diode-bars.

-0.84 °C/A for bar GC 098 and -0.62 °C/A for GB 073.

5.2.2 Coupling Optics

Two identical two-lens arrangements were used to couple the pump light from each diode-bar into the gain medium. The coupling arrangement is shown in Figure 5.3. Both lenses were AR coated to improve their transmission. A summary of the lens characteristics is given in Table 5.2. The main aim in the design was to bring both planes into focus at the same horizontal distance from the coupling system whilst keeping the arrangement relatively insensitive to any vertical misalignment with the diode-bar. The lenses were mounted together and could be moved independently of the diode-bar.

In the horizontal plane (parallel to the emitting junction of the bar) the emission diverges with a half-angle of ≈ 5°. The principal plane of the condenser lens was located 10 mm from the facet of the diode-bar, causing the horizontal plane of the beam to be brought to a focus 8.5 mm from this plane. The horizontal diameter of the focal spot in free space was 1.65 mm. The half-angle divergence to the focus in this plane was ≈ 30°.

In the vertical plane (perpendicular to the plane of the bar) the diode emission was first captured by a cylindrical lens of diameter 5 mm placed 3 mm from the diode-bar facet so that the numerical aperture of this lens was fully utilised. After collimation and passage through the aspheric lens, a waist was produced 8.5 mm from the principal plane of the aspheric. Assuming negligible losses in the system, the divergence and

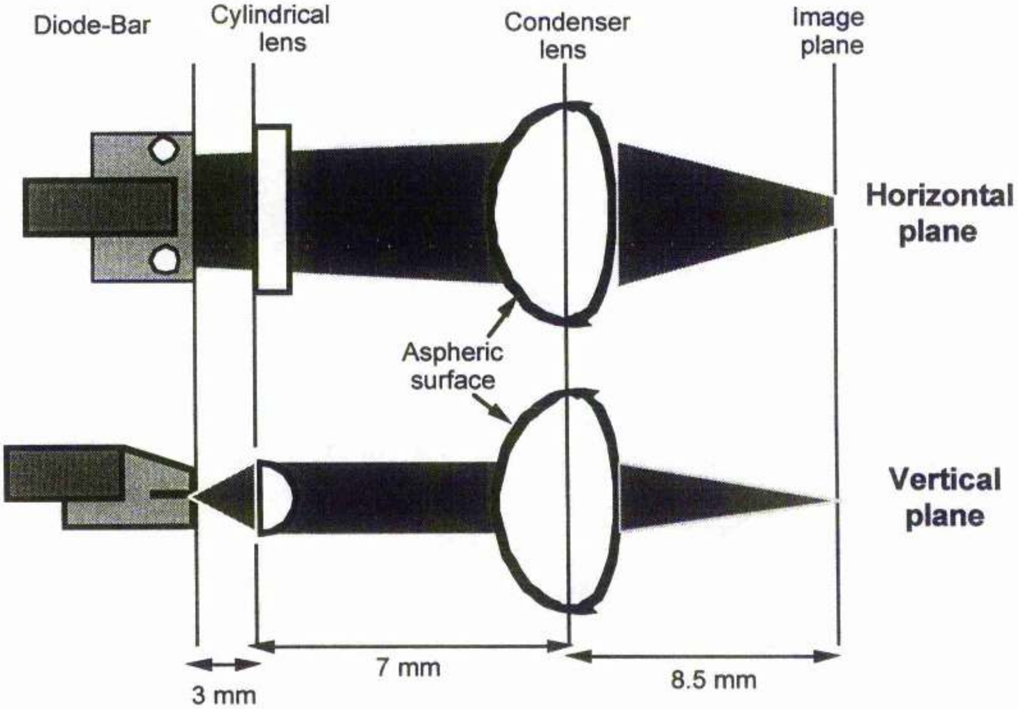

Figure 5.3. Coupling optics for the diode-bars.

Lens	Cylindrical	Aspheric
Model	Spindler & Hoyer	Melles Griot 01LAG000
Material	BK7	Optical Crown
Focal length f	5 mm	8.5 mm
Diameter	5 mm (length 12 mm)	12 mm
f-number	1	0.71
Front surface	Plane	Aspheric
Rear surface	Semi-circular	Spherical

Table 5.2. Summary of coupling lenses' characteristics.

vertical spot diameter at the focus were estimated to be 16° and 2.4 μm respectively.

Aspheric lenses are ideal for use in coupling the emission from diode-bars into laser crystals because they introduce no spherical aberration. This allows more energy to be concentrated into a small area, improving the pump-mode overlap and overall efficiency of a laser. Aspheric lenses also have much shorter focal lengths than are possible with spherical glass lenses of the same diameter. This allows compact coupling systems to be designed; in the present case, the distance from the diode-bar to the pump input point was 18.5 mm.

The power transmitted through the coupling optics was measured as a function of drive current, and for both bars was found to be higher than that specified by the manufacturer for currents up to ≈ 16 A for GC 098 and ≈ 20 A for GB 973. The results are shown in Figures 5.4.

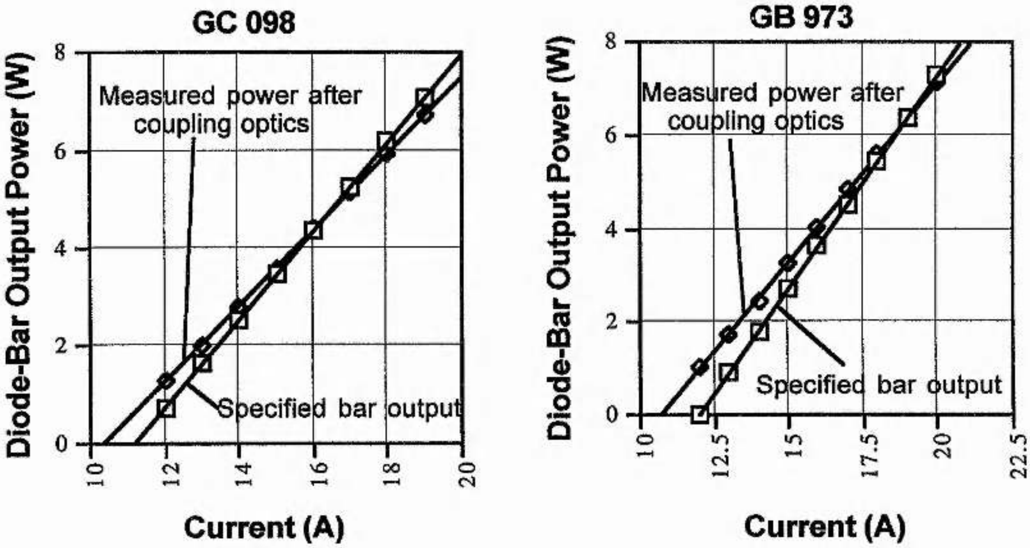

Figure 5.4. Pump power available after coupling optics.

5.3 Amplifier

The gain element for the laser consisted of a truncated prism of 1%-doped Nd:YLF as shown in Figure 5.5. The longest edge measured 18 mm; the prism was 6 mm wide and 2 mm high. The design was such that on entering the slab at the Brewster angle via the polished front surface, the laser mode was reflected by the sloping faces, exiting at the complementary Brewster angle, again via the front surface. Mirror coatings were applied directly to the sides of the prism to allow close positioning of the diode-bars and their coupling optics. The section of the laser mode between the two sloping faces of the prism was end-pumped from both sides. The prism was cut so that the *c* axis was perpendicular to this part of the beam, thereby giving polarised operation in the plane of the slab on the high-gain 1047 nm π transition. The output from the diode-bars was polarised in the planes of their junction so that both pump and laser modes were polarised along the *c* axis.

The birefringence of the YLF crystal had to be taken into account in designing the prism. If the laser mode enters the prism at the Brewster angle α, the complementary Brewster angle α' is related to this angle by

$$\frac{1}{\tan^2\alpha}=\frac{\cos^2\alpha'}{n_a^{\,2}}+\frac{\sin^2\alpha'}{n_c^{\,2}} \tag{5.1}$$

since α' is also the angle that the mode makes with the optic axis on entering the YLF prism. The Brewster angle α is given by the solution of

$$\frac{1}{\tan^2\alpha}=\frac{\sin^2\alpha}{n_a^{\,2}}+\frac{\cos^2\alpha}{n_c^{\,2}}, \tag{5.2}$$

since $\alpha + \alpha' = 90^\circ$. Taking $n_a = n_o = 1.45$ and $n_c = n_e = 1.47$ it is found that $\alpha = 55.52^\circ$

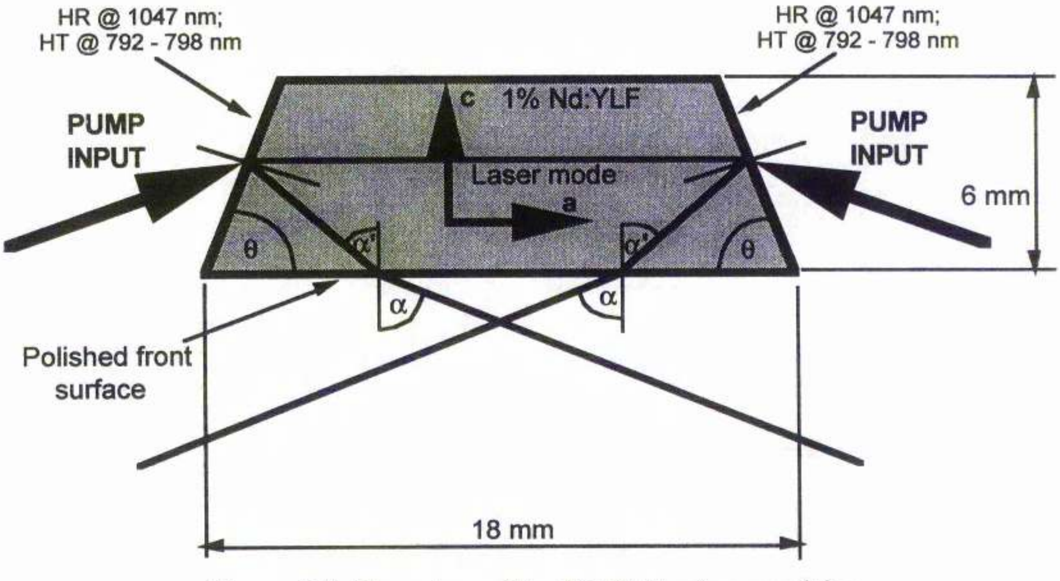

Figure 5.5. Plan view of the Nd:YLF prism amplifier.

and $\alpha' = 34.48^\circ$. The base angle of the prism is $45^\circ + \alpha'/2 = 62.24^\circ$ and the angle of incidence on the sloping faces is $\alpha/2 = 27.76^\circ$.

The Nd:YLF prism was contacted to a water-cooled brass mount using 125 μm thick indium foil allowing heat extraction from the bottom of the prism. Additional cooling from the top surface was also carried out for some of the time by using a brass cap in thermal contact with the base, although this was observed to have no beneficial effect; thermal damage to the prism was invariably caused when pumping > 8 W at a single point.

Nd:YLF was chosen as the gain medium in order to investigate some of its alleged advantages. Its negative $\partial n / \partial t$ acts to lessen thermal lensing at high pump powers, so that cavity stability is maintained over a range of operating levels. Another important feature of YLF is its natural birefringence which far exceeds any pump-induced thermal birefringence. This is useful because the *b* and *c* axes of the crystal are therefore fixed with reference to the vertical front surface of the prism and are independent of the pumping level. On entering the front surface of the prism at the Brewster angle, the laser mode is therefore polarised along a fixed and known axis ensuring that the circulating field remains linearly polarised in the horizontal plane. An equivalent prism of YAG would suffer from thermal birefringence causing some degree of elliptical polarisation in the circulating field, with concomitant loss at the front surface of the prism and reduced conversion efficiency in the doubling crystal (LBO, type I phase-matching.)

The concept of internal folding of the laser mode inside the gain material is an extremely useful one. One fold allows potentially two pump input points. Multiple folds allow systems to be scaled up in power whilst maintaining the efficiency of end-pumped devices. Multiple pump input points also allow thermal problems to be avoided by distributing the heat load amongst the various pump ports. Probably the first such laser to use this concept was that of Scheps and Myers in 1991 [5.3]. The gain element was a simple cuboid of Nd:YAG in which the mode was folded once; pumping was along both of the resulting two axes. Although the logical extremum of this concept is the monolithic non-planar ring oscillator, lasers combining internal folds with external resonators are useful for Q-switching, mode-locking or internal frequency-doubling. The tightly-folded resonator is one example of this type of combination [5.4]; however, "internally-folded lasers" (IFLs) with one or two folds allow greater flexibility in resonator design. The IFL amplifier described above allowed a ring resonator design to be combined with double end-pumping, giving efficient single-frequency operation. A high power version of this amplifier was reported by Alfrey [5.5] who used separate thin mirrors rather than HR coatings applied directly on the gain element in order to avoid bulging of the surfaces under high pump levels. Scheps and co-workers have subsequently exploited the design flexibility of the IFL concept in a number of prismatic diode-pumped Nd lasers [5.6, 7]. As illustrated above for the case of YLF, they also pointed out the care in design needed when using birefringent gain materials such as YVO_4.

5.4 Resonator

The layout of the resonator is shown in Figure 5.6. To build up the system, a standing-wave cavity was first aligned (typically with a 2% output coupler and a 2 m high reflector) with pumping provided at one end only. The distances between the coupling optics and the prism and between the diode-bar and the coupling optics were then adjusted to give maximum output power. In addition, the angle of incidence of the pump light on the prism was adjusted to maximise the output. After repeating this procedure for the other diode-bar and set of coupling optics, the rest of the resonator was aligned using the output from the standing wave laser. A lens-curved mirror combination was used to provide a focus for efficient intracavity doubling.

Two lens-curved mirror combinations were used. In the first case a lens of focal length 50.2 mm and a curved mirror of radius 100 mm were used; in the second case the lens had a focal length of 38.1 mm and the radius of the curved mirror was 85 mm. Both lenses were AR coated to reduce the internal loss of the laser. The lens was mounted in a mirror mount (giving yaw and pitch control), which was itself fixed to an *xyz* translation stage. Adjustment of the lens - curved mirror separation was an

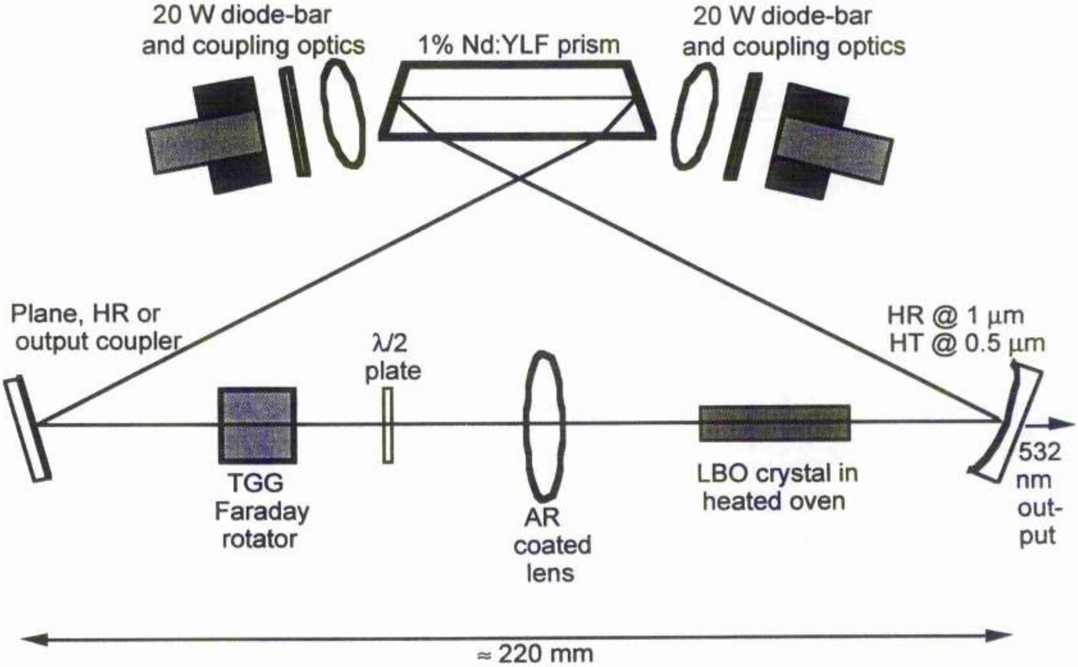

Figure 5.6. Internally-frequency-doubled Nd:YLF single-frequency ring laser.

important means of maximising the output power of the laser in both the visible and infrared. When frequency-doubling, this was an important means of controlling the waist size in the nonlinear crystal.

As in the system described in Chapter 4, unidirectional, single-frequency operation was achieved by inserting a Faraday rotator and a half-wave plate into the cavity. The Brewster-angled entry points to the YLF prism gave the necessary loss-difference for the two directions in the ring. A zero-order wave plate was used to keep the internal loss to a minimum. When the laser was operated at 1047 nm, the half-wave plate was rotated so that the lasing direction was from right to left between the curved mirror and the plane mirror (see Figure 5.6). This allowed a series of plane output couplers to be used in order to assess the performance at 1047 nm. When intracavity doubling (using LBO or KTP), the output coupler was replaced with a plane high reflector and the half-wave plate was suitably rotated to reverse the lasing direction. The output at 523.5 nm then issued from the 100 mm mirror. When using the laser as a green pump source, the visible output was collimated with a 100 mm focal length AR coated lens.

When internally doubling with LBO, the crystal mounting and heating arrangements were the same as that for the laser described in Chapter 4. The temperature of the crystal was stabilised to ± 0.01 °C using a commercial device (Smatex LAB10). The LBO crystal used was again 25 mm in length, with a square cross-section of side 3 mm. Positioning of the oven and crystal was again facilitated by a combination of an *xyz* stage and rotation/tilt platform. Six degrees of freedom were possible allowing the doubling efficiency to be fully maximised. Frequency doubling was also carried out using an AR coated cube of KTP of side 5 mm which was permanently mounted in a glass disc. An electrically heated brass oven was purpose-built to heat the disc in order to allow the total phase shift between the two fundamental beam polarisation components to be adjusted to a multiple of 2π. (Type II phase-matching was used in the KTP.) This reduced loss at the Brewster-angled entry points of the Nd:YLF prism. The temperature controller used for this (Marlow 5010) allowed stabilisation to ± 0.1 °C.

Estimates of the mode radius in the Nd:YLF prism at the sloping faces and of the waist radius at the focus of the resonator were made using the *ABCD*-matrix analysis described in Chapter 4. The results are shown graphically in Figures 5.7, 5.8 and 5.9 which show the mode radii as a function of the lens-curved mirror separation. Figure 5.7 shows the mode size in the YLF prism without the LBO crystal present in the cavity. Figure 5.8 gives the mode size in the YLF when the LBO crystal is inserted at the resonator focus. Figure 5.9 shows the behaviour of the waist radius in the LBO crystal. The two sets of results for the 100 mm radius mirror with the 50.2 mm focal length lens and the 85 mm radius mirror with the 38.1 mm focal length lens are quite

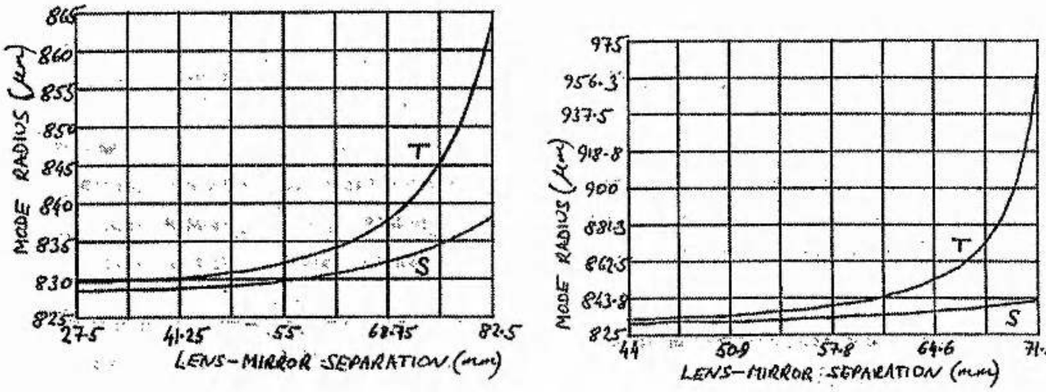

Figure 5.7. Mode radius in the Nd:YLF prism with no LBO crystal in the laser. Left - 100/50 optics; right - 85/38 optics.

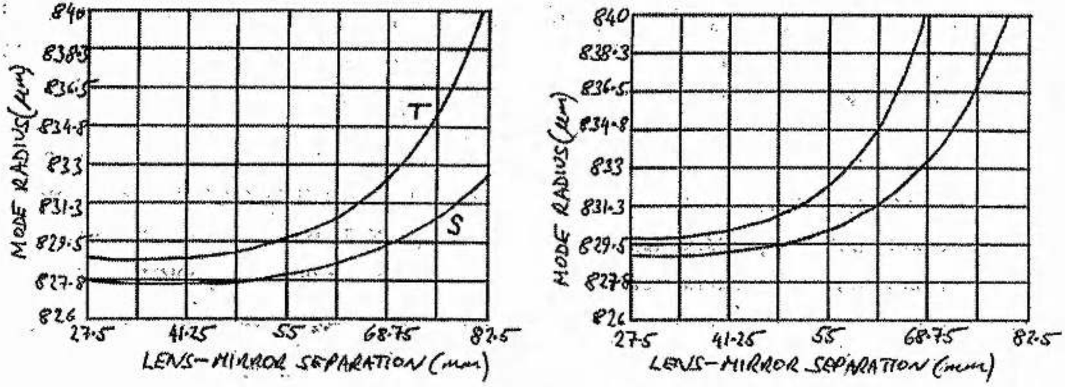

Figure 5.8. Mode radius in the Nd:YLF prism with LBO crystal inserted at the resonator focus. Left - 100/50 optics; right - 85/38 optics.

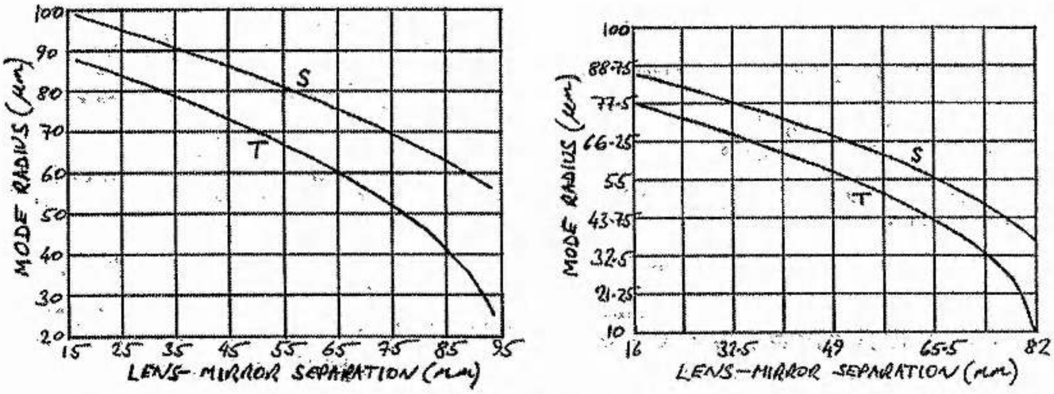

Figure 5.9. Waist radii in the LBO crystal. Left - 100/50 optics; right - 85/38 optics.

similar, with similar mode and waist radii being achieved with the shorter focal length optics for a smaller lens-mirror separation. In the 100/50 case the maximum separation was found to be ≈ 108 mm, compared to ≈ 90 mm for the 85/38 case. Insertion of the 25 mm LBO crystal does not significantly change the mode radius in the YLF prism, although the astigmatism of the mode is slightly increased over the whole stability range. The waist size in the LBO crystal decreases with increasing lens-mirror separation, and this coincides with increasing mode size in the YLF crystal: this is a useful coincidence which is not the case with all resonator designs. Thus nonlinear coupling and pump-mode overlap both increase with increasing lens-mirror separation. The 100/50 system requires a larger lens-mirror separation to achieve small waist radii in the non-linear crystal. As in the ring laser described in Chapter 4, the waist in the nonlinear crystal suffers from appreciable astigmatism. Both lens-curved mirror sets were capable of producing waist radii of 20 μm in the tangential plane and 40 μm in the saggital plane; this is smaller than in the YAG ring laser but still involves a 100% difference between the two planes. Boyd and Kleinman focusing in the LBO crystal could therefore be only approximately attained. 30 μm is the optimum waist size for a 25 mm crystal, corresponding to a confocal parameter of 4.4 mm.

This *ABCD*-matrix analysis was consistent with the actual behaviour of the laser in that the power output was found to be greatest for both 1047 nm and 523.5 nm operation when the lens-mirror separation was set at the large-separation end of the stability range.

5.5 Laser Performance

5.5.1 Operation at 1047 nm

5.5.1.1 Output Power

The laser was operated at 1047 nm using a series of plane output couplers. Two arrangements were analysed: the first using a 100 mm radius curved mirror with a 50.2 mm focal length lens, and the second using an 85 mm mirror with a 38.1 mm lens. Bidirectional and unidirectional output power characteristics for the first laser are shown in Figure 5.10 and 5.11. The highest bi-directional power achieved was 3.43 W, and the highest single-frequency unidirectional power obtained was 2.92 W. Both these results were obtained with a 5% output coupler and a total pump power of 12 W, representing optical-to-optical efficiencies of 29% and 24% respectively. The slope efficiencies were 34% and 29% respectively. The lens-curved mirror separation in both cases was 106 mm.

The second system, employing the shorter focal length optics, gave 2.29 W when operated bidirectionally, and 1.87 W when the optical diode was inserted. The pump power in both cases was 9.3 W, giving efficiencies of 25% and 20% respectively. The output coupling was again 5%. The respective slope efficiencies were 36% and 29%. Figures 5.12 and 5.13 show the slopes obtained with other output couplers. In addition, this laser was operated with the frequency-doubling (LBO) crystal inserted at the resonator focus in order to obtain some estimate of the *linear* loss introduced by the

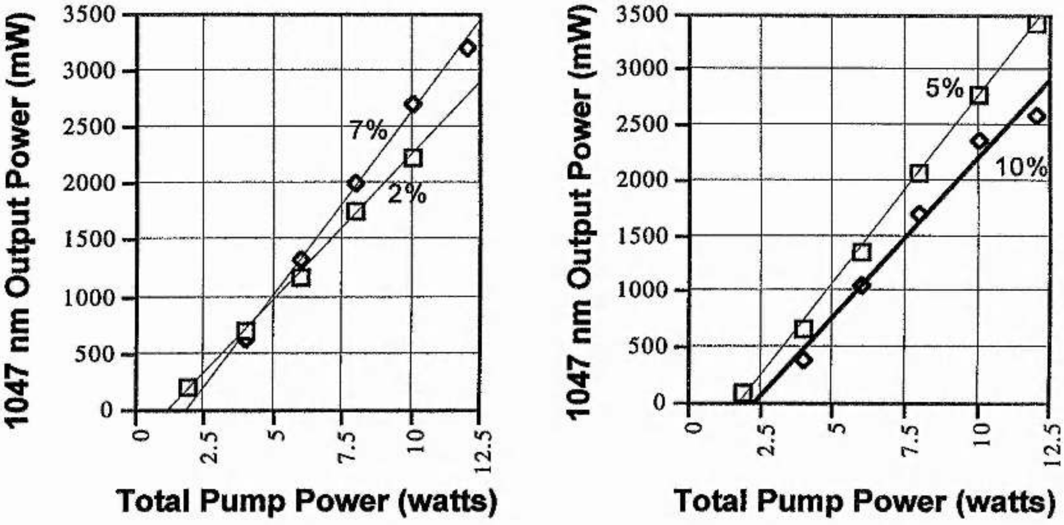

Figure 5.10. Bidirectional output power characteristics for ring laser with 100 mm mirror and 50.2 mm lens.

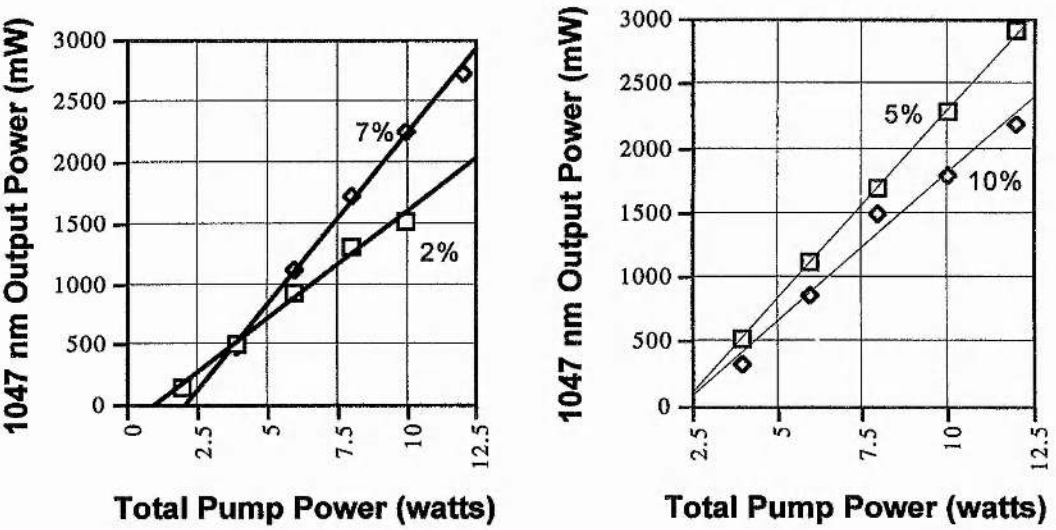

Figure 5.11. Unidirectional output power characteristics for ring laser with 100 mm mirror and 50.2 mm lens.

crystal. Figure 5.14 shows the slopes obtained with this arrangement.

Comparing the slope efficiencies of the various arrangements as in Chapter 4, the internal loss for the first device was estimated to be 1.37% for the bidirectional laser and 4.13% for the unidirectional system. The loss introduced by the optical diode was therefore 2.76%. For the second laser (with shorter focal length optics) the internal loss for the unidirectional laser was estimated as 3.09%; this increased to 3.28% when the (room-temperature) LBO crystal was inserted. The linear loss of the crystal was

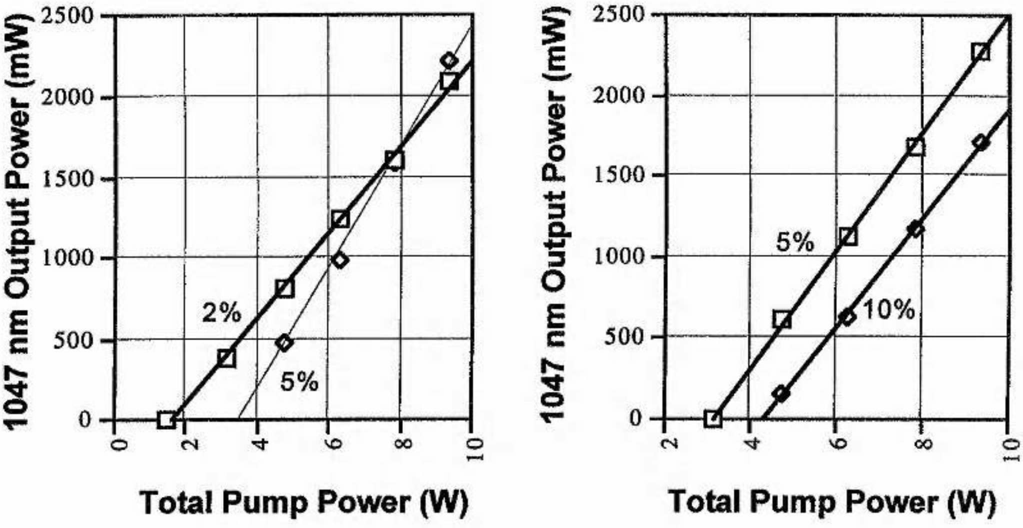

Figure 5.12. Bidirectional output power characteristics for ring laser with 85 mm mirror and 38.1 mm lens.

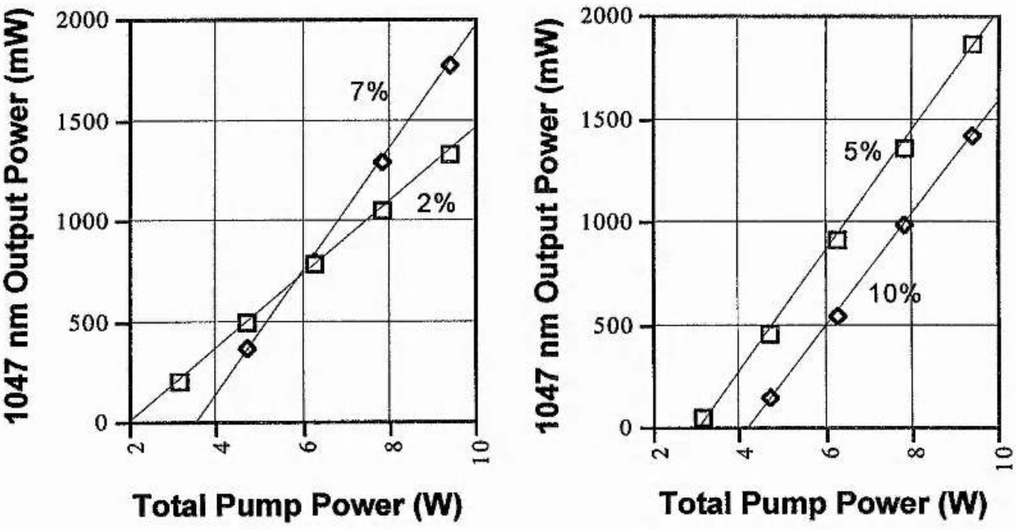

Figure 5.13. Unidirectional output power characteristics for ring laser with 85 mm mirror and 38.1 mm lens.

therefore ≈ 0.2%.

The loss of the rotator is similar to that estimated in Chapter 4, and, as in that laser, was an important limiting factor on the amount of extractable second harmonic power. The extremely low loss of the LBO crystal was encouraging and indicated high quality in both the AR coatings and the bulk material.

An estimate of the unsaturated gain of the lasers was made by plotting output

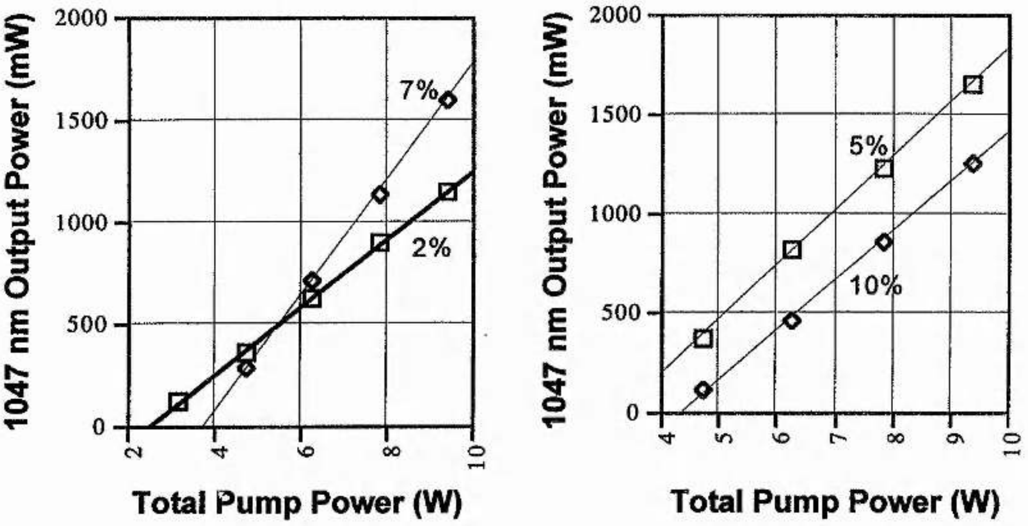

Figure 5.14. Unidirectional output power characteristics for ring laser with 85 mm mirror and 38.1 mm lens, with 25 mm LBO crystal inserted at room temperature.

power against output coupling, as for the system in Chapter 4. The resulting curves for the two unidirectional lasers are shown in Figure 5.15. By estimating the point at which the curves cut the horizontal axis, the unsaturated gain at the highest pump power used (15.8 W) was estimated to be approximately 25%.

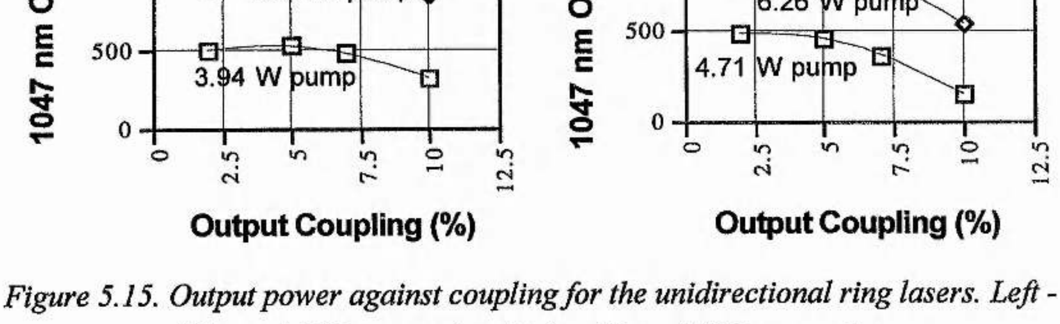

Figure 5.15. Output power against coupling for the unidirectional ring lasers. Left - 100 mm / 50.2 mm optics. Right - 85 mm/ 38.1 mm optics.

5.5.1.2 Beam Quality

The end-pumping employed in this laser allowed high-quality TEM_{00} output even at the highest pump levels. Figure 5.16 shows profiles of the 1047 nm output beam at distances of 150 mm and 137 mm from the output coupler. The pump power was 12 W. If the small distortion of the output coupler is neglected, these represent the mode cross-sections at the front of the Nd:YLF prism and at the lens, respectively.

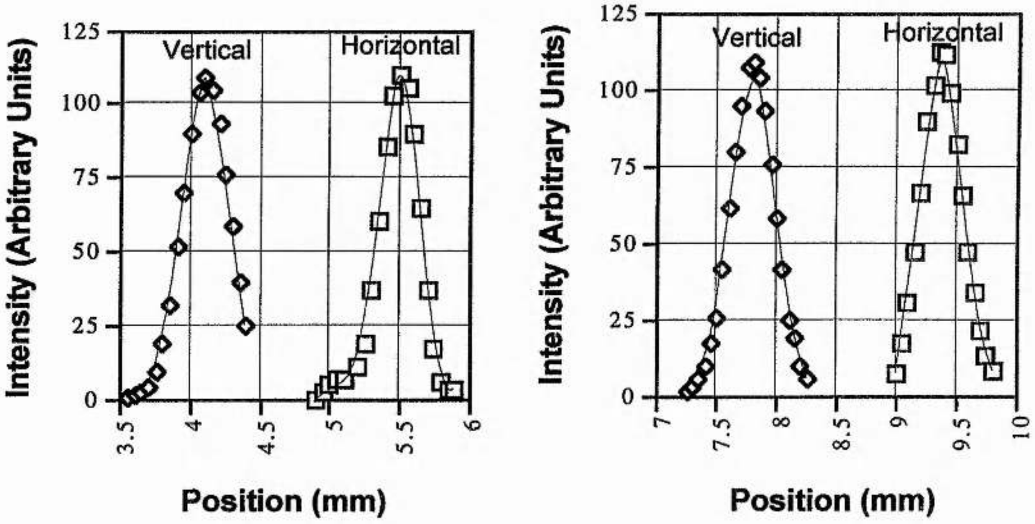

Figure 5.16. Profiles of the 1047 nm output beam. Pump power = 12 W.

TEM_{00} operation was easily achievable at all pumping levels. Only if the intracavity lens was significantly transversely displaced would higher order modes oscillate. Figure 5.17 shows 00, 10, and 20 modes inside the prism which were induced by moving the lens. The pictures were taken with a CCD camera; pump radiation was excluded using a RG 850 filter.

5.5.2 Operation at 523.5 nm

By using a plane high reflector and adjusting the optical diode, single-frequency output was obtained from the curved mirror at 523.5 nm when the oven-heated 25 mm LBO crystal was placed at the focus of the resonator. The phase-matching temperature for the 1047 nm → 523.5 nm process was found to be slightly higher than for Nd:YAG at 151 °C. The FWHM temperature bandwidth was again ≈ 1.5 °C. The visible output power characteristics for the system with each of the two sets of optics are given in Figure 5.18. The highest visible output powers obtained were 1143 mW using the 100 mm / 50.2 mm optics, and 790 mW using the 85 mm / 38.1 mm optics. The pump powers were 15.8 W and 14.5 W respectively, corresponding to optical-to-optical conversion efficiencies from pump to visible of 7% and 5%. Single-frequency operation

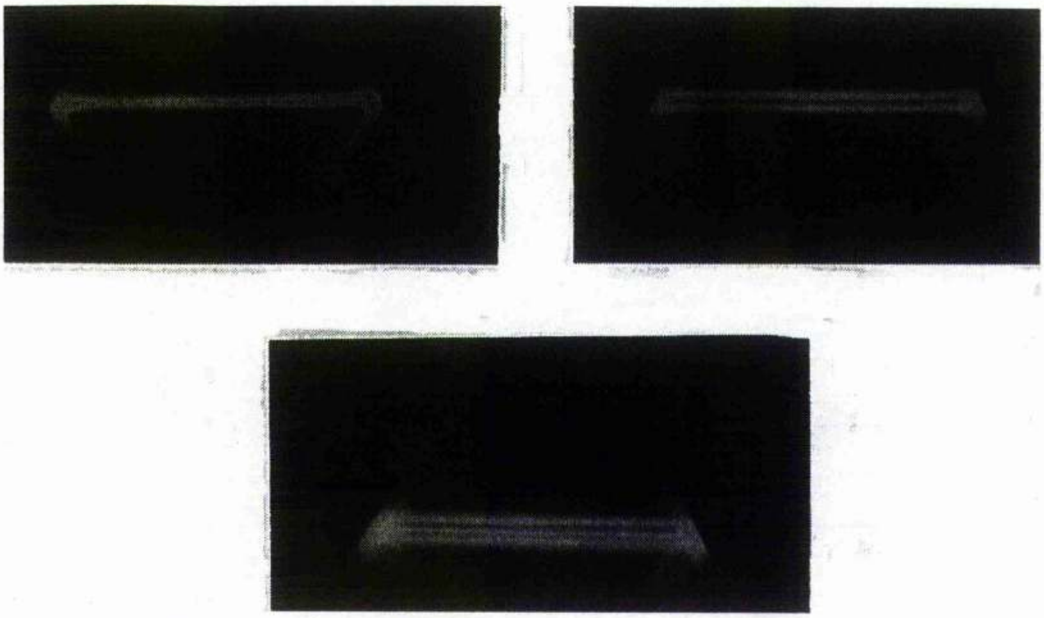

Figure 5.17. TEM_{00}, TEM_{10} and TEM_{20} transverse modes inside the Nd:YLF prism.

was confirmed by monitoring the 1 μm leakage from the plane high reflector on a scanning confocal Fabry-Perot interferometer.

Although the power output using the short focal length optics was rather low, the efficiency obtained with the 100 / 50.2 mm optics was satisfactory, being approximately twice that typically obtained from the side-pumped Nd:YAG laser described in Chapter 4. Unfortunately this enhanced efficiency due to the end-pumped design could not be fully exploited because of the poor thermal conductivity of the Nd:YLF material. In common with other researchers, for example [5.8], it was found

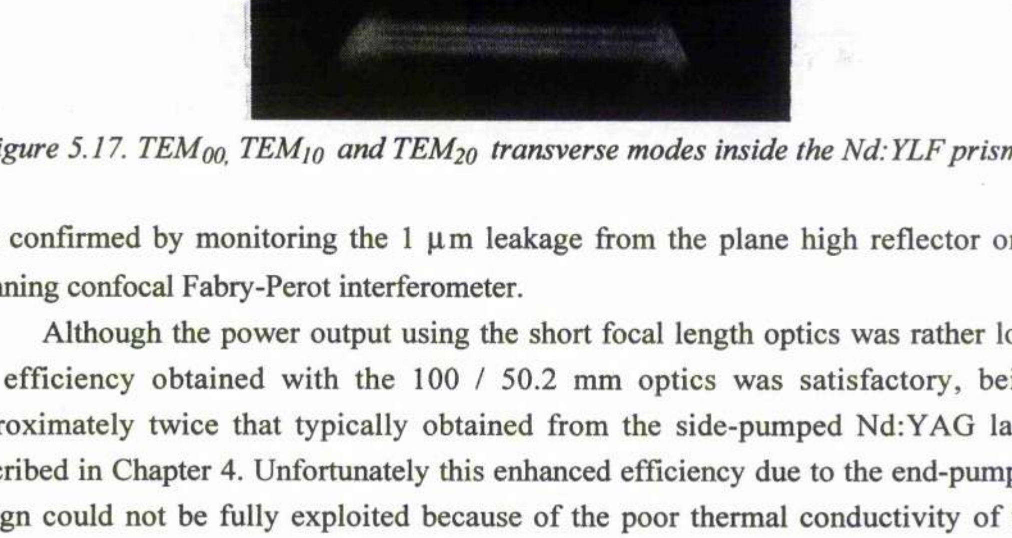

Figure 5.18. Harmonic output power for the intracavity-doubled ring lasers. Left - using 100 mm / 50.2 mm optics. Right - with 85 mm / 38.1 mm optics.

that pumping above the ≈ 8 W level at a single point invariably led to catastrophic damage to the bulk material. The benefits of reduced thermal lensing were not, therefore, seen. The roll-off of the slope efficiency characteristic of Nd:YAG devices simply being replaced with a sharp cut-off at the pump power at which the prism became damaged.

As in the previous laser, some analysis of the harmonic output power performance can be made. For the device based on the 100 / 50 mm optics, the maximum unidirectional 1 μm output power was 2.92 W, and the corresponding unsaturated gain was ≈ 25%. The internal linear loss was estimated as ≈ 4%. Assuming that the output coupling was near to optimum for this maximum output, the saturation power of the laser can be estimated as 33 W, and the optimum nonlinear coupling for the laser as 1.25×10^{-3} W^{-1}. As mentioned before, the highest attainable nonlinear coupling using a 25 mm LBO crystal (with "Boyd and Kleinman" focusing) is 7.3×10^{-4} W^{-1}, which is ≈ 0.6 times the optimum value. Under the Boyd and Kleinman conditions, 2.64 W at 523.5 nm should have been extractable. The actual maximum harmonic power of 1.14 W indicates that the actual nonlinear coupling was only ≈ 11% of the Boyd and Kleinman value. Again, this can be attributed to the less-than-ideal focusing in the LBO crystal and in particular to the significant astigmatism of the laser mode in the crystal.

5.5.3 Intracavity doubling with KTP

5.5.3.1 Harmonic Output Power Performance

The modest nonlinearity of LBO generally meant that the laser was under-coupled for intracavity frequency doubling with this material, even if Boyd and Kleinman focusing could have been achieved. This is generally true of ring lasers because the optimum nonlinear coupling factor κ is twice that of a standing-wave cavity with the same linear loss. The effective nonlinear coefficient of KTP is about six times that of LBO, allowing the possibility of achieving nonlinear coupling close to the optimum value. However, the type II phase-matching means that the birefringence of the crystal has to be compensated for. Using a 5 mm crystal with Boyd and Kleinman focusing should allow a coupling factor of 4.5×10^{-3} W^{-1} to be achieved, although this requires a waist radius of 13 μm. A κ value of this magnitude would optimally couple a laser with a 9% internal linear loss, assuming a saturation power of ≈ 20 W. The idea was that the 4 - 5% internal linear loss of the Nd:YLF ring laser (using 100 mm and 50 mm optics) would be quite easily accommodated by using KTP rather than LBO.

The 5 mm KTP crystal (cut for 1047 nm doubling) used in the present laser was mounted in a purpose-built electrically heated brass oven and maintained at a constant temperature using a Marlow 5010 temperature controller. Figure 5.19 shows the harmonic output power behaviour. For a given pumping level, the oven temperature was adjusted to give maximum output, in addition to positional adjustment. Maximum output was achieved using a lens-curved mirror separation of ≈ 70 mm. The maximum output was around 500 mW. A probable reason for this low power output was damage to the AR coatings on the surfaces of the crystal.

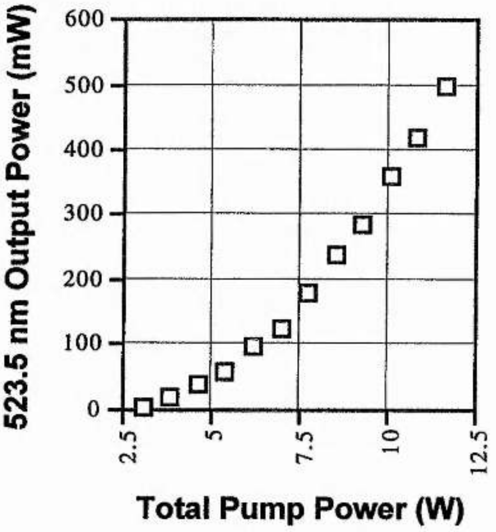

Figure 5.19. 523.5 nm output power with KTP as the doubling crystal.

5.5.3.2 Observation of Large Amplitude Fluctuations in the Harmonic Power

The observation by Baer [3.25] of large amplitude fluctuations in the harmonic output from intracavity-doubled standing-wave lasers was discussed in Chapter 3. Similar pulsed output behaviour was observed from the present laser for certain positions of the KTP crystal. Simultaneous examination of the 1 μm and 0.5 μm output showed the laser to be pulsing on and off as shown in Figure 5.20. Figures 5.21 to 5.26 show pulse trains and pulse shapes for pump powers of 6, 10 and 12 W repectively. The pulse period was between 20 and 55 μs. As the pump power was increased to 12 W, the period became more constant in the 40 - 50 μs range. This is consistent with Baer's observation that the period is only a weak function of the pumping level. For two-mode operation, he reported a period of 40 μs.

The pulse shapes (Figures 5.21, 23, 25) are very close to those observed by Baer although they are much shorter than those reported in [3.25]. Baer found pulse durations of ≈ 20 - 30 μs, whereas the pulses observed from the ring laser were ≈ 2 μs in length.

The most likely cause of this behaviour is the birefringence of the KTP crystal reducing the efficacy of the optical diode. This may have resulted in bidirectional lasing and thus modulation of the main output direction by intermodal coupling through the nonlinear process. The explanation for the short duration of the pulses is unclear.

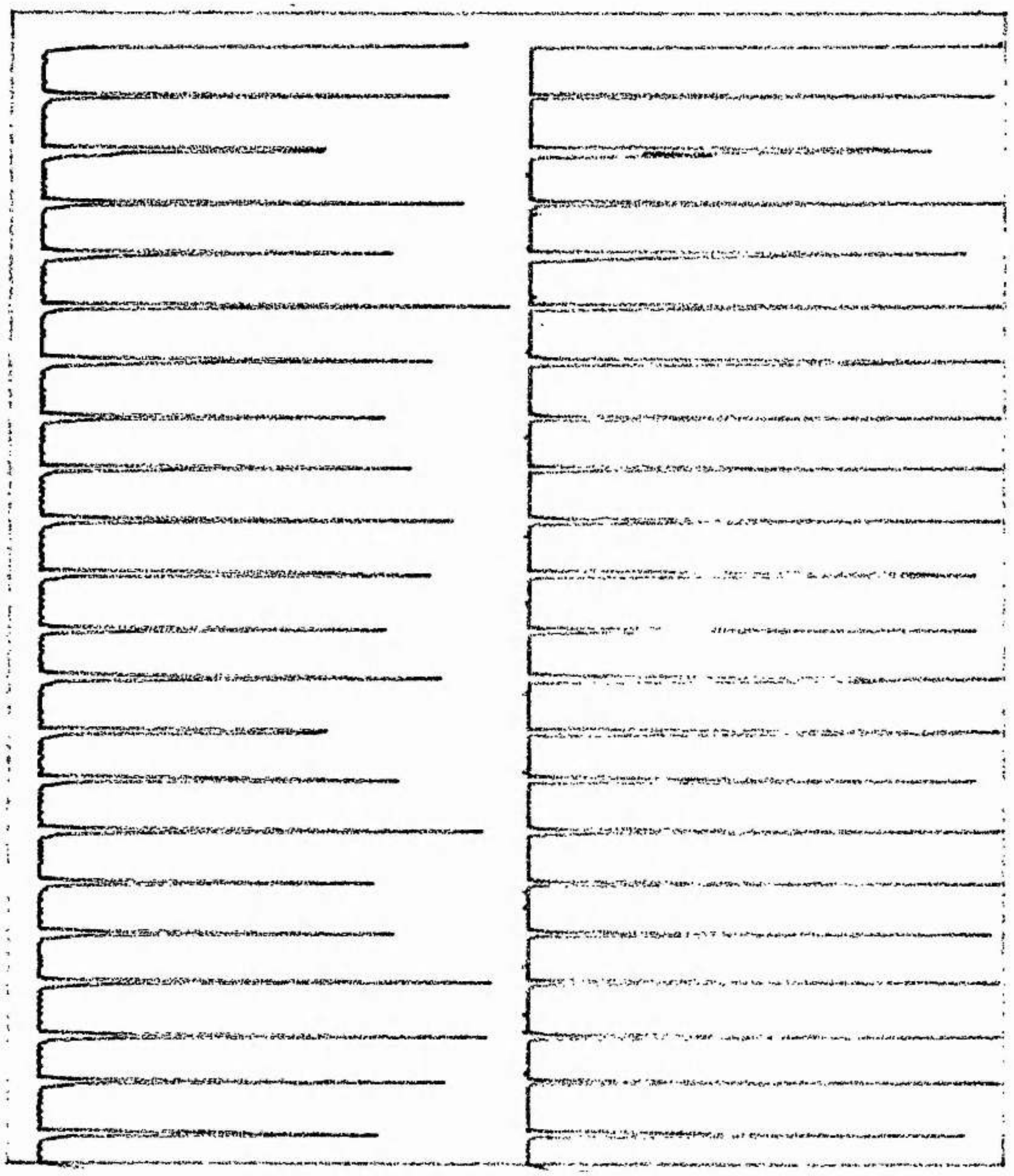

CH2: > 0V : 100us 1047 nm

DATE: Dec 15/93

TIME: 16: 45: 20

PUMP : 10 W

CH1: 05.0mV : 100us 523-5 nm

Figure 5.20. Harmonic (upper trace) and simultaneous fundamental pulses produced by using KTP as the doubling crystal.

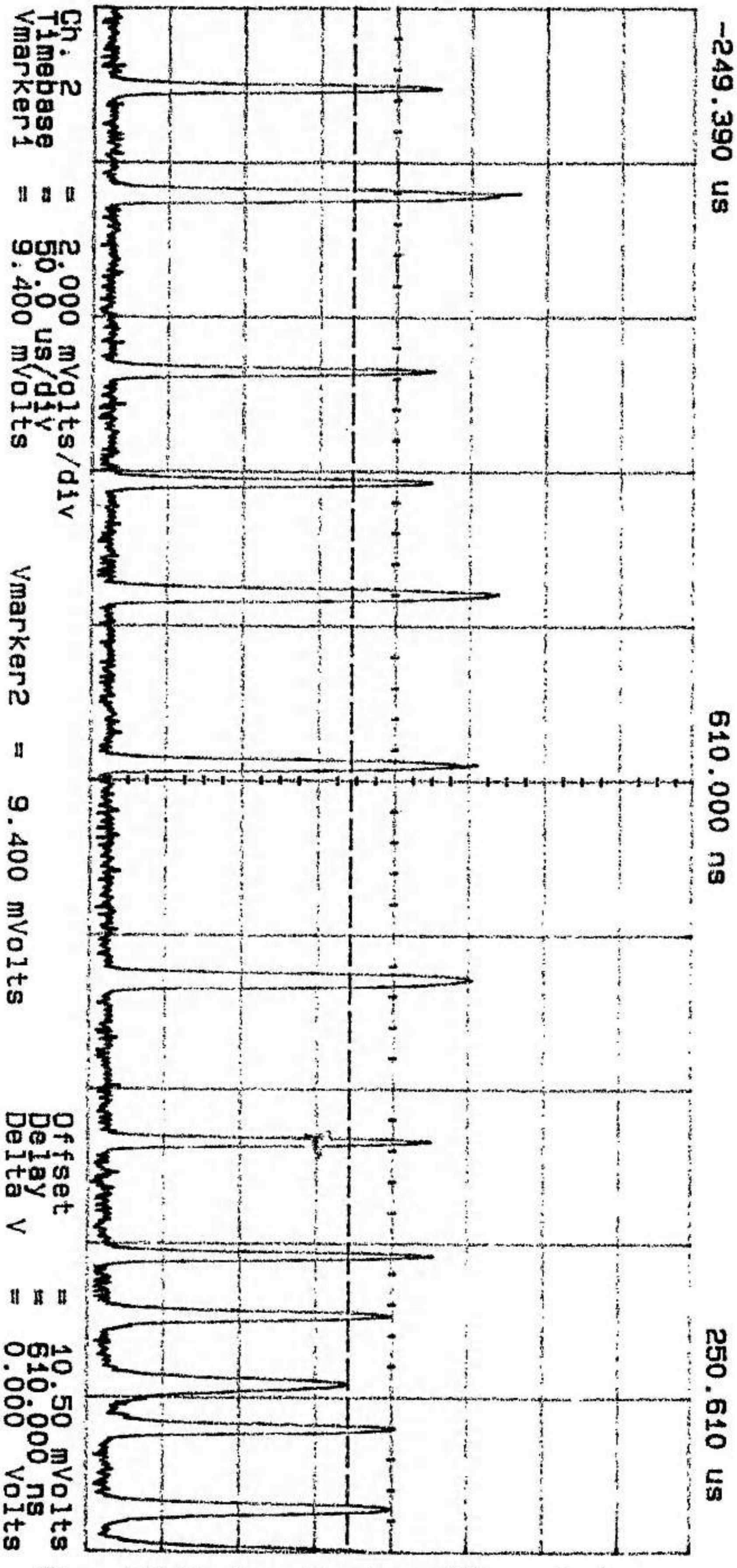

1047 nm, PUMP 6W

Figure 5.21. Fundamental pulses at 6 W pump level.

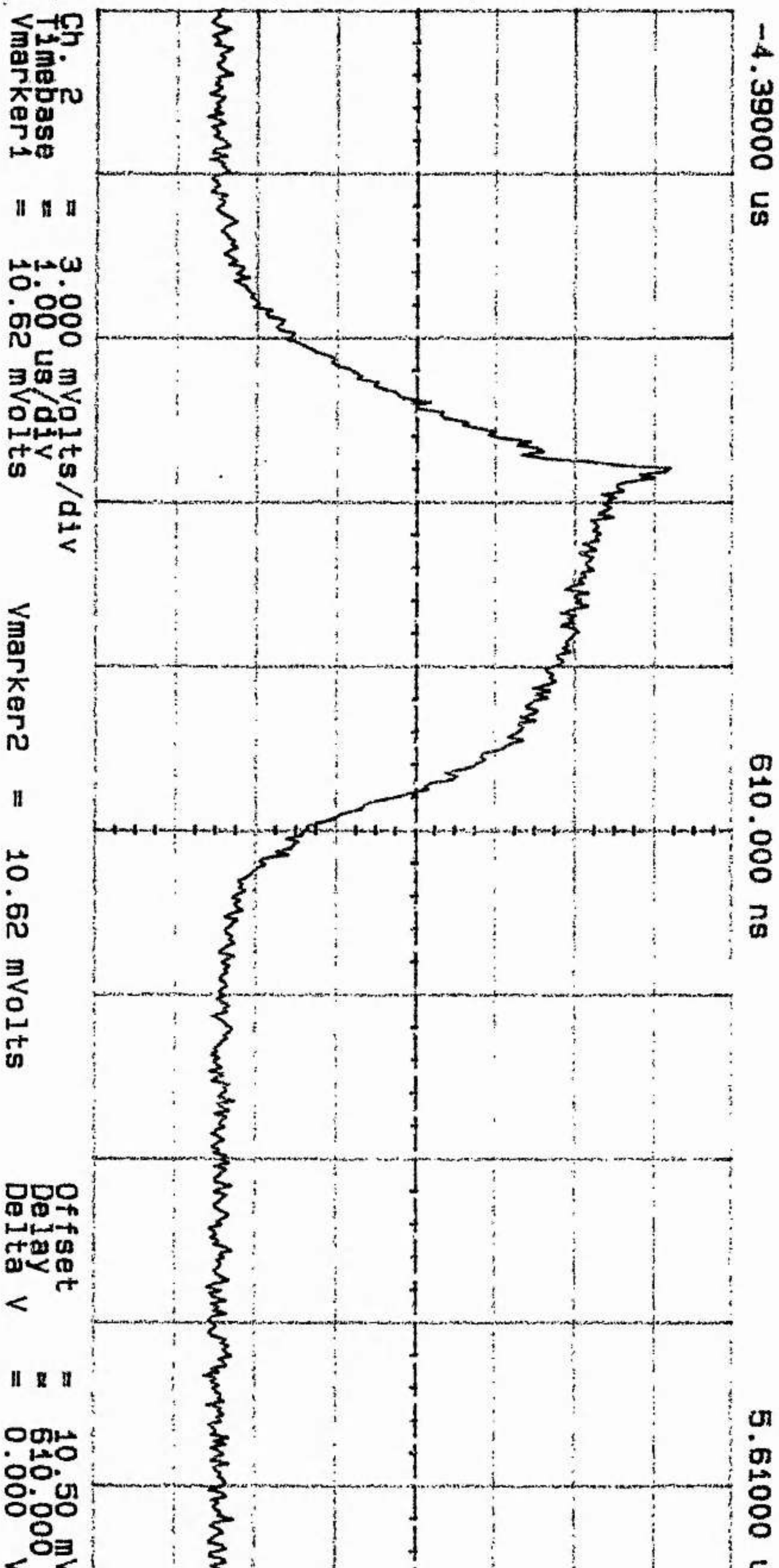

Ch. 2 = 3.000 mVolts/div
Timebase = 1.00 us/div
Vmarker1 = 10.62 mVolts
Vmarker2 = 10.62 mVolts
Offset = 10.50 mVolts
Delay = 610.000 ns
Delta V = 0.000 Volts

523.5nm
pump: 6W

Figure 5.22. Harmonic pulse shape; 6 W pump level.

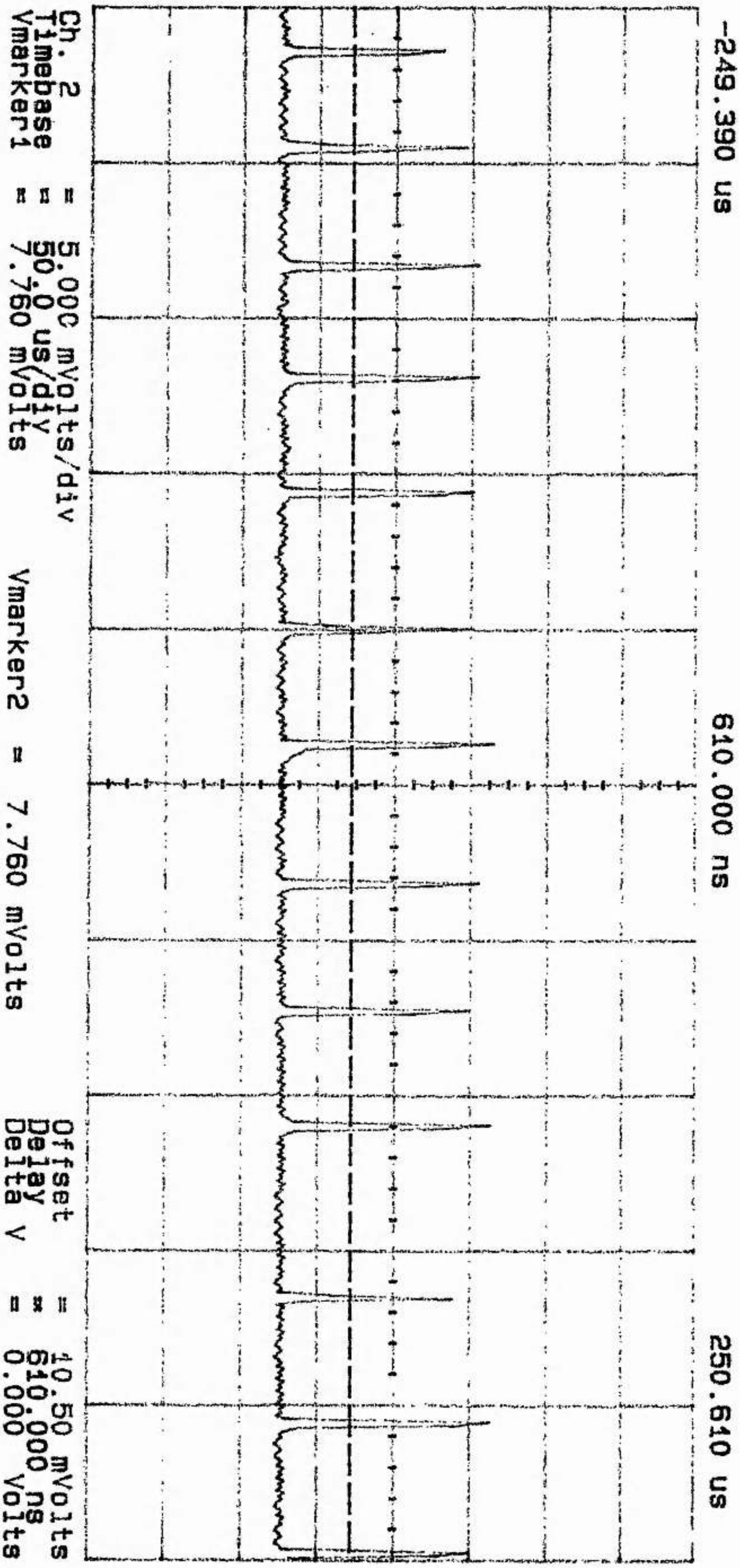

Figure 5.23. Harmonic pulses; 10 W pump level.

523.5nm
pump: 10W

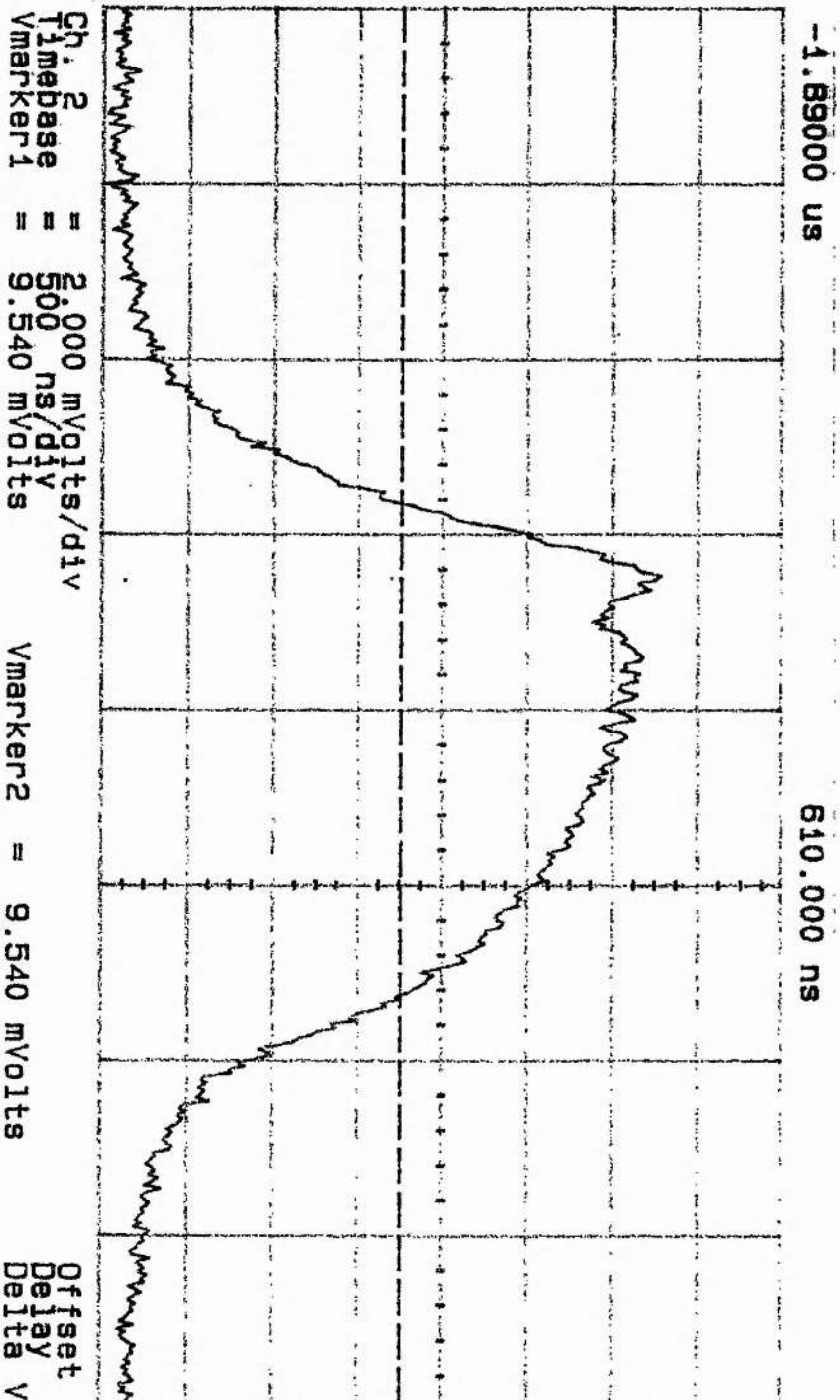

523.5nm
Amp: 10 W

Figure 5.24. Harmonic pulse shape; 10 W pump level.

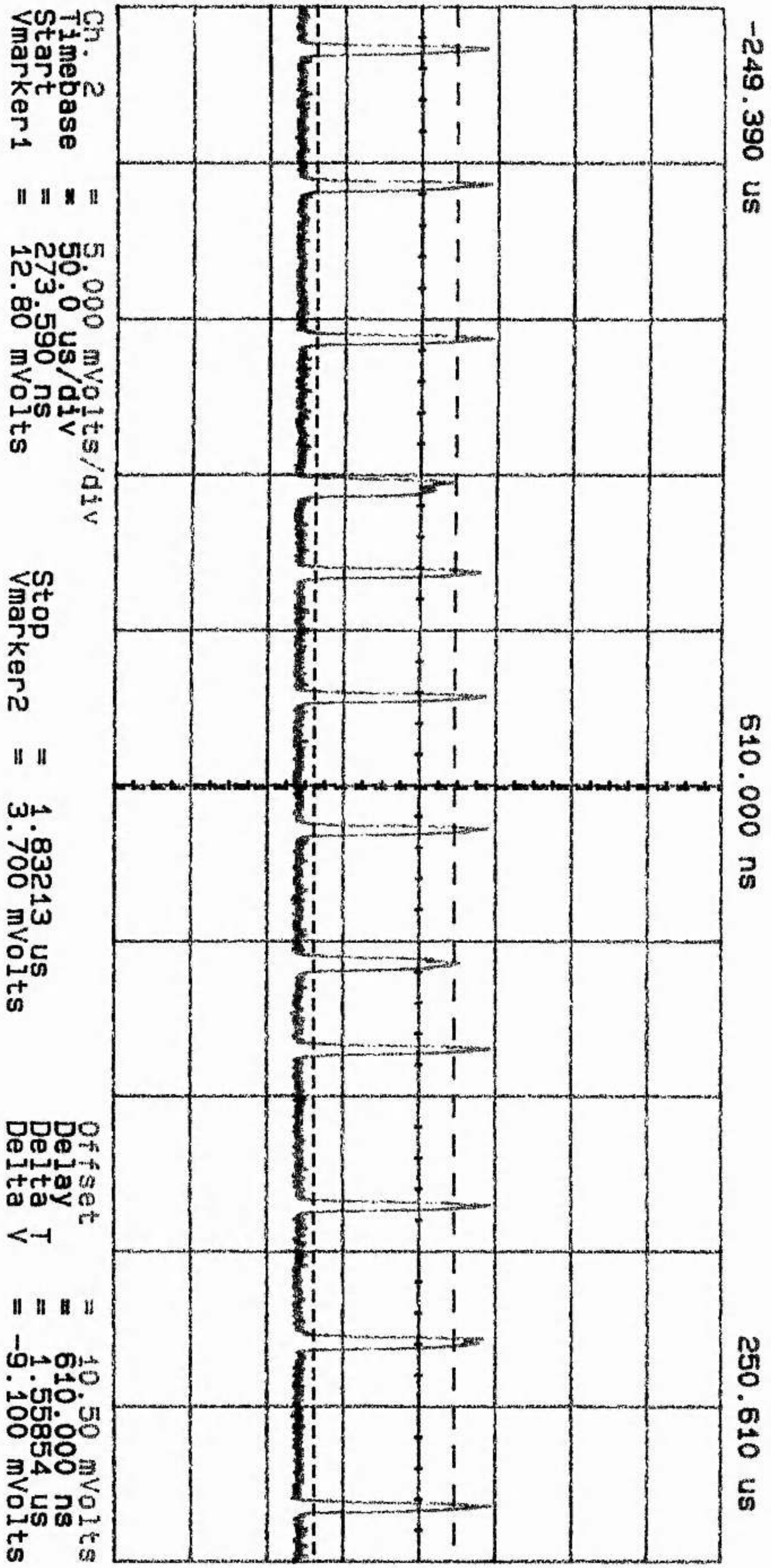

Ch. 2 = 5.000 mVolts/div
Timebase = 50.0 us/div
Start = 273.590 ns
Vmarker1 = 12.80 mVolts
Stop = 1.83213 us
Vmarker2 = 3.700 mVolts
Offset = 10.50 mVolts
Delay = 610.000 ns
Delta T = 1.55854 us
Delta V = -9.100 mVolts

1047 nm
pump : 12W

Figure 5.25. Fundamental pulses; 12 W pump level.

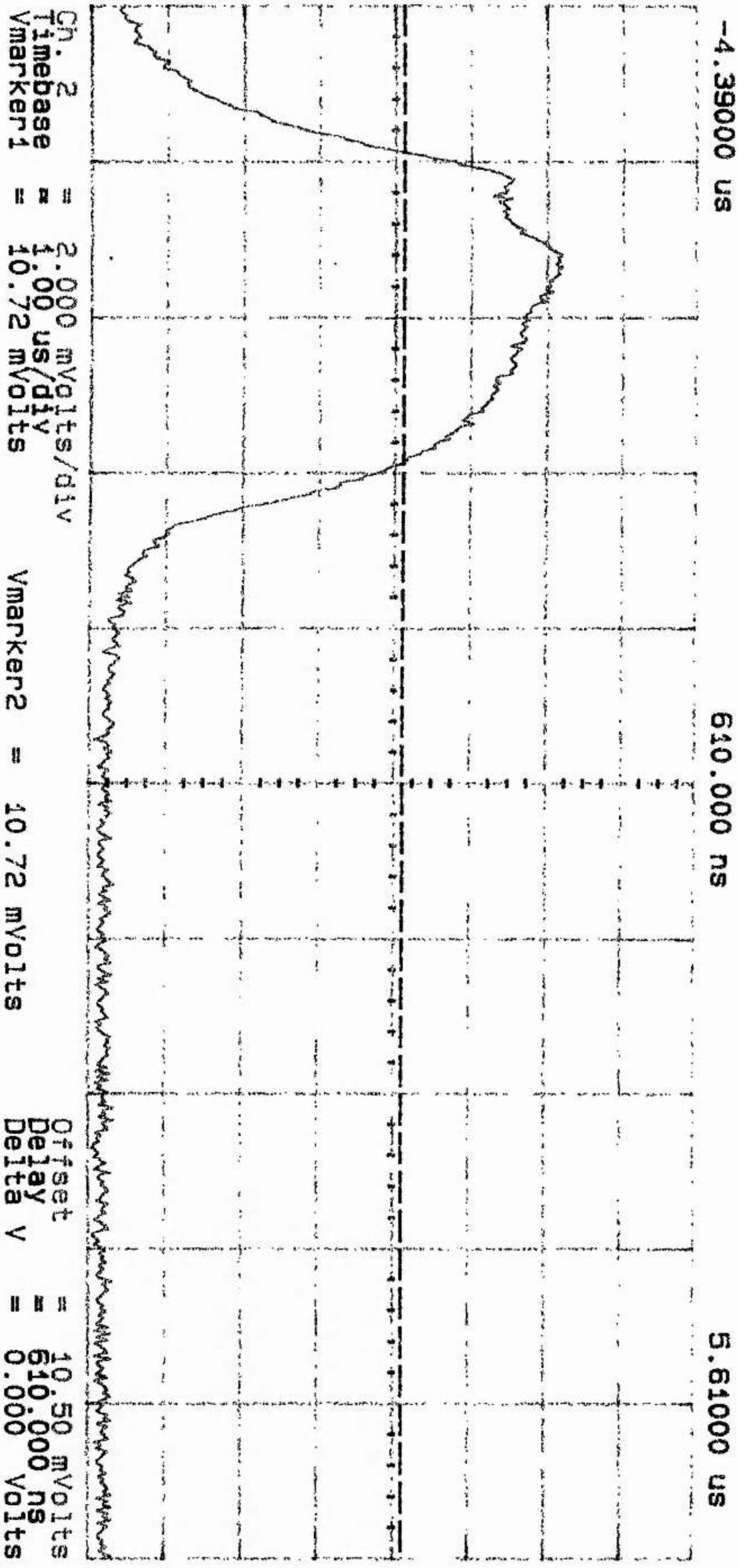

1047 nm
pump: 12 W

Figure 5.26. Fundamental pulse shape; 12 W pump level.

5.6 Concluding Remarks

The end-pumped internally folded design of this laser allowed the generation of 1 μm and 0.5 μm output with much greater efficiency than the side-pumped system described in Chapter 4. Although the maximum single-frequency 1 μm harmonic output power was ≈ 1 W as was the case for the Nd:YAG ring laser, this result was achieved using about half as much pump power.

Although a much more promising laser than the side-pumped system, there were two principal obstacles to realising its full potential in terms of high power operation at the fundamental and second harmonic. The first was the choice of host crystal. The very poor thermal conductivity of YLF meant that the pump power was limited to ≈ 15 W: higher pump levels resulted in thermal damage to the material. An identical design in Nd:YAG would undoubtedly have allowed pump powers in the region of 30 W to be applied. Thermal lensing and birefringence would then be limiting factors but higher output power could probably have been achieved.

The second limitation was the strongly astigmatic pump beams from the diode-bars. Possibly the use of Nd:YVO_4 as the gain material would have reduced the pump absorption depth and therefore improved the pump-mode overlap, given that there was no attempt to remove the bars' astigmatism. The use of fibre-coupled or beam-reshaped diode-bars would have improved threshold, efficiency and maximum power output.

Although the Brewster-angled entry and exit to the Nd:YLF prism was a convenient polarising system, it resulted in a 34° internal angle for the ring laser. This resulted in significant astigmatism in the laser mode, due both to the angle of incidence on the curved mirror and the Brewster surfaces themselves. This could be overcome either by redesigning the gain material shape to remove this Brewster surface (as in, for example [5.7]) or by using a simple folded resonator employing a simple rod of gain material, as in [5.5].

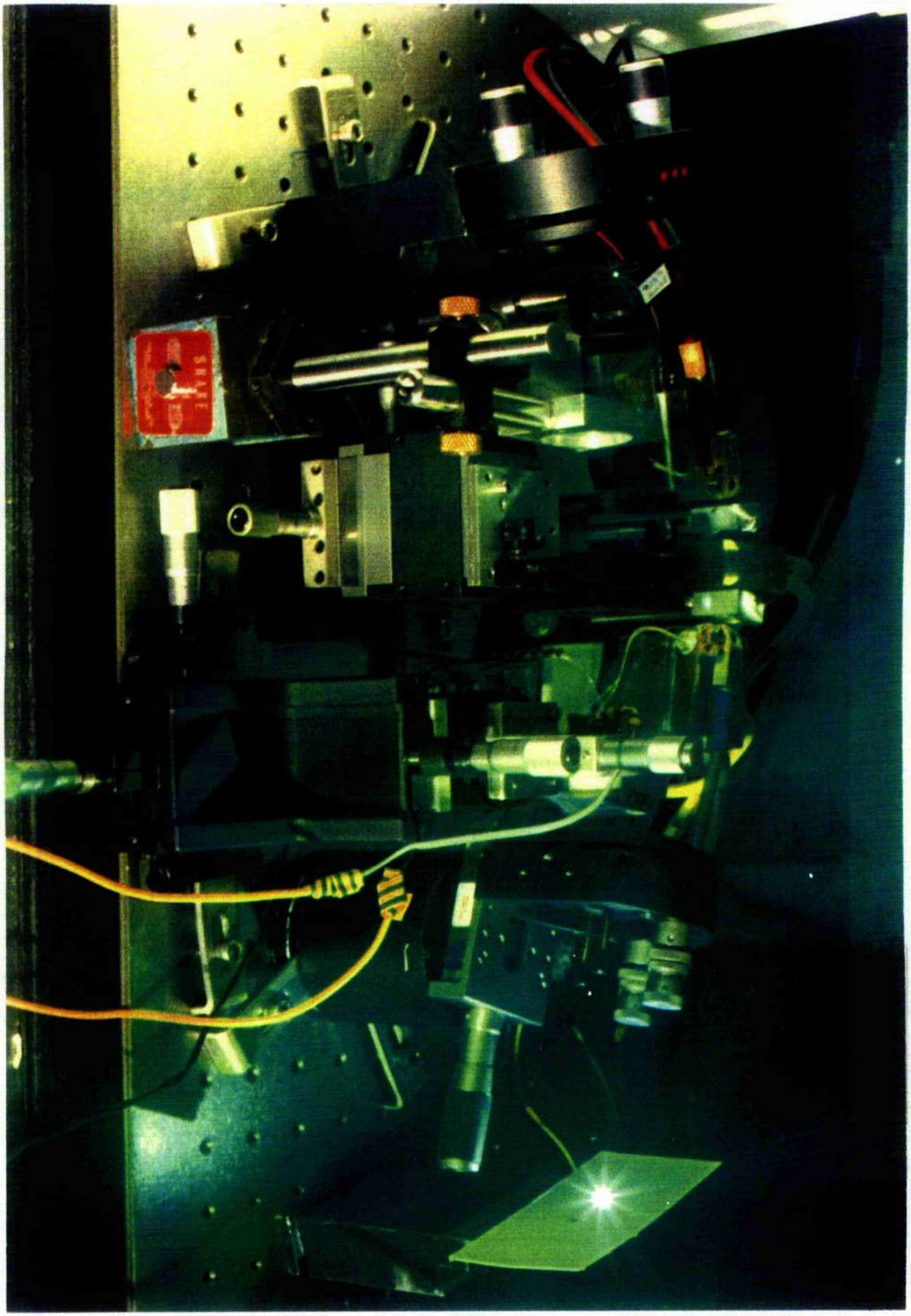

References

[5.1] K. Lamb, D. E. Spence, J. Hong, C. Yelland, W. Sibbett: "All-solid-state femtosecond Ti:sapphire laser": *Conf. On Lasers & Electroopt. OSA Tech. Dig.* **8** 235 (1994, paper CWI3)

[5.2] K. Lamb, D. E. Spence, J. Hong, C. Yelland, W. Sibbett: "All-solid-state self-modelocked Ti:sapphire laser": *Opt. Lett.* **19** 1864 (1994)

[5.3] R. Scheps, J. F. Myers: "Scalable single-frequency diode-pumped ring laser": *App. Opt.* **31** 1221 (1992)

[5.4] T. M. Baer, D. F. Head, P. Gooding, G. J. Kintz, S. Hutchison: "Performance of diode-pumped Nd:YAG and Nd:YLF lasers in a tightly-folded resonator configuration": *IEEE J. Quant. Elec.* **28** 1131 (1992)

[5.5] A. J. Alfrey: "Simple 1 μm ring laser oscillators pumped by fibre-coupled laser-diodes": *IEEE J. Quant. Elec.* **30** 2350 (1994)

[5.6] R. Scheps, J. F. Myers: "Efficient, scalable, internally folded Nd:YAG laser end-pumped by laser diodes": *IEEE J. Quant. Elec.* **29** 1515 (1993)

[5.7] R. Scheps, J. F. Myers, G. Mizell, K. Yates: "Internally folded Nd:YAG and Nd:YVO_4 lasers pumped by laser diodes": *IEEE J. Quant. Elec.* **30** 2132 (1994)

[5.8] D. C. Shannon, D. L. Vecht, S. Re, J. Alonis: "High average power diode-pumped lasers near 2 μm": *SPIE* **1865** 164 (1993)

Chapter 6

Nd LASERS PUMPED BY FIBRE-COUPLED DIODE-LASER BARS

6.1 Introduction

As discussed in Chapter 1, the fibre-coupling of diode-laser bars is one route to an azimuthally symmetric pump beam. The symmetrical M^2 of the resulting beam allows enhanced pump-mode overlap giving reduced thresholds, higher efficiencies and higher maximum output power at both 1 and 0.5 μm. When used together with folded resonators (discussed in Chapter 5) the result is highly powerful and efficient devices such as those recently demonstrated by the *Spectra-Physics* [6.1, 2] and *Coherent* [6.3] corporations. These lasers have produced > 13 W at 1 μm [6.1], 6 W multimode 0.5 μm output [6.2] , and > 8.5 W single-frequency output at 0.5 μm [6.3], all in high quality TEM_{00} beams. The 1 μm device in [6.1] was more than 50% efficient, while the 0.5 μm system in [6.3] had a pump-to-visible efficiency of around 27%, which is the highest 0.5 μm power and the highest efficiency ever to be reported from any diode-pumped, intracavity-doubled laser.

Fibre-coupling of diode lasers and bars for end-pumping is not a new idea of course. An early system to use the concept was the LNP chip laser of Kubodera and Noda in 1982 [6.4]. The pumping system comprised seven discrete AlGaAs diode-lasers coupled to a fibre-bundle. Advances in fibre-coupled pump systems have followed developments in the diode-bars themselves. Thus by 1988, after the power scaling of the mid-1980s, we arrive at systems such as the fibre-bundle coupled, end-pumped Nd:YAG laser of Berger *et al* [6.5]. Seven diode-arrays were individually coupled into 110 μm core 0.37 NA fibres giving a bundle diameter of 330 μm. The maximum output power was ≈ 2 W. The Nd:YAG laser gave ≈ 700 mW of CW output power with a slope efficiency of ≈ 35%. At this stage, the pump power losses due to the fibre-coupling of diode-bars were generally seen as something of an obstacle. The benefits for high-power lasers had yet to be demonstrated. By 1992, such scaling was well underway. Kaneda *et al* generated 7.6 W CW at 1 μm in a TEM_{00} beam by end-pumping a Nd:YAG laser using a bundle of 19 fibres, each individually coupled to a separate 900 mW broad-area AlGaAs laser [6.6]. The fibres had 125 μm cores and a 0.35 numerical aperture. The total deliverable power was > 21 W. The 1 μm laser was reported to have a slope efficiency of 69% (76% is the theoretical limit) and an optical-to-optical efficiency of nearly 50%. The increased efficiency meant that thermal lensing was less of a problem, and the excellent beam quality (M^2 of 1.01 ± 8%) coupled with high output power tended to eclipse reservations about coupling losses. Choosing to lose power in coupling diode-lasers to fibres was now seen to be preferable to poor mode matching in the laser crystal, which leads to thermal problems. The benefits of the fibre-coupled approach were especially seen in other rare-earth solid-state lasers such as Tm^{3+} and Ho^{3+} [6.7].

Intracavity frequency-doubling of these lasers initially involved linear cavities with KTP as the doubling material because of its high nonlinearity. Chaotic visible output was avoided either by obtaining single-frequency operation or by suitable manipulation of polarisation eigenstates within the laser cavity. For example, single-frequency operation could be selected by using a Brewster plate with the KTP crystal to produce a birefringent filter [6.8, 9]. Careful arrangements of the polarisation eigenstates were described by James *et al* [6.10] and Oka and Kubota [6.11]. The polarisation scheme of Oka and Kubota was reported to be reliable even during high power operation, and 3.5 W of two-mode 532 nm output was generated by this method [6.12, 13]. The other techniques for avoiding chaotic visible output tended to break down under high pump levels. In the case of the birefringent filter method, this is due to insufficient loss discrimination between adjacent low-loss modes.

The birefringence problem of KTP in the type II phase-matching arrangement has meant that LBO has now come back into favour, due to its type I non-critical phase matching which allows a simple and reliable intracavity polarisation scheme to be established. This, together with its large angular acceptance and high damage threshold are now seen to outweigh its modest nonlinearity, which can be overcome by using a long crystal length. In fact a long length of crystal can even be advantageous in that the requirement for a tight focus is relaxed. In addition to the resurgence of LBO, the ring laser has been shown to be the most reliable configuration for producing reliable high-power single-frequency output. A ring laser end-pumped by fibre-coupled diode-bars was reported by Alfrey [6.14] and this is likely to have been a prototype for the *Coherent* system [6.3]. This laser gave a reliable 8.5 W single frequency-output at 1 μm. For linear cavities, the multimode approach to internal doubling now seems the only reliable high-power option, as in the *Spectra-Physics* laser [6.2].

In this chapter, details of three intracavity-doubled devices pumped by a fibre-coupled diode-bar system are described. The first is a Nd:YAG laser employing the scheme of Oka and Kubota [6.11]. The second laser used Nd:YVO_4 as the gain material. Both of these lasers were doubled with KTP. The third laser was an end-pumped Nd:YAG ring laser, intracavity doubled using LBO.

6.2 Pumping Arrangement

6.2.1 Fibre-Coupled Diode-Bars

The pump source for the lasers described below was a commercial system (*OptoPower* model *B030*) which comprised two 20 W AlGaAs diode-bars (model *B020*) coupled into a 1.5 mm diameter 0.11 NA fibre bundle consisting of 38 individual fibres. (There were 19 emitters in each bar.) The two bars were driven in series using a single constant-current supply, but were separately heat-sunk on thermoelectric coolers. The specifications of the two constituent bars are given in Table 6.1. Temperature regulation was achieved by the means described in Chapter 4. By varying the heat-sink temperature in the range 15 - 28 °C, the output was tunable over the range 803 - 811 nm. A typical scanning monochromator trace is shown in Figure 6.1. This tunability allowed control over the pump absorption depth. The spectral FWHM of the output was measured to be 2 ± 0.2 nm. Variations in the output wavelength from the fibre-bundle with heat-sink temperature and drive current are shown in Figure 6.2. The tuning rates were + 0.26 nm/°C and 0.22 nm/A, which is similar to the behaviour of the *SDL 3460S*

Serial Number	200557	200679
Threshold Current	5.02 A	4.33 A
Slope Efficiency	0.9 W/A	0.9 W/A
I @ 20W	26.69 A	26.51 A
Spectral FWHM	2.4 nm	2.3 nm
Specified Peak λ @ 27.5 °C	809.8 nm	809.6 nm
Output Power Characteristic	P= 0.9I - 4.52	P = 0.9I - 3.90

Table 6.1. Manufacturer's specifications for the individual diode-bars.

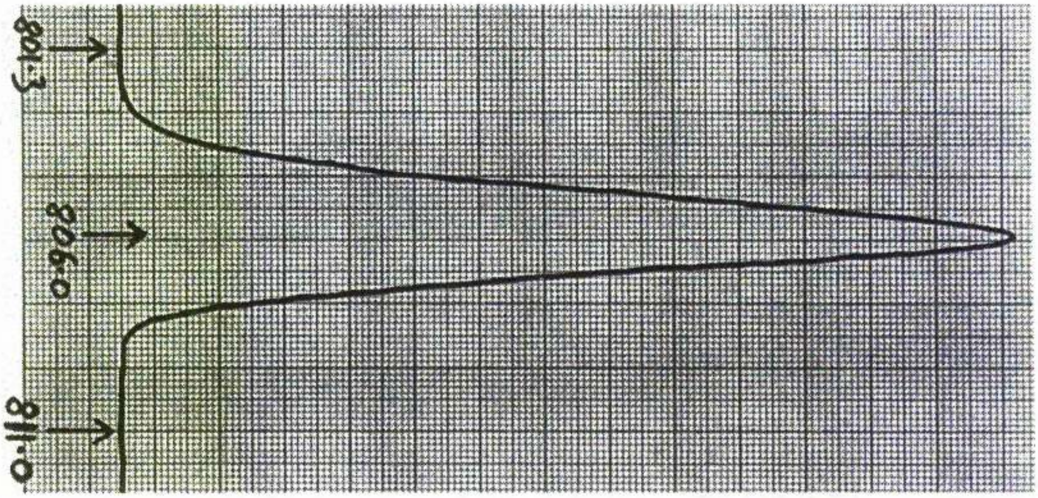

Figure 6.1. Scanning monochromator trace of the output from the fibre-coupled diode-bars. Wavelength in nm. (20 A, 17 °C.)

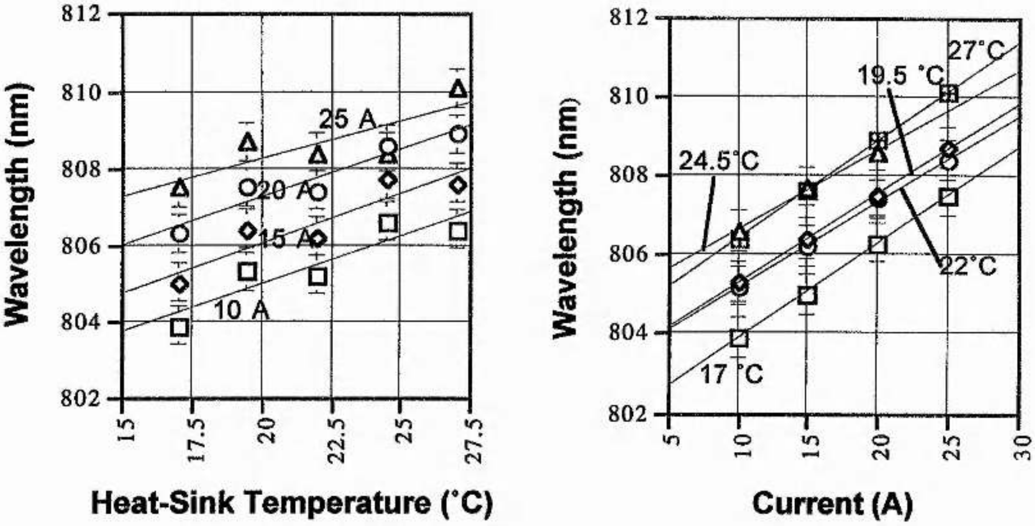

Figure 6.2. Wavelength tuning with heat-sink temperature and drive current.

devices described in Chapters 4 and 5.

The fibre bundle was capable of delivering 35 W of output power at the full current of 30 A. Using a two-lens coupling device, 30 W could be coupled into a 600 μm core, 0.37 NA single multimode fibre, representing ≈ 85% coupling efficiency. 17 W (≈ 50%) could be coupled into a 400 μm core, 0.37 NA fibre. The 400 μm fibre was preferable due its lower *etendue*, but in practice heating of the fibre-tip due to uncoupled radiation at the coupler limited the output power to ≈ 10 W. The 600 μm fibre was adopted as the main delivery system. The use of single fibres allowed the brightness of the source to be increased at the cost of a reduction in power. Figure 6.3 shows the output power characteristics for the fibre-bundle and the 600 μm and 400 μm fibres. The slope efficiencies were 1.37, 1.18, and 0.56 WA^{-1} respectively. A major advantage of this *OptoPower* system was the much lower threshold current: ≈ 5 A compared to ≈ 11 A for the *SDL 3460S* bars.

6.2.2 Coupling Optics

The symmetrical output beams from the multimode fibres allowed a very simple coupling optics system to be used. This comprised two identical AR-coated aspheric condenser lenses with their convex surfaces facing each other. For the linear cavities described below, the lens used was *Melles Griot* model 01 LAG 000/076. (The characteristics of this lens were given in Chapter 5.) The lenses were mounted in a single aluminium holder; the spacing between them at the closest point was < 1 mm. For the ring laser, a greater working distance between the coupling optics and the pump light image plane was required because of the requirement to tilt the thin mirror in order

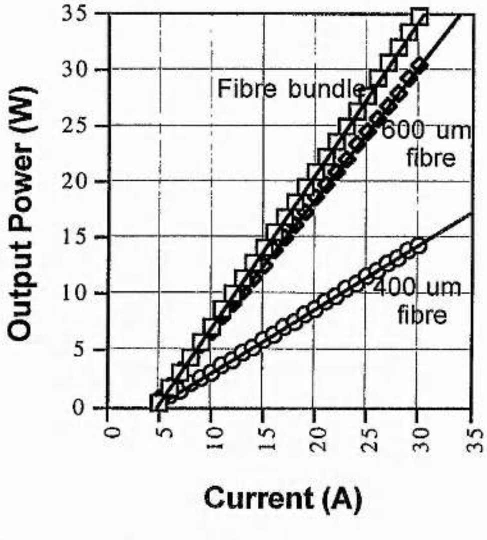

Figure 6.3. Output power from the bundle and the two multimode fibres versus current.

to produce the necessary fold in the beam path. This meant that the thin mirror was further away from the Nd:YAG rod; hence the need for a greater working distance. In this case two much larger aspheric lenses were used : *Melles Griot* model 01 LAG 019/076. The focal length, diameter and f# of this lens were 53 mm, 65 mm and 0.82 respectively. The mounting system was similar to that used for the smaller lenses. An additional benefit of the conical output from the fibre-coupled system was the fact that the coupling optics system produced no spherical aberration: unlike the system described in Chapter 5, both planes were brought to an image point exactly the same distance from the second lens, resulting in more efficient pumping. The power transmission of the coupling optics was measured to be 97%.

6.2.3 Positioning of Fibre-Tip and Coupling Optics

The fibre-tips were terminated with either standard SMA or FCPC connectors. These could be attached to a suitable socket mounted on 1" aluminium disc fitted to a mirror mount. The fibre assembly and the coupling optics system were both fixed to *xyz* translation stages to allow the separations of the gain material, optics and fibre-tip to be adjusted. This gave flexibility in the pump spot size and divergence so that the pump-mode overlap could be maximised. 1:1 imaging of the pump radiation was obtained for the smaller lenses when the fibre tip was 12 mm from the first (plane) surface of the first aspheric lens; the pump spot was formed 12 mm from the plane surface of the second lens. For the larger lenses, the 1:1 imaging distance was 40 mm.

6.3 End-Pumped Nd:YAG Laser

6.3.1 Introduction

A diagram of this laser, as set up for intracavity doubling, is shown in Figure 6.4. The pump light output from the fibre-tip was coupled through a thin (≈ 1 mm) $\lambda/4$ plate into a Nd:YAG rod, which was heat-sunk with indium foil in a water-cooled copper block. Rods of length 6 mm and 8 mm were used; the results given below are for the longer rod. The rod diameter in each case was 3.5 mm. The $\lambda/4$ plate was for 1064 nm and was required for stable intracavity doubling (see section 6.3.6). The plate was AR coated for 808 nm on both sides, HR coated for 1064 nm on the side nearest the fibre-tip and AR coated for 1064 nm on the side nearest the Nd:YAG rod. The close proximity of the gain element to the end mirror was intended to reduce spatial hole-burning as described in [6.14], in order to more easily achieve lasing on one or two longitudinal modes when internally frequency doubling. For operation at 1 μm, the end plane high reflector was replaced by a plane output coupler. The total physical length of the resonator was ≈ 330 mm. This simple three-mirror cavity was designed to achieve three main objectives. First, to produce as large a signal-mode diameter inside the Nd:YAG crystal as possible, so that a large capture etendue was presented for the pump light and the overlap integral was maximised. Second, to simultaneously produce a

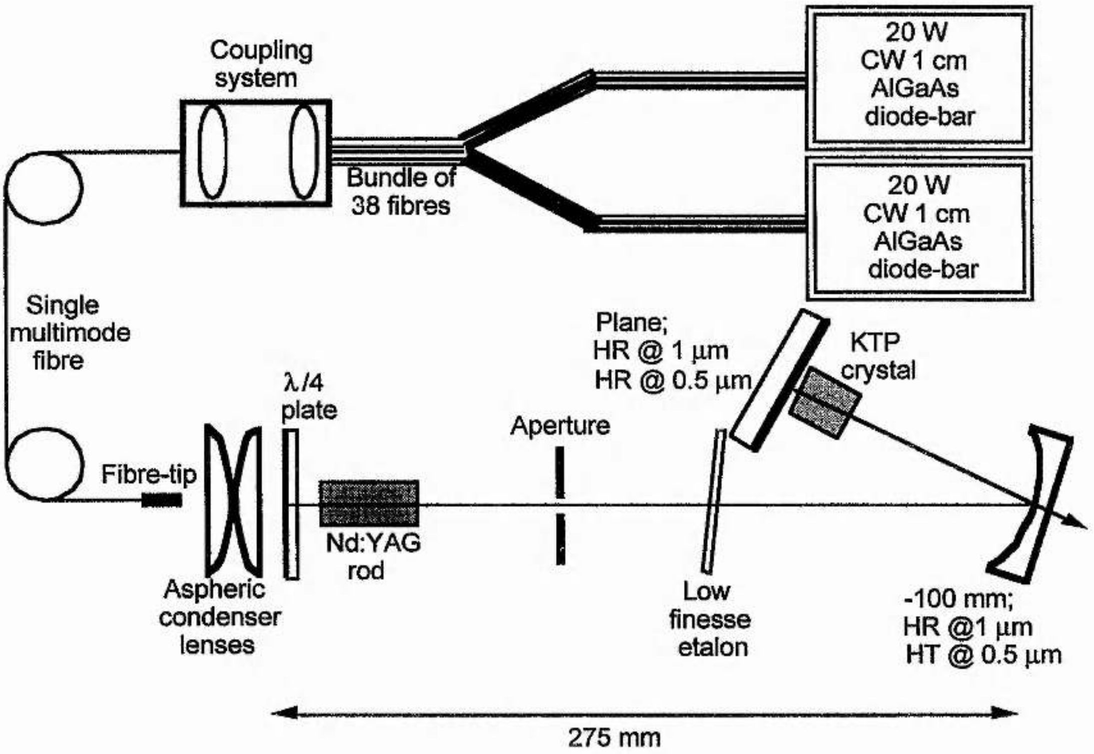

Figure 6.4. Intracavity-doubled Nd:YAG laser end-pumped by fibre-coupled diode-laser arrays.

small waist at the end plane mirror for efficient doubling. Thirdly, by using only three mirrors in a simple cavity scheme, it was hoped to keep internal linear losses to a minimum.

The mode radius inside the Nd:YAG rod and the waist radius inside the KTP crystal are shown as functions of the separation between the curved mirror and the plane mirror in Figure 6.5. For separations in the region of 45 mm, a mode diameter inside the Nd:YAG rod of ≈ 1 mm can be combined with a spot diameter inside the KTP crystal of ≈ 140 µm.

The laser was operated using both 600 and 400 µm diameter core single multimode fibres to couple the pump from the bundle into the gain rod. Using the method described in section 1.3.2.4 the depth over which the pump is fully contained within the signal was calculated as 426 µm in the case of the 600 µm fibre, and 737 µm in the case of the 400 µm fibre. The smaller etendue of the 400 µm fibre is thus seen to be beneficial in terms of pump-signal overlap. The corresponding optimum pump spot sizes were calculated as 601 µm in the case of the 600 µm (*i.e.* roughly 1:1 imaging), while for the 400 µm fibre slight magnification was required, the optimum spot size being 525 µm.

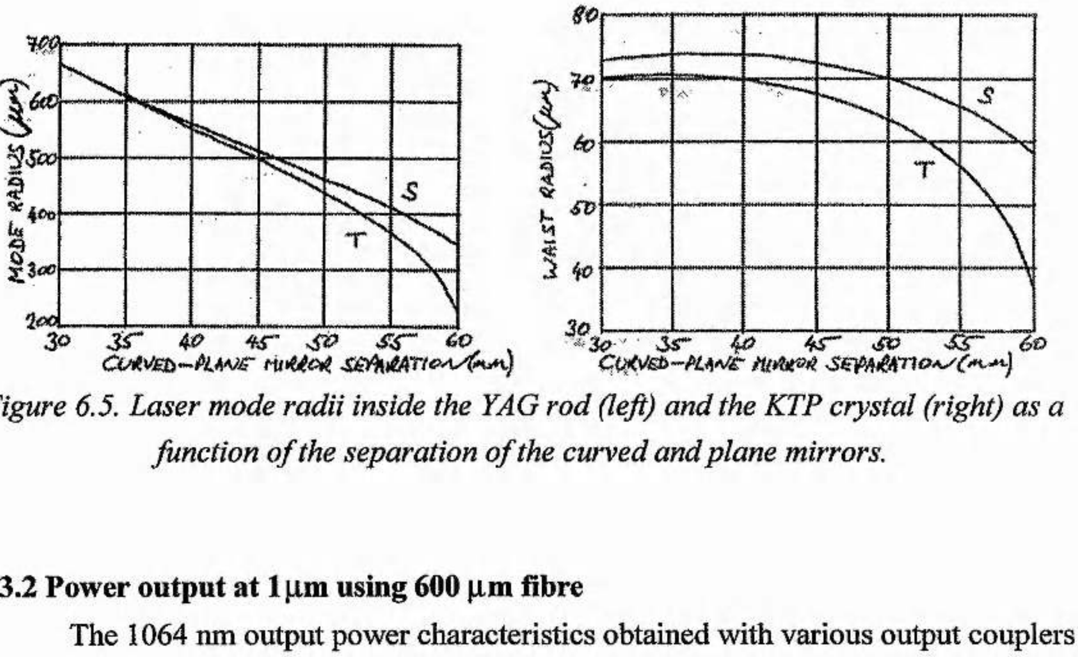

Figure 6.5. Laser mode radii inside the YAG rod (left) and the KTP crystal (right) as a function of the separation of the curved and plane mirrors.

6.3.2 Power output at 1 µm using 600 µm fibre

The 1064 nm output power characteristics obtained with various output couplers are shown in Figure 6.6. The pump power is that incident on the quarter-wave plate after passing through the coupling optics. For pump powers higher than ≈ 20 W, the slope efficiencies dropped appreciably due to thermal lensing effects. The highest slope efficiency obtained was 43% (for pumping < 20 W), using a 10% output coupler. For a pump power of 30 W, 10 W of output power at 1064 nm were obtained. As predicted in section 6.3.1, maximum output and slope efficiency were obtained using a pump spot size of ≈ 600 µm in the Nd:YAG rod, *i.e.* the fibre tip and the end of the rod were both

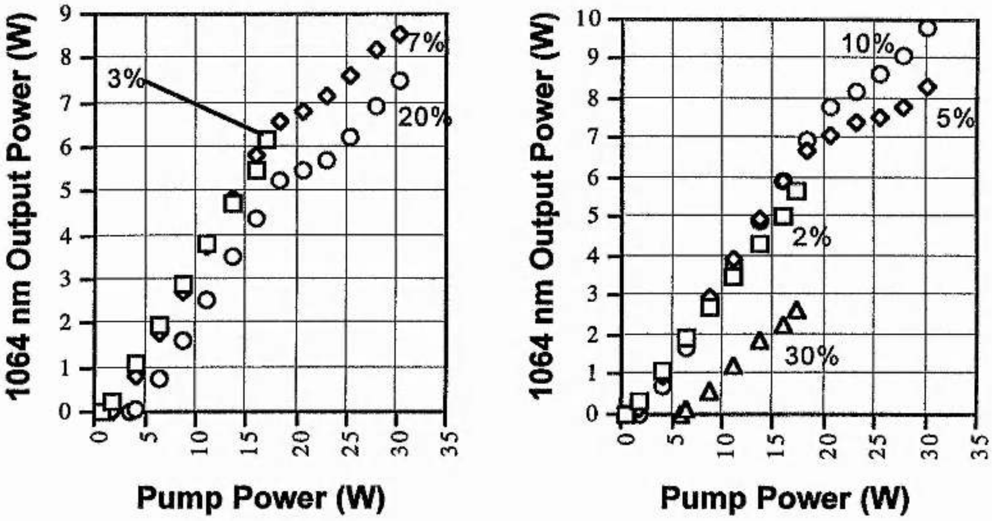

Figure 6.6. 1064 nm Nd:YAG laser output using 600 μm fibre.

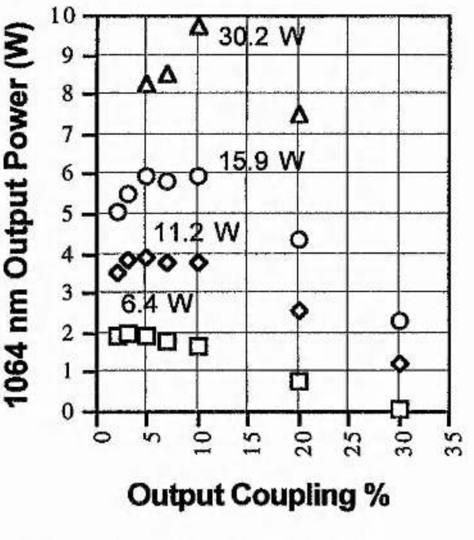

Figure 6.7. Output power against output coupling using the 600 μm fibre.

≈ 12 mm from the coupling optics. Other slope efficiencies were 34% using a 2% coupler, and 40% using a 5% coupler. By comparing the various slopes, the internal loss of the laser was estimated as ≈ 0.6 %. Plotting output power against coupling for various pumping levels, the unsaturated gain at the full pump of 30 W was estimated to be in the region of 45%. Given the very low internal loss of the laser, the slope efficiencies can be used to give an estimate of the product $\eta_1\eta_2$ as described in Chapter 1. Given $\lambda_p / \lambda_s = 0.76$, a slope efficiency of 0.43 indicates that $\eta_1\eta_2 \approx 0.43 / 0.76 = 0.57$.

6.3.3 Power output at 1 μm using 400 μm fibre

The laser was also operated at 1 μm using a 400 μm core mutlimode fibre to deliver the pump radiation. The available power from the fibre tip had to be limited to ≈ 10 W in this case in order to avoid damage to the bundle end of the fibre. Damage often resulted by excessive heating caused by the relatively inefficient (≈ 50%) coupling from bundle to fibre when using the 400 μm fibre. Figure 6.8 shows the various slopes obtained. Optimum operation was achieved when the fibre tip was ≈ 9 mm from the coupling optics and the pump spot ≈ 15 mm from the optics. The pump spot was therefore slightly magnified compared to the fibre-tip. A 10% output coupler again produced the best result, giving 3.27 W at 1064 nm for 9.7 W pump power. The slope efficiency was 39%. The efficiency at this pumping level was slightly higher than when using the the 600 μm fibre, which gave 3.14 W at 9.7 W pumping. Given the smaller core, the 400 μm fibre should also have produced a higher slope efficiency but this was not found to be the case.

By comparing slope efficiencies, the internal loss was this time estimated to be 0.7%. Output power as a function of output coupling is shown in Figure 6.9 for four different pumping levels. At the 10 W level, the unsaturated gain was ≈ 35%.

6.3.4 1 μm beam quality

The M^2 factor of the 1064 nm output beam was measured at two pumping levels; the separation of the curved and plane mirrors for this was 45 mm. The pump radiation was delivered by the 600 μm fibre. The results are summarsied in Table 6.2. The beam diameter was measured immediately after the output coupler, and also at distances of 15 cm and 30 cm in order to determine the beam divergence. The far field

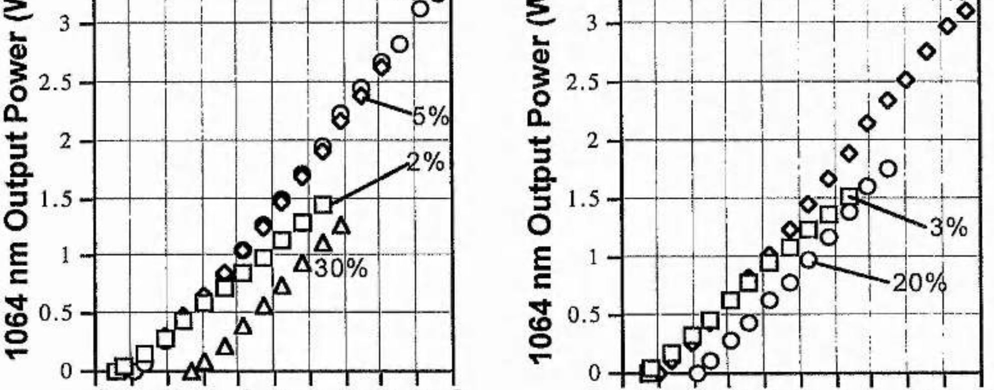

Figure 6.8. 1064 nm Nd:YAG laser output using 400 μm fibre.

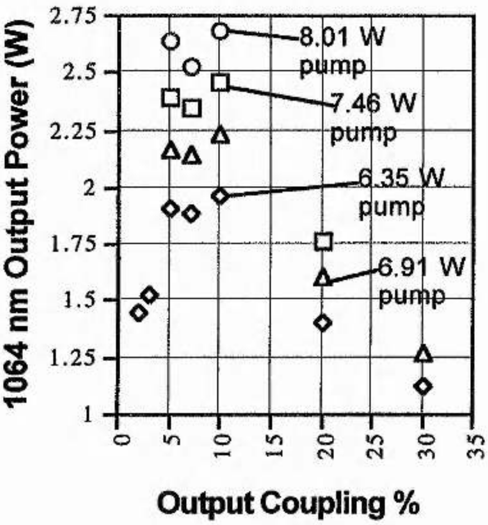

Figure 6.9. Output power against output coupling using the 400 μm fibre.

	Vertical plane	Horizontal plane
Waist Radius W_0 (μm)	78 (79)	75 (83)
Far field diffractiion angle θ (mrads)	4.57 (5.11)	5.64 (5.40)
M^2	1.0 (1.2)	1.2 (1.3)

Table 6.2. Beam quality measurements for 1064 nm. Pump power = 12.7 W; values for 19.3 W pump shown in parentheses.

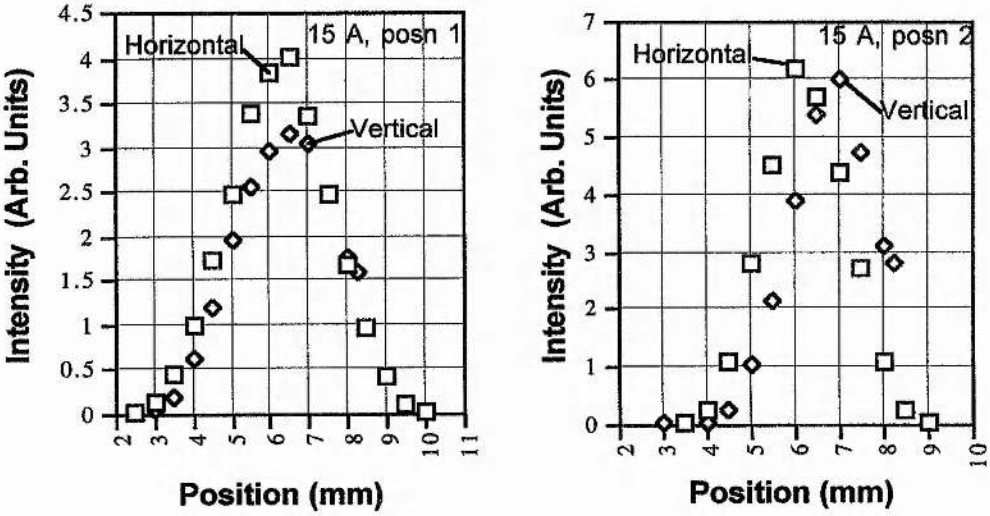

Figure 6.10. 1064 nm beam profiles at 15 cm (left) and 30 cm from the output coupler. (Pump power = 12.7 W.)

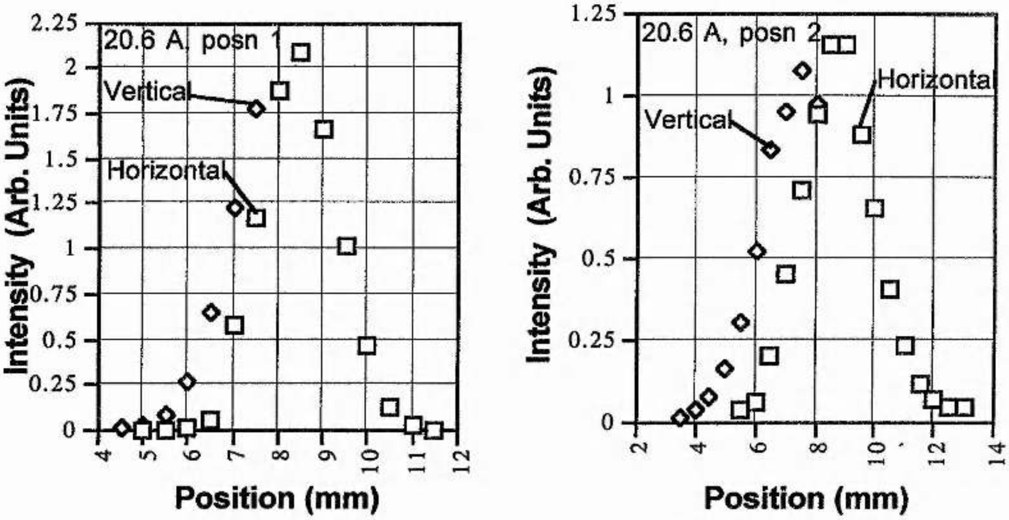

Figure 6.11. 1064 nm beam profiles at 15 cm (left) and 30 cm from the output coupler. (Pump power = 19.3 W.)

profiles are shown in Figure 6.10 and 6.11. These show the beam quality to be much better than those obtained from the two ring lasers, and this can be attributed to the superior quality of the pump-beam.

6.3.5 Intracavity frequency-doubling using KTP

6.3.5.1 Polarisation scheme of Oka and Kubota

The polariation scheme of Oka and Kubota [6.11] was used to avoid chaotic behaviour in the green output. Intracavity polarisation schemes are best analysed using Jones matrices to find the eigenvectors and eigenstates, as was described in Chapter 4. Several good reviews have been written on the method [6.15, 16, 4.9], which is applicable to any anisotropic resonator. For example, the scheme whereby a KTP crystal and a Brewster plate form a birefringent filter giving single-frequency operation at low pump powers can be analysed by this technique [6.17, 18].

The Jones method can be used to show that in any anisotropic resonator there are two possible polarisation eigenstates. The two states are linearly polarised, mutually orthogonal and aligned along the principal birefringent axes. The round-trip Jones matrix in this case is

$$\begin{pmatrix} e^{i\Gamma} & 0 \\ 0 & e^{-i\Gamma} \end{pmatrix},$$

where Γ is the single-pass phase retardation. The eigenvalues are simply $e^{\pm i\Gamma}$, indicating unity intensity transmission, as expected if there are no elements introducing loss, such as a Brewster plate. To find the polarisation eigenstates, the simplest method

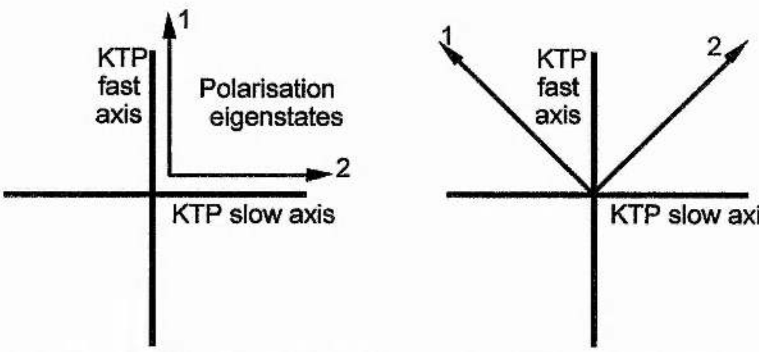

Figure 6.12. Polarisation eigenstates for a resonator with KTP. Left - without λ /4 plate; right - with λ /4 plate

is to work in a frame which is rotated from the birefringent axes by 45°. The round-trip Jones matrix is then

$$\begin{pmatrix}1 & -1\\ 1 & 1\end{pmatrix}\begin{pmatrix}e^{i\Gamma} & 0\\ 0 & e^{-i\Gamma}\end{pmatrix}\begin{pmatrix}1 & 1\\ -1 & 1\end{pmatrix}=\begin{pmatrix}\cos\Gamma & i\sin\Gamma\\ i\sin\Gamma & \cos\Gamma\end{pmatrix}.$$

The ratios E_y / E_x of the components of the eigenstates for this matrix are 1 and -1, *i.e.* the two components have equal moduli and are either in phase or 180° out of phase, corresponding to linearly polarised states polarised along the birefringent axes. Thus simply by inserting a KTP crystal into an isotropic resonator will automatically give two polarisation eigenstates which satisfy the type II phase-matching requirement, as shown in Figure 6.12 (left). Unfortunately, this arrangement leads to the "green problem". If the two states (modes) have frequencies ω_1, ω_2 the intensity at the second-harmonic (or more accurately, the sum-frequency) is given by

$$I(\omega_1+\omega_2)\sim\left\langle P(\omega_1+\omega_2)P^*(\omega_1+\omega_2)\right\rangle = d_{eff}{}^2|E_1(\omega_1)|^2|E_2(\omega_2)|^2 = d_{eff}{}^2 I_1(\omega_1)I_2(\omega_2).$$

The coupling of the two modes by the nonlinear process leads to instability.

By using a quarter-wave plate inside the cavity, with its axes at 45° to those of the KTP crystal, as in the Oka and Kubota scheme, separate doubling of the two modes is achieved, removing the nonlinear coupling of the fundamental modes. The Jones-matrix analysis of this arrangement is tiresome to carry out analytically, and is best done by computer. The round-trip Jones matrix (starting and finishing at the KTP crystal) is given by the product

$$\begin{pmatrix}e^{i\Gamma/2} & 0\\ 0 & e^{-i\Gamma/2}\end{pmatrix}\begin{pmatrix}1 & -1\\ 1 & 1\end{pmatrix}\begin{pmatrix}e^{i\pi/2} & 0\\ 0 & e^{-i\pi/2}\end{pmatrix}\begin{pmatrix}1 & 1\\ -1 & 1\end{pmatrix}\begin{pmatrix}e^{i\Gamma/2} & 0\\ 0 & e^{-i\Gamma/2}\end{pmatrix}.$$

Here the laboratory frame coincides with the KTP axes. The central matrix accounts for the double-passing of the quarter-wave plate. The round-trip intensity transmission of both states is unity for all Γ. The arguments of the component ratios E_y / E_x for the two states are shown in Figure 6.13 as a function of the single-pass phase retardation of the KTP, Γ. The moduli are always unity (independent of Γ). The relative phases of the components for the two states rapidly switch between 180° and -180°, and the states are therefore linearly polarised at ± 45° to the KTP axes, as shown in Figure 6.12 (right). The polarisation at the sum-frequency of the two modes is

$$P(\omega_1+\omega_2)\sim d_{eff}\left(\frac{E_1(\omega_1)+E_2(\omega_2)}{\sqrt{2}}\right)\left(\frac{E_1(\omega_1)-E_2(\omega_2)}{\sqrt{2}}\right)=\frac{d_{eff}}{2}\left[E_1^{\,2}(\omega_1)-E_2^{\,2}(\omega_2)\right],$$

and the sum-frequency intensity is now given by

$$I(\omega_1+\omega_2)\sim d_{eff}^{\;2}\left\langle[E_1^{\,2}(\omega_1)-E_2^{\,2}(\omega_2)][E_1^{\,2}(\omega_1)-E_2^{\,2}(\omega_2)]^*\right\rangle$$

$$=\frac{d_{eff}^{\;2}}{4}\left\{|E_1(\omega_1)|^4+|E_2(\omega_2)|^4-2|E_1(\omega_1)|^2|E_2(\omega_2)|^2\langle\cos2[(\omega_1-\omega_2)t-(\phi_1-\phi_2)]\rangle\right\}$$

$$=\frac{d_{eff}^{\;2}}{4}\left\{I_1^{\,2}(\omega_1)+I_2^{\,2}(\omega_2)\right\}.$$

The modes are therefore separately doubled and not coupled together by the nonlinear process. Even if more than two modes are above threshold, no two modes are coupled: if they have the same polarisation eigenstate they will not satisfy the type II phase-matching requirement.

One possible cause of instability in the Oka and Kubota system is the presence of significant birefringence in the Nd:YAG rod, which may be produced at high pumping levels. As a simple demonstration of the effect this might have, a matrix of the form

$$\begin{pmatrix} e^{i\psi} & 0 \\ 0 & e^{-i\psi} \end{pmatrix}$$

can be included in the round-trip Jones matrix, where ψ is the single-pass phase retardation of the Nd:YAG rod. Taking ψ = 30° as an example, it is found that the moduli of the ratios E_y / E_x for the two eigenstates again switch rapidly between -180° and +180° as Γ is increased from 0° to 180°. However the moduli no longer stay fixed at unity as Γ varies, but behave as shown in Figure 6.14. This figure also displays rapid switching between the two egdes of the envelope. At a given Γ the two states are on opposite edges. The implication is that the eigenstates at the KTP crystal are elliptically polarised, the extent of ellipticity increasing with increasing birefringence in the YAG rod. This may well cause the Oka and Kubota scheme to break down at high pump powers.

6.3.5.2 Output Power at 532 nm

Intracavity frequency-doubling was carried out by replacing the plane output coupler with a plane high reflector (at both 1064 nm and 532 nm) so that the visible light issued from the curved mirror. The KTP was placed as close as possible to the plane mirror in order to access the small mode size, and the crystal was rotated so that its axes were at 45° to those of the quarter-wave plate. An adjustable aperture was inserted into the cavity near to the Nd:YAG rod to avoid operation on higher order

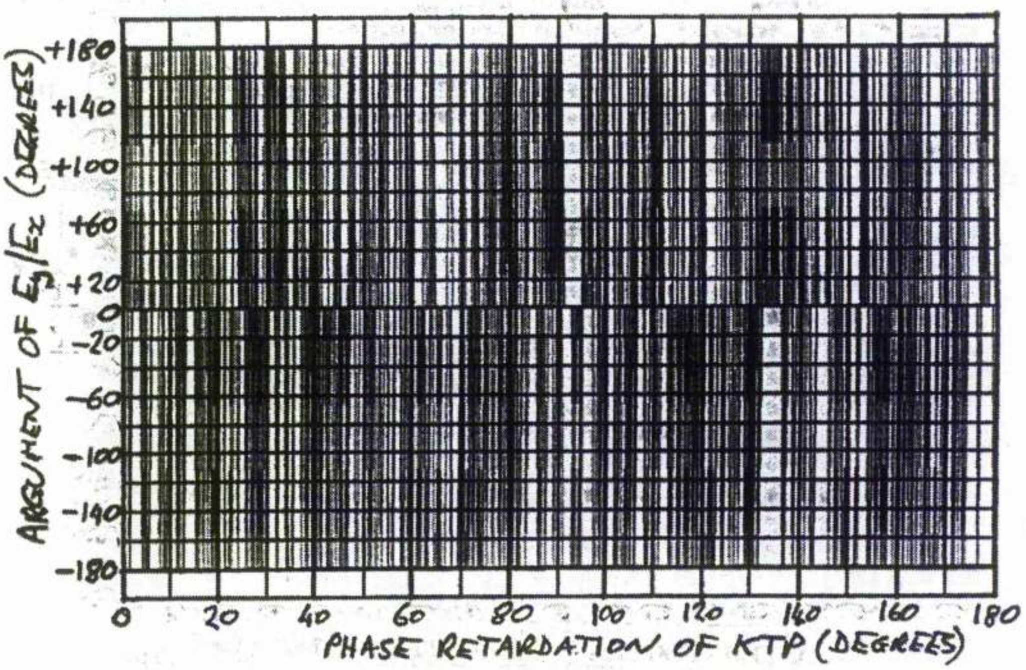

Figure 6.13. Relative phases of the components of the polarisation eigenstates versus phase retardation of the KTP crystal in the Oka and Kubota scheme.

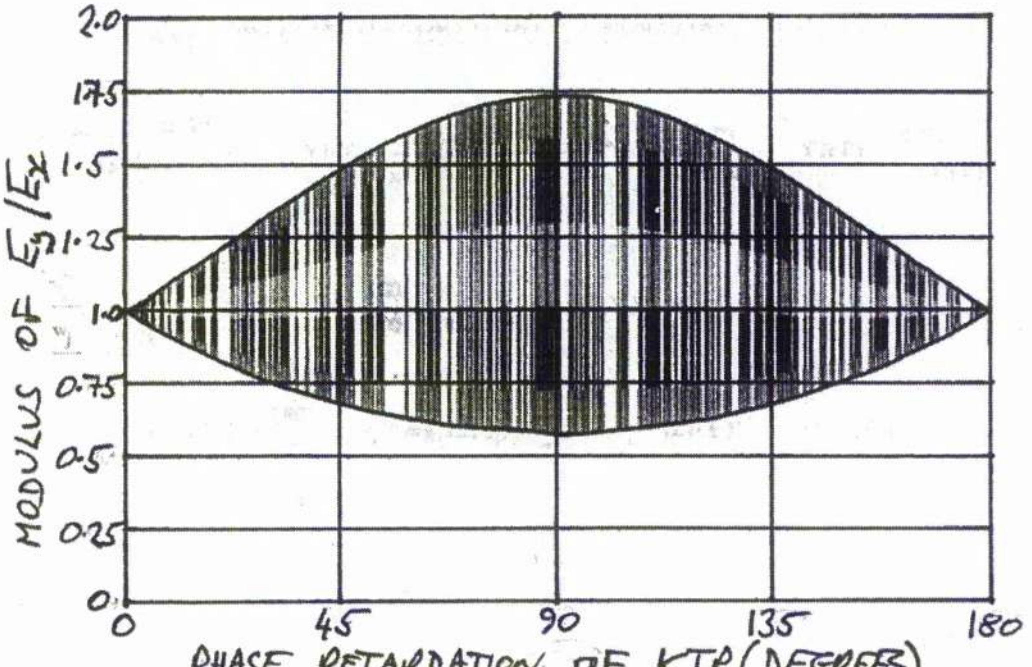

Figure 6.14. Modulii of the ratios of the components of the eigenvectors versus phase retardation of KTP; retardation of Nd:YAG = 30°.

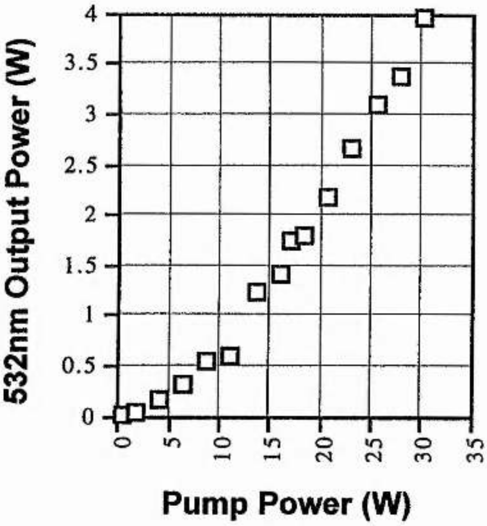

Figure 6.15. 532 nm output power.

transverse modes. To restrict the number of longitudinal modes, a low finesse etalon was also inserted.

An example of the 532 nm output power behaviour (when the pump light was delivered with the 600 μm fibre) is shown in Figure 6.15. The highest visible power achieved was 3.98 W at the full pump power of 30 W, representing an optical-to-optical conversion efficiency of 13%. Each of the points in Figure 6.15 represents the power achieved after full optimisation of the system, *i.e.* adjustment of the KTP crystal, aperture, etalon, plane mirror, fibre-tip position and coupling optics. When operating stably, the laser oscillated on two fundamental longitudinal modes which were spaced by approximately 450 MHz. (The beat frequency in the visible output was measured on a spectrum analyser and found to be typically 900 MHz.) The resonator was typically 320 mm long during visible operation, corresponding to a mode spacing of 469 MHz. The slightly lower frequency spacing of the longitudinal modes indicates that the etalon selected one longitudinal mode from each polarisation set.

The 1 μm leakage from the plane high reflector was monitored on a scanning confocal Fabry-Perot interferometer. A typical dual-peaked trace is shown in Figure 6.16 (two scans are shown.) The laser operated quietly in this state for output powers up to ≈ 2 W. At pump powers over 20 W, more than two modes generally oscillated and there was considerable instability in the output power. At full pump power, stable two-mode operation was not achieved for more than ≈ 5 seconds. The instability was caused by two main factors. Firstly, although the etalons had free spectral ranges of 180 - 200 GHz (*i.e.* greater than the gain bandwidth of Nd:YAG) their finesses were low (in the range 1.4 - 3.8). For example, for one of the etalons used, the spectral FWHM was equivalent to 110 mode spacings. At high pump powers there was therefore insufficient discrimination between the longitudinal modes. Low finesse etalons were chosen in order not to restrict the visible power output, but at high pump levels there is clearly a compromise to be reached if quiet operation is to be maintained. Another reason for the instability may have been the presence of birefringence in the Nd:YAG rod. As explained in section 6.3.5.1 above, this may have led to slightly elliptical polarisation eigenstates and therefore some nonlinear coupling of the fundamental modes, giving rise to chaotic operation.

The green power performance of the laser can be assessed as for the other lasers. The round trip unsaturated gain was estimated as ≈ 45% and the internal linear loss ≈ 0.6%. Assuming that the maximum 1064 nm power was achieved at approximately optimum output coupling, the saturation power of the laser was

$$P_{sat} \approx \frac{2\times 10}{\left(\sqrt{0.45}-\sqrt{0.006}\right)^2} = 57W.$$

The optimum nonlinear coupling was therefore

$$\kappa_{opt} = \frac{0.006}{2\times 57} = 5.26\times 10^{-5} W^{-1}.$$

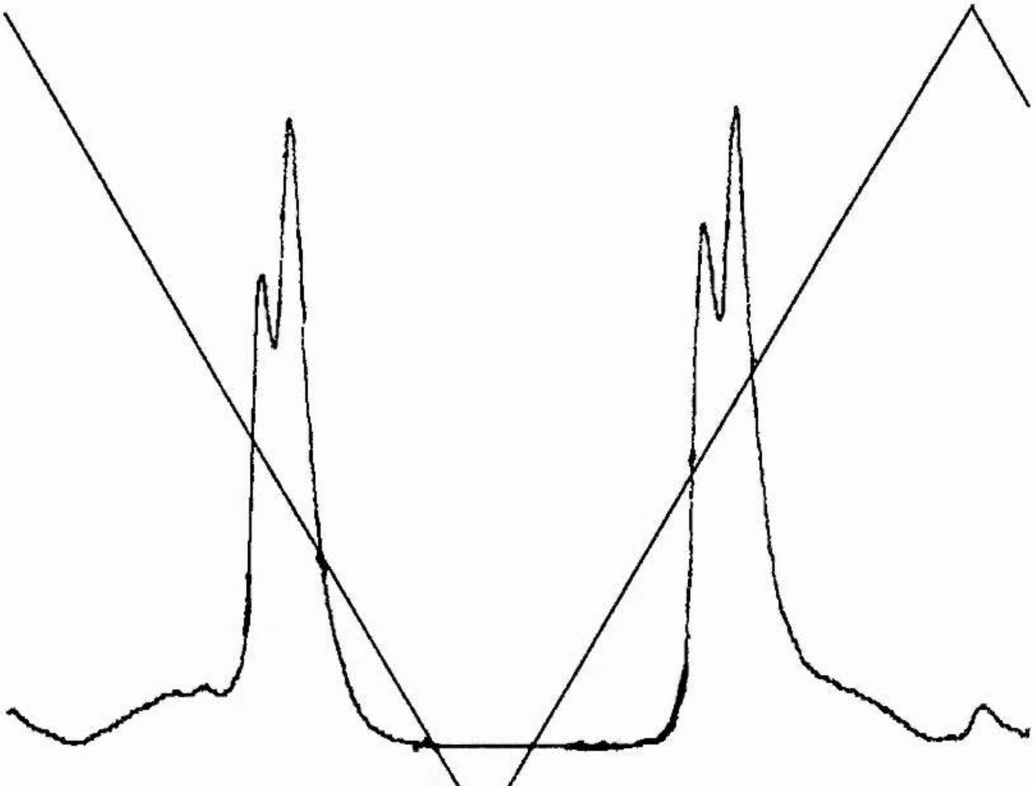

Figure 6.16. Longitudinal fundamental mode structure of the intracavity-doubled Nd:YAG standing-wave laser.

The Boyd and Kleinman value for optimum nonlinearity in a 5 mm length of KTP is 4.39×10^{-3} W^{-1}, although this is something of an over-estimate due to Poynting vector walk-off. Nevertheless, the high effective nonlinearity of KTP coupled with the high gain and low internal linear loss of the laser would indicate that optimum coupling may have been achievable resulting in green output powers of perhaps 7 - 8 W. The generation of 4 W of visible power is equivalent to a nonlinear coupling two orders of magnitude below the optimum value. Although some loss of power may be attributed to under-coupling due to the relatively large (≈ 70 μm) waist radius in the KTP, other factors such as the loss introduced by the etalon and self-misalignment of the laser due to walk-off in the KTP may have also been responsible for the green power not reaching its full potential.

6.3.5.3 532 nm Beam Quality

The 532 nm beam quality was investigated at the 2 W level. A 50 mm focal length lens was used to produce a waist radius of 96 μm (in both planes) and a scanning pinhole was used to measure the far-field beam divergence. The beam divergence was measured as 4.23 mrad in the horizontal plane and 3.87 mrad in the vertical plane, corresponding to M^2 values of 1.2 and 1.1 respectively. A pair of profiles is shown in Figure 6.17. Careful use of the aperture allowed TEM_{00} visible output up to the full pump power of 30 W.

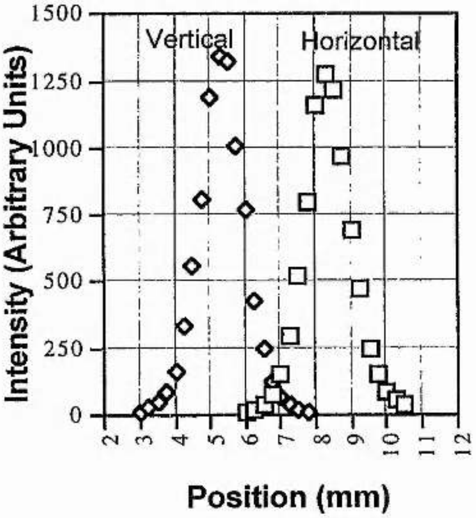

Figure 6.17. Beam profiles of visible output.

6.4 End-Pumped Nd:YVO$_4$ Laser

6.4.1 Introduction

Recently, diode-pumped bulk Nd:YVO$_4$ lasers have shown very impressive performance both at 1 μm and when intracavity frequency-doubled [6.1, 2, 3], achieving unprecedented output powers and efficiencies. This new generation of high-power systems all have the common features of end-pumping with fibre-coupled diode-bars and the use of Nd:YVO$_4$ as the gain material. In the past, the very strong π absorption of this gain medium has been exploited only in low-power and microchip lasers because of its very low thermal conductivity, which is even less than that of YLF. However, the bright, symmetrical pump beams available from fibre-coupled diode-bars have allowed accurate end-pumping of the laser mode-volume, and the short absorption depth of Nd:YVO$_4$ has meant that almost all of the pump light is absorbed before the spatial extent of the pump extends beyond that of the signal. This high degree of pump-mode overlap leads not only to very low thresholds and high slopes efficiencies (often > 50%), but also to reduced heating and thermal lensing.

Given these ideas, the Nd:YAG system decribed in section 6.3 above was rebuilt with a 6 mm long block of Nd:YVO$_4$ as the gain element. The cross-section was square with side 3 mm. As before, the laser crystal was heat-sunk with indium foil in a water-cooled copper block. The resonator was left unchanged. Both 600 μm and 400μm-core multimode fibres were used to deliver the pump power, and internal frequency-doubling was again carried out using KTP. A scanning monochromator trace of the Nd:YVO$_4$ fluorescence is shown in Figure 6.18. The principal radiative emission is at ≈ 1064 nm.

6.4.2 Power Output at 1 μm

Various slopes obtained using the 600 μm fibre are shown in Figure 6.19. Using a 10% output coupler, the highest output power achieved was 5.1 W for a pump power of 13.5 W. The slope efficiency using the 10% output coupler was 41.3%; this was actually less than that achieved with the same coupler in the Nd:YAG laser. Comparing slopes indicated an internal loss of ≈ 1.5% which explains the reduced slope compared to the Nd:YAG laser. Since the rest of the laser was unchanged, it would seem that the quality of the YAG crystal was better than that of the YVO$_4$. At the 13.5 W pump level, the unsaturated gain was estimated at 35 - 40%.

The maximum pump power delivered using the 400μm fibre was 9.2 W. At this level, 3.27 W output was achieved with a slope efficiency of 40.8%, again using a 10% output coupler. As with the Nd:YAG system, there was no increase in slope efficiency when using the smaller-core fibre. However the slope obtained with the YVO$_4$ laser

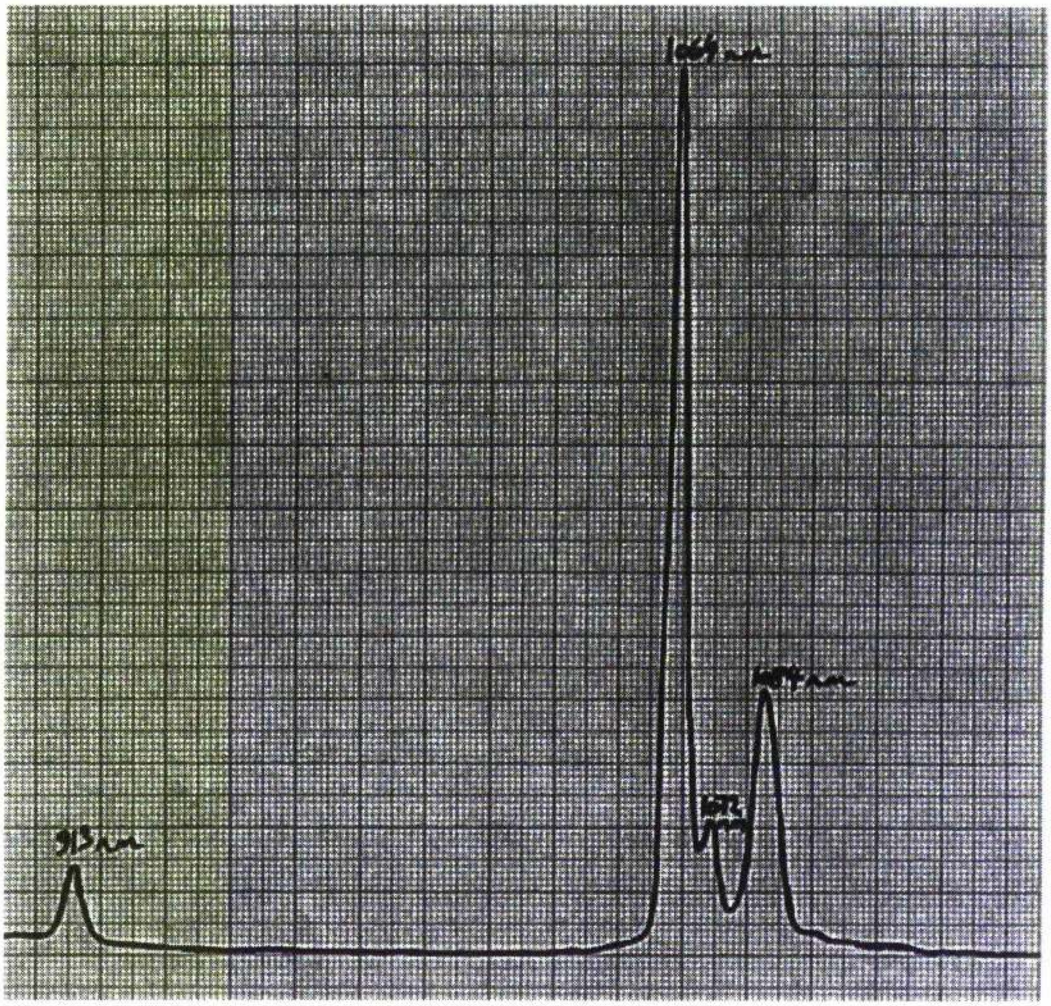

Figure 6.18. Nd:YVO$_4$ fluorescence.

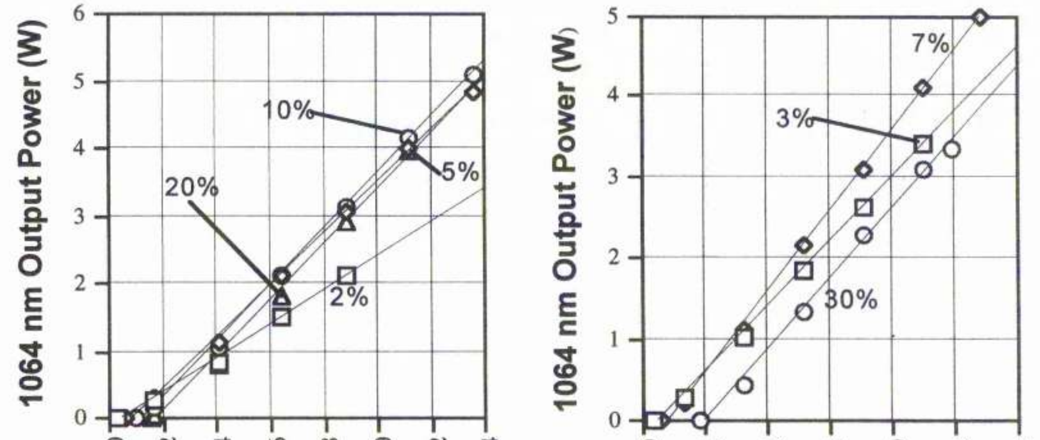

Figure 6.19. Nd:YVO$_4$ laser output using 600 μm fibre.

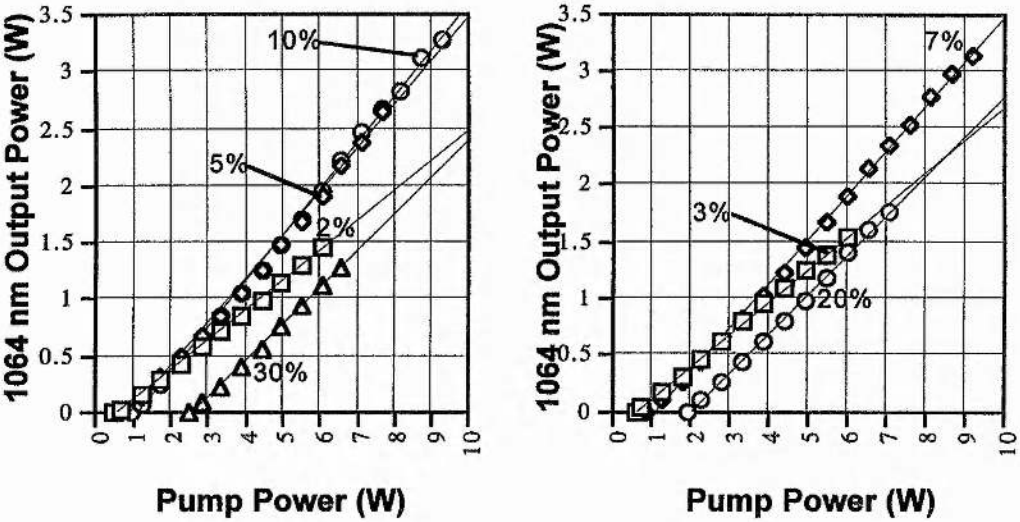

Figure 6.20. Nd:YVO$_4$ laser output using 400 μm fibre.

with the 400 μm fibre was greater than that obtained with the YAG laser, but only by 1.8%. Other slopes are shown in Figure 6.20. The internal loss and highest unsaturated gain were estimsted as 1.8% and 35% repectively.

6.4.3 Internal Frequency-Doubling Using KTP

Given the fact that the Oka and Kubota polarisation scheme works regardless of the retardation of the KTP crystal, it can be adapted easily for use with birefringent gain media such as Nd:YLF and Nd:YVO$_4$. In the present case, the KTP was arranged with

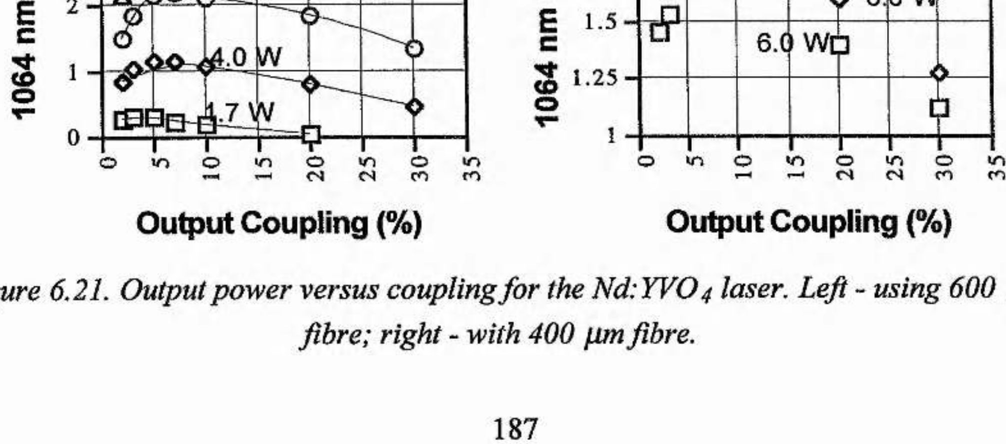

Figure 6.21. Output power versus coupling for the Nd:YVO$_4$ laser. Left - using 600 μm fibre; right - with 400 μm fibre.

its axes coincident with those of the Nd:YVO_4 crystal, and the quarter-wave plate was set with its axes at 45° to this frame. As with the Nd:YAG laser, stable two-mode green output was achieved up to 2 W, the mode structure being similar to that shown in Figure 6.16. For a pump power of 13.5 W (from the 600 μm fibre) 2.01 W green power was achieved, representing an optical-to optical efficiency of 15%.

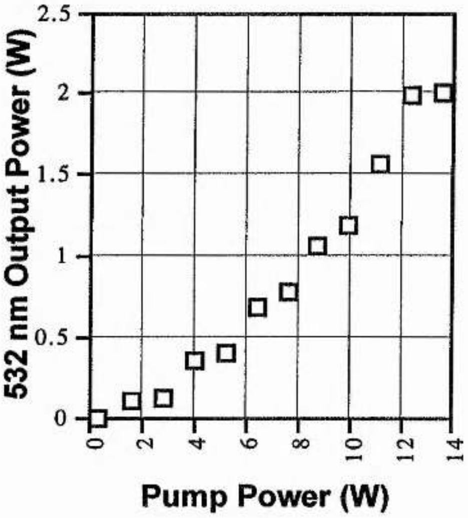

Figure 6.22. Visible output power from the intracavity-doubled Nd:YVO_4 laser.

6.5 End-Pumped Nd:YAG Ring Laser

6.5.1 Introduction

The concept of internal beam-folding together with end-pumping can be easily extended to form a ring laser. When end-pumped by a symmetrical beam such as that from a fibre-coupled diode-bar or a re-shaped bar, efficient, quiet single-frequency visible lasers have been produced by internal frequency-doubling [6.3, 19].

The fibre-coupled diode-bars used previously were used with the 600 μm fibre to pump such a ring laser, as shown in Figure 6.23. Given the thermal problems experienced with the Nd:YVO_4 sample, a 6 mm Nd:YAG rod was used as the gain medium. The simplicity of this ring meant that the internal angle could be reduced to ≈ 15°, almost eliminating astigmatism in the output beams. The limiting factors on the internal angle were the diameter of the Nd:YAG rod and the brightness of the pump source. Unidirectional operation was achieved by the use of a Faraday rotator, half-wave plate and a glass Brewster plate. Large aspheric lenses of focal length 53 mm were used to couple the pump light into the Nd:YAG rod. These gave a working

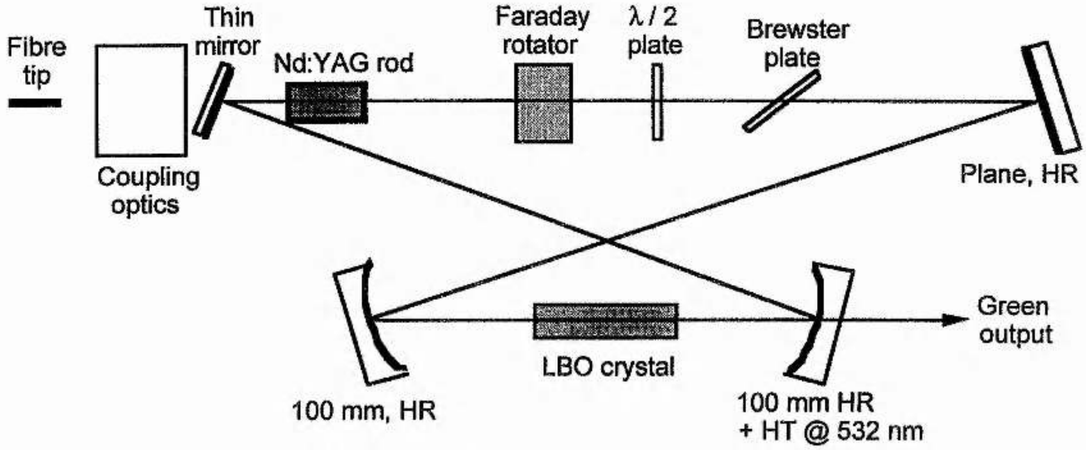

Figure 6.23. Intracavity-doubled Nd:YAG ring laser.

distance of 40 mm from the plane surface of the second aspheric lens to the pump image for 1:1 imaging from fibre-tip to the pump spot. This was required because of the folding of the beam path.

The 1 μm output performance of the bidirectional laser is shown in Figure 6.24. Unlike the standing wave YAG laser discussed in section 6.3, this device showed significant thermal problems in the output. The output power is also less; both problems were probably a result of lower pump-mode overlap because of the smaller mode size. The highest power output was 4.2 W at a pump power of 24.3 W. A 3% output coupler was used; the slope efficiency was 40%. Comparing the slope efficiencies at pump powers up to 12 W indicated an internal loss of ≈ 0.2%. The unsaturated gain at full pump power (24.3 W) was ≈ 15%.

The performance of the unidirectional laser is shown in Figure 6.25. The highest

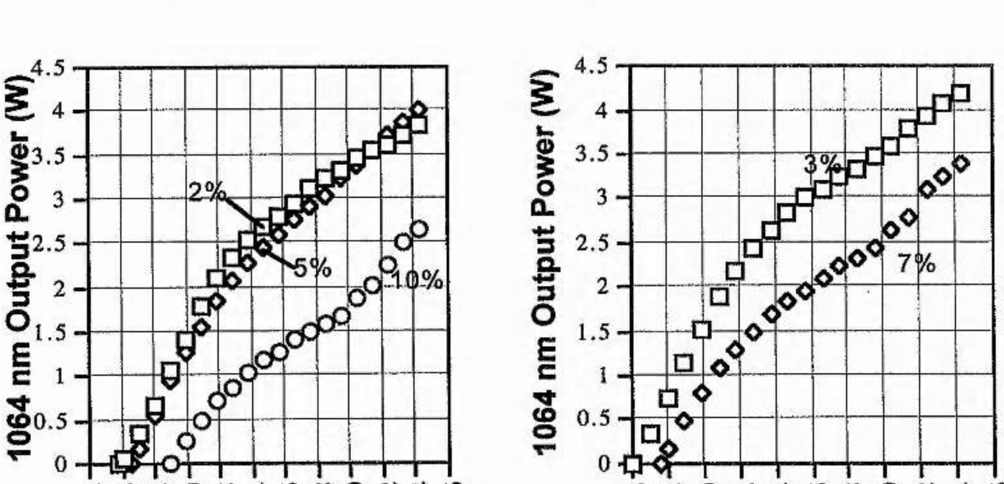

Figure 6.24. Output at 1 μm for the bidirectional laser.

output power obtained was 2.28 W at a pump power of of 23.3 W. The output coupling was 5%; the slope efficiency was 20%. The low output power and slope were probably due to the loss of the Faraday rotator, although comparison of the slope efficiencies up to ≈ 14 W pump power indicated an internal loss of only ≈ 1%. Given the internal loss and the maximum output and estimated unsaturated gain, the saturation power can be estimated as

$$P_{sat} = \frac{2.28}{\left(\sqrt{0.15} - \sqrt{0.01}\right)^2} \approx 28W.$$

The optimum nonlinear coupling was therefore

$$\kappa_{opt} = \frac{\delta}{P_{sat}} = 3.6 \times 10^{-4} W^{-1}.$$

With Boyd and Kleinman focusing, a coupling of $7.3 \times 10^{-4}\ W^{-1}$ should be achievable in a 25 mm LBO crystal. The possiblilty of extracting the full 2.28 W as green output should therefore have been possible. However, the maximum power generated at 532 nm was only 1.29 W. This corresponds to the actual κ being approximately 18 times less than the optimum value.

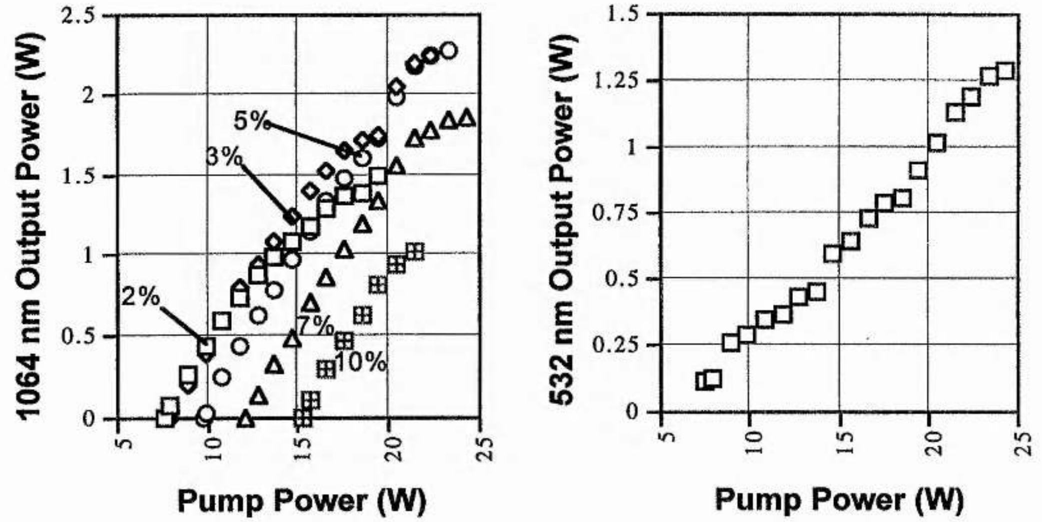

Figure 6.25. Output power from the unidirectional laser: left - 1064 nm; right - 532 nm.

6.6 Concluding Remarks

The lasers discussed in this chapter demonstrate the effectiveness of using fibre-coupled diode-bars as pump devices. The standing-wave Nd:YAG laser in particular showed powers and efficiencies unattainable from simple side-pumped devices or lasers

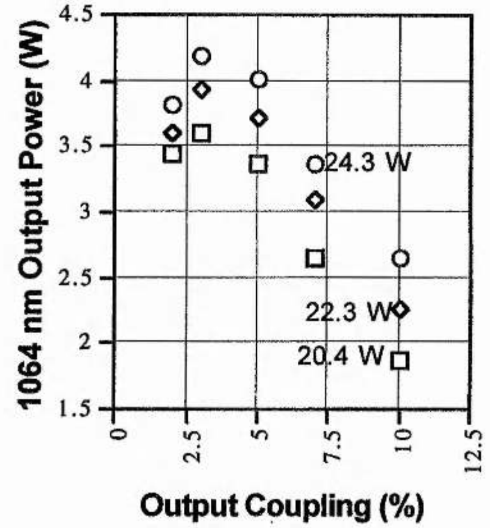

Figure 6.26. Output power versus output coupling for the bidirectional laser.

end-pumped directly by the output of a diode-bar. Very low thresholds and high slope efficiencies in the region of 40 - 50% are now quite commonplace when these pump devices are used, the result being that 1 μm powers in the 10 - 15 W range are quite readily achieved using only two bars, whereas two or three years ago such output could only be obtained from large side-pumped systems employing multiple stacks of bars.

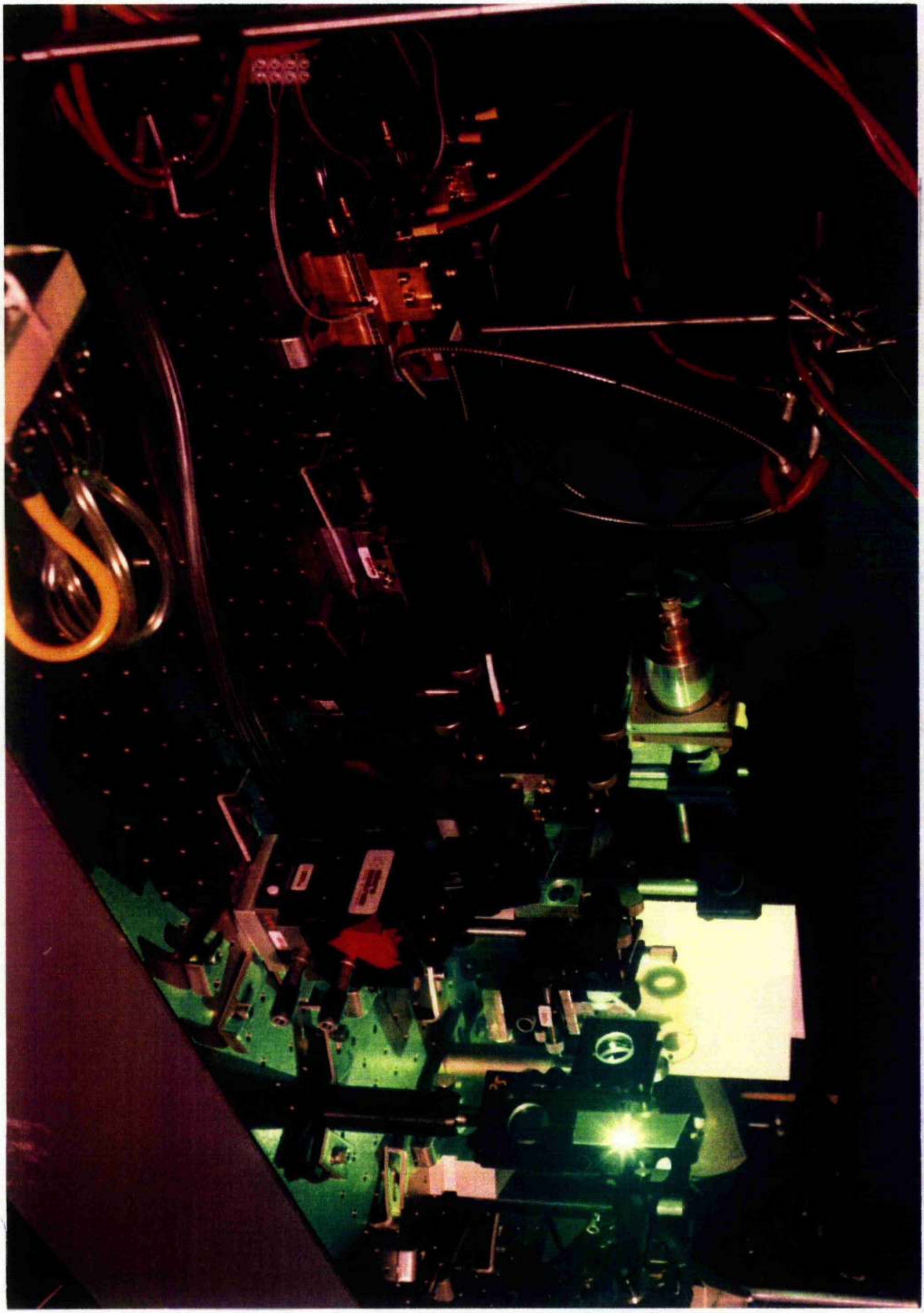

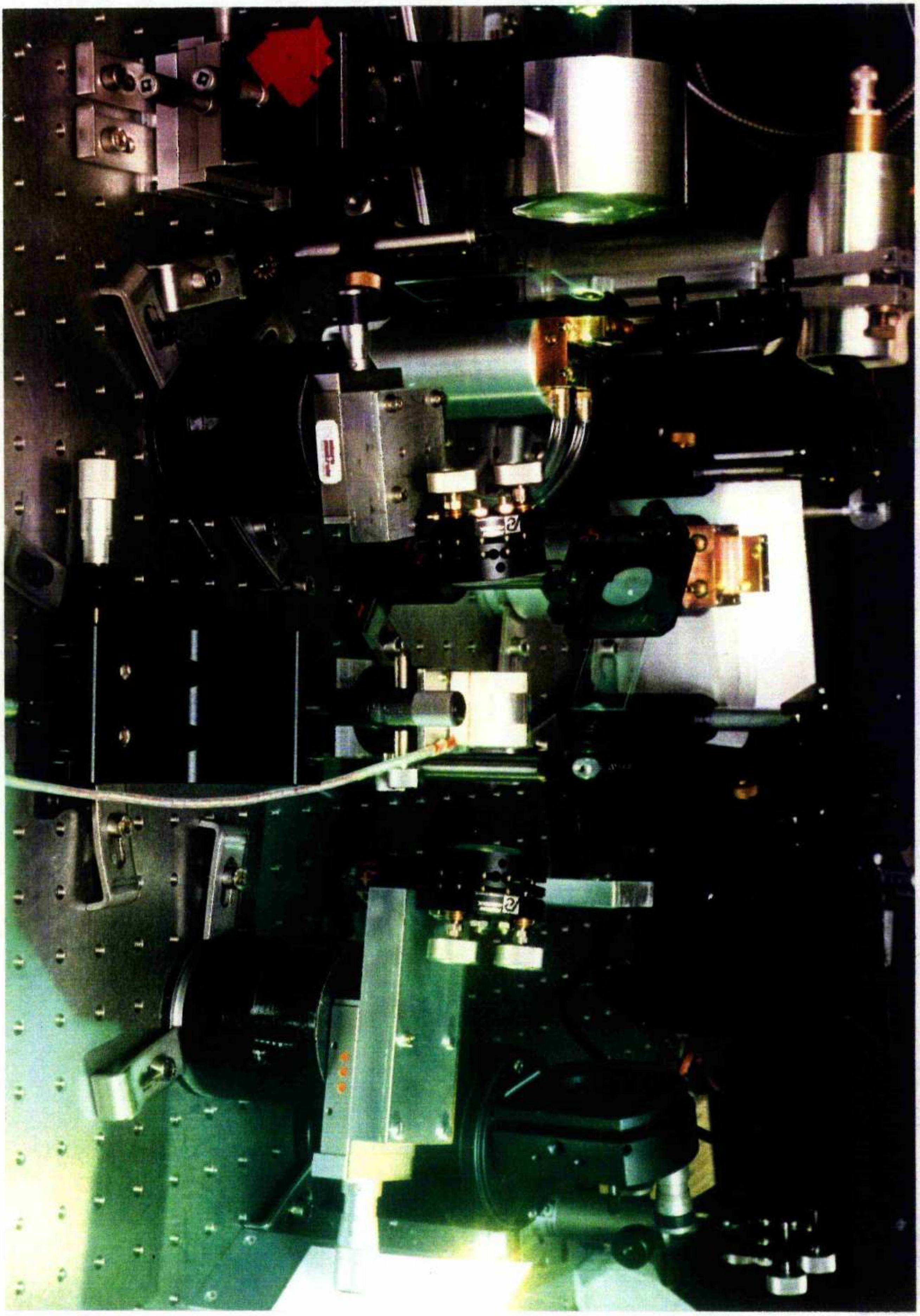

References

[6.1] W. L. Nighan Jr., D. Dudley, M. S. Kierstead: "Diode-bar-pumped Nd:YVO_4 lasers with > 13 W TEM_{00} output at >50% efficiency": *Conf. on Lasers & Electroopt. OSA Tech. Dig.* **15** 17 (1995) paper CMD5

[6.2] W. L. Nighan Jr., J. Cole: "> 6 W of stable 532 nm TEM_{00} output at 30% efficiency from an intra-cavity doubled diode-pumped multiaxial mode Nd:YVO_4 laser": *Conf. on Advanced Solid-State Lasers* (1996)

[6.3] M. D. Selker, T. J. Johnston, G. Frangineas, J. L. Nightingale, D. K. Negas: ">8.5 W single-frequency 532 nm light from a diode-pumped intra-cavity doubled ring laser": *Conf. on Lasers & Electroopt.* post-deadline paper CPD21 (1995)

[6.4] K. Kubodera, J. Noda: "Pure single-mode LNP solid-state laser transmitter for 1.3 μm fibre-optic communication": *App. Opt.* **21** 3466 (1982)

[6.5] J. Berger, D. F. Welch, W. Streifer, D. R. Scifres, N. J. Hoffman, J. J. Smith, D. Radecki: "Fiber-bundle coupled, diode end-pumped Nd:YAG laser": *Opt. Lett.* **13** 306 (1988)

[6.6] Y. Kaneda, M. Oka, H. Masuda, S. Kubota: "7.6 W of continuous-wave radiation in a TEM_{00} mode from a laser-diode end-pumped Nd:YAG laser": *Opt. Lett.* **17** 1003 (1992)

[6.7] D. C. Shannon, D. L. Vecht, S. Re, J. Alonis, R. W. Wallace: "High average diode-pumped lasers near 2 μm": *SPIE* **1865** 164 (1993)

[6.8] T. Y. Fan: "Single-axial mode intracavity-doubled Nd:YAG laser": *IEEE J. Quant. Elec.* **27** 2091 (1991)

[6.9] H. Nagai, M. Kume, I. Ohta, H. Shimizu, M. Kazumura: "Low-noise operation of a diode-pumped intracavity-doubled Nd:YAG laser using a Brewster plate": *IEEE J. Quant. Elec.* **28** 1164 (1992)

[6.10] G. E. James, E. M. Harrell II, C. Brackiowski, K. Wiesenfield, R. Roy: "Elimination of chaos in an intracavity-doubled Nd:YAG laser": *Opt. Lett.* **15** 1141 (1990)

[6.11] M. Oka, K. Kubota: "Stable intracavity doubling of orthogonal linearly polarised modes in diode-pumped Nd:YAG lasers": *Opt. Lett.* **13** 805 (1988)

[6.12] L. Liu, M. Oka, W. Wiechmann, S. Kubota: "Longitudinally diode-pumped continuous-wave 3.5 W green laser": *Opt. Lett.* **19** 189 (1994)

[6.13] M. Oka, S. Kubota: "Second-harmonic generation green laser for higher-density optical disks": *Jap. J. App. Phys.* **31** 513 (1992)

[6.14] G. J. Kintz, T. Baer: "Single-frequency operation in solid-state laser materials with short absorption depths": *IEEE J. Quant. Elec.* **26** 1457 (1990)

[6.15] V. Ya. Molchanov, G. V. Strotskii: "Matrix method for the calculation of the polarisation eigenstates of anisotropic optical resonators": *Sov. J. Quant. Elec.* **1** 315 (1972)

[6.16] J. Junghans, M. Keller, H. Weber: "Laser resonators with polarising elements - eigenstates and eigenvalues of polarisation": *App. Opt.* **13** 2793 (1974)

[6.17] T. Y. Fan: "Single-axial mode, intracavity doubled Nd:YAG laser": *IEEE J. Quant. Elec.* **27** 2091 (1991)

[6.18] H. Nagai, M. Kume, I. Ohta, H. Shimizu, M. Kazumura: "Low-noise operation of a diode-pumped intracavity-doubled Nd:YAG laser using a Brewster plate": *IEEE J. Quant. Elec.* **28** 1164 (1992)

[6.19] W. A. Clarkson, K. I. Martin, D. C. Hanna: "High-power single-frequency operation and efficient intracavity frequency-doubling of a Nd:YAG ring laser end-pumped by a 20 W diode-bar": *Conf. on Lasers & Electroopt. OSA Tech. Dig.* **15** 19 (1995) paper CMD8

Chapter 7

CONCLUSIONS

The intracavity frequency-doubling of 1 μm Nd:YAG lasers in the mid-1960s was one of the pioneering topics of research in quantum electronics. The theory of internally doubled CW and Q-switched lasers was fully established by 1970; that of actively modelocked systems by 1975. The key physical principles involved are now well understood so that the further development of these devices rests primarily on technological advances rather than on any great scientific insight. The major design issues for high-power bulk intracavity-doubled systems are discussed below.

In most laboratory situations, only a few tens of watts of pump power are normally available. To obtain high-power operation from a simple system therefore demands emphasis on efficiency, which tends to lead to longitudinal rather than transverse pumping. The experimental work described in this thesis has shown that, while side-pumping is simple and reliable, it cannot compete with end-pumping in terms of raw power. Of course, for very high power 1 μm operation where output powers of hundreds of watts are required, side-pumped designs are still common, but these are generally pumped by multiple stacks of diode-bars; efficiency is not a prime concern. The accurate deposition of pump energy within the laser mode volume that is associated with end-pumping leads to a number of benefits. Most obvious is the increased pump-mode overlap integral due to better spatial matching of the pump and signal fields and the increased interaction length. In addition to reduced thresholds and higher slope efficiencies this pumping geometry allows better transverse mode control and reduced thermal lensing, thermal birefringence and thermal damage caused by "wasted" pump energy, *i.e.* pump energy not absorbed within the mode volume. Reduced thermal problems lead back to even more output power; a higher operating level can be reached before thermal limitations set in.

The current high level of interest in high-power diode-pumped lasers and their intracavity frequency-doubling has highlighted the question of beam quality available from diode-laser devices. Symmetry and brightness are key issues in end-pumping as they govern the pump-signal interaction length. The fibre-coupling of diode-laser arrays is currently a popular route to a symmetrical pump beam. Achieving high brightness by the use low small-core low NA fibres is more important than raw power. The total pump power can be scaled up by using more than one input point, and this also has the advantage of distributing the thermal load. The advent of high-power, bright fibre-coupled systems has meant that coupling losses are now far outweighed by the improved efficiency from fibre-tip to laser.

Another current avenue of research on the improvement of pump beams is the direct reshaping of the output of diode-bars. The efficacy of this approach has been clearly demonstrated, and it has the potential to challenge the efficiency and reliability of the fibre-coupled methodology.

Resonator design must encompass a number of aims if efficient high-power harmonic output is to be achieved. High gain (discussed above) and low linear loss are the two principal goals for an intracavity doubled laser. One general principle is therefore to keep the ratio of gain to linear loss as high as possible. Maximising the mode size in the gain medium to improve pump-mode overlap while keeping the number of cavity elements to a minimum are generally desirable objectives. High gain and low linear loss mean that only modest nonlinearity is needed for a laser to achieve its full potential in terms of harmonic output power. Focusing requirements may be relaxed if these two objectives are met.

For several years, the issue of the intracavity doubling of single and multi-longitudinal mode lasers has been a subject of considerable interest. Quiet multimode operation has been achieved by the use of standing wave cavities in which a large number of modes are above threshold. Although several novel single-frequency schemes have been developed over recent years for standing-wave cavities, these tend to break down for high-gain lasers. High power single-frequency output now generally means the use of a unidirectional ring resonator.

Crystal technology is still an important aspect of the development of these lasers. Recently, the exploitation of the strong 808 nm absorption feature of $Nd:YVO_4$ has led to high-power operation at 1 and 0.5 μm, despite its low thermal conductivity. The use of LBO as the nonlinear crystal, as opposed to KTP, is now common to high-power 0.5 μm sources. The main reason for this is the possibility for type I non-critical phase-matching, eliminating birefringence and allowing a simple (linear) intracavity polarisation state. Although its nonlinearity is quite modest, the high gains now achievable mean that this is not quite the problem it once was; optimum nonlinear coupling for intracavity doubled lasers is falling as the 1 μm output powers continue to increase. The large angular acceptance bandwidth of LBO is ideal for focused beams. The absence of walk-off is another advantage. Given the extremely high intracavity powers that are now being demonstrated, the high damage threshold of LBO could prove to be its most important attribute.

The diode-pumped, intracavity-doubled Nd laser is now at a very high level of development, and high-power, high-efficiency devices are becoming commercially available. Further increases in green output powers are likely to be reported if the brightness from fibre-coupled diode-bars increases, or if some brighter and equally reliable pumping technology is developed. The development of new Nd-host crystals with greater absorption coefficients and thermal conductivities would also have a beneficial impact on these lasers.

Appendix 1

PROGRAM FOR THE CALCULATION OF POLARISATION ROTATION IN A NON-PLANAR RING RESONATOR: BEAM-BASED METHOD

	A	B	C	D	E	F
1		i	j	k	**Modulus**	**DPs/Ang/Other**
2	**NP angle Ω in degs**				00.00000	10.00000
3	**Height h**				00.00000	55.00000
4	**Plane Mirror Sep L**				00.00000	220.00000
5	**Curved Mirror Sep D**				00.00000	100.00000
6	**OSA rads**				00.00000	00.07242
7	**OSA degs**				00.00000	04.14912
8	**Input Ray I1**	00.07267	-01.00000	00.00000	01.00264	
9	**Normalised input ray i1**	00.07248	-00.99737	00.00000	01.00000	
10					00.00000	
11	**NP angle in rads**				00.00000	00.17453
12	**L^2 /4**				00.00000	12100.00000
13	**D^2/4**				00.00000	2500.00000
14	**(L*D)*0.5*cosΩ**				00.00000	10832.88528
15	**l**				00.00000	159.47691
16					00.00000	
17	**R1**	-08.68241	159.24039	55.00000	168.69465	
18	**r1**	-00.05147	00.94396	00.32603	01.00000	
19	**r1 X i1**	00.32518	00.02363	-00.01708	00.32648	
20	**r1 X i1 hat =N1**	00.99600	00.07238	-00.05233	01.00000	
21					00.00000	
22	**i1.r1**				00.00000	-00.94520
23	**AOI 1 in rads**				00.00000	00.16629
24	**AOI 1 in degs**				00.00000	09.52764

	A	B	C	D	E	F
25					00.00000	
26	**Angle z in rads**				00.00000	00.05447
27	**Angle z in degs**				00.00000	03.12090
28	**Angle x in rads**				00.00000	00.12006
29	**Angle x in degs**				00.00000	06.87910
30	**z+x in degs**				00.00000	10.00000
31					00.00000	
32	**(-i1-r1)**	-00.02101	00.05341	-00.32603	00.33105	
33	**(-i1-r1)hat = A**	-00.06347	00.16135	-00.98485	01.00000	
34	**(-N1) = B**	-00.99600	-00.07238	00.05233	01.00000	
35	**A X B = n1**	-00.06284	00.98424	00.16530	01.00000	
36					00.00000	
37	**i2 (=r1)**	-00.05147	00.94396	00.32603	01.00000	
38	**R2**	00.17633	-01.00000	00.00000	01.01543	
39	**r2**	00.17365	-00.98481	00.00000	01.00000	
40	**r2 X i2**	-00.32108	-00.05662	00.11323	00.34514	
41	**r2 X i2 hat =N2**	-00.93030	-00.16404	00.32807	01.00000	
42					00.00000	
43	**i2.r2**				00.00000	-00.93855
44	**AOI 2 in rads**				00.00000	00.17619
45	**AOI 2 in degs**				00.00000	10.09503
46					00.00000	
47	**(-i2-r2)**	-00.12218	00.04085	-00.32603	00.35056	
48	**(-i2-r2)hat = C**	-00.34853	00.11653	-00.93003	01.00000	

	A	B	C	D	E	F
49	(-N2) = D	00.93030	00.16404	-00.32807	01.00000	
50	C X D = n2	00.11433	-00.97955	-00.16558	01.00000	
51					00.00000	
52	N1.N2				00.00000	-00.95562
53	Angle POI1,2 in rads				00.00000	02.84256
54	Angle POI1,2 in degs				00.00000	162.86695
55					00.00000	
56	i3 (=r2)	00.17365	-00.98481	00.00000	01.00000	
57	R3	-08.68241	159.24039	-55.00000	168.69465	
58	r3	-00.05147	00.94396	-00.32603	01.00000	
59	r3 X i3	-00.32108	-00.05662	-00.11323	00.34514	
60	(r3 X i3) hat = N3	-00.93030	-00.16404	-00.32807	01.00000	
61					00.00000	
62	(-i3-r3)	-00.12218	00.04085	00.32603	00.35056	
63	(-i3-r3)hat = E	-00.34853	00.11653	00.93003	01.00000	
64	(-N3) = F	00.93030	00.16404	00.32807	01.00000	
65	E X F = n3	-00.11433	00.97955	-00.16558	01.00000	
66						
67	i3.r3					-00.93855
68	AOI 3 in rads					00.17619
69	AOI 3 in degs					10.09503
70					00.00000	
71	N2.N3				00.00000	00.78473
72	Angle POI2,3 in rads				00.00000	00.66853

	A	B	C	D	E	F
73	**Angle POI2,3 in degs**				00.00000	38.30386
74					00.00000	
75	**i4 (=r3)**	-00.05147	00.94396	-00.32603	01.00000	
76	**r4 = i1**	00.07248	-00.99737	00.00000	01.00000	
77	**r4 X i4**	00.32518	00.02363	00.01708	00.32648	
78	**(r4 X i4) hat = N4**	00.99600	00.07238	00.05233	01.00000	
79	**(-i4-r4)**	-00.02101	00.05341	00.32603	00.33105	
80	**(-i4-r4)hat = G**	-00.06347	00.16135	00.98485	01.00000	
81	**(-N4) = H**	-00.99600	-00.07238	-00.05233	01.00000	
82	**G X H = n4**	00.06284	-00.98424	00.16530	01.00000	
83						
84	**i4.r4**					-00.94520
85	**AOI 4 in rads**					00.16629
86	**AOI 4 in degs**					09.52764
87					00.00000	
88					00.00000	
89	**N3.N4**				00.00000	-00.95562
90	**Angle POI3,4 in rads**				00.00000	02.84256
91	**Angle POI3,4 in degs**				00.00000	162.86695
92					00.00000	
93	**N4.N1**				00.00000	00.99452
94	**Angle POI4,1 in rads**				00.00000	00.10471
95	**Angle POI4,1 in degs**				00.00000	05.99917
96					00.00000	

	A	B	C	D	E	F
97					00.00000	
98					00.00000	
99	**p1 in lab XYZ**	00.00000	01.00000	00.00000	01.00000	
100	**p1 in ijk**	00.99738	00.07235	00.00000	01.00000	
101					00.00000	
102					00.00000	
103	**p1.N1 in ijk system**				00.00000	00.99863
104	**Angle XYZ,x1y1z1 in rads**				00.00000	00.05235
105	**Angle XYZ,x1y1z1 in degs**				00.00000	02.99959
106					00.00000	
107	**Matrix XYZ to x1y1z1**	00.99863	00.05233	00.00000	01.00000	
108	**Matrix XYZ to x1y1z1**	-00.05233	00.99863	00.00000	01.00000	
109	**Matrix XYZ to x1y1z1**	00.00000	00.00000	01.00000	01.00000	
110					00.00000	
111	**p1 in x1y1z1**	00.05233	00.99863	00.00000	01.00000	
112	**p1' in x1'y1'z1'**	-00.05233	00.99863	00.00000	01.00000	
113					00.00000	
114	**C(1,2) x1'y1'z1' to x2y2z2**	00.95562	00.29459	00.00000	01.00000	
115	**C(1,2) x1'y1'z1' to x2y2z2**	-00.29459	00.95562	00.00000	01.00000	
116	**C(1,2) x1'y1'z1' to x2y2z2**	00.00000	00.00000	01.00000	01.00000	
117					00.00000	
118	**p1' in x2y2z2 =p2**	00.24418	00.96973	00.00000	01.00000	
119	**p2' in x2'y2'z2'**	-00.24418	00.96973	00.00000	01.00000	
120					00.00000	

	A	B	C	D	E	F
121	**C(2,3) x2'y2'z2' to x3y3z3**	-00.78473	-00.61983	00.00000	01.00000	
122	**C(2,3) x2'y2'z2' to x3y3z3**	00.61983	-00.78473	00.00000	01.00000	
123	**C(2,3) x2'y2'z2' to x3y3z3**	00.00000	00.00000	01.00000	01.00000	
124					00.00000	
125	**p2' in x3y3z3 = p3**	-00.40945	-00.91233	00.00000	01.00000	
126	**p3' in x3'y3'z3'**	00.40945	-00.91233	00.00000	01.00000	
127					00.00000	
128	**C(3,4) x3'y3'z3' to x4y4z4**	00.95562	00.29459	00.00000	01.00000	
129	**C(3,4) x3'y3'z3' to x4y4z4**	-00.29459	00.95562	00.00000	01.00000	
130	**C(3,4) x3'y3'z3' to x4y4z4**	00.00000	00.00000	01.00000	01.00000	
131					00.00000	
132	**p3' in x4y4z4 = p4**	00.12252	-00.99247	00.00000	01.00000	
133	**p4' in x4y4z4**	-00.12252	-00.99247	00.00000	01.00000	
134					00.00000	
135	**C(4,1) x4'y4'z4' to x1y1z1**	-00.99452	00.10451	00.00000	01.00000	
136	**C(4,1) x4'y4'z4' to x1y1z1**	-00.10451	-00.99452	00.00000	01.00000	
137	**C(4,1) x4'y4'z4' to x1y1z1**	00.00000	00.00000	01.00000	01.00000	
138					00.00000	
139	**p4' in x1y1z1 = rotated p1**	00.01812	00.99984	00.00000	01.00000	
140					00.00000	
141	**p1.rotated p1**				00.00000	00.99941
142	**Angle of rotation in rads**				00.00000	00.03423
143	**Angle of rotation in degs**				00.00000	01.96141
144					00.00000	

	A	B	C	D	E	F
145	**Reflection Matrices:**				00.00000	
146					00.00000	
147	**R(1) x1y1z1 to x1'y1'z1'**	01.00000	00.00000	00.00000	01.00000	
148	**R(1) x1y1z1 to x1'y1'z1'**	00.00000	-00.94520	-00.32648	01.00000	
149	**R(1) x1y1z1 to x1'y1'z1'**	00.00000	00.32648	-00.94520	01.00000	
150					00.00000	
151	**R(2) x2y2z2 to x2'y2'z2'**	01.00000	00.00000	00.00000	01.00000	
152	**R(2) x2y2z2 to x2'y2'z2'**	00.00000	-00.93855	00.34514	01.00000	
153	**R(2) x2y2z2 to x2'y2'z2'**	00.00000	-00.34514	-00.93855	01.00000	
154					00.00000	
155	**R(3) x3y3z3 to x3'y3'z3'**	01.00000	00.00000	00.00000	01.00000	
156	**R(3) x3y3z3 to x3'y3'z3'**	00.00000	-00.93855	-00.34514	01.00000	
157	**R(3) x3y3z3 to x3'y3'z3'**	00.00000	00.34514	-00.93855	01.00000	
158					00.00000	
159	**R(4) x4y4z4 to x4'y4'z4'**	01.00000	00.00000	00.00000	01.00000	
160	**R(4) x4y4z4 to x4'y4'z4'**	00.00000	-00.94520	00.32648	01.00000	
161	**R(4) x4y4z4 to x4'y4'z4'**	00.00000	-00.32648	-00.94520	01.00000	
162					00.00000	
163					00.00000	
164	**Round Trip Matrix**				00.00000	
165					00.00000	
166	C(1,2)R(1)	00.95562	-00.27845	-00.09618	01.00000	
167		-00.29459	-00.90326	-00.31199	01.00000	
168		00.00000	00.32648	-00.94520	01.00000	

	A	B	C	D	E	F
169					00.00000	
170	R(2)C(1,2)R(1)	00.95562	-00.27845	-00.09618	01.00000	
171		00.27649	00.96044	-00.03340	01.00000	
172		00.10167	00.00533	00.99480	01.00000	
173					00.00000	
174	C(2,3)R(2)C(1,2)R(1)	-00.92129	-00.37680	00.09618	01.00000	
175		00.37535	-00.92628	-00.03340	01.00000	
176		00.10167	00.00533	00.99480	01.00000	
177					00.00000	
178	R(3)C(2,3)R(2)C(1,2)R(1)	-00.92129	-00.37680	00.09618	01.00000	
179		-00.38738	00.86752	-00.31199	01.00000	
180		00.03412	-00.32469	-00.94520	01.00000	
181					00.00000	
182	C(3,4)R(3)C(2,3)R(2)C(1,2)R(1)	-00.99452	-00.10451	00.00000	01.00000	
183		-00.09879	00.94003	-00.32648	01.00000	
184		00.03412	-00.32469	-00.94520	01.00000	
185					00.00000	
186	R(4)C(3,4)R(3)C(2,3)R(2)C(1,2)R(1)	-00.99452	-00.10451	00.00000	01.00000	
187		00.10451	-00.99452	00.00000	01.00000	
188		00.00000	00.00000	01.00000	01.00000	
189					00.00000	
190	C(4,1)R(4)C(3,4)R(3)C(2,3)R(2)C(1,2)R(1)	01.00000	00.00000	00.00000	01.00000	
191		00.00000	01.00000	00.00000	01.00000	
192		00.00000	00.00000	01.00000	01.00000	

	A	B	C	D	E	F
193					00.00000	
194	p1 in x1y1z1	00.05233	00.99863	00.00000	01.00000	
195					00.00000	
196	RTMp(1)	00.05233	00.99863	00.00000	01.00000	
197					00.00000	
198	p1.RTMp1				00.00000	01.00000
199	Geometrical Rotation Angle in rads				00.00000	#NUM!
200	Geometrical Rotation Angle in degs				00.00000	#NUM!

Appendix 2

PROGRAM FOR THE CALCULATION OF POLARISATION ROTATION IN A NON-PLANAR RING RESONATOR: VECTOR METHOD

	A	B	C	D	E	F	G	H	I	J	K	L	M	N	O	P	Q
1							Calculation for polarisation						Calculation for ray direction				
2			i	j	k			i	j	k				i	j	k	
3	data input	**input pol**	**0.997**	**0.072**	**0.000**		*input pol=p*	*0.997*	*0.072*	*0.000*			*input ray= i*	*0.072*	*-0.997*	*0.000*	
4		*input pol*	*0.997*	*0.072*	*0.000*		*mirror = n*	*-0.063*	*0.984*	*0.165*			*mirror = n*	*-0.063*	*0.984*	*0.165*	
5	data input	**input ray**	**0.072**	**-0.997**	**0.000**		*p.n*	-0.063	0.071	0.000	0.009		*n.-i*	0.005	0.982	0.000	0.986
6		*input ray*	*0.072*	*-0.997*	*0.000*		*p.n (n)*	-0.001	0.008	0.001			reflected ray	-0.051	0.944	0.326	
7	data input	**mirror 1**	**-0.063**	**0.984**	**0.165**								*r*	*-0.051*	*0.944*	*0.326*	
8		*mirror*	*-0.063*	*0.984*	*0.165*		*p*	*0.997*	*0.072*	*0.000*							
9							*n*	*-0.063*	*0.984*	*0.165*			check p.r=0 ?	0.051	-0.052	0.001	0.000
10							pXn	0.012	-0.165	0.986							
11		*reflected pol*	*-0.998*	*-0.056*	*0.003*		*pXn*	*0.012*	*-0.165*	*0.986*							
12							*n*	*-0.063*	*0.984*	*0.165*							
13		*reflected ray*	*-0.051*	*0.944*	*0.326*		(pXn)Xn	-0.998	-0.064	0.001							
14							*(pXn)Xn*	*-0.998*	*-0.064*	*0.001*							
15							*p*	*0.997*	*0.072*	*0.000*							
16							*p.(pXn)Xn*	-0.995	-0.005	0.000	-1.000						
17							*p.(pXn)Xn(pXn)Xn*	0.998	0.064	-0.001							
18																	
19							*input pol=p*	*-0.998*	*-0.056*	*0.003*			*input ray= i*	*-0.051*	*0.944*	*0.326*	
20		*input pol*	*-0.998*	*-0.056*	*0.003*		*mirror = n*	*0.114*	*-0.980*	*-0.166*			*mirror = n*	*0.114*	*-0.980*	*-0.166*	
21		*input ray*	*-0.051*	*0.944*	*0.326*		*p.n*	-0.114	0.054	0.000	-0.060		*n.-i*	0.006	0.925	0.054	0.985
22							*p.n (n)*	-0.007	0.059	0.010			reflected ray	0.174	-0.985	0.000	
23	data input	**mirror 2**	**0.114**	**-0.980**	**-0.166**								*r*	*0.174*	*-0.985*	*0.000*	
24		*mirror*	*0.114*	*-0.980*	*-0.166*		*p*	*-0.998*	*-0.056*	*0.003*							
25							*n*	*0.114*	*-0.980*	*-0.166*			check p.r=0 ?	0.171	-0.171	0.000	0.000
26							pXn	0.012	-0.165	0.984							
27		*reflected pol*	*0.985*	*0.173*	*0.017*		*pXn*	*0.012*	*-0.165*	*0.986*							
28							*n*	*0.114*	*-0.980*	*-0.166*							
29		*reflected ray*	*0.174*	*-0.985*	*0.000*		(pXn)Xn	0.993	0.115	0.007							
30							*(pXn)Xn*	*0.993*	*0.115*	*0.007*							
31							*p*	*-0.998*	*-0.056*	*0.003*							
32							*p.(pXn)Xn*	-0.992	-0.006	0.000	-0.998						
33							*p.(pXn)Xn(pXn)Xn*	-0.992	-0.115	-0.007							
34																	
35																	
36																	
37																	

	A	B	C	D	E	F	G	H	I	J	K	L	M	N	O	P	Q
38																	
39																	
40							*input pol=p*	*0.985*	*0.173*	*0.017*			*input ray= i*	*0.174*	*-0.985*	*0.000*	
41		*input pol*	*0.985*	*0.173*	*0.017*		*mirror = n*	*-0.114*	*0.980*	*-0.166*			*mirror = n*	*-0.114*	*0.980*	*-0.166*	
42		*input ray*	*0.174*	*-0.985*	*0.000*		*p.n*	-0.113	0.170	-0.003	0.055		*n.-i*	0.020	0.965	0.000	0.985
43							*p.n (n)*	-0.006	0.053	-0.009			reflected ray	-0.051	0.944	-0.326	
44	data input	**mirror 3**	**-0.114**	**0.980**	**-0.166**								*r*	*-0.051*	*0.944*	*-0.326*	
45		*mirror*	*-0.114*	*0.980*	*-0.166*		*p*	*0.985*	*0.173*	*0.017*							
46							*n*	*-0.114*	*0.980*	*-0.166*			check p.r=0	0.051	-0.063	0.011	0.000
47							pXn	-0.045	0.161	0.984							
48		*reflected pol*	*-0.997*	*-0.067*	*-0.035*		*pXn*	*-0.046*	*0.161*	*0.986*							
49							*n*	*-0.114*	*0.980*	*-0.166*							
50		*reflected ray*	*-0.051*	*0.944*	*-0.326*		(pXn)Xn	-0.992	-0.120	-0.026							
51							*(pXn)Xn*	*-0.992*	*-0.120*	*-0.026*							
52							*p*	*0.985*	*0.173*	*0.017*							
53							*p.(pXn)Xn*	-0.977	-0.021	0.000	-0.999						
54							*p.(pXn)Xn(pXn)Xn*	0.991	0.120	0.026							
55																	
56							*input pol=p*	*-0.997*	*-0.067*	*-0.035*			*input ray= i*	*-0.051*	*0.944*	*-0.326*	
57		*input pol*	*-0.997*	*-0.067*	*-0.035*		*mirror = n*	*0.063*	*-0.984*	*0.166*			*mirror = n*	*0.063*	*-0.984*	*0.166*	
58		*input ray*	*-0.051*	*0.944*	*-0.326*		*p.n*	-0.063	0.066	-0.006	-0.003		*n.-i*	0.003	0.929	0.054	0.986
59							*p.n (n)*	0.000	0.003	0.000			reflected ray	0.073	-0.998	0.001	
60		**mirror 4**	**0.063**	**-0.984**	**0.165**								*r*	*0.072*	*-0.997*	*0.001*	
61		*mirror*	*0.063*	*-0.984*	*0.166*		*p*	*-0.997*	*-0.067*	*-0.035*							
62							*n*	*0.063*	*-0.984*	*0.166*			check p.r=0	0.072	-0.072	0.000	0.000
63							pXn	-0.046	0.163	0.986							
64		*reflected pol*	*0.997*	*0.072*	*0.034*		*pXn*	*-0.046*	*0.163*	*0.986*							
65							*n*	*0.063*	*-0.984*	*0.166*							
66		*reflected ray*	*0.072*	*-0.997*	*0.001*		(pXn)Xn	0.997	0.070	0.035			**Output pol**		**0.997**	**0.072**	**0.034**
67							*(pXn)Xn*	*0.997*	*0.070*	*0.035*			**Net Rotation**		**1.961**	**degrees**	
68							*p*	*-0.997*	*-0.067*	*-0.035*			**Output Ray**		**0.072**	**-0.997**	**0.001**
69							*p.(pXn)Xn*	-0.994	-0.005	-0.001	-1.000						
70							*p.(pXn)Xn(pXn)Xn*	-0.997	-0.070	-0.035							
71																	
72																	
73																	